CRANFIELD INSTITUTE OF TECHNOLOGY

SCHOOL OF MECHANICAL ENGINEERING

Ph.D. THESIS

L.KABARI

FLOW AND HEAT TRANSFERS ASSOCIATED WITH IMPINGING JETS IN CROSSFLOWS

SUPERVISOR: J.WARD

November, 1977

SUMMARY

This thesis reports the results of an experimental study into the flow and heat transfers associated with both inclined and orthogonally impinging axisymmetric air jets. The majority of previously reported studies have been mainly confined to orthogonally impinging jets in stagnant surroundings. In this investigation, free jets as well as the effects of crossflows are considered.

This investigation is primarily concerned with local heat transfer variations. The experimental tests were conducted with a single 12.7 mm diameter jet impinging on a flat surface, and heat transfers were evaluated using a heat-mass transfer analogy (the Chilton-Colburn analogy). The sublimation of naphthalene was employed as the mass transfer technique.

The flowfield associated with impinging jets has a significant influence on their heat transfer characteristics. In view of the present limited level of understanding of this 'complex' flowfield, extensive flow visualisation techniques were employed in this present investigation. These were primarily intended to aid interpretation of the experimental heat transfer results, and also to provide further physical understanding of the flowfields resulting from the interactions between impinging jets and crossflowing streams.

The flow and heat transfer tests conducted in the programme of work reported in this thesis covered typical ranges of flow parameters of interest in many practical applications of jet impingement systems. Jet inclinations of 45°, 60°, and 90°, nozzle to target spacings of 2, 4, and 8 nozzle diameters were studied. The Reynolds numbers were 30,200, 32,700 and 55,100 and mass velocity ratios in the range 4.0 to 8.8 were studied.

The effects of these parameters on the flow and heat transfers associated with impinging jets are reported. Comparisons were drawn between the heat transfer results and those of previously reported studies where appropriate.

ACKNOWLEDGEMENTS

The author would like to express his sincere and profound thanks to his Project Supervisor, Mr. J.Ward for his advice, guidance, and encouragement throughout the course of this work. His willingness to discuss without delay, the problems encountered during the work, made the author's task considerably easier.

Thanks are also due to Mr. B.Hunt and the staff of the Photographic Department for their patience and co-operation, particularly during the flow visualisation tests.

Acknowledgement is made to Messrs F.W.Pearman, D.C.Beattie, L.Relton, and the other Workshop staff for their assistance in the construction of various parts of the rig. Particular mention should also be made of Mr. J.Jewell who also assisted with the rig assembly.

Thanks are also due to Mr. C.Chapman for his practical assistance at various stages of the work.

Acknowledgement is made to Mr. R.T.Wilson and the Drawing Office staff. In this connection, special thanks are due to Mr. R.H.Dewar who was responsible for producing the graphs and diagrams in the thesis.

Finally, the author wishes to extend his thanks to his family for their encouragement throughout this work, and to express his gratitude to the Government of the Rivers State of Nigeria for the financial support given him throughout his stay in Cranfield.

CONTENTS

Page

APPENDICES

LIST OF TABLES

LIST OF FIGURES

NOMENCLATURE

Symbols used, unless defined at the point where they are introduced into the text, have the following meanings:-

Symbol	Meaning
A	Area of nozzle Constant in King's Law expression (Eqn. D.2) Constant in Jayatillaka's analogy (Ref. 112)
b	Mass transfer coefficient
B	Width of slot jet Constant in King's law expression (Eqn. D.2)
C	Mass concentration of vapour
C_f	Friction factor $\left[\tau_w/(\frac{1}{2}\rho U^2)\right]$
C_o	Mass concentration of vapour in free stream
C_p	Specific heat at constant pressure
C_N	Mass concentration of vapour at solid boundary
d	Nozzle diameter Jet exit diameter Wire diameter
D	Mass diffusion coefficient
E	Voltage proportional to mean velocity under flow conditions
E_i	Input quantity
E_o	Voltage proportional to mean velocity in still air Output quantity
G	Flow rate per unit flow area

$G(d,s)$	Mass flow rate per unit nozzle area over local impingement plate designated by s
$G(X,s-1)$	Mass flow rate per unit crossflow area upstream of the local impingement plate designated by s
h	Local heat transfer coefficient
h_o	Local heat transfer coefficient at stagnation point.
I	Ratio of momentum flux for jet and crossflowing stream $\left[I = (\rho_j U_j^2)/(\rho_c U_c^2)\right]$
j_H	Dimensionless heat transfer factor
j_M	Dimensionless mass transfer factor
k	Thermal conductivity
K	Constant
L	Length
m	Mass loss of naphthalene
M	Jet-to-crossflow mass velocity ratio, or Blowing rate $\left[M = (\rho_j U_j)/(\rho_c U_c)\right]$
n	Index in hot-wire expression (Eqn. D.3)
N	Rate of mass transfer per unit area
P	Saturation vapour pressure
q	Dynamic pressure
$\dot{q}$	Rate of heat transfer per unit area
Q	Volume flow rate
Q	Rate of heat transfer
R	Gas constant Absolute error Jet-to-crossflow velocity ratio $\left[R = U_j/U_c\right]$
R_{gN}, R_v	Gas constant for naphthalene vapour

t	Time Temperature in boundary layer in appendix B
t^+	Dimensionless temperature $\left[\dfrac{t_w - t}{q_w/\rho C_p U}\right]$
T	Absolute temperature
T_L	Absolute temperature of air in supply line
T_o	Absolute temperature of vapour in free stream
T_N	Absolute temperature of vapour at solid boundary
Tu	Turbulence intensity $\left[\dfrac{u'}{U_{max}}\right]$
u'	Axial component of turbulent velocity fluctuation
U	Velocity component in stream direction
U_j	Axial component of jet velocity
U_c	Velocity of crossflowing stream
U^+	Dimensionless velocity (U/U_τ)
U_τ	Wall shear velocity $\sqrt{(\tau_w/\rho)}$
U_{max}	Maximum axial velocity of jet across a section
W_x	Mass flow
x	Streamwise position co-ordinate Distance from stagnation point
X	Nozzle spacing or pitch
y	Lateral distance co-ordinate from centre-line of initially free orthogonal jet Vertical distance from wall in boundary layer flow in appendix B
y^+	Dimensionless distance from wall $(U_\tau y/\nu)$

Z	Distance between nozzle and impingement plates

DIMENSIONLESS NUMBERS

Nu_d	Local or average Nusselt number based on nozzle diameter
Nu_o	Local Nusselt number at stagnation point based on nozzle diameter or width (hd/k or hB/k)
Kn	Knudsen number based on wire diameter (λ/d)
Pr	Molecular Prandtl number $(c_p\mu/k)$
Pr_t	Turbulent Prandtl number (ϵ_m/ϵ_h)
Re_a	Reynolds number based on nozzle diameter and arrival velocity at impingement plate
Re_e	Reynolds number based on nozzle diameter and exit velocity from nozzle
Sc	Schmidt number $(\mu/\rho D)$
Sc_t	Turbulent Schmidt number (ϵ_m/ϵ_D)
Sh	Sherwood number (bd/D)

GREEK SYMBOLS

α	Thermal diffusivity Jet inclination to horizontal axis
Δ	Naphthalene loss expressed in mm
ϵ	Eddy diffusivity
λ	Mean free path of gas molecules
μ	Dynamic viscosity
υ	Kinematic viscosity
ρ	Density of fluid

σ	Uncertainty
τ	Shear stress

SUBSCRIPTS

av	Average value
A	Approximate flow
b	Bulk mean value
c	Of crossflow Corrected flow
d	Based on nozzle diameter
D	For mass
f	In free stream in appendix D
h	For heat
j	Of jet
l	At edge of sublayer
L	In-line value Laminar condition
m	Mean film value For momentum
M	Mass transfer value
N	At naphthalene surface
o	Stagnation value Main stream value
r	Based on jet exit radius
T, t	Turbulent condition
w	At the wall Of wire

CHAPTER 1

INTRODUCTION.

1.1 The Nature of the Problem.

This thesis is concerned with the flows and heat transfers associated with both inclined and orthogonally impinging axisymmetric air jets. Free jets as well as the effects of crossflows are considered. The tests were conducted with single jets impinging on a flat surface and the heat transfers were evaluated by using a heat-mass transfer analogy (the sublimation of Naphthalene). The project is part of a programme of research to improve the design of rapid heating furnaces, by using isothermal models to simulate the furnace chamber.

The flow structure associated with impinging jets has considerable influence on their heat transfer characteristics, and as will be seen in Chapter II of this thesis, this is so complex that the flowfield must be broken down into subregions to assist the analysis. The flowfield is even more complicated when the impinging jet is modified by a crossflowing stream. The heat transfer mechanism in these cases is, clearly, forced convection.

A thorough understanding of jet flow and heat transfer is fundamental to the effective application of jets in other applications as well as in jet impingement furnaces. Despite the vast number of published reports now available, the flowfield and heat transfer under impinging jets are still not completely understood. No completely comprehensive theory to predict the flow or heat transfer exists.

Recent advances now suggest that considerable experimental and theoretical work is still needed; for while experiments without theory can only lead to particular rather than general conclusions, theory without experiments can rarely be practically useful.

In an economic climate affected by scarce and limited fuel resources, and with increasing trends towards more efficient utilisation of the energy now available, there are exciting possibilities for the use of impinging jets in a wider variety of industrial processes and activities. This can only be possible if the flowfield and heat transfer associated with impinging jets are clearly understood.

Current industrial and process applications of impinging jets can be divided broadly into four categories, namely,

(1) jet heating as in rapid heating furnaces
(2) jet drying as in the textile and printing industries
(3) jet cooling as in glass and metal heat-treatment, and turbine blade cooling applications, and
(4) flow applications such as in Vertical Take-off and landing (VTOL) aircrafts in which the flow dynamics of impinging jets are utilised.

Situations where jets are subject to crossflows can also arise e.g. the injection of fuel into Combustion Chambers, Thrust Vector Control of rocket trajectories, and the discharge from chimneys into the atmosphere. Crossflows also arise in rapid heating furnaces since the combustion gases are usually exhausted from one end of the system. The use of jets in rapid heating furnaces and other important engineering situations will be examined briefly in subsequent sections of this introduction.

1.2 Jet-Impingement Furnaces.

Over the years, furnaces have been used in industry for a variety of purposes, notably for heating metals such as Aluminium, Steel and Copper to their hot-working temperatures. Rapid heating furnaces are furnaces in which remarkably high heat transfer rates can be obtained by means of the "high-speed convective heating". Impinging jets are often used for this purpose, and heat is transferred to the stock by a fast-moving stream of hot combustion products.

In conventional fuel-fired furnaces, radiation is the predominant mode (up to 95%) of heat transfer. Heat can be transferred directly from the flame to the stock and indirectly from the refractory walls. This restricts the attainable heating rates because of operational problems with the furnace materials and the rate at which energy can effectively be received from the flame.

Jet-Impingement heating, however, overcomes the above limitations, since it produces the desirable increased heating rates, thus reducing the metallurgical problems which arise during heating. This is achieved by ensuring that the jet of gas impinging on the stock is very hot; thus implying stoichiometric combustion within the burner. Secondly, the velocity of the impinging jet must be high enough to break down the stagnant boundary layer on the surface of the stock. The gas velocity is controlled partly by the gas temperature, and partly by the static pressure within the burner which is converted into dynamic head when the gas is discharged from the burner nozzle.

Fig. 1.1 illustrates the essential features of a typical jet impingement furnace. Such a furnace consists of:-

(a) A preheat zone. As the name implies, the stock is preheated in this zone both by radiation from the refractories and by convection from the exhaust gases as they flow over the in-coming material.

(b) A rapid heating zone. In this zone, heating is predominantly by forced convection from the impinging jets.

(c) A soak zone. This zone allows internal conduction to improve the temperature distribution within the stock. The main mechanism of heat transfer to the stock here, is by radiation from the furnace refractories.

The most important advantages associated with this heating technique can be summarised as follows (Refs. 1 - 10):-

(1) The relatively high heat transfers and high heating rates ensure that the time the stock spends in the hot zone of the furnace is greatly reduced. This renders jet impingement heating particularly attractive in applications where metallurgical problems can arise, through decarburisation, oxidation or other time/temperature dependent phenomena.

Oxidation produces a 'Scale' on the surface, resulting in a loss of useful and valuable metal. Decarburisation occurs near the surface of the metal beneath the scale, and leads to inferior mechanical properties (e.g. ductility and hardness).

Jet impingement furnaces prevent excessive decarburistion and lead to reduced 'Scale' formation. Apart from reduced metallurgical defects, higher productivity and more compact machinery are additional benefits.

(2) Since the mode of heat transfer is predominantly forced convection from the hot gases, such systems can have very low thermal inertia. Therefore rapid start-up and short-down are possible. This opens up attractive possibilities for improved temperature control and automation.

(3) The directional nature of the impinging jets permits localised or concentrated heating of a defined zone of limited extent. Thus, a localised area can be heated to a much higher temperature than the adjacent material (depending on the thermal conductivity of the material). The short heating times are a considerable advantage in avoiding undesirable heat conduction effects.

(4) Commercial gases such as propane, butane or natural gas are the main fuels used in these furnaces. So that reduced atmospheric pollution results.

(5) Because of the simplicity of the design, maintenance costs for rapid heating furnaces are very much reduced, particularly for smaller furnaces. Overall operating costs depend however, to an extent on the relative fuel prices. However, the actual capital costs of a jet impingement furnace may often be considerably lower than the equivalent conventional furnace.

1.3 Jet Flow in Engineering Practice.

The jet impingement furnaces discussed so far, constitute just one of several other engineering applications of impinging jets. Remarkably high heat transfer rates, which can be localised at specific zones on the impingement surface, together with the ease of automation, and precise control of the intensity are some of the attractive characteristics, so that the jet impingement technique is widely used in heating, cooling and drying operations.

Cooling applications include turbine disc cooling systems, spot cooling of electronic components, cooling of turbojet structures, cryogenic treatment of tumors, cooling of glass and metals, and maintenance of turbine blade temperatures below the metallurgical limits.

By proper installation of heating and cooling jets, one can locally speed up certain processes such as age-hardening, or vary mechanical properties such as Tensile strength, ductility and hardness over the surface of metals. A recent application is in the manufacture of prestressed automobile windscreens.

Engineering applications of jets for heating include the rapid heating furnaces discussed in the previous section of this introduction. Thermal surface treatments as in tempering or toughening of metals and glass, together with localised heat treatment of plastics and glass plates also employ impinging jets as do de-icing systemsfor air-craft wings, the de-misting of car windscreens and heating-and-air-conditioning systems.

A significant development in the last two decades is the adoption of jet dryers in which hot air is blown orthogonally onto the surface of the material.

Such impingement dryers have been used extensively in the textile industry for drying veneer, cardboard, paper, and aqueous coatings. In photography, by using hot gas jets, thermal development of photographic films has been possible.

In recent years, tests have been conducted to extend the use of jets for drying the ink in printing machines (Refs. 11 - 15). These drying operations require high rates of heat and mass transfer because of the high production speeds and the limited length of the dryer.

Engineering situations in which the flow characteristicsof jets have been utilised include jet pumps which use the momentum exchange in the mixing fluid streams to bring about a pressure rise. The VTOL aircraft mentioned previously is capable of taking off and landing in a short distance. This is achieved by the use of lifting jets installed in the wing or fuselage of the aircraft, thus providing the necessary thrust to raise the aircraft off the the ground.

Other important flow applications of jets in Engineering practice are in the simple mixing of fluid streams, gas turbine exhaust ejectors, Aerodynamic flame-holders, and the production of underwater bubble screens.

1.4 Scope and Purpose of Present Tests.

It can be seen from the preceding sections of this introduction that a sound knowledge of the flow structure and heat transfer associated with jets is fundamental to their efficient industrial application even in situations other than rapid heating furnaces.

Local heat transfer is a central concern of designers e.g. in operations in which local temperatures must be kept within metallurgical limits. This present experimental investigation will thus be concerned with local variations of heat transfer.

The flowfield associated with impinging jets has an enormous influence on their heat transfer characteristics. However as may be seen in the next chapter of this thesis, previous investigations have usually concentrated on either the flow or heat transfer aspects of the problem. This study investigates experimentally, both the heat transfer and the fundamental flow structure involved.

Velocity and turbulence measurements are reported, and the effects of jet to crossflow velocity ratios on flow and heat transfer are examined.

In view of their importance on the heat transfer characteristics, the surface flow patterns associated with impinging jets are studied. These should give a clear impression of the local patterns of the flow and hence explain variations in local heat transfer. To this end, extensive flow visualisation tests are employed, to assist in explaining the heat transfer phenomena.

This investigation also examines the effects of variations of geometrical parameters such as nozzle-to-target spacing and nozzle inclination on flow and heat transfer for impinging jets, with and without crossflows. In all cases, the jets were inclined towards the upstream direction of the crossflowing air-streams.

This thesis describes the above aspects of the current programme of research, and in addition to extending the scope of work already carried out in this field, has the following objectives:-

(1) To gain further knowledge of jet flow and heat transfer to assist in practical thermal applications of impinging jets.

(2) To propose an explanation for, and physical evidence of (through flow visualisation studies) the complicated flow field associated with impinging jets in crossflows.

(3) To investigate lines of development that might improve the jet impingement technique.

(4) To highlight areas where further research could be helpful for a deeper understanding and more effective application of the jet impingement technique.

In addition to the above objectives, the programme of work described here will provide experimental information for proposed Numerical studies on this subject which will be started in the near future at Cranfield Institute of Technology.

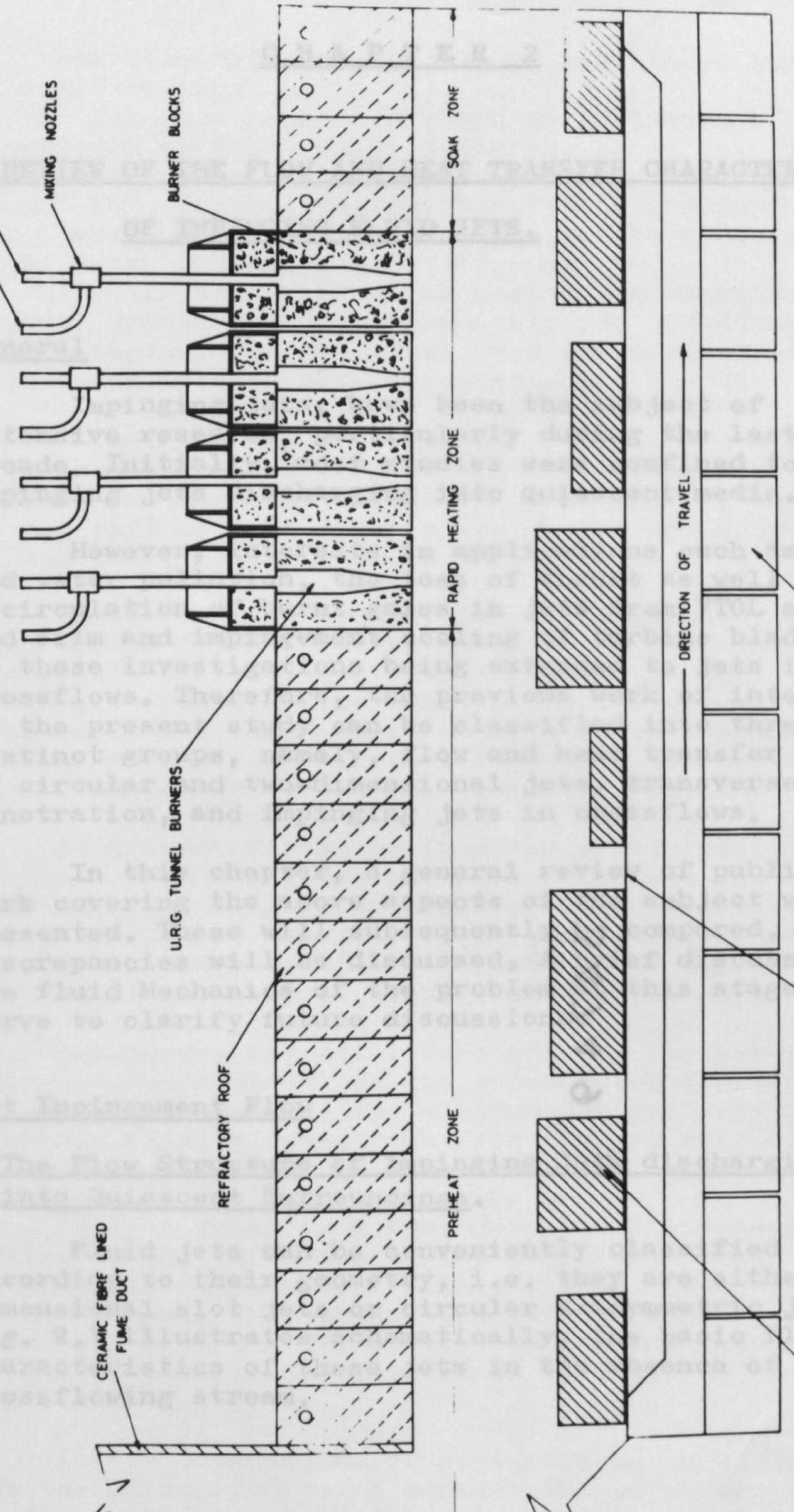

FIG. 1.1 TYPICAL JET IMPINGEMENT FURNACE.

CHAPTER 2

A REVIEW OF THE FLOW AND HEAT TRANSFER CHARACTERISTICS OF IMPINGING FLUID JETS.

2.1 General

Impinging jets, have been the subject of extensive research, particularly during the last decade. Initially, most studies were confined to impinging jets discharging into quiescent media.

However, interests in applications such as air and water pollution, the loss of thrust as well as the recirculation of burnt gases in jets from VTOL aircraft and film and impingement cooling of turbine blades, led to these investigations being extended to jets in crossflows. Therefore, the previous work of interest to the present study can be classified into three distinct groups, namely, flow and heat transfer studies of circular and two-dimensional jets, transverse jet penetration, and impinging jets in crossflows.

In this chapter, a general review of published work covering the above aspects of the subject will be presented. These will subsequently be compared, and any discrepancies will be discussed. A brief discussion of the fluid Mechanics of the problem at this stage should serve to clarify future discussions.

2.2 Jet Impingement Flow

2.2.1 The Flow Structure of Impinging Jets discharging into Quiescent Surroundings.

Fluid jets can be conveniently classified according to their geometry, i.e. they are either two-dimensional slot jets or circular axisymmetric jets. Fig. 2.1 illustrates schematically, the basic flow characteristics of these jets in the absence of a crossflowing stream.

The flowfield may be divided into three regions as shown, namely:
(1) The free jet region in which no influence of the impingement surface can be detected.
(2) The impingement region in which the flow turns through 90°. In this region, the static pressure varies from a maximum value at the centre to the ambient value at its outer boundary (Ref. 16), and
(3) The wall jet region which begins for circular jets, at radii greater than approximately one jet diameter. In this region, the jet flows over the surface with an essentially zero pressure gradient.

The free jet and wall jet regions are mainly influenced by viscous forces. In the impingement region, pressure and momentum forces are predominant, provided the jet exit is reasonably close to the impingement surface (Ref. 17).

On leaving the nozzle, the outer boundary of the jet entrains fluid from the surrounding environment. As a result of this, the velocity near the jet boundary is reduced. The central core, however, is not affected by the entrainment at this initial stage; so that the velocity within this region is unaltered. This central region is termed the 'Potential Core' of the jet.

At greater distances from the nozzle exit, the potential core decreases in width, although the central velocity is unchanged. Eventually, entrainment effects extend throughout the jet. It is generally agreed that the cone-shaped potential core extends to approximately five jet diameters downstream from the jet exit.

Beyond the potential core region, further viscous mixing and entrainment of the surrounding fluid result in further jet spread. The maximum jet velocity thus decreases axially downstream from the jet exit since momentum is conserved in this process.

After flowing as a free jet, the fluid begins to experience the influence of the impingement surface, and the so-called impingement region ensues. The jet velocity thus decreases, the streamlines turn through 90°, and the static pressure rises. The centre-line velocity of the jet eventually decelerates to zero at the stagnation point.

A wall boundary layer builds up on this surface from the stagnation point beneath the outer impinging jet flow. This boundary layer has been shown to have a constant thickness over a near-stagnation region of 1.2 jet diameters (Ref. 18), beyond which layer growth occurs. After impingement, the centre-line velocity of the jet accelerates from zero at the stagnation point until the end of the impingement region where acceleration ceases. Accordingly, the static pressure decreases from a maximum value at the stagnation point to the ambient value at the end of the so-called impingement region.

There is a negligibly small transition between this impingement zone and the subsequent third region 3 where the flow behaves as the well-known 'turbulent wall jet'. In this wall jet region, the centre-line velocity decays in a similar manner to that in the free jet. Boundary layer spread due to entrainment is also similar.

The above brief and simplified description illustrates the complexity of the flowfield of impinging jets. The problem has however been subject to considerable attention, both experimentally and theoretically. A theoretical solution for the wall jet is given by Glauert (Ref. 19), whilst experimental data are available in Bakke (Ref. 20). Further experimental results for a circular impinging jet have been presented by Bradshaw and Love (Ref. 21) and Pot (Ref. 22).

A theoretical analysis for determining the boundaries of an impinging jet was carried out by Strand (Ref. 17). Schach (Ref. 23), using Green's theorem, obtained an integral equation for the velocity potential for the bending of an axisymmetric jet impinging orthogonally on a flat plate. The flowfield generated by a vertical axisymmetrical jet of an inviscid and incompressible fluid was obtained by Shen (Ref. 24) using the Legendre Series.

Ludwig, Brady et al (Ref. 25) presented experimetal data and made theoretical studies of uniform and non-uniform jets. General information about impinging jet flows are presented by Pai (Ref. 26), Birkhoff and Zarantonello (Ref. 27), Schlichting (Ref. 28), and Abramovich (Ref. 29). Hardisty (Ref. 13) as well as Norster (Ref. 30) and Gauntner et at (Ref. 31) have also published comprehensive reviews.

Recently, Wolfshtein's numerical solutions (Ref. 32) of the impingement problem are worthy of mention, and this author together with Strotter (Ref. 33) solved the case of a laminar jet with a non-uniform wall temperature (i.e. the wall temperature was a power function of the radius).

Turbulence is known to have considerable influence on heat transfers associated with impinging jets. Only limited published information exists on jet turbulence. Corrsin (Ref. 34) was one of the earliest workers who measured axial components of turbulence at several locations between the end of the potential core up to an axial distance of forty jet diameters from the exit. He employed 25.4mm diameter jet which was heated. He also took oscillograms of the axial fluctuations at several points along the jet radius at a distance of twenty jet diameters from the nozzle exit. Turbulence measurements from the present tests will be compared with Corrsin's results in later chapters of this thesis.

2.2.2 The Flow Structure of an Impinging Jet in a Crossflowing Fluid.

The effect of a crossflowing stream on an impinging jet is to produce a more complicated three-dimensional flowfield, so that analysis is difficult. Consequently, only limited theoretical information is available on the subject. Furthermore, the experimental data also tends to be rather sparse. Whilst considerable analytical and experimental work has been carried out on free jets in a deflecting stream; the absence of an impingement surface limits their usefulness in jet impingement situations.

The following model is, however, based on the results of the present investigation and the limited volume of previously published information. A crossflowing stream of even comparatively low velocity relative to that of the jet can produce considerable changes in the flowfield. Fig. 2.2(b) illustrates the flow structure of an impinging jet in a crossflow. Fig. 2.3 illustrates the flow structure found from flow visualisation undertaken in this investigation.

As it approaches the boundaries of the jet, the crossflowing stream decelerates, in a similar fashion to the behaviour when blocked by a solid body. It can be seen from these diagrams that the flow structure at the nozzle exit is considerably influenced by the extensive mixing and entrainment. Once again, there is a potential core beyond which the maximum velocity in the cross-section decays with distance from the nozzle exit (Refs. 35 - 37).

The jet is deflected partly by viscous entrainment, and partly by pressure forces acting on the jet boundary, so that the initially circular cross-section of the jet is deformed into what is variously described as a 'kidney-shaped' or 'horse-shoe shaped' cross-section see Jordison (Ref. 37).

The presence of the crossflowing stream results in the wall jet-flow separating from the surface at some upstream distance, and curving back on itself. This results in the formation of a strong vortex denoted by V in Fig. 2.2(b). This vortex, can be seen near the impingement surface just upstream of the impingement plane in fig. 2.3. The formation of this vortex depends on the velocity of the jet relative to that of the crossflowing stream.

The separation line where the wall jet is lifted away from the plate is thus horse-shoe shaped. This represents the maximum upstream or lateral penetration of the wall jet along the impingement surface. The location and shape of this separation line is a function of jet-to-crossflow mass velocity ratio, nozzle-to-target spacing, and jet impingement angle.

The presence of the crossflowing stream also results in the impingement region being displaced downstream.

As stated earlier, only limited experimental data are available for impinging jets in crossflow. Colin and Olivari (Ref. 16) investigated the flowfield under a circular jet impinging orthogonally on a flat surface. They split the flowfield into three regions, the free jet region, the impingement region, and the wall jet region together with the recirculation bubble. Their 'recirculation bubble'region is actually the vortex region described earlier. They used flow visualisation techniques and obtained an expression based on energy concepts, for the position of the horse-shoe shaped separation line. Their expression agreed well with their experimental data at least near the upstream portion of the stagnation region.

Tyler and Williamson (Refs. 38 & 39) used a series of single vertical jets installed between side walls in a wind tunnel. They determined experimentally, the centre-line location of the tunnel flow separation, and the forward penetration, using wool tuft observations. The use of wool tufts, instead of techniques such as the oil film method of the present investigation rendered their measurements approximate and uncertain.

To quote their own statement, "within the range of test variables and the limits of observational accuracy", they found that they could correlate their measured data by the following empirical relationship:

$$S_3/Z \quad = \quad 0.024(Z/(d\sqrt{I}))^{16/3} - 0.30/(Z/d\sqrt{I})^{4/3} \qquad (2.1)$$

They tried to extend their correlation to inclined jets and made a 'crude' estimate of the effect of jet inclination on tunnel flow separation. Their approximate extension of equation (2.1) to inclined jets is given by:

$$S_3\text{Cos}\alpha/Z = \text{Sin}\,\alpha + 0.024(Z/(d\sqrt{I}))^{16/3} - 0.30/(Z/(d\sqrt{I})).(0.152/\text{Tan}\xi)^{1/8} \qquad (2.2)$$

where $\xi \quad = \quad + \text{Tan}^{-1}0.152(Z/(d\sqrt{I}))^{16/3}$

Callaghan and Ruggeri (Ref. 40) investigated the effect of velocity and density ratios for circular jets issuing into a wind tunnel. Their correlation was based on blowing rate, defined as $\rho_j U_j/(\rho_c U_c)$.

Abramovich (Ref. 29) published results obtained for the location of the centre-line of a jet in a deflecting stream. Analytical and empirical equations were defined. Keffer and Baines (Ref. 36) investigated jet penetration for a round turbulent jet. Their experimental results showed that there is a distinct edge to the jet. They also obtained a correlation for the centre-line of the jet as a function of the momentum flux ratio ($R^2 = U_j^2/U_c^2$). Their measurements were however limited to small downstream distances because of uncertainty in the measurements.

Schetz and Billig (Ref. 41) were particularly interested in the interaction of a jet with a supersonic crossflowing stream. They used a solid body drag model to predict the centre-line location and found good agreement with experiment at low velocities. Reilly (Ref. 42) modified their solid body assumptions and obtained results which closely matched the available data. Margason (Ref. 43) investigated the path and general shape of a single jet exiting at large angles into a crossflowing stream. His jet exit deflection angles ranged from 30° to 180° from the free stream direction. He undertook extensive flow visualisation and made comparison with previous studies. His data fell in the middle of a spread of previously published results. Fig. 2.4 presents the results of Schetz and Billig (Ref. 41), Margason (Ref. 43), and Shandorov (Ref. 44).

Platten and Keffer (Ref. 45) present experimental data whilst Wooler et al (Ref. 46) also predicts jet tracjectories.

Ramsey and Goldstein (Ref. 47) measured axial turbulence intensity profiles for an unheated jet injected normally into a deflecting stream. They found that turbulence intensity was high in low velocity regions, but as the jet moved farther downstream, the low velocity region was accelerated by the mainstream and turbulence level then decreased. They also showed that the maximum temperature line of the jet was closer than the maximum velocity line. This was later confirmed by Kamotani and Greber (Ref. 48). The latter, also measured turbulence intensity distributions for jets issuing into a crossflow. Both heated and unheated jets were studied. They found that turbulence intensity increases with increasing jet-to-crossflow momentum ratio and that the turbulence intensity distribution was quantitatively similar to their measured temperature distribution.

Stoy and Ben-haim (Ref. 49) conducted an experimental and analytical study of the deflection and impingement of turbulent jets in a confined crossflow. They developed a simple one-dimensional analysis to predict jet trajectory, average jet properties and the impingement point for spatially variable crossflow velocity profiles. Fearn and Weston (Ref. 50) used a round jet injected into a subsonic crosswind of the same temperature for a range of jet-to-crossflow velocity ratios of 2 to 10. They found from their static pressure measurements that for all velocity ratios, there is a positive pressure region upstream of the jet, but the maximum pressure attained generally decreased with increasing jet to crossflow velocity ratio. They attributed this to increased entrainment of crossflow fluid as the relative jet velocity was increased.

More recently, Taylor (Ref. 51) studied an inclined turbulent jet exhausting into a subsonic crosswind. They varied the inclination of the jet from 0^{o} to 60^{o}, in increments of 15^{o} and found that the suction force (lift-loss), the jet penetration into the crosswind,and the rate of decay of total pressure along the centre line of the jet were all reduced as the jet inclination was increased. They attributed this to a decrease in the entrainment rate of the jet as its inclination increased in the downstream direction.

Another recently reported investigation in this field was by Rudinger and Moon (Ref. 52) who made Laser-Doppler measurements in a subsonic jet injected into a subsonic crossflow. Lee (Ref. 53) has published a good review (up until 1966) of published information on jet interaction with an external stream. Skifstad (Ref. 54) has also comprehensively reviewed the structure of impinging jets in crossflow with particular application to VTOL aircraft.

2.3 Jet Heat Transfer.

The majority of the heat transfer investigations are on either an orthogonally impinging single jet or arrays of these jets. Studies of the heat transfer characteristics of inclined jets are sparse. Furthermore, most studies have been carried out with jets in the absence of crossflows.

Arganbright and Resch (Ref. 55), and Hardisty (Ref. 13) have published excellent and informative summaries of the state of the art up until 1972. A large number of experimental investigations on single circular or slot jets and various arrays of jets have been conducted. The most of these studies have been concerned with average heat transfer over large areas, and the tests, in most cases covered very limited ranges of Reynolds number. Most investigators also used different lengths and sizes of nozzles so that the velocity distributions at the nozzle exits differed considerably. As a result there are significant variations in the reported data. In this review, the relationship between heat transfer coefficients and parameters such as jet exit velocity, dimensionless nozzle-to-target spacing, jet size, and impingement angle will be examined.

One of the earliest publications on inclined jets impinging on a flat surface was that of Perry (Ref. 56). He investigated average heat transfer coefficients for a heated jet impinging at different angles on a flat surface. The nozzle-to-target spacing was kept constant at 8.0 diameters. He proposed an equation for the Nusselt number at the impingement point which is similar to that applying to flow over a flat plate. The influence of the angle of impingement was included by modifying one of the constants in the correlation so that

$$Nu_d = C Re_d^{0.7} Pr^{0.77} \qquad (2.3)$$

where $C = 0.181$ for impingement at 90°
$= 0.1579$ " " " 60°
$= 0.1422$ " " " 45°

Perry's results have been critisized on the grounds that he used a fixed nozzle-to-target spacing, and the correlation should therefore be used with caution for alternative nozzle to target spacings. Furthermore, the correlation does not indicate any influence of the size and type of nozzle used since his nozzle was of fixed geometry ($d = 16.5$mm). The range of Reynolds number varied from 11,000 to 30,000.

Thurlow (Ref. 57) investigated the influence of nozzle to target spacing on average heat transfer. The heat transfers decreased sharply with increase in separation distance. He proposed the following formula for average heat transfer for an orthogonally impinging circular jet:

$$Nu_d = C Re_d^{\frac{1}{3}} \exp(-0.037Z/d) \qquad (2.4)$$

where $C = 1.06$ for 25.4mm diameter nozzles, and
$= 0.33$ for 12.7mm diameter nozzles.

Smirnov et al (Ref. 58) investigated submerged inclined liquid jets. Their work resulted in slight modification of Perry's coefficients (Ref. 56). Also the distance between the jet and the surface was taken into account. So that for $0.5 < Z/d < 10$

$$Nu_d = C Re_d^{0.64} Pr^{\frac{1}{3}} \exp(-0.037Z/d) \qquad (2.5)$$

where $C = 0.034 d^{0.9}$
and for $Z/d > 10$

$$Nu_d = 0.034 d^{\frac{1}{3}} (Re_d Pr)^{\frac{1}{3}} \exp(-0.037Z/d) \qquad (2.6)$$

where d is the jet diameter.

Gardon and Cobonpue (Ref. 59) investigated heat transfer under axially symmetrical impinging air jets. Their investigations involved both a single turbulent ($Re_d > 14,000$) jet and also several arrays of circular jets. They found that the local heat transfer reaches an absolute maximum at the impingement point when the jet is located at 6 or 7 jet diameters above the impingement surface. They also pointed out that at high jet velocities the temperature difference between the plate, and the recovery temperature should be allowed for when correlating the heat transfer coefficients. Their stagnation point heat transfer results were found to correlate well for nozzle to target spacings greater than 20 jet diameters. For single turbulent air jets, their correlation was:

$$Nu_o = 13 Re_d^{0.5} (Z/d)^{-1} \qquad (2.7)$$

For arrays of jets, their correlation for average heat transfer coefficients was:

$$Nu_{av} = 0.286Re_x^{0.625} \quad \text{for } Z/d > 1$$

where Nu_{av} is the average Nusselt number based on jet pitch, and the Reynolds number is based on jet pitch and arrival velocity. This is the axial velocity which a free non-impinging jet would have at the plane of the plate. It was also concluded that the local heat transfer coefficients associated with a single jet were always higher than those due to a jet in an array.

Huang (Ref. 60) studied single and multiple jets impinging orthogonally on flat circular discs. The experiments were conducted for Reynolds numbers ranging from 10^3 to 10^4 and jet diameters in the range $3.175 \leqslant d \leqslant 6.35$mm. Local and average heat transfer coefficients were obtained and empirical equations derived. For a single jet, his correlation for local heat transfer coefficients at the stagnation point is:

$$Nu = 0.0233Pr^{\frac{1}{3}}Re_d^{0.87} \qquad (2.8)$$

Huang's local measurements have been criticised due to the finite size of his measurement probe so that in reality they are average heat transfers over a target of $0.000645m^2$. This is comparable in size to the jet see Refs. 66 & 80.

For a single jet, Huang's correlation of average heat transfer coefficient is:

$$Nu_{av} = 0.0180Pr^{\frac{1}{3}}Re^{0.87} \qquad (2.9)$$

This is valid for $1 \leqslant Z/d \leqslant 10$.
Huang did not find the large gradients in the local heat transfer distribution near the stagnation point measured by Gardon and Cobonpue (Ref. 59). There are also considerable differences between these two studies in the Reynolds number exponents. If the Stanton number is expressed as a function of Reynolds number, the exponents were -0.13 and -0.5 for Huang and Gardon and Cobonpue (Ref. 59) respectively. These variations may be due to differing jet flow structures since in one case the jet issued from a nozzle, and in the other study the jet discharged from an orifice.

Donaldson et al (Refs. 61 & 62) studied the heat transfer from subsonic symmetric impinging jets. They also investigated the influence of turbulence on heat transfer. An important proposition from their investigation was that for the region near the stagnation point, they suggested that the heat transfers can be calculated as that due to the laminar flow that would ensue over a surface with the same pressure distribution. This should be multiplied by a correction factor to account for the structure of the turbulent jet. Away from the stagnation point, the heat transfer should be calculated using the earlier published results of Rosenbaum and Donaldson (Ref. 63).

Vickers (Ref. 64) obtained local heat transfer coefficients for an orthogonally impinging circular air jet. His Reynolds number ranged from 550 to 1200, and nozzle to target spacing from 7 to 22. A fixed (1.29mm) diameter nozzle was employed. The range of Reynolds number was very low, so that only the laminar flow situation was covered.

Ward et al (Ref. 65) using a mass transfer technique studied average heat transfer from an array of round jets, and found that results obtained with the method were in good agreement with those of previous investigators. They concluded that the Naphthalene sublimation technique was suitable for local and average heat transfer measurements under impinging jets.

Koopman (Ref. 66) also employed this sublimation technique and investigated local mass transfer variations due to the impingement of a row of circular jets on a plane surface. He also conducted single jet experiments. Nozzle to target spacings of 2, 4, 7 and 10, jet-pitches of 4 and 6.67, and Reynolds number (Re_d) ranging from 2500 to 10,000 were studied. The stagnation heat transfer maxima were a function of nozzle to target spacing as previously reported by Gardon and Cobonpue (Ref. 59). This author also found that the presence of additional jets produced lower stagnation region heat transfers; also the single jet heat transfer coefficients diminished more rapidly in the radial direction than those of the multiple jets. His single jet data however was in poor agreement with those of Gardon.

Daane and Han (Ref. 67) reported that heat transfer coefficient was a function of open or free area. They studied single and multiple jets impinging orthogonally on a flat surface using both slot and circular jets.

Turbulence is known to have considerable influence on heat transfers associated with impinging jets. Gardon and Akfirat (Ref. 68) studied the influence of turbulence on heat transfer from slot jets. They placed an 18 mesh screen in the nozzle to promote turbulence. By altering the position of the screen relative to the nozzle exit, they obtained and plotted the effects of artificially induced turbulence on local heat transfer. These were found to increase as the centre-line turbulence intensity increased. They were also able to explain the anomalous heat transfer phenomena of secondary peaks associated with lateral variation of heat transfer under impinging jets. They attributed this to transition from laminar to turbulent boundary layer in the wall jet. They also noted that turbulence in jets varies with the axial position downstream of the jet exit. Gardon and Akfirat's result, generally indicated that turbulence plays an important role in the magnitude of heat transfer in addition to producing relative maxima at 'off-stagnation regions' at close nozzle to target spacings. For nozzle to target spacings less than 3 jet diameters, they found that the absolute maxima of heat transfer in the stagnation region occurs in an annular region positioned one-half jet diameter from the geometrical stagnation point.

Ouden and Hoogendoorn (Ref. 69) used a liquid crystal technique to determine local heat transfer coefficients from a heated surface to an impinging jet. They measured the local heat transfer coefficients near the stagnation point and found that the influence of turbulence on their results was significant. They found that, taking turbulence effects into account, the Nusselt number at the stagnation point could be correlated by:

$$Nu_d/Re_d^{0.5} = 0.497 + 3.48(TuRe_d^{\frac{1}{2}}/100) - 3.99(TuRe_d^{\frac{1}{2}}/100)^2 \quad (2.10)$$

(valid for $Z/d < 4.0$)
where Tu is the local turbulence level at the nozzle exit or in the boundary layer.
The above expression is only valid at the stagnation point "if the nozzle to target spacing is less than the length of the potential core" so that this limits the expression to low nozzle to target spacings ($Z/d \leqslant 4.0$).

Kestin and Wood (Ref. 70) found that turbulence had an effect on heat transfer at the stagnation point, and obtained a correlation for the local Nusselt number at this point on a cylinder, allowing for the effects of turbulence intensity.

Kataoka and Mizushina (Ref. 71) studied the effect of free stream turbulence on the local rate of heat transfer with an impinging round jet of large Prandtl number. They used an electrochemical mass transfer method and found that local enhancement of heat transfer could be explained by the penetration of mixing-induced turbulence across the laminar boundary layer in the presence of negative pressure gradients. Subsequent transition from laminar to turbulent boundary layer when the pressure gradients had disappeared also played a part. This is in agreement with Gardon and Akfirat's conclusions (Ref. 68). Further information on turbulence are presented in Hinze(Ref. 147).

Other important work on local heat transfers under single circular jets include the analytical work by Eckert (Ref.73). He discussed heat transfers in the laminar boundary layer around submerged bodies, and obtained an expression for heat transfer at the stagnation point for situations for which the flat plate is a limiting case, so that:

$$Nu_r = 0.44Pr^{0.36}Re_r^{\frac{1}{2}} \qquad (2.11)$$

Lewis (Ref.74) modified Eckert's solution and obtained the following expression for stagnation point heat transfer:

$$Nu_d = 1.12Re_d^{\frac{1}{2}}Pr^{\frac{1}{3}} \qquad (2.12)$$

and for air with $Pr = 0.7$,

$$Nu_d = 0.994Re_d^{\frac{1}{2}} \qquad (2.13)$$

Two-dimensional jets have been studied extensively by many researchers, and only the most important will be mentioned here. More information on this subject can be found in the reviews by Arganbright and Resch (Ref. 55) and Hardisty (Ref. 13).

Gardon and Akfirat (Ref. 75) measured local and average heat transfer for both single and arrays of two-dimensional jets impinging normally onto a flat surface. Their results were similar to those previously reported for circular jets (Ref. 59), where the Nusselt number reached a maximum at nozzle to target spacings of 7 or 8 equivalent widths. Another similar result was that for a single jet the local heat transfer exhibits a peak value at the stagnation point, and decreases rapidly on each side subsequent with further small localised peaks. These secondary peaks were attributed to the transition from laminar to turbulent conditions in the wall jet. The results of Gardon and Cobonpue (Ref. 59) on the circular jet and Gardon and Akfirat (Ref. 75) on the two-dimensional jet are presented in figs. 2.5 and 2.6 respectively.

Korger and Krizek (Ref. 76) used the Naphthalene sublimation technique, and determined local mass transfer coefficients under impinging slot jets. They observed that the stagnation point heat transfer attained a peak in the region $6 \leqslant Z/B \leqslant 10$. At low nozzle to target spacings, they also observed secondary stagnation peaks for which no explanation was given, although this is now understood from the work done by Gardon and Akfirat (Ref. 75). They however, established relationships for the maximum and mean mass transfer coefficients, and developed a critical equation which they expressed in dimensionless form as:

$$Sh_{mean} = KRe^{0.77}Sc^{\frac{1}{3}} \qquad (2.14)$$

Hilgeroth (Ref. 77) reported that the interaction of multiple jets resulted in lower heat transfer coefficients relative to those of single jets. All these studies have been concerned with jet impingement in quiescent surroundings.

The impingement of a jet in a crossflowing stream has however, received very little attention. This is mainly due to the complicated three-dimensional flowfield arising from the interaction . As seen previously, (section 2.2) most of the work has been concerned with the location of the impingement point, the greatest upstream penetration of the jet, and the size of the "jet mixing zone" (Ref. 16).

One of earliest researchers into heat transfers were Metzger and Korstad (Ref. 78) who employed arrays of jets. Their results are concerned with average values over a rectangular impingement area. They showed that as a result of the superimposed crossflow, the upstream penetration distance of the impinging jets was relatively short. The magnitude of the upstream 'degradation' and the simultaneous downstream 'enhancement' in heat transfer rates is a function of the jet spacing parameter. The net result of crossflow also is a decrease in the overall heat transfer

Kercher and Tabakoff (Ref. 79) showed that increasing the crossflow decreases the heat transfer performance of an array of round jets. Also for the range $1 < Z/d < 4.8$, increasing Z/d increases the heat transfer in the absence of crossflow but decreases the heat transfer when crossflows are imposed. A controlled crossflow however, was not employed in the investigation only 'spent air' from other jets in the array was used as the crossflow. Furthermore, the range of nozzle to target spacing studied was small.

Bouchez (Ref. 81) measured local heat transfer under a single impinging air jet in a crossflow. The jet discharged through an orifice, and he considered only initially orthogonal cases. The tests were confined to nozzle to target spacings ranging from 6 to 12; and were conducted for blowing rates (defined as $(\rho_j U_j)/(\rho_c U_c)$, ranging from 3.5 to 12.0. The heat transfer coefficients (measured on the centre-line of the flow) were very high near the stagnation point. With a nozzle to target spacing of 6 jet diameters, and a blowing rate of 12, the heat transfer coefficient reached a maximum of about sixteen times the value (h_o) measured under crossflow alone. He concluded that heat transfer is strongly influenced by the blowing rate and varies rapidly with distance from the stagnation point.

Sparrow et al (Ref. 82) investigated the effect of nozzle to target spacing on jet impingement heat transfer in the presence of crossflows. They found that jet deflection by crossflow was minimal for mass velocity ratios (blowing rates), $M \geqslant 8$. For these mass velocity ratios, the impingement point heat transfer was a maximum at nozzle to target spacings of 5 to 6.

From the foregoing, it can be seen that there is little reported work for heat transfer from inclined jets in the presence of crossflowing streams. The cases of orthogonal impingement so far reported do not adequately cover the ranges of nozzle to target spacing and Reynolds number of interest in many practical situations. The data so far available are also inadequate for reliable heat transfer correlations. Also the flow structure and associated fluid mechanics are not well understood because of limited experimental information.

This present work is primarily intended to extend the scope of previous work, and in particular will study the combined effects of jet inclination and crossflows. Flow visualisation and mass transfer measurements will be employed for this purpose.

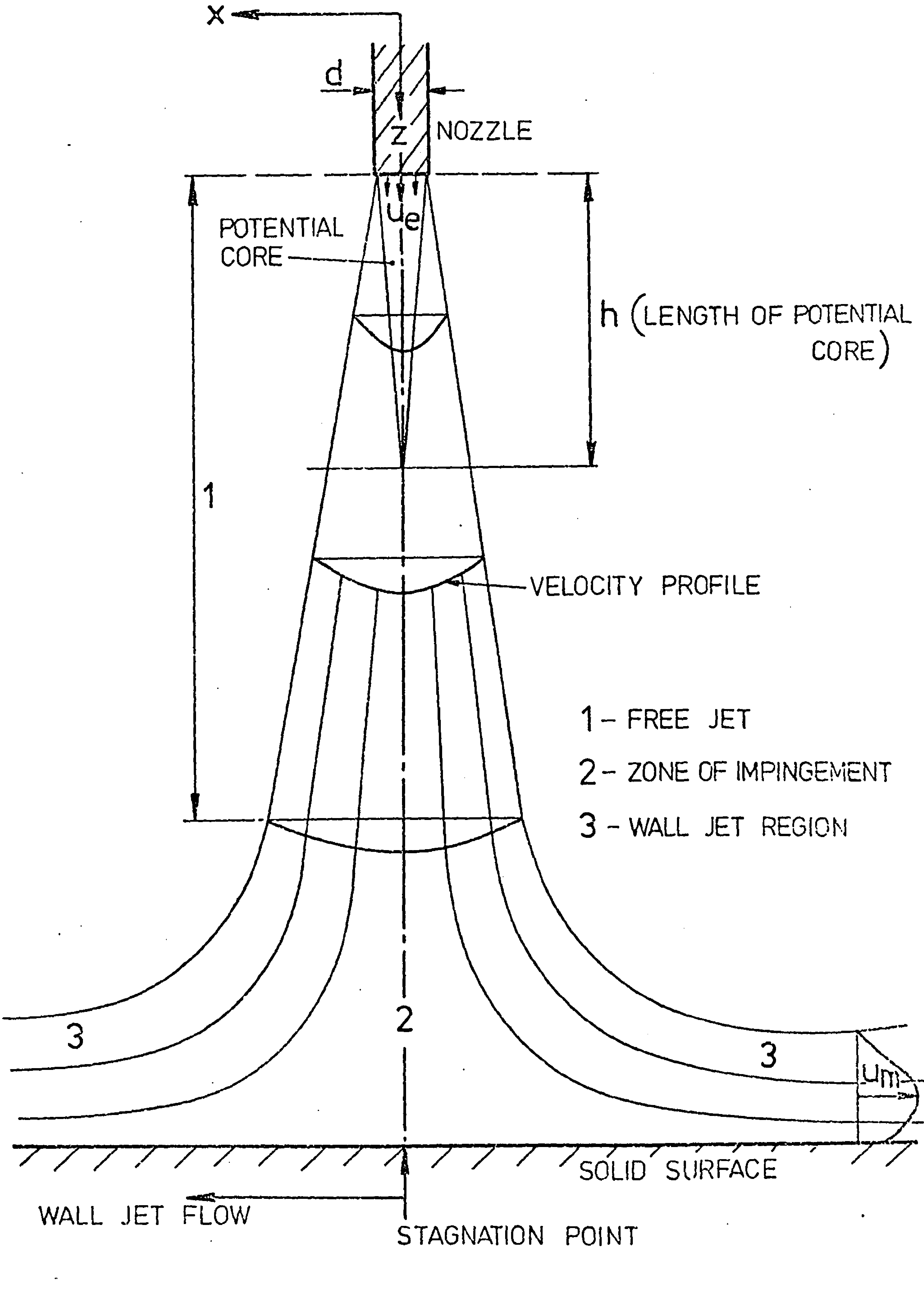

FIG. 2.1. SCHEMATIC OF AN IMPINGING JET, AND ASSOCIATED NOMENCLATURE.

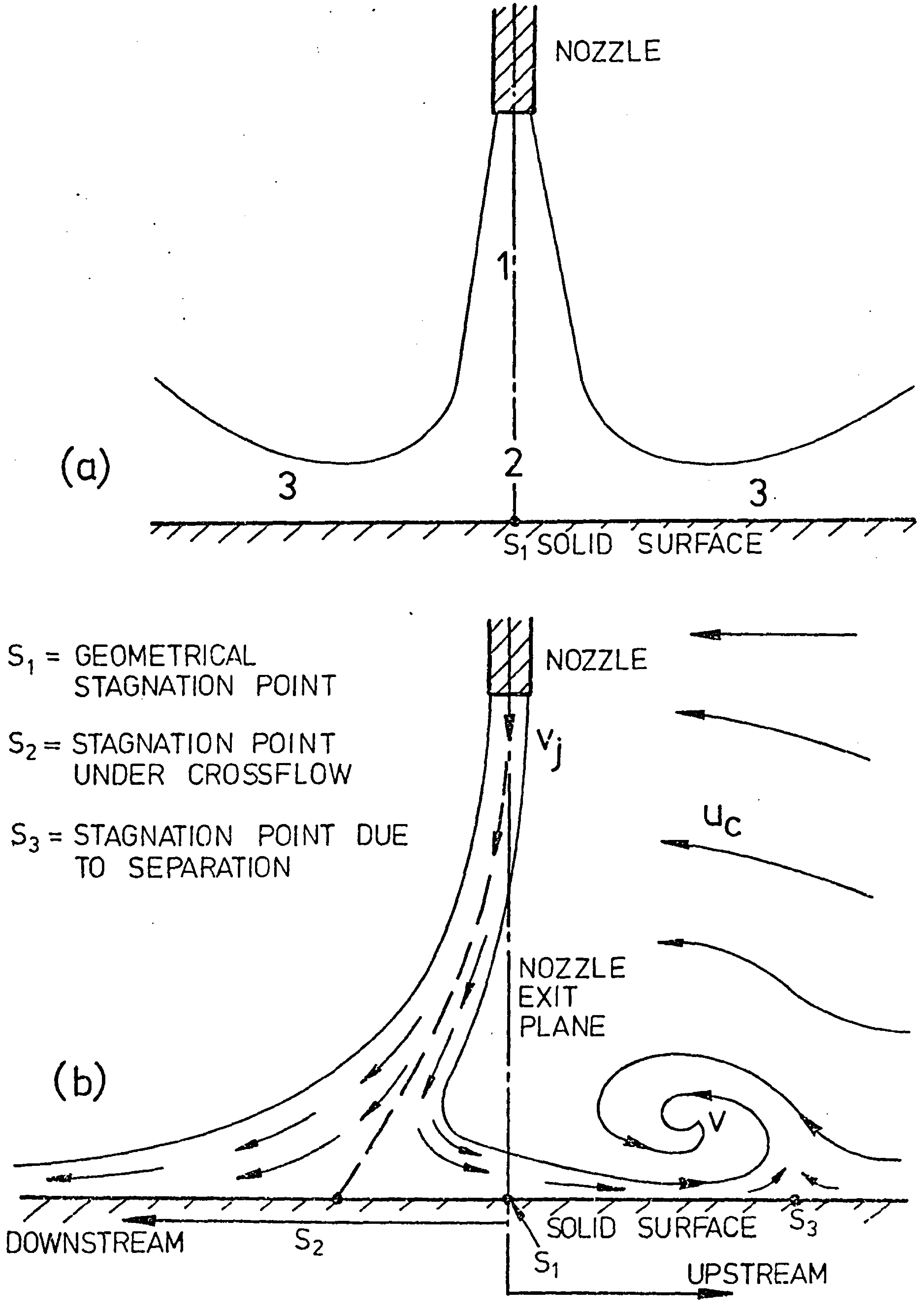

(a) JET IMPINGEMENT IN STILL AMBIENT CONDITIONS

(b) JET IMPINGEMENT IN CROSSFLOW

FIG. 2.2. SCHEMATIC REPRESENTATION OF THE EFFECT OF CROSSFLOW ON FLOW STRUCTURE OF AN IMPINGING JET.

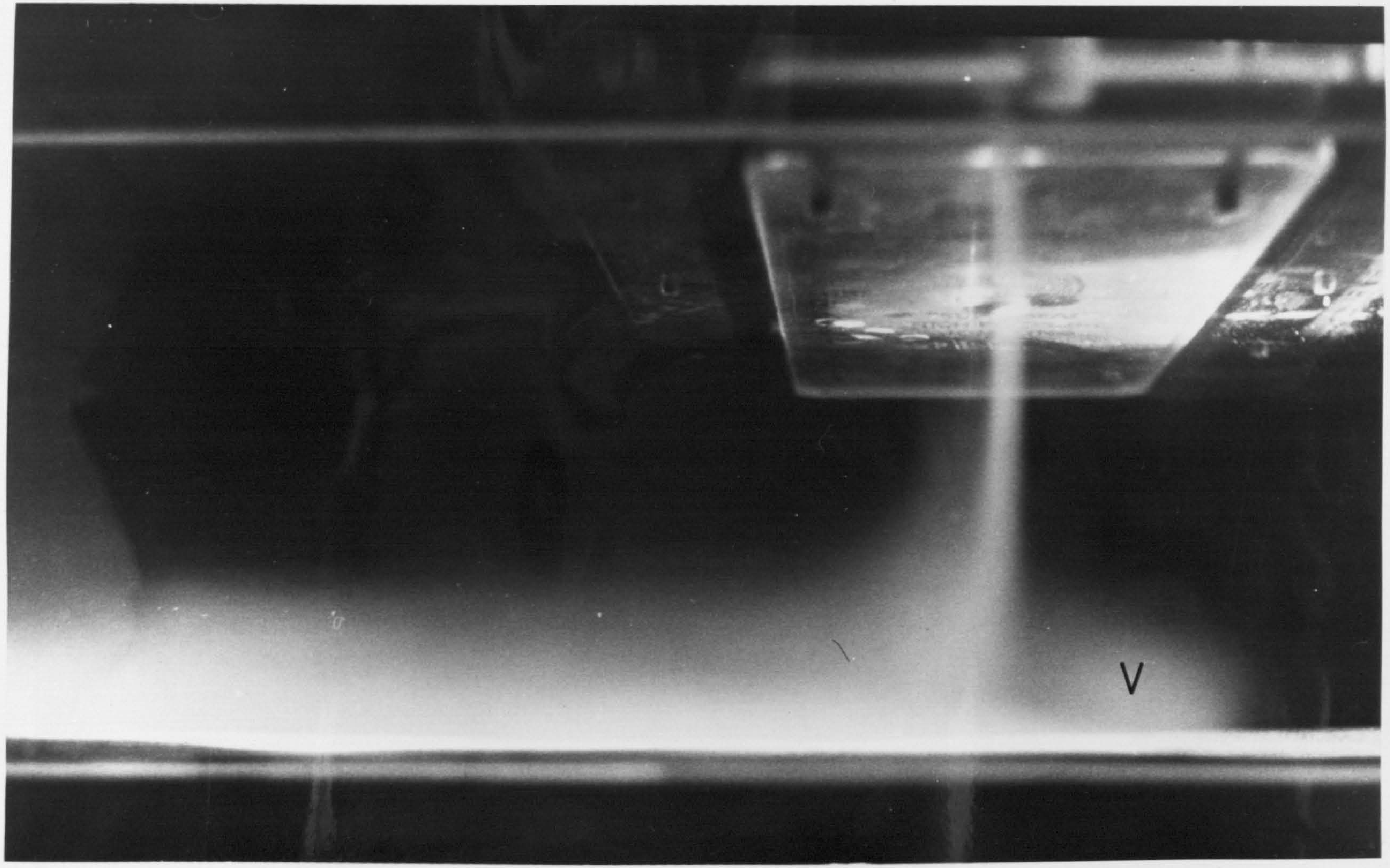

FIG. 2.3 FLOW STRUCTURE OF AN IMPINGING JET IN A CROSSFLOW—AS OBSERVED BY FLOW VISUALISATION.

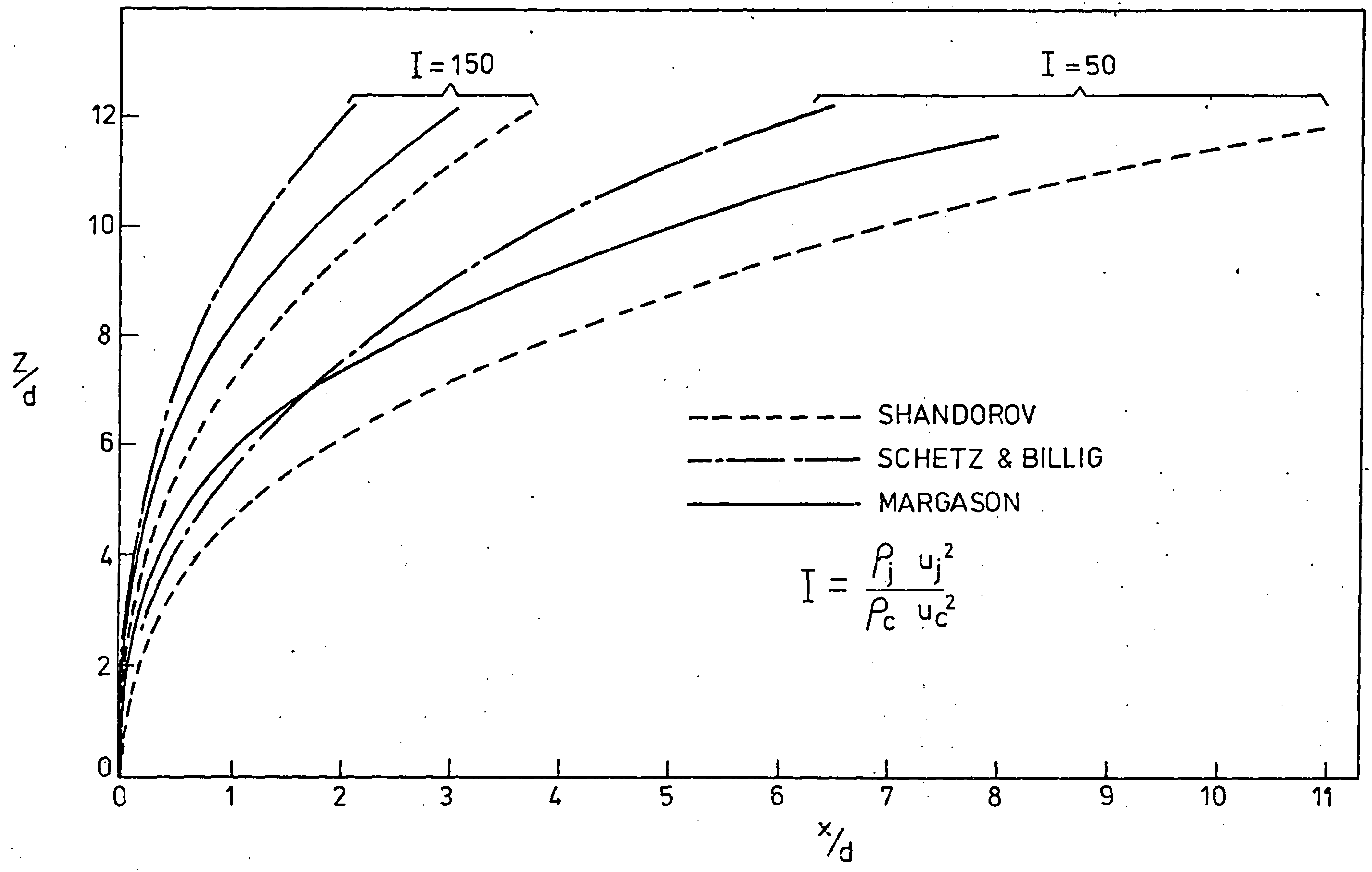

FIG. 2. 4. CENTRE LINE OF JETS IN CROSSFLOW

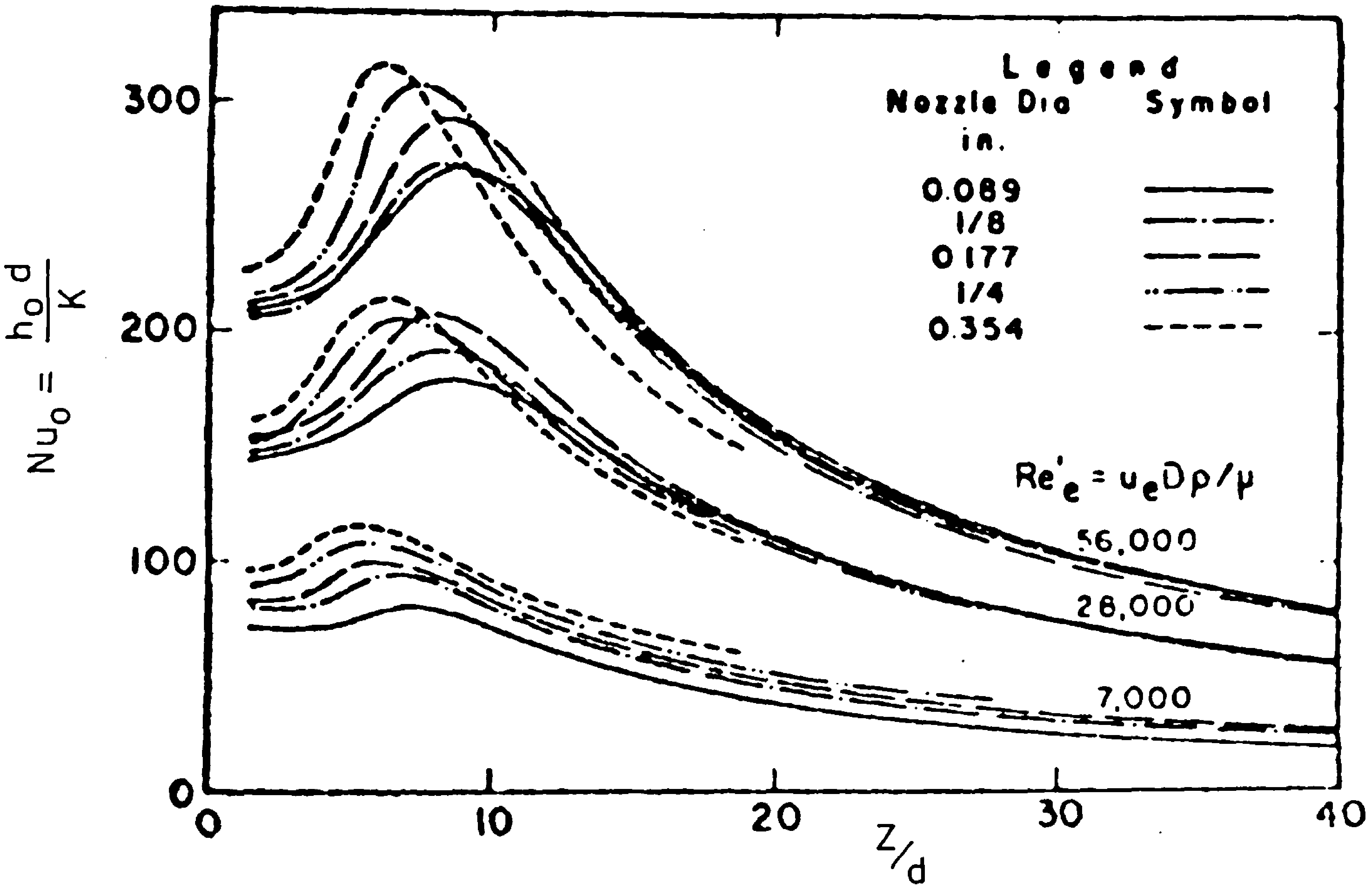

FIG. 2.5. CORRELATION OF HEAT TRANSFER AT THE STAGNATION POINT OF A CIRCULAR JET (REF. 59)

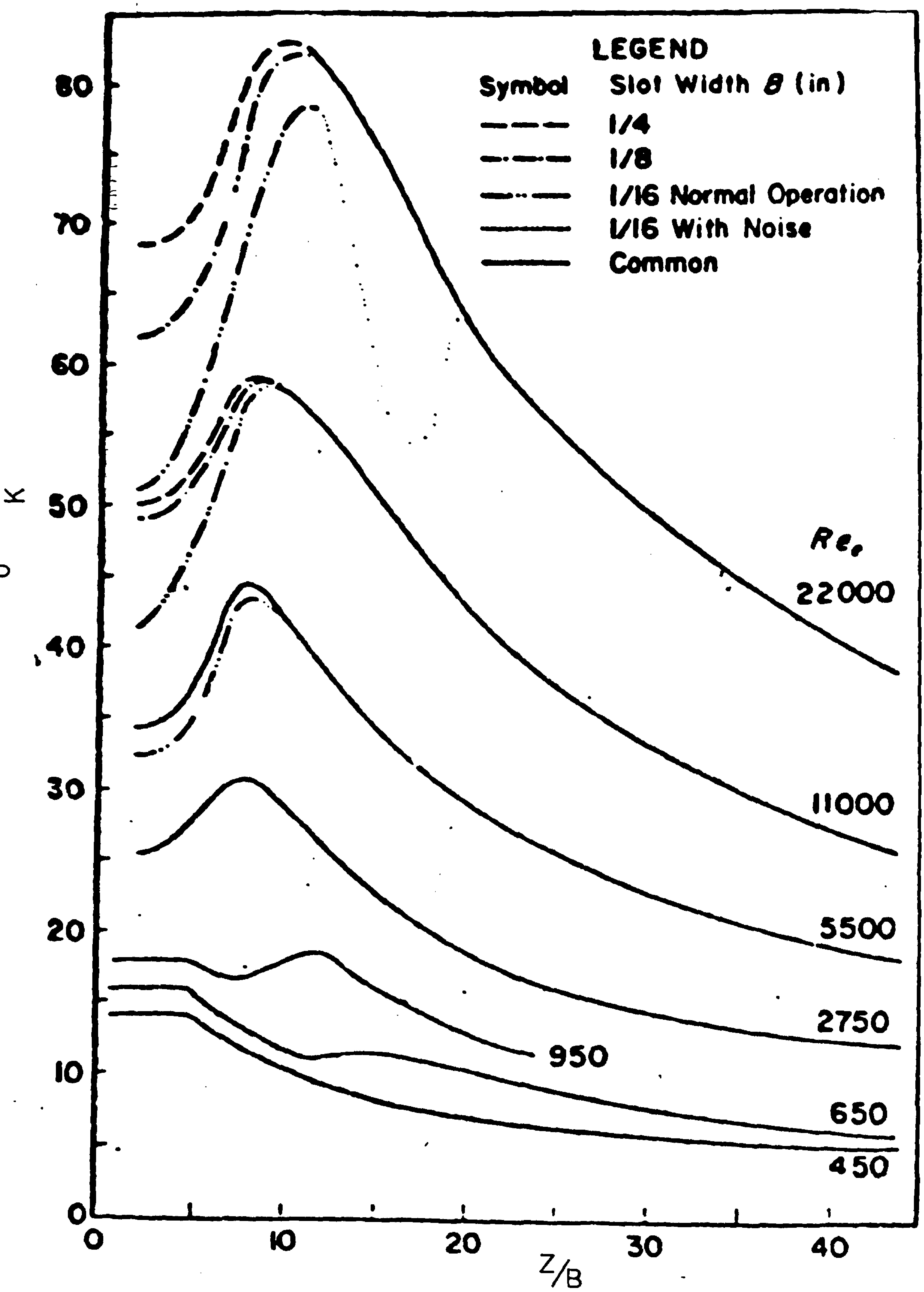

FIG. 2. 6. CORRELATION OF HEAT TRANSFER AT THE STAGNATION POINT OF A TWO-DIMENSIONAL JET (REF 75)

CHAPTER 3

THE DETERMINATION OF HEAT TRANSFERS BY ANALOGY.

3.1 Basis of an Analogy For Jet Impingement Heat Transfer.

In a number of important heat transfer problems, the flow is mainly turbulent. The complex nature of this turbulent motion often makes any analytical approach too complicated to be feasible. This is particularly true of jet impingement systems in which fluctuating, large scale eddies occur in a disordered manner. Thus there is neither the theory nor sufficient experimental data to assist an accurate analysis. Since direct heat transfer measurements are often difficult and time consuming, it is convenient when studying jet-impingement to resort to some analogy.

In turbulent fluid flow problems, direct heat transfer measurements have nevertheless sometimes been used. These have involved making surface temperature and/or heat flux measurements at various points to determine local heat transfer coefficients.

However, these direct measurement methods often require elaborate equipment; considerable care must be taken and the procedure can be tedious. There is thus a need for relatively simple and more convenient methods of estimating heat transfers. Consequently, a technique which is now widely used is to determine 'heat transfers by analogy'. The use of an analogy in experimental measurements is feasible since the physical processes underlying the transfer mechanisms of momentum, heat and mass are similar:-

For momentum transfer τ = f(velocity gradient) (3.1)

For heat transfer $\dot{q}$ = f(temperature gradient) (3.2)

For mass transfer N = f(concentration gradient) (3.3)

The momentum transfer analogy has been used to determine heat and mass transfer coefficients from data (often available) for skin friction coefficients. It is in principle an attractive method for estimating average heat and mass transfer coefficients. However, the transfer area, should be sufficiently large for the associated force or pressure drop to be measurable accurately.

It is very difficult to obtain local friction coefficients either directly or by velocity profile measurements. Thus, a heat-mass transfer analogy is in general more attractive and suitable.

The flow patterns which uniquely control the transfer rates (heat or mass) from a surface will be similar, provided identical geometrical, dynamic, and kinematic conditions prevail. The transfer rates depend on the relative diffusion properties of the fluid, and the thermal and concentration gradients associated with the flow. If a subliming solid is employed as the transfer surface, local mass transfer measurements, (using for instance a profilometric technique), can be made quite accurately. These local measurements, can then be employed to infer the local heat transfer coefficients. It is often easier to make these mass transfer measurements so that the heat-mass transfer analogy is attractive in complex experimental situations.

In this present study, the sublimation of naphthalene was used, and this chapter briefly reviews published work on the heat-mass transfer technique. The theoretical basis for the heat-mass transfer analogy is also considered. The advantages and limitations of the technique are then discussed.

3.2 Review of Previous Mass Transfer Investigations.

In the previous section, the desirability of applying a heat/mass transfer analogy to infer heat transfer coefficients was discussed. Such a technique is particularly suitable for determining local heat transfers in complicated situations such as those which occur in jet-impingement systems. It is therefore relevant at this stage, to review briefly the extensive previously published applications of the method.

Osborne Reynolds (Refs. 83 & 84) was the first investigator to point out the similarity between the transfer of momentum and heat. He established a theoretical relationship between heat transfer and skin friction. This analogy can be used in two situations, namely:
(a) when the diffusion constants of heat and momentum in turbulent flows are equal, and
(b) when the Stanton number is equal to one half of the friction factor.

Reynolds' discovery was subsequently taken up by Prandtl (Ref. 85), Taylor (Ref. 86) and Von Karman (Ref. 87) who developed theories of heat, mass, and momentum transport for fluids. In 1933, Colburn (Ref. 88) established a correlation between the convective film coefficient and the friction coefficient for flows in circular cylinders. An empirical relationship in the form of a so-called 'j-factor' was established. Thus:

$$j_H = St(Pr)^{\frac{2}{3}} = 0.023(Re)^{-0.2} \qquad (3.4)$$

To employ a heat-mass transfer analogy, it is necessary to consider the heat transfer process as the diffusion of hot molecules through cold ones in one direction, and the diffusion of cold molecules through hot ones in the opposite direction. Chilton and Colburn (Ref. 89) realised this similarity so that the mechanisms of heat, mass and momentum can be related. They thus extended the correlation of equation (3.4) to the transfer of mass. The Prandtl number(Pr) was replaced by the Schmidt number (Sc), so that a mass transfer j-factor, j_M can be defined in similar manner to that for heat transfer. Therefore, for flow along flat surfaces, and inside tubes, Chilton and Colburn suggested that

$$j = St_M Sc^{\frac{2}{3}} = StPr^{\frac{2}{3}} = C_f/2 \qquad (3.5)$$

The analogies between the three transport mechanisms soon became more widely known so that subsequently heat transfer data has frequently been deduced from mass transfer measurements.

Liquids such as water, benzene, toluene, Carbon tetrachloride, chlorobenzene, and tetrachloroethylene are suitable for these measurements. However, solids such as Camphor, Naphthalene, and Parachlorobenzol are often more convenient to use when investigating mass/heat transfers from fluid streams. Other techniques are also available.

Klein (Ref. 90) employed heated air streams to melt cylinders constructed of ice. The latent heat of fusion of ice is constant, so that the overall heat transfers were proportional to the weights of the melted ice. For local heat transfers, the deformed cylinders were cast in plasticine, and reproductions then made in plaster of Paris. The changes in the dimensions of the cylinders were then obtained from these models. Errors occured due to radiation transfer and conduction losses along the tube. Also the humidity of the air was not taken into account. This publication however led to the use of solids with relatively high vapour pressures, but with melting points higher than the ambient temperature. The mass transfer coefficients can then be calculated from the sublimation rates.

Winding and Cheney (Ref. 91) cast naphthalene tubes using split brass moulds. They employed air as the working fluid. Average and local heat transfer coefficients were determined by the change in the weight of naphthalene and the change in the local dimensions of the tubes. These local variations were found by using feeler gauges to measure the gaps between the naphthalene and the moulds. Both average and local heat transfers were then evaluated by invoking the Chilton-Colburn analogy.

Bedingfield and Drew (Ref. 92) made a theoretical study of the analogy between heat and mass transfer, and attempted to clarify the conditions under which the analogy is valid. They employed the sublimation of naphthalene, camphor, para-dichlorobenzol and para-dichlorobenzene for flows around single cylinders.

The relationship between heat, mass and momentum transfer have also been studied by Sherwood (Ref. 93). This author together with Bryant (Ref. 94) presented mass transfers for cylinders mounted longitudinally in air flows. Both subsonic and supersonic flows were studied and the cylinders were constructed of naphthalene, thymol or camphor. Their data and those of seven previous mass transfer investigations were then correlated using the Chilton-Colburn mass transfer j-factor, j_M, and the Reynolds number. The correlations were compared with the Prandtl number relationship between friction factor and Reynolds number for a turbulent boundary layer, see Schlichting (Ref. 28). Agreement between these relationships was remarkably good. They further reported that the Mach number has an important influence on both skin friction and mass transfer.

Christian and Kezios (Ref. 95) investigated mass transfer from sharp-edged cylinders in axisymmetric flow with laminar boundary layers. They measured the sublimation rate of naphthalene with a micrometer dial indicator and found that the overall mass transfers obtained by integrating these local results agreed to within ± 3% with those determined by direct weight-loss measurements.

Kreith et al (Ref. 96) using the mass transfer technique, investigated the laminar and turbulent boundary layers on a rotating disc. Sherwood and Trass (Ref. 97) used naphthalene sublimation data to determine friction factors for flat plates in supersonic flows. They obtained an expression for the Schmidt number in terms of the naphthalene temperature. This has been widely used in subsequent mass transfer investigations.

Houston (Ref. 98) employed a profilometric technique to obtain local mass losses due to the sublimation of naphthalene cast to form the surface of a nozzle. This nozzle modelled a solid fuel rocket. The method was less time consuming than those employed in previous studies. Therefore errors due to sublimation losses during the measurement process, were reduced.

Macleod et al (Ref. 99) also used a profilometric technique to measure local changes of thickness of a thin volatile surface coating. Their probe combined pneumatic and magnetic proximity gauges and they measured the changes in coating thickness to an accuracy of 1.5μm.

Luikov (Ref. 100) investigated transpiration cooling using a heat-mass transfer method. Wong (Ref. 101) also used the sublimation of naphthalene to determine local heat transfer variations over the surface of a finned cylinder in crossflow.

Korger and Krizek (Ref. 76) employed similar techniques to determine the average mass transfer coefficients associated with impinging slot air jets. The coefficients were similar to and exhibited common features to the heat transfer distributions found by Gardon and co-workers (Refs. 59 & 75) using direct measurement methods.

South (Ref. 102) using superheated steam jets inclined at various angles investigated heat and mass transfers with application to the drying of plywood veneer. Maxwell and Nash (Ref. 103) presented results of mass transfer tests using a mercury evaporation technique. They compared their results with published data on heat transfer for systems (e.g. flat surfaces under an impinging jet) where the mechanics of the processes were similar and found close agreement.

Electrolytic methods have been used by Kakaoka and Mizushina (Ref. 71) and Francis (Ref. 104). The latter, used nickel electrodes and an alkaline potassium ferro-ferricyanide solution to determine the mass transfers. The Chilton-Colburn analogy was then employed to evaluate the heat transfer coefficients.

Further studies of jet impingement have been carried out by Schrader (Ref. 18), who worked with single circular jets. The average mass transfer coefficients were determined by measuring the evaporation rate of water contained in sand beds. Schlunder and Gnielinski (Ref. 72) conducted a similar study using a porous stone surface. Ouden and Hoogendoorn (Ref. 69) used liquid crystals suspended in polyacrylate resin to determine local heat transfer coefficients from an impinging turbulent jet.

Koopman and Sparrow (Ref. 105) investigated local and average mass transfer coefficients under a row of impinging air jets. They also used the naphthalene sublimation technique. Black and Hardisty (Ref. 14), using the heat-mass transfer technique studied local heat transfer variations under impinging slot jets. They found close agreement between their experimental results and those previously reported by Gardon and Akfirat (Ref. 75).

Macleod and Todd (Ref. 106) determined mass transfer coefficients using plasticized surface coatings. Neal (Ref. 107) in a particularly interesting study developed a thin-film naphthalene mass-transfer analogue technique. This method is much less time consuming than the conventional profilometric set-ups.

Furthermore, Neal et al (Ref. 108), Lewis (Ref. 109) and Ward et al (Refs. 65 & 110) are amongst a host of others who have successfully employed the mass transfer technique to evaluate local and average heat transfer coefficients in important engineering applications. The successful use of the mass-heat transfer analogy over the years thus justifies the validity and continued application of the method to determine both local and average heat transfer coefficients in various systems.

3.3 Heat-Mass Transfer Analogy.

As previously mentioned, Reynolds (Refs. 83 & 84) related the shear stress and heat flux in the turbulent boundary layer. He suggested that the eddy diffusivities of heat and momentum are equal since both phenomena are caused by the motion of turbulent eddies. Thus for a Prandtl number of unity the velocity and temperature profiles are similar. This results in $St = C_f/2$ and is known as Reynolds' analogy. The expression is obviously of limited validity, (due to the assumption of $Pr = 1$), but is sometimes used because of its simplicity.

Further analogies were proposed by Prandtl, Taylor, and Von Karman who refined and extended Reynolds original proposition to cover all the regimes of boundary layer flow. These analogies relate heat, mass and momentum transport in fluid flow.

The importance of these analogies is that if correlating equations are known for one of the transport phenomena, then the remaining transport processes can be described by similar functional relationships obtained by insertion of the appropriate dimensionless parameters. For example, to obtain mass transfer relationships from heat transfer correlations, the Sherwood (Sh) and Schmidt (Sc) numbers replace respectively the Nusselt (Nu) and Prandtl (Pr) numbers.

For the turbulent flow of a fluid parallel to a smooth surface, three zones can be defined as:-

(1) A laminar sublayer where transfer is by molecular diffusion.
(2) A buffer layer where turbulent and molecular processes are active.
(3) The turbulent zone with predominantly eddy transfer.

Molecular transfer is a less effective mechanism than eddy transfer, so that the laminar sublayer presents the greatest barrier to transfer from the surface. In this layer, the equations describing the three transport processes are:-

For momentum transfer

$$\tau_L = \mu\partial U/\partial y = \nu(\partial U)/\partial y \quad \text{Newton's law of friction} \qquad (3.6)$$

For heat transfer

$$\dot{q}_L = -k\partial T/\partial y = -\alpha\partial(\rho c_p T)/\partial y \quad \text{Fourier's law} \qquad (3.7)$$

For mass transfer

$$N_L = -D\partial C/\partial y \quad \text{Fick's law} \qquad (3.8)$$

where ν, α, and D are all of dimensions (L^2T^{-1}).

The dimensionless equations governing momentum, mass, and heat transfers are presented in Appendix A.

In order to correlate mass transfer results with heat transfer data, it is necessary to invoke an analogy. Reynolds analogy (see Appendix B) is rarely used since it is only valid for special circumstances, when the Prandtl (Pr) or Schmidt (Sc) numbers are equal to unity and the transfer medium is fairly homogeneous. Thus Reynolds analogy is not generally employed to predict mass transfer coefficients.

To overcome this difficulty, the Prandtl-Taylor, Von Karman and later analogies were proposed. These have proved particularly useful when dealing with complex turbulent boundary layer problems. The restrictions of $Pr = 1$ can now be relaxed.

By applying Von Karman's analogy to the turbulent boundary layer region, it is shown in Appendix B that:-

$$St = \frac{C_f/2}{1 + 5\sqrt{(C_f/2)}\left[(Pr - 1) + \ln((5Pr + 1)/6)\right]} \tag{3.9}$$

The corresponding mass transfer Stanton number is then

$$St_M = \frac{C_f/2}{1 + 5\sqrt{(C_f/2)}\left[(Sc - 1) + \ln((5Sc + 1)/6)\right]} \tag{3.10}$$

For turbulent flow over a flat plate we can write:

$$C_f = 0.059Re_x^{-0.2}$$

so that $St = f(Re, Pr)$ .... (3.11)

and $St_M = f(Re, Sc)$ .... (3.12)

But $Nu = St.Re.Pr$ .... (3.13)

$Nu = \phi(Re, Pr)$ .... (3.14)

and similarly, the corresponding mass transfer equivalent (Sh) is expressed by:

$$Sh = \phi(Re, Sc) \tag{3.15}$$

For more complicated forced convective flows, dimensional analysis indicates that similar relationships exist so that:

$$Nu = \phi_1(Re, Pr) \tag{3.16}$$

and

$$Sh = \phi_1(Re, Sc) \tag{3.17}$$

Geometrical parameters may also be included in these relationships. Kercher and Tabakoff (Ref. 79), for example, have shown by dimensional analysis that the functional relationship for impingement cooling under a square array of round jets with cross exhaust flows can be expressed as:-

(flowrate/unit flow area)

$$Nu = \phi_2\left[Re, Pr, X/d, \frac{G(X,(s-1))}{G(d, s)}\right] \tag{3.18}$$

The corresponding mass transfer expression will thus be:

$$Sh = \phi_2\left[Re, Sc, X/d, \frac{G(X,(s-1))}{G(d, s)}\right] \tag{3.19}$$

All the symbols are in accordance with the definitions presented in the nomenclature.

The heat and mass transfer analogies thus demand that for conditions of kinematic, geometric and dynamic similarity, the functions ϕ in the corresponding expressions are identical. Kinematic similarity implies equal velocity ratios, dynamic similarity implies equal Reynolds numbers, and geometric similarity requires equal ratios of linear dimensions (see Ref. 111).

The functions ϕ (or analogy factors) can be found by invoking a suitable analogy. The Chilton-Colburn analogy for example (which is based on limited theoretical analyses and widespread experimental corroborating evidence) assumes equivalence of the j-factors

i.e. $j_H = j_M =$ a function of Reynolds number, the geometry and boundary conditions.

Alternatively, the analogy factors may be derived (in cases for which skin friction data are available) using Von Karman's analogy, see equation (3.9), or a relationship derived by Jayatillaka (Ref. 112), see Appendix B. These various analogy factors for the case of fully developed flow are presented in Fig. 3.1

In the present study of jet-impingement mass/heat transfers, there is a paucity of skin friction data so that the Chilton-Colburn analogy is used. Furthermore, as discussed in section 3.2 previous investigatiors have found it to provide valid data for these systems.

3.4 Theory of Mass Transfer Modelling.

Isothermal models which conform to the necessary conditions of dynamic, kinematic, and geometric similarity mentioned in the previous section may be used to obtain convective heat transfer data from mass transfer measurements, using a suitable analogy.

A mean mass transfer coefficient b, may be defined as:-

$$m/t = b.A_N(C_N - C_o) \qquad (3.4.1)$$

where m is the sublimation loss in a time t.
The partial pressure of naphthalene vapour is negligibly small, so that the vapour can be regarded as a perfect gas with a temperature T_N, equal to that of the mass transfer surface. Thus:-

$$C_N = \frac{P_N}{R_{gN}T_N} \qquad (3.4.2)$$

where P_N and T_N are vapour-solid equilibrium values.

The vapour concentration of the naphthalene in the free stream region is negligibly small. Therefore $C_o = 0$, and from equation (3.4.1),

$$b = \frac{m}{tA_N} \frac{(R_{gN} T_N)}{P_N} \qquad (3.4.3)$$

Although sublimation depresses the surface temperature of the naphthalene below that of the free stream, this difference is negligible (Ref. 101).

Therefore the saturation vapour pressure P_N is evaluated at the mean free stream temperature T_o ($\simeq T_N$). The relationship between vapour pressure and temperature is discussed in section 3.6. In this study, the correlation of Sherwood and Bryant (Ref. 94) is used,

$$\text{i.e} \quad \log_{10} P_N = 11.55 - \frac{3765}{T_N} \qquad (3.4.4)$$

where P_N is in mm of mercury, and

T_N is in $^\circ$K.

Equation (3.4.4) is valid for T_N in the range 0 to 30°C

Using the Chilton-Colburn analogy (i.e. equivalence of j-factors) as described in Appendix B to evaluate the heat transfer coefficients from the mass transfer measurements yields:-

$$h = b\rho C_p \left(\frac{Sc}{Pr}\right)^{\frac{2}{3}} \qquad (3.4.5)$$

It has been estimated by Sherwood and Trass (Ref. 97) that $Sc = 7.0^{-0.185}$ for $100 < T_o < 500K$

Equation (3.4.5) applies to both local and average heat transfer coefficients provided the appropriate mass transfer coefficient is utilised.

3.5 Merits and Limitations in the Use of a Heat-Mass Transfer Analogy.

An important advantage of using a heat-mass transfer analogy in complex engineering problems lies in the fact that mass transfer measurements are generally easier and more convenient to make than direct measurements of heat transfer. This is particularly true in the case of local measurements for which profilometric techniques can be used. Direct heat transfer determinations in this case are particularly tiresome, and can be subject to conduction errors etc.

However, the mass transfer analogy is limited due to:-

(1) it is necessary to satisfy the conditions of geometric, kinematic, and dynamic similarity.

(2) the system should be such that the mass transfer rates can be measured readily.

(3) the driving force (often the vapour pressure) is constant over the transfer surface so that this technique only corresponds to the situation in which the heat transfer surface is isothermal.

Flat surfaces subject to impinging jets usually conform to these demands. In these cases, it is difficult to obtain theoretical analyses so that mass transfer techniques have proved particularly useful. It should be noted however that a mass transfer analogy is based on the assumption that mass transfer takes place without simultaneous heat transfer. In other words, it assumes that the system is isothermal. In practical situations, however, some heat transfer does take place at the mass transfer surface, although this can often be neglected. Thus under appropriate conditions, a mass-heat transfer analogy can be used to estimate heat transfer coefficients.

3.6 Properties of Naphthalene.

Naphthalene is a white crystalline solid with a characteristic aromatic odour, and a melting point of 353.1°K. This is well above normal ambient laboratory temperatures.

The most important physical property with regard to its use as a mass transfer substance is the vapour pressure. This follows since the driving force in a sublimation process is this vapour pressure so that an accurate knowledge of the relationship between temperature and vapour pressure is necessary. Several temperature-vapour pressure relationships for naphthalene are available in the published literature and these include:-

Sherwood and Bryant (Ref. 94):-

$$P_N = \text{Antilog}\left(11.55 - \frac{3765}{T^\circ K}\right) \qquad (3.6.1)$$

Christian and Kezios (Ref. 95):-

$$P_N = \text{Antilog}\left(11.73 - \frac{3825}{T^\circ K}\right) \qquad (3.6.2)$$

International Critical Tables (Ref. 113):-

$$P_N = \text{Antilog}\left(11.45 - \frac{0.5223 \times 71401}{T^\circ K}\right) \qquad (3.6.3)$$

Sogin (Ref. 114):-

$$P_N = \text{Antilog}\left(11.884 - \frac{6713}{T^\circ K}\right) \qquad (3.6.4)$$

Handbook of Chemistry and Physics (Ref. 115):-

$$P_N = \text{Antilog}\left(11.45 - \frac{3729}{T^\circ K}\right) \qquad (3.6.5)$$

In all cases, P_N is in mm of mercury except in Sogin's expression where P_N is in lbs/in^2. The vapour pressures predicted by the various expressions are in close agreement. In this investigation, however, Sherwood and Bryant's expression i.e. equation (3.6.1) was used. Further physical properties of naphthalene are presented in Appendix C.

3.7 Advantages of Using Naphthalene For Mass Transfer Measurements.

As mentioned in the previous section, the driving force for the sublimation of a solid is the vapour pressure at the surface. The vapour pressure of naphthalene can be readily obtained if the surface temperature is known.

Measurements of the actual surface temperature is, however, difficult, and it is more convenient to measure the temperature of the surrounding air. The naphthalene surface and air stream temperatures will differ due to:-

(a) sublimation of the surface layers
(b) radiative heat exchange with the surroundings
(c) conduction losses within the naphthalene, and
(d) aerodynamic heating

Wong(Ref. 101) however, found that the difference between the surface and air stream temperatures is negligible. Hence the naphthalene vapour pressure can be obtained from a measurement of the air stream temperatures.

In local heat transfer investigations (as in this project), where surface profiles have to be traced, coefficients of volumetric expansion are important. Naphthalene has a remarkably low coefficient of volumetric expansion (0.00028/deg. C). Hence errors arising from sudden volume changes (such as expansion under test conditions), and/or subsequent volume changes when making profile traces under laboratory conditions, are negligibly small. Naphthalene, moreover, sublimes at a rate sufficient to give a measurable volume reduction under an impinging jet over a few hours.

Other solid subliming substances can, however, be used, and these include solid hydrocarbons such as camphor, urethene, acetonaphthalene, and hexachloroethane. However, these generally posses unsuitable sublimation rates (Ref. 113) within the temperature range of the present investigation (273^{o}K to 303^{o}K). Nevertheless camphor can be suitable, although the vapour pressure of camphor tends to be very high beyond about 303^{o}K (see fig. 3.2). Camphor, however, melts at 449.4^{o}K so that it is more difficult to cast.

In a jet impingement investigation where a flat surface is necessary, naphthalene is suitable since the surface can be machined or scraped easily after casting to produce the desired finish. With regard to the explosive limits, toxicity, and other safety properties, naphthalene is a comparatively safe organic compound to handle. The other relevant properties of naphthalene relevant to its use as a sublimate in mass-heat transfer tests are presented in Appendix C.

FIG.3.1. GRAPH SHOWING MASS/HEAT TRANSFER ANALOGY FACTORS vs REYNOLDS NUMBER

FIG.3.2. VARIATION OF VAPOUR PRESSURE WITH TEMPERATURE FOR CAMPHOR AND NAPHTHALENE

CHAPTER 4

EXPERIMENTAL APPARATUS

4.1 General.

The present investigation involved the measurement of local heat transfer distributions, and the variations of the radial velocity and turbulence intensity for nozzle-to-target spacings ranging from 2 to 8 jet diameters. The design of the experimental apparatus used for these flow and heat transfer tests was similar to the set-ups employed in previously reported work on the subject. Flow visualisation studies were also undertaken, and these are discussed in chapter 6.

4.2 General Layout of Experimental Rig.

A general view of the experimental rig is shown in fig. 4.1. The part numbers shown in this figure refer to the various components, and the detailed drawings are available in the School of Mechanical Engineering at the Cranfield Institute of Technology.

A schematic representation of the rig, together with details of the test chamber is shown in fig. 4.2. Two separate air supplies were used, one for the impinging jet, and the other supplied for the crossflowing air stream. For the jet impingement supply, the air was delivered by a Keith Blackman single stage blower driven by a 2 kw 3-phase electric motor running at 2,900 r.p.m. For the crossflow supply, a Secomak Centrifugal air blower was used. This was driven by a 4 kw 3-phase electric motor running at 2,870 r.p.m..

Both the 'jet' air and the crossflowing stream were delivered to Plenum Chambers prior to entry to the test section. These air supplies were cooled (if required) by means of circulatory water coolers mounted in the supply ducts prior to the plenum chambers. These coolers provided the means of regulating the temperatures of the air supply at values very near to those of surrounding ambient conditions (thus avoiding expansion errors). The air supply temperatures were measured using 'Rototherm' thermometers which could be read to a precision of 0.1°C over a range from 0 to 30°C.

The air flows were determined using orifice plates designed to the specifications of B.S.1042. The delivery line pressures and the difference across the orifice plates were measured using water manometers. The pressure tappings for this purpose were located at one pipe-diameter upstream, and one-half pipe-diameter downstream of the orifice plates. Audco slimseal regulating valves were used to control the air supplies.

The plenum chambers were fitted with flow-straighting screens. The jet plenum chamber exited directly into the test section, whereas the crossflow plenum chamber was connected to the working section through a connecting duct section whose size corresponded to the appropriate nozzle-to-target spacing. This connecting duct section was fabricated from mild steel plates and incorporated honeycomb-type flow straighteners.

4.3 Test Section - Design and Construction.

4.3.1 General Outline

The test section is shown in fig. 4.3. It was 508mm long, 304.8 mm wide, and its height was varied by using perspex spacers which extended the full length of the test section. Thus the tests were conducted over a range of nozzle-to-target spacings. The connecting 'crossflow' air supply ducting was fitted to one end of the test section and the exhaust was removed from the other end. The 'jet' plenum chamber was mounted on the top of the test section. The nozzle plate assembly was contained in the base of this plenum chamber so that the jet discharged along the longitudinal axis of the system. 'Target trays' incorporating the naphthalene test surfaces were positioned in guides in the base of the test section. The whole assembley was held together by bolts running through the nozzle and target plates. Plasticine was moulded around the edges and corners of the section to prevent leakage.

4.3.2 The Jet Assembly.

The jet supply plenum chamber was fabricated from 1.6 mm thick mild steel sheet and its cross-section measured 381.0 mm by 330 mm. It was 0.61 m in height and the metered air supply was delivered via a flexible pipe. The plenum chamber entry connection was constructed of 83 mm diameter pipe and the air was delivered radially into the chamber through a number of small holes drilled in the wall of this pipe. A series of 'flow straighteners' were then employed to provide a reasonably uniform flow.

The first 'straightener' consisted of a mild steel perforated sheet which was welded across the plenum chamber at a distance of 152 mm from the end of the delivery pipe. The second mesh was composed of a 25.4 mm thick honeycomb welded at a distance of 76.2 mm downstream of the perforated sheet. After passage through these flow straighteners, the air entered the test section through the nozzle as shown in figs. 4.1 and 4.2. Detailed dimensions of this jet plenum chamber are available in drawing number PC 11596.

The majority of previous jet-impingement investigations employed jets issuing from orifices. The nozzle exit velocity profile has an effect on the heat transfer from the jets (see Sparrow and Lee (Ref. 116)). In this investigation approximately fully developed exit velocity profiles were obtained since the nozzles were sufficiently long for this purpose. The brass nozzles were 12.7 mm in internal diameter, and 63.5 mm long. They were cemented into nozzle plates using an Araldite adhesive. The nozzle plates were constructed of 12.7 mm thick perspex and measured 279.4 mm by 101.6 mm in width. These nozzle plates fitted into a slot on the main nozzle housing on the top of the test section and were clamped rigidly in position by means of 2BA studs. A gasket was employed for sealing purposes. To induce some turbulence into the jet, a 1.60 mm diameter wire was brazed across the inlet of each nozzle. Fig. 4.4 illustrates the nozzles used in this investigation. The method of mounting the nozzle plate in the main housing is shown in Fig. 4.5

This main nozzle housing was made of 25.4 mm thick perspex and formed the top surface of the test section. Detailed dimensions of this component are presented in drawing number PC 11604. The central slot in this housing was such that inclined jets (at inclination angles up to 45°) could be accommodated. A pair of grooves 12.7 mm wide and 3.2 mm in depth were machined along the length of the housing and the perspex sides spacers were located by these means. Hence the jets could be inclined at various angles towards the upstream direction and the tests could be conducted for a variety of nozzle to target spacings.

After the nozzle plate was positioned, the jet plenum chamber was fitted and fixed to the main nozzle housing using fourteen suitably placed 2BA bolts. Sealing was provided by a gasket and any slight leakage was prevented using plasticine.

4.3.3 Side-Spacers and Target Tray Assembly.

The spacers were made of 12.7 mm thick perspex and extended the full 508 mm length of the test section. For this present investigation, spacers of width 25.4, 50.8, and 101.6 mm were used. These spacers were fixed by means of Allen screws to the connecting crossflow air supply duct.

The target plate or tray was constructed of Aluminium and was 381 mm long, and 343 mm wide. Detailed dimensions of this target tray are shown in drawing number PC 11593. The naphthalene was cast into a 5 mm deep cavity machined in this tray. The mass transfer surface area was 0.0975 m^2. The target tray is illustrated in Fig. 4.6, and it is shown positioned in the test section in Fig. 4.3. A pair of 12.7 mm wide grooves were machined along the length of the target plate to accommodate the appropriate side spacers.

The target plate was designed to slide into a U-shaped guide in the test section base. Detailed dimensions of this base are presented in drawing number PC-11592. The base was then fixed by Allen screws to the cross-flow connecting duct. Final assembly was completed by securing bolts which passed through the main nozzle housing and the test section base, see Fig. 4.3

4.4 Naphthalene Surface Profile Measurement

A general view of the profile measurement equipment used in this investigation is shown in Fig. 4.7. It consisted of a lathe which was employed as a traversing mechanism and two displacement transducers one of which was excited from a voltage stabiliser. The outputs were fed into an X-Y recorder and a specially machined block was employed as a calibration device.

The profiles were measured in the direction of cross-flow with the lathe providing an accurate motorised traversing mechanism. A base plate was mounted on the lathe bed and suitably placed location holes in this plate (machined to take 2BA screws) ensured that the target plate was mounted flat and in the same relative position each time. Local mass transfers were determined by measuring the naphthalene surface profile before and after each test using a short stroke linear displacement transducer (type SE 355). The position of this transducer was indicated by a long stroke (± 254 mm) linear displacement transducer (also type SE 355). This was connected from the lathe saddle to the base plate, and ran parallel to the measurement axis (lathe bed), as shown in Fig. 4.8 This transducer operated the X-scale of the X-Y recorder.

The short stroke transducer was bolted on to a mounting fixed to the lathe cross slide, see Fig. 4.9. This transducer had a measuring range of ± 5 mm, and was traversed over the naphthalene surface. Its output was fed to the Y-axis of the recorder. The transducer calibration block (also shown in Fig. 4.9) was used to calibrate the output of the transducers before and after each test. This aluminium block 101.6 mm long, and 12.7 mm wide, was carefully ground to obtain ten smooth steps each of 1 mm in depth. The short stroke transducer was also calibrated using this block by moving the transducer over the steps of the block.

The X-Y recorder used in this study was a Bryans-22000 series unit. In this investigation, a highly sensitive transducer setting was required, so that slight erosion depths could be monitored accurately. A voltage of 9 V d.c (supplied from a Farnell stablised voltage supply, type L.30) was sufficient to give the required sensitivity after suitable adjustment of the X-Y recorder settings. The voltage stabiliser together with the X-Y recorder are shown in Fig. 4.7. This equipment was used to obtain profiles over the entire mass transfer surface by traversing the short-stroke transducer along the longitudinal axis of the plate (i.e. the cross-flow direction). The profile measurements were repeated at symmetrical positions relative to the centre line of the base plate. The spacing between adjacent positions was 25.4 mm. Details of the measurement procedure are presented in chapter 5.

4.5 Pitot Tubes and Associated Instrumentation.

The velocity profiles at locations along the axis of the crossflowing air stream were obtained by means of a pitot-static tube. The dimensions of this were:

The total pressure tube: Outside diameter = 1.82 mm
Inner diameter = 1.35 mm

The static pressure tube: Outside diameter = 5.46 mm
Inner diameter = 4.55 mm

A ring of 0.99 mm diameter holes were evenly distributed around the circumference of the static pressure tube, at a distance of 12 mm from the hemispherical end. The total and static pressure tubes were connected across a Furness Controls transducer-type meter-reading micro-manometer. A liquid manometer was used periodically to calibrate the micro-manometer to eliminate drift.

In this micro-manometer, the pressure acts on a diaphragm which forms one plate of a capacitor. Pressure variations thus produce variations in the capacitance and an electrical output can be obtained. The manometer was graduated in the range 0 to 100 torr. Readings were made to an accuracy of either ± 0.01 torr. or ± 0.1 torr. depending on the range. The transducer is shown in Fig. 4.10 together with the DISA equipment used for turbulence measurements.

4.6 Velocity and Turbulence Intensity Instrumentation.

Velocity and turbulence intensity distributions at locations along the axes of the jets were undertaken using the hot-wire anemometer equipment shown in Figs. 4.10 and 4.11. Fig. 4.10 shows the DISA Anemometer Unit and Fig. 4.11 illustrates the DISA probe and its traversing mechanism.

This probe was a DISA type 55A25 and was mounted with its axis parallel to the direction of the jet flow. The electrical output generated from the probe was fed into the DISA measurement unit. The DISA measurement Unit consisted of:

(1) an Integrator	(type 52B30)
(2) a Linearizer	(type 55D10)
(3) a Root Mean Square meter	(type 55D35)
(4) a Constant Temperature Anemometer	(type 55D01)
(5) an Auxiliary Unit	(type 55D25)

An oscilloscope (Tektronix type 516) was used to display the signals for reference purposes.

The hot-wire probe was calibrated by independently measuring the jet exit velocity using a hypodermic pitot-tube of 2.34 mm outside diameter and 1.70 mm inside diameter. The total pressure indicated by this tube was measured relative to ambient using the micro-manometer. The jet velocity was then calculated assuming that the static pressure was equal to the ambient value. The root mean square of the fluctuating axial component of velocity was measured using the linearised type 55D01 constant temperature hot-wire anemometer directly coupled to the DISA 55D35 RMS meter. For completeness, the hot-wire anemometer is described in Appendix D.

KEY TO FIGS. 4.3 - 6.3

1	Jet Plenum Chamber
2	Nozzle Plate
3	Target Plate
4	Connecting Duct
5	Crossflow Plenum Chamber
6	Target Tray Containing Naphthalene
7	Lathe Saddle
8	Target Tray Positioned on Lathe-bed
9	Target Plate Mountings
10	Farnell Voltage Stabiliser
11	X-Y Recorder
12	Long Stroke Transducer
13	Lathe Bed
14	Short Stroke Transducer
15	Naphthalene Mass Transfer Surface
16	Transducer Calibration Block
17	Furness Controls Transducer-type Micro-Manometer
18	Hypodermic Pitot-Tube
19	Type 52B30 Integretor
20	Type 55D10 Lineariser
21	Type 55D35 Root Mean Square Metre
22	Digital Voltmeter
23	Type 55D25 Auxiliary Unit
24	Type 55D01 Constant Temperature Anemometer
25	Tektronix Type 516 Oscilloscope

26	Probe Holder
27	Type 55H01 Traversing Mechanism
28	Projector Lamp
29	Oil Film Pattern Forming on Target Plate
30	Camera
31	Smoke Drum
32	Hand-Operated Pump

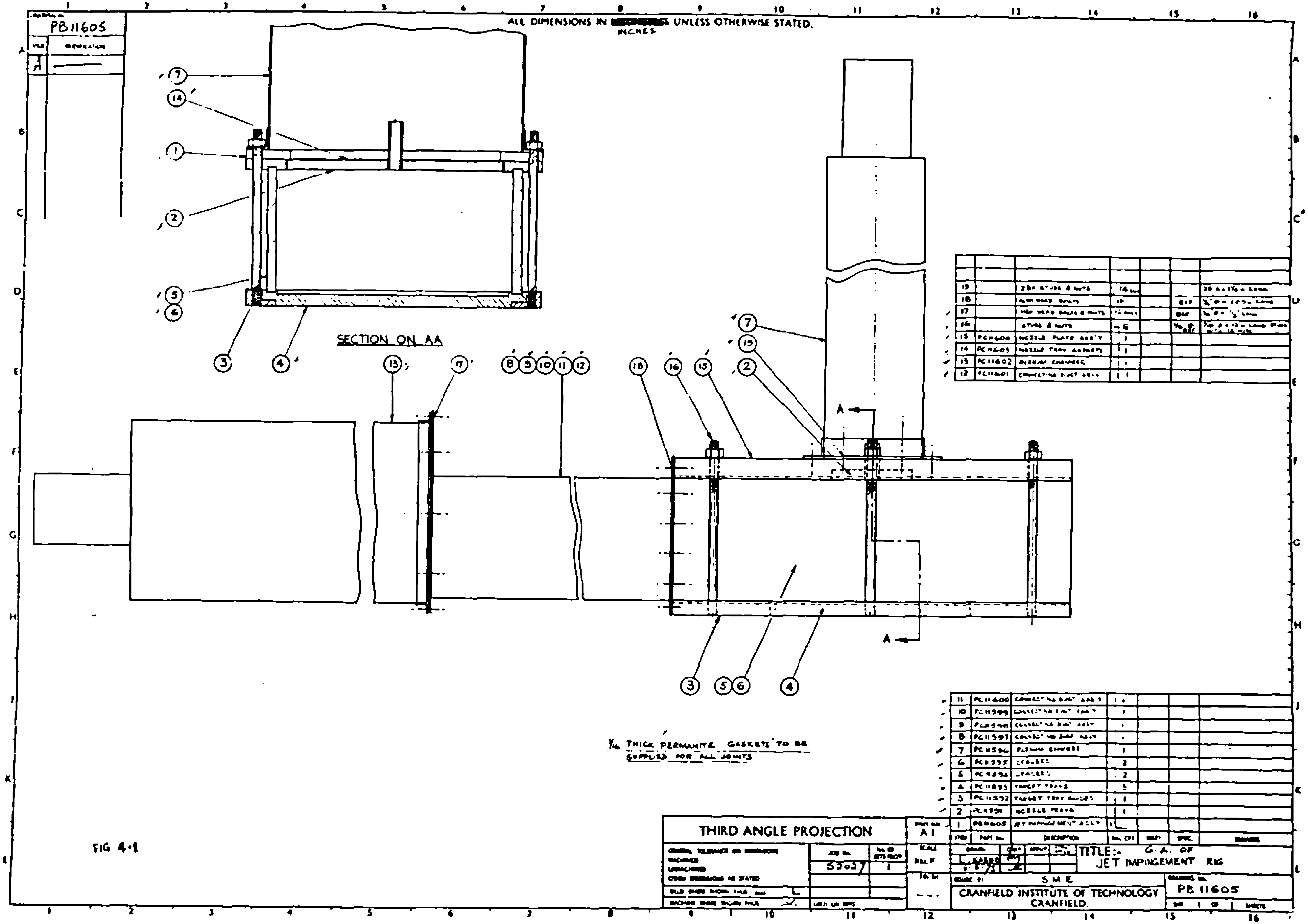
PB11605
ALL DIMENSIONS IN INCHES UNLESS OTHERWISE STATED.
SECTION ON AA
A
A
⑦
⑭
①
②
⑤
⑥
③
④
⑬
⑰
⑧⑨⑩⑪⑫
⑱
⑯
⑮
⑲
③
⑤⑥
④
1/16 THICK PERMANITE GASKETS TO BE SUPPLIED FOR ALL JOINTS
THIRD ANGLE PROJECTION
A1
JOB No. 53037
TITLE:- G.A. OF JET IMPINGEMENT RIG
SME
CRANFIELD INSTITUTE OF TECHNOLOGY CRANFIELD.
DRAWING No. PB 11605
SH 1 OF 1 SHEETS
19 2BA STUDS & NUTS
16 STUDS & NUTS
15 PC11604 NOZZLE PLATE ASS'Y
14 PC11603 NOZZLE TRAY GASKETS
13 PC11602 PLENUM CHAMBER
12 PC11601 CONNECTING DUCT ASSY
11 PC11600 CONNECTING DUCT ASSY
7 PC11596 PLENUM CHAMBER
6 PC11595 SPACERS
5 PC11594 SPACERS
4 PC11593 TARGET TRAYS
3 PC11592 TARGET TRAY GUIDES
2 NOZZLE TRAYS
1 PB11605 JET IMPINGEMENT ASSY
ITEM PART No. DESCRIPTION No. OFF MAT. SPEC. REMARKS

FIG 4·1

(a) – GENERAL LAYOUT (b)-DETAILS OF TEST CHAMBER

FIG. 4.2. SCHEMATIC REPRESENTATION OF EXPERIMENTAL RIG

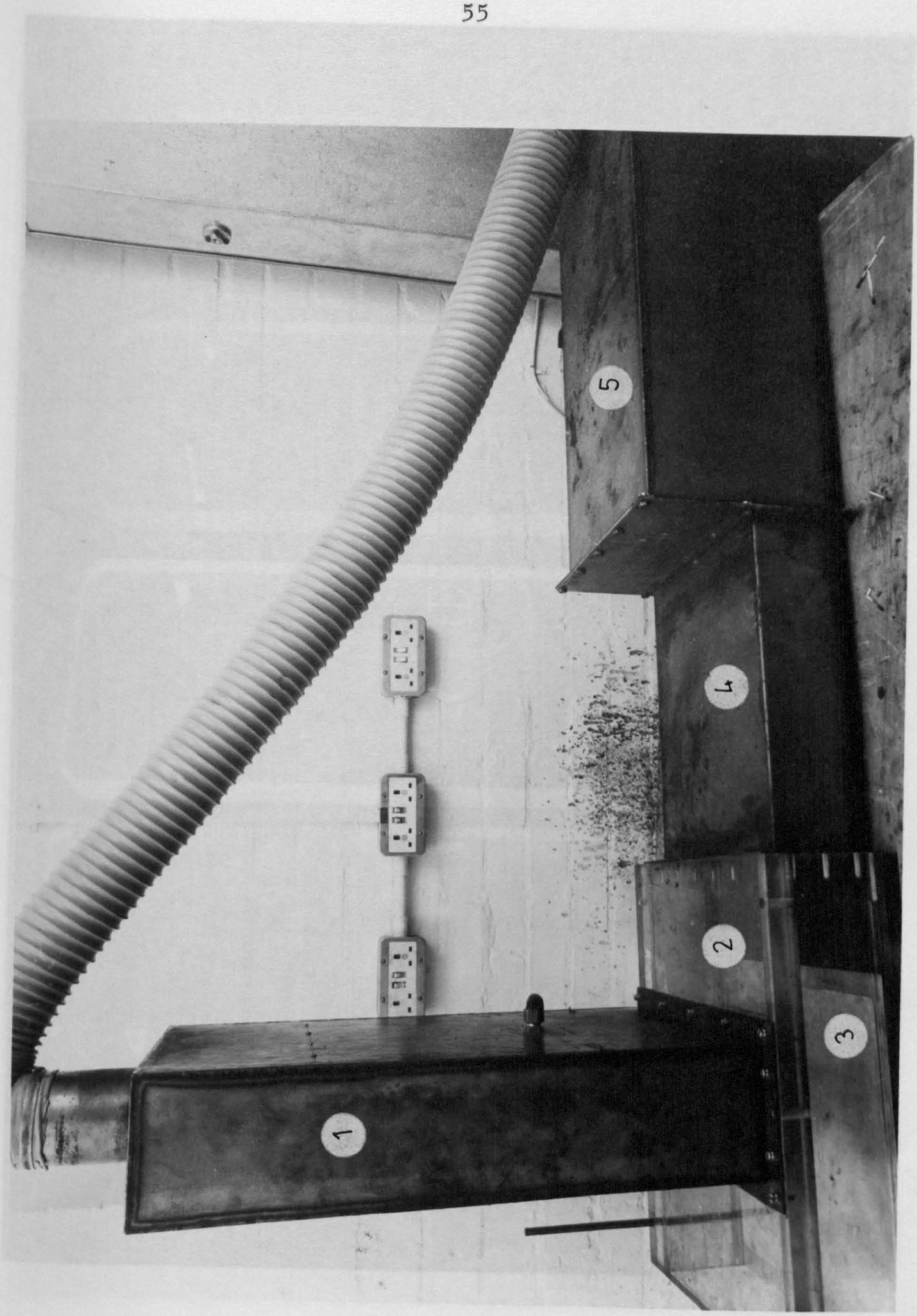

FIG. 4.3. TEST SECTION AND ASSOCIATED COMPONENTS

FIG. 4.4. NOZZLE TRAYS WITH INCLINED AND ORTHOGONAL NOZZLES USED IN THE TESTS

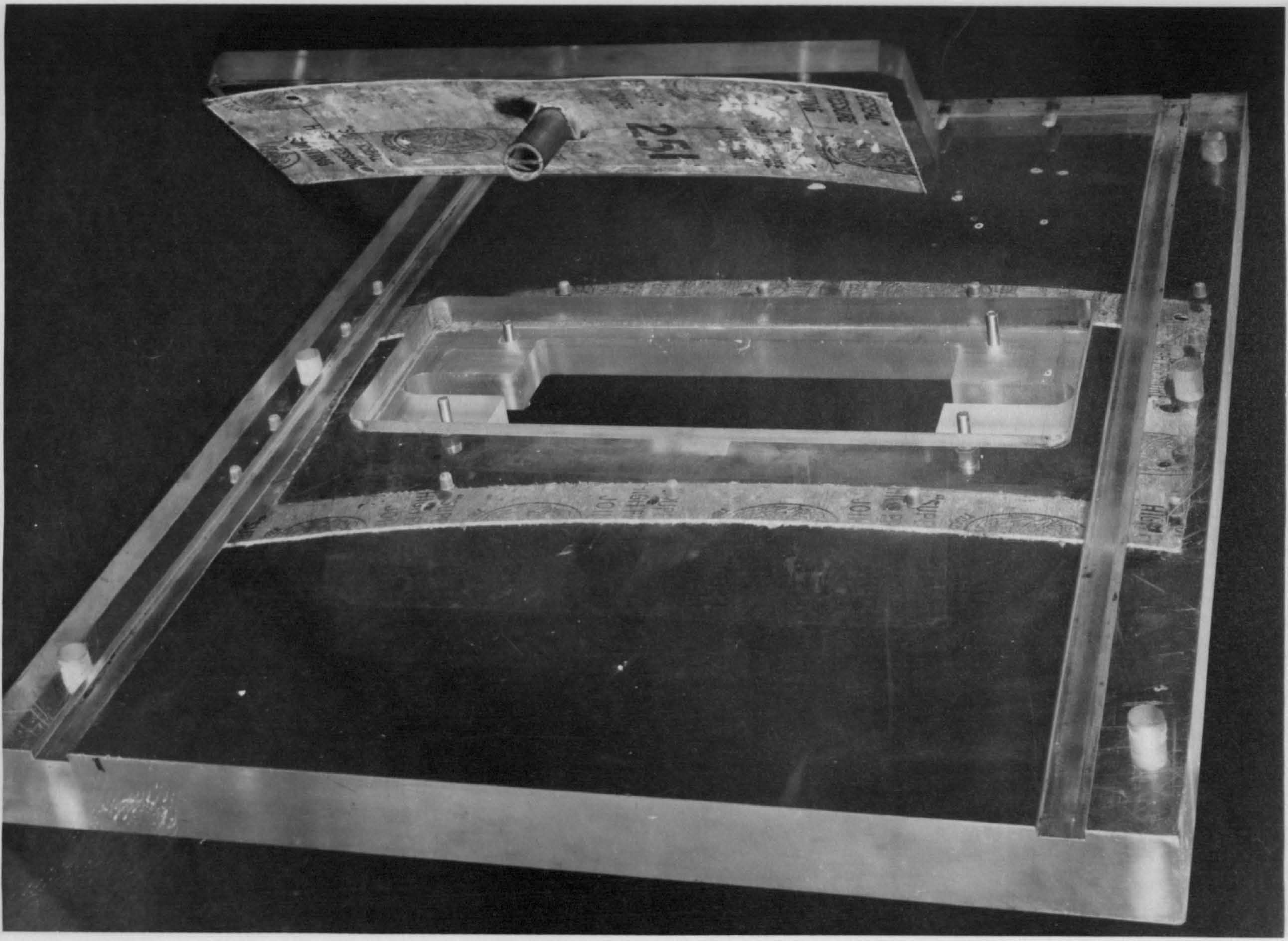

FIG. 4.5. NOZZLE TRAY FITTING INTO POSITION ON NOZZLE PLATE

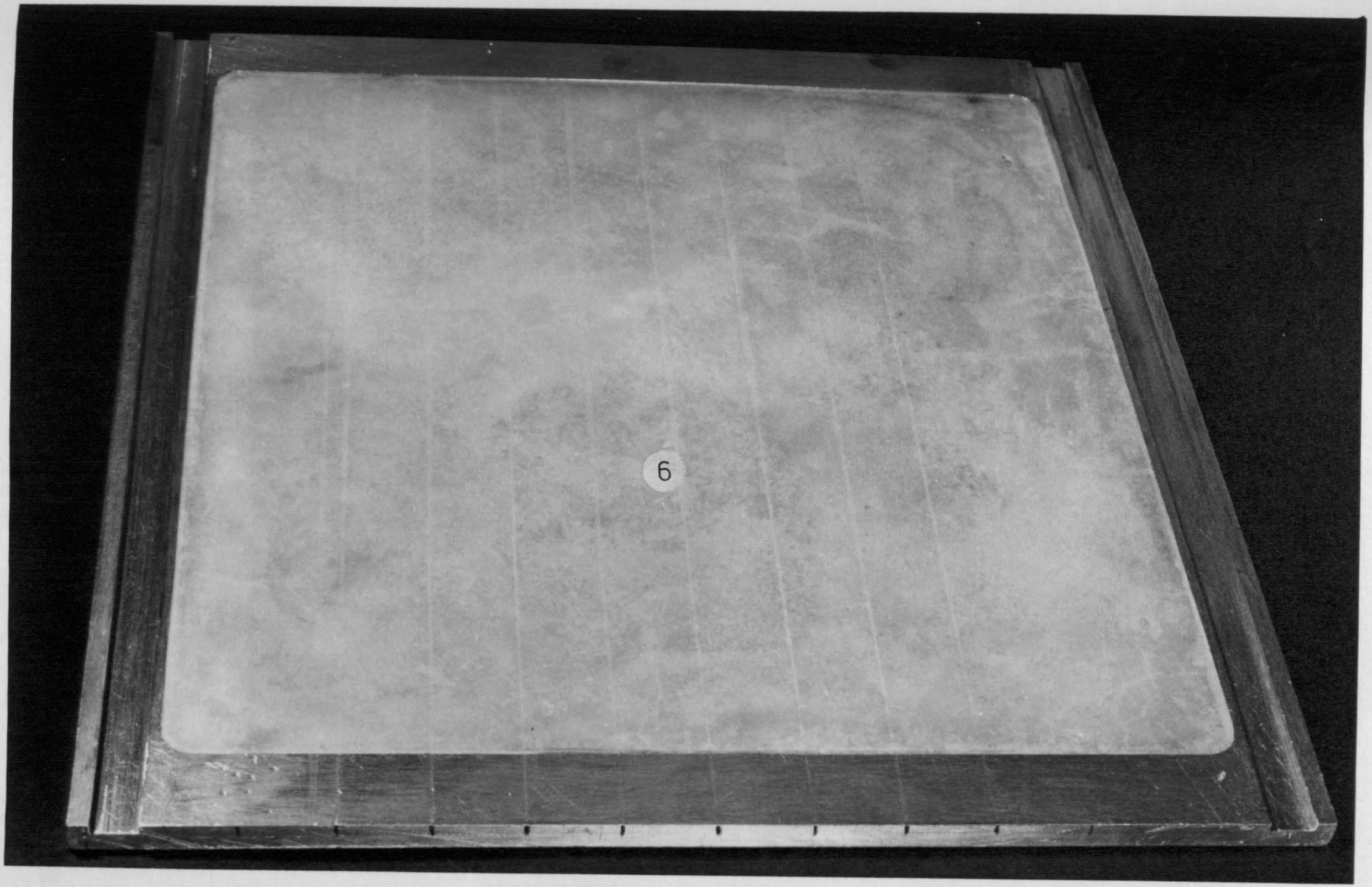

FIG. 4.6. TARGET TRAY WITH CAST NAPHTHALENE

FIG. 4.7. GENERAL VIEW OF EQUIPMENT FOR SURFACE PROFILE MEASUREMENT

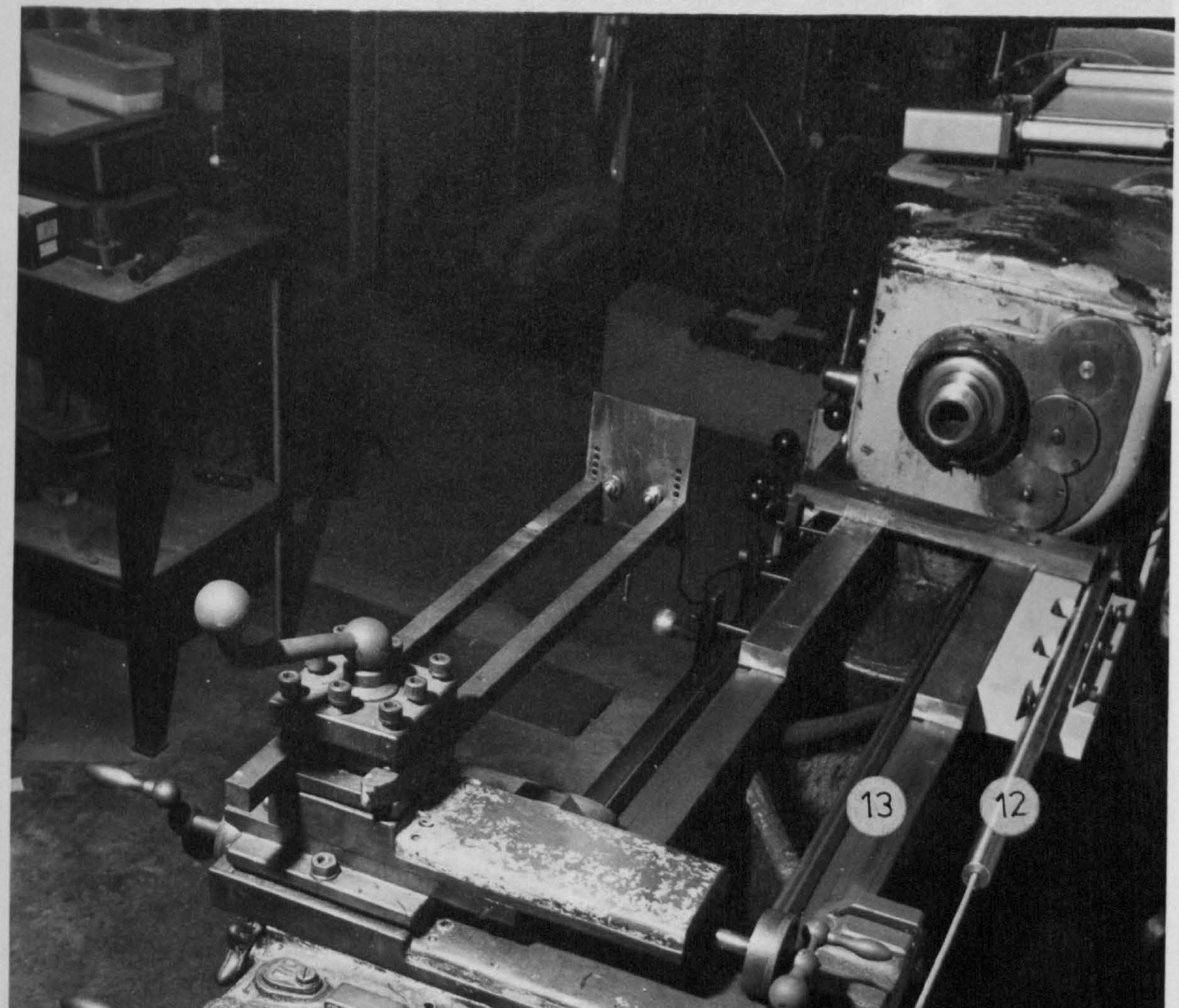

FIG. 4.8. GENERAL VIEW OF LATHE BED — SHOWING LONG STROKE TRANSDUCER

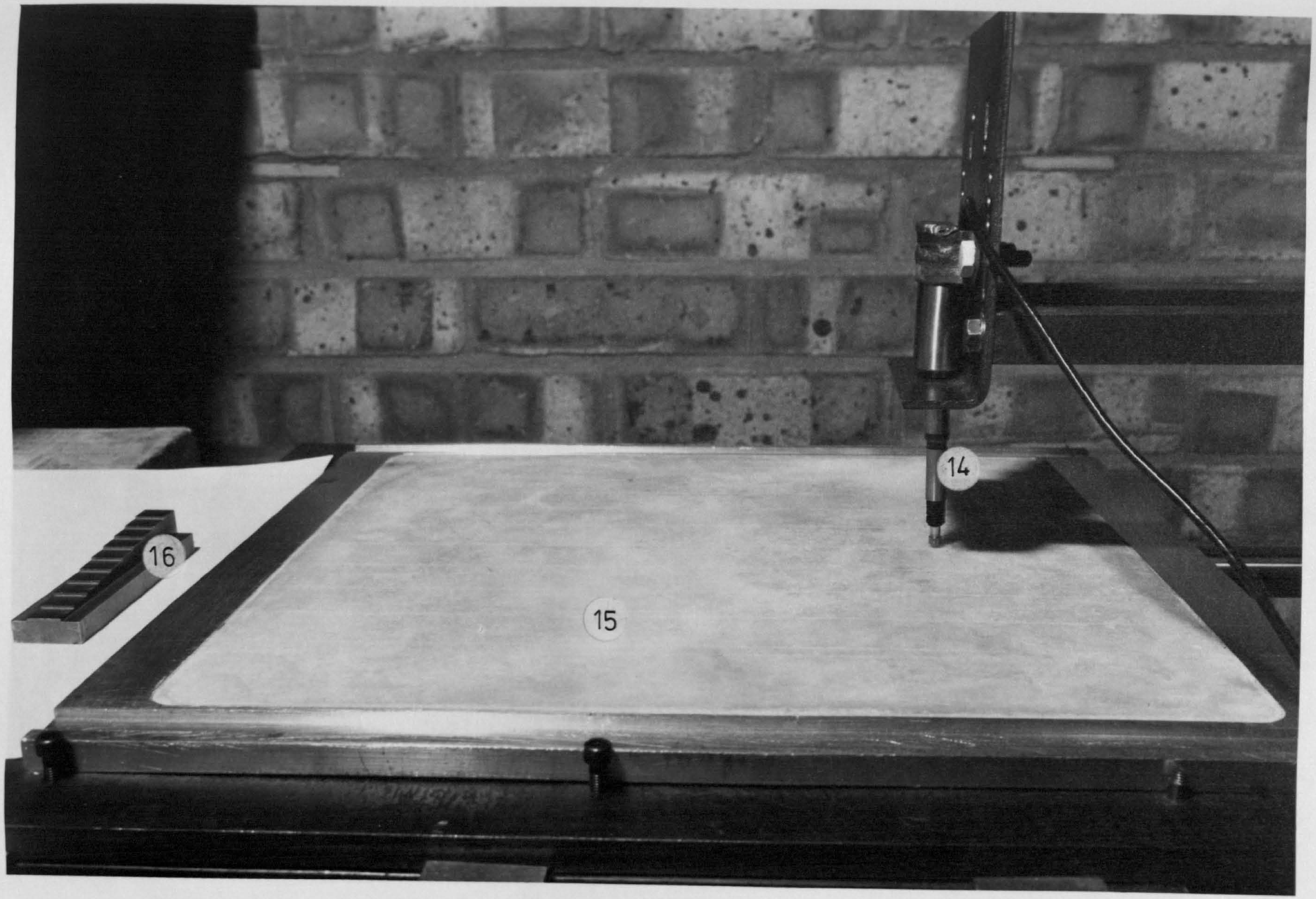

FIG. 4.9. SHORT STROKE TRANSDUCER IN OPERATION ON NAPHTHALENE SURFACE OF TARGET PLATE

FIG. 4. 10. MICRO-MANOMETER AND DISA UNIT FOR TURBULENCE MEASUREMENTS

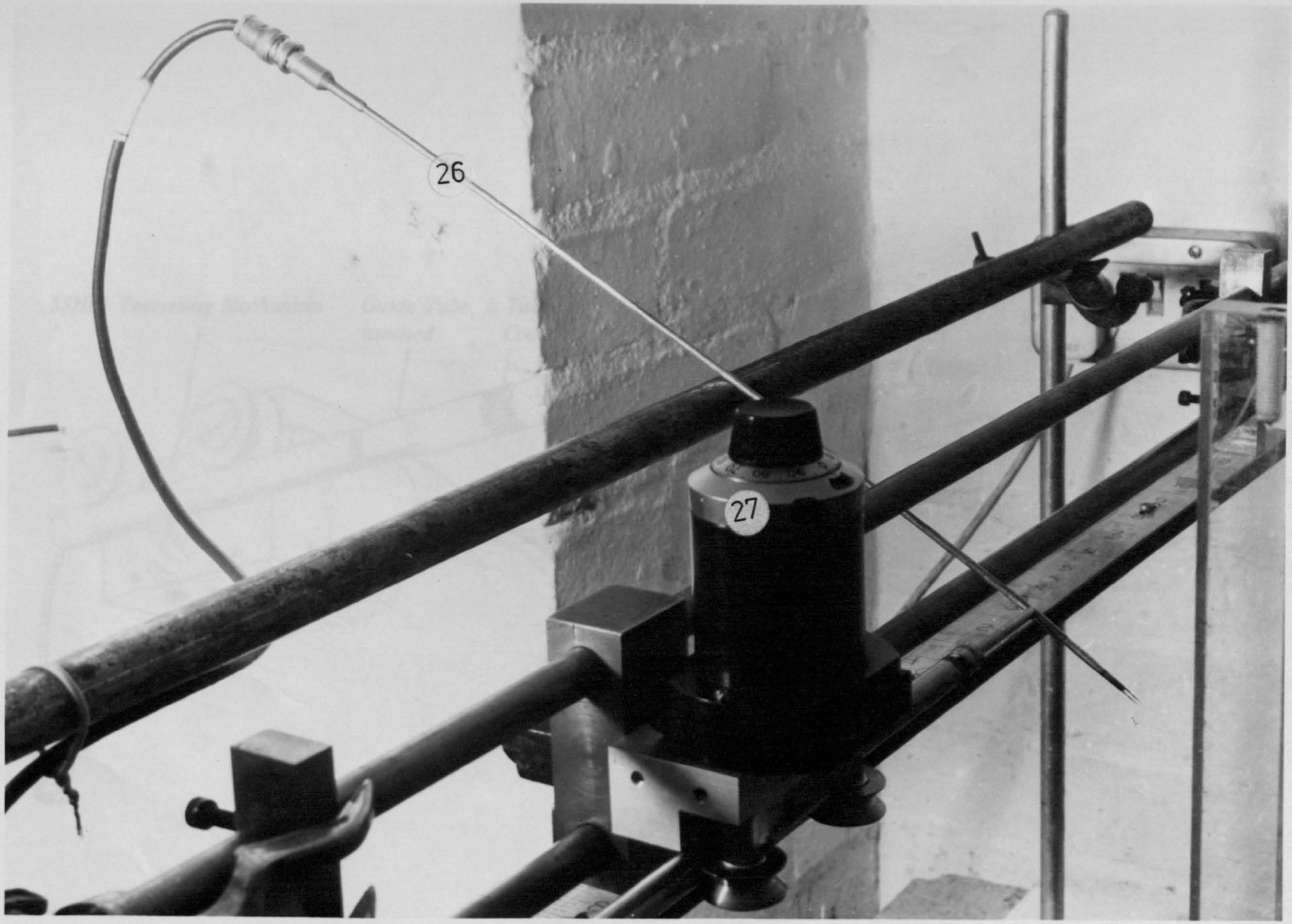

FIG. 4.11. HOT WIRE PROBE MOUNTED WITH TRAVERSING MECHANISM FOR VELOCITY AND TURBULENCE MEASUREMENT

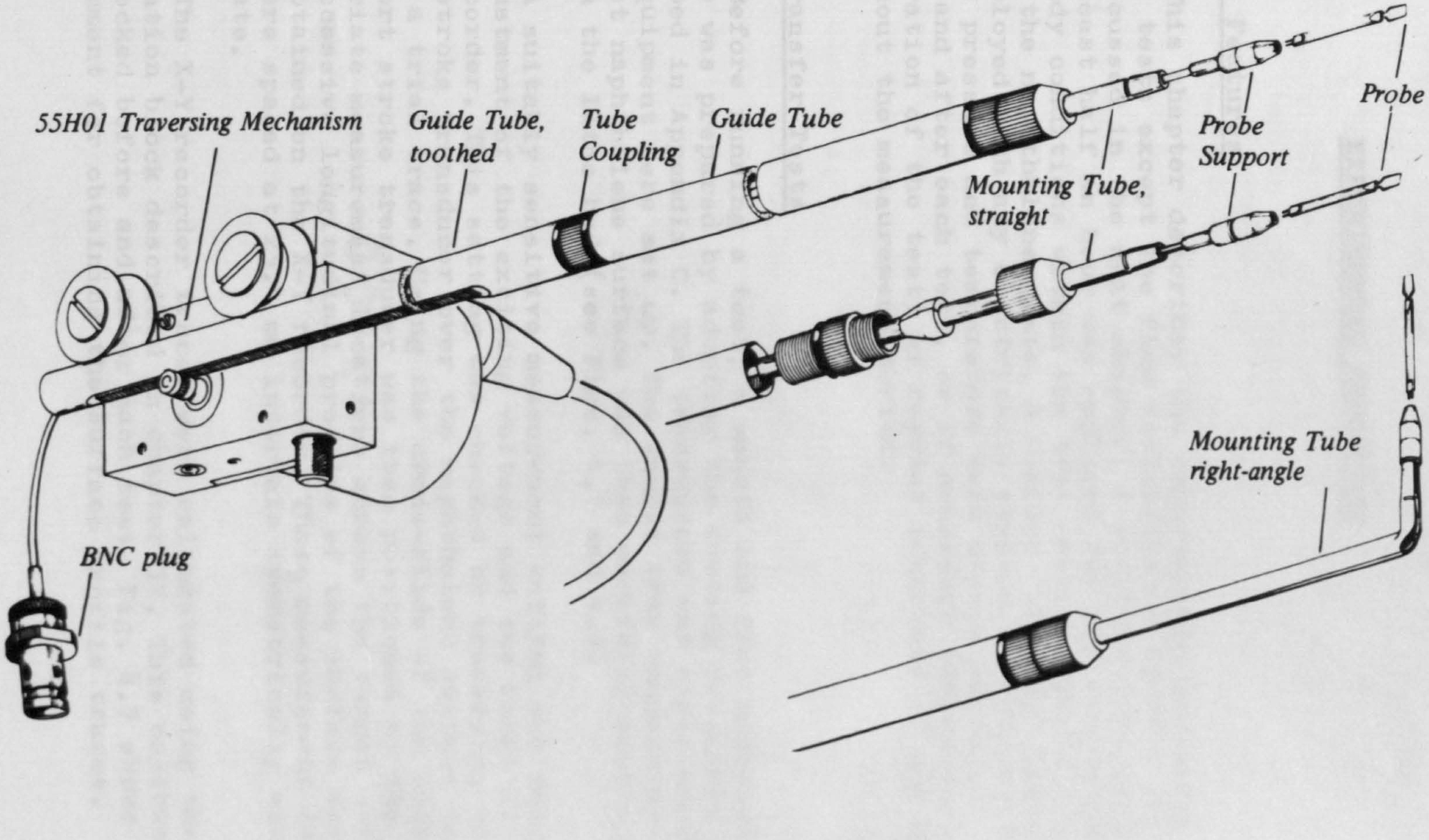

FIG. 4.12. PROBE MOUNTING TECHNIQUE

CHAPTER 5

EXPERIMENTAL PROCEDURE

5.1 General Features

This chapter describes the experimental procedure for all tests except the flow visualisation studies which are discussed in the next chapter. A settling down period of at least half an hour was employed for the attainment of steady conditions within the test section before insertion of the naphthalene plate. A similar 'warm-up' period was employed with any electrically powered instrumentation. Ambient pressure and temperature were always recorded before and after each test, or if necessary (depending on the duration of the test) at regular intervals of one hour throughout the measurement period.

5.2 Mass Transfer Tests

Before running a test, a smooth and flat naphthalene surface was prepared by adopting the casting procedure described in Appendix C. The transducers and other measurement equipment were set up. The target tray containing the cast naphthalene surface was then carefully mounted flat on the lathe bed (see Figs. 4.7 and 4.9)

A suitably sensitive measurement setting was obtained by adjustment of the exciting voltage and the range of the X-Y recorder. This setting was checked by traversing the short stroke transducer over the naphthalene surface to obtain a trial trace. Using the cross-slide of the lathe, the short stroke transducer was then positioned at the appropriate measurement locations across the target surface. Ten successive longitudinal profiles of the surface were then obtained on the X-Y recorder. These measurement locations were spaced at 25.4 mm intervals symmetrically across the plate.

The X-Y recorder traces were calibrated using the calibration block described in chapter IV. This calibration was checked before and after each test. Fig. 4.7 shows the arrangement for obtaining the surface profile traces.

After measurement of the initial surface profiles, the target plate containing the naphthalene casting was positioned in the rig as shown in Fig. 4.3 and the pre-set air flow switched on as required. The temperature at the naphthalene surface (i.e. the air temperature within the test section) was maintained at a value very near to ambient so that thermal expansion or contraction of the naphthalene and changes in its vapour pressure were minimised. During each test, the ambient temperature, the naphthalene surface temperature, and the temperature of the air stream entering the orifice plate were recorded at regular intervals. The Barometric pressure, the inlet pressure at the orifice plate, and the pressure difference across this plate were also all recorded.

The duration of the tests varied from 1 to 6 hours, depending on the flow rate and the nozzle to target spacing, i.e. on the mass transfer rate. In the longer duration tests, the barometric pressure and the ambient temperature were subject to some degree of drift. Consequently, all the readings were averaged, and mean values used in the calculations.

At the end of the test, the target tray was removed and remounted on the lathe bed. By careful positioning of the short stroke transducer on the target tray, and also repositioning of the pen on the corresponding X-Y recorder trace, the final suface profiles were superimposed on the appropriate initial profiles as shown in Fig. 5.1. The differences between the two surface profiles were then used to calculate the local mass losses. The corresponding heat transfer coefficients were inferred from the Chilton-Colburn analogy as discussed in Appendix B.

5.3 Velocity and Turbulence Measurements

5.3.1 Crossflow Velocity Measuremens.

For the crossflow velocity traverses, the pitot-static tube described in chapter IV was employed, and the experimental set-up was similar to that shown in Fig. 4.11
The velocity traverses were made at exit from the connecting duct. These velocity profiles were plotted in non-dimensional form. The mean crossflow was measured by standard orifice plates and was kept invariant during the test by means of flow regulating valves.

5.3.2. Jet Velocity and Turbulence Measurements.

The mass-transfer tests were conducted at fairly low nozzle to target spacings of 2, 4, and 8 jet diameters. Consequently, in view of the difficulty of using the hot-wire anemometer in such a confined space, jet velocity and turbulence measurements were carried out on free jets (for both the orthogonal and inclined assemblies). The traverses were undertaken at the nozzle exit and at 2, 4, and 8 nozzle downstream diameters as shown in Figs. 4.10 and 4.11

The DISA hot-wire anemometer was switched on and between one and three hours allowed for stabilisation. The DISA type 55A25 probe was then mounted in the probe-holder, and the assembly positioned in the traversing mechanism as shown in Fig. 4.12. Care was taken to ensure that the probe was mounted with its axis parallel to the direction of jet flow, so that the hot wire was placed perpendicular to the mean flow direction. In this way, the probe was capable of sensing the mean velocity and the streamwise component of the turbulent fluctuations.

The probe was then calibrated for the Reynolds number range in which it was to be used. This was accomplished by first using a shunt to determine the resistance of the probe wire and lead at room temperature, under no-flow conditions. The 'lineariser' was then zeroed and its gain control was set to provide a full scale meter deflection for the maximum calibrating jet velocity. The 'Auxiliary Unit' was also adjusted during the calibrating process. This is a low pass filter which reduces the noise generated by the sensor when in operation, so that a high signal to noise ratio can be obtained.

After the necessary adjustments of the DISA Unit to obtain optimal calibrating settings, the unit was calibrated by comparing the mean output voltage with the velocity as measured by hypodermic pitot-tube. This procedure was repeated for several velocity settings within the range appropriate to the present study, i.e. 14 to 56 m/s . After calibration, velocity and turbulence measurements were made by suitably traversing the hot-wire probe across the jet at various axial locations. At each traverse position, voltages proportional to the mean velocity and the turbulent fluctuations were recorded. The velocity and turbulence intensity were evaluated as described in Appendix D.

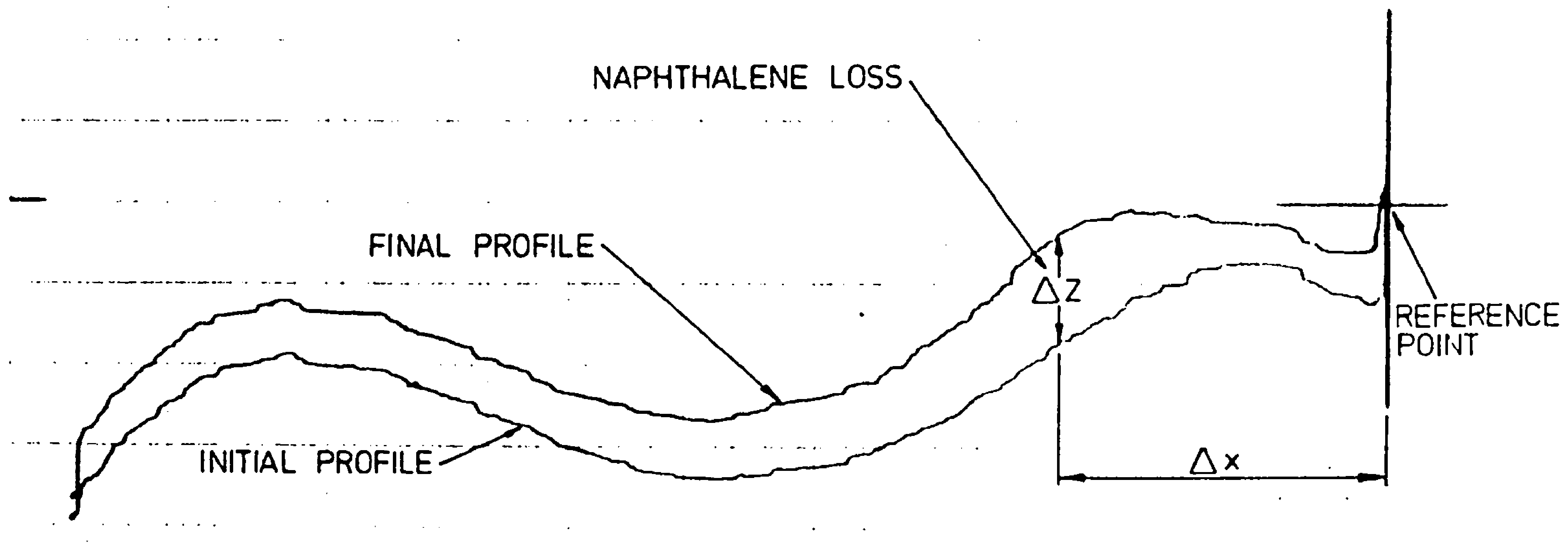

CALIBRATION GIVES Δz IN TERMS OF NAPHTHALENE LOSS AND Δx IN TERMS OF ACTUAL AXIAL DISTANCE ALONG TEST SURFACE

FIG. 5.1. TYPICAL PROFILE TRACE FROM X-Y PLOTTER

CHAPTER 6

FLOW VISUALISATION STUDIES

6.1 General Introduction

Flow visualisation studies can often lead to a greater understanding of heat transfer phenomena, particularly in complicated flowfields. Suitable seeding renders the flow visible so that a clear idea of the general nature of the flowfield is possible. Flow visualisation can thus reveal the physical structure of the flowfield, and provide information concerning the overall features which can be grasped quickly. Many flow visualisation techniques (for example Mach-Zehnder Interferometry) can also provide quantitative as well as qualitative data. The photographs obtained in flow visualisation studies can form permanent records of an investigation and assist in the interpretation of further quantitative measurements.

Commonly used flow visualisation techniques can be divided into two broad categories, namely:

(a) Surface flow techniques (such as oil film methods), and

(b) Flow structure techniques (e.g. Schlieren or smoke methods) which are used to observe flow trajectories and associated features.

As mentioned previously, the flowfield under an impinging jet in crossflow is complicated so that in this present investigation, both flow structure and surface flow techniques were employed. These flow visualisation tests were carried out with the following objectives:-

(1) to qualitatively examine the flow patterns over the impingement surface and to locate the stagnation points, separation lines and other important features of the flow

(2) to aid in the interpretation of the heat transfer measurements, and

(3) to obtain data for the flows so that comparisons could be made with previously published results.

In this chapter, the various flow visualisation techniques which were considered for use in this investigation are briefly reviewed. The techniques which were adopted are then described in detail, and particular emphasis is placed on the practical problems which arose.

6.2 Surface Flow Visualisation Techniques.

These provide information concerning the flow patterns over the entire flow surface. Possible techniques include the use of paper tabs, tufts, and chemical and evaporative methods. These can indicate local flow directions, and also locate the positions of boundary layer transition and flow separation. The main methods considered for use in the present investigation included:-

(a) 'Tuft' Techniques and similar methods

(b) Volatile liquid films, and

(c) Oil film methods.

The 'tuft method' has been used by Tyler and Williamson (Refs. 38 & 39) to investigate the flow separation associated with impinging jets in crossflows. The surface under examination is covered with short strands of thread or wool which are fastened to this surface by tapes or adhesives. The threads used for this purpose must be small, light, and flexible so that they readily align with the flow direction. However, in separated flow regions, the threads will be unsteady and can even point in a direction opposite to the main direction of flow. The 'tuft method' suffers from the following disadvantages, so was not employed in the present investigation:-

(i) It is a rather crude method of flow visualisation, and quantitative measurements (as in Refs. 38 & 39) are only approximate.

(ii) Fixing of the 'tufts' is a tedious process, and furthermore, in high velocity flows, the tufts can be blown away.

(iii) Stagnation points or separation lines cannot be located accurately using tufts. These lines or regions can only be clearly defined if a large number of tufts are present in these areas. The separation lines associated with impinging jets under crossflow conditions are continous. The use of tufts however, (regardless of the tuft spacing) will indicate only a discontinous estimate and will not provide whole field visualisation.

(iv) In this present investigation, it was hoped to obtain a clear photographic record of the main features of the surface flow patterns. Most of these features would not have been clearly visible if tufts were used.

(v) The presence of the tufts can affect the structure of the boundary layer associated with the flow. Turbulence can be generated, and this can alter the resulting flow pattern. This is a particularly serious effect if comparatively long and stiff threads are used. Thus Pope and Harper (Ref. 117) suggest that the length of the tufts should not exceed 50.8 mm.

(vi) The tuft technique is particularly suitable when only visual observations of the flow pattern are needed. It can also be applied in situations with ample working space (such as in large wind-tunnels). The limited size of the test section in this present study thus also ruled out the use of the technique.

Apart from the use of tufts and similar methods, e.g. tufted wire grids (Ref. 117) and paper tabs (Ref. 118) the use of volatile liquid films was also considered. These are based on the principle that the rate of evaporation of a volatile liquid from a test surface depends on the nature of the flow boundary layer. Evaporation rates in turbulent boundary layers for example are greater than those in laminar boundary layers. These thin film evaporative techniques are described in detail in Refs.(117, 119, and 120). They were not employed in this present study for the following reasons:-

Firstly, correct application of the films (particularly if highly volatile chemicals are employed) is essentially 'an art' and considerable experience is required to achieve satisfactory application. If the film is too thick it will run, and if too thin, it is very difficult to adjust to the duration of the test run to obtain the desired flow patterns. If the films are not applied uniformly, the resulting flow patterns will depend on these non-uniformities as well as on the nature of the flow. If a test surface is left in the flow for too long, all the volatile liquid will evaporate. On the contrary, if the test surface is not left in the flow long enough, most of the surface will still be wet. Furthermore, the required chemicals can be expensive and special illumination techniques may be required. On account of the difficulies involved in the use of these thin volatile films, and the fact that they do not always provide an adequate picture of the entire flowfield, it was decided to employ an 'oil film' technique, and this is described in detail in the next sections.

6.3 Oil Film Flow Visualisation

6.3.1 General Review

This investigation employed an oil film surface flow visualisation technique to examine the flow patterns associated with impinging jets in crossflows. This oil film technique was first introduced in water tunnels (ref. 121), and is now widely adopted as an adequate method of flow visualisation. It is particularly effective in high speed flow investigations where it has been used to examine surface streamlines, and such phenomena as shock waves, separation lines, and vortices. The use of these oil films on any significant scale for surface flow visualisation is, however of fairly recent origin. Amongst the earliest reported applications of the technique, were those of Hills (Ref. 122), Black (Ref. 123), Stalker (Ref. 124), Stanbrook (Refs. 121 & 125), and Maltby and Keating (Ref. 126).

In investigations of jet flows, the oil film technique has been particularly useful for locating stagnation points, and the surface flow patterns on the impingement surfaces. Colin and Olivari (Ref. 16), Ludwig, Brady et al (Ref. 25), Sterland and Hollingsworth (Ref. 118), Wu et al (Ref. 127), Black and Hardisty (Ref. 14) have all used the technique either to aid in the interpretation of quantitative measurements or to gain a clear insight into the general nature of the flow.

In general the oil film method has been used only rarely for quantitative studies, and there is also a lack of understanding of the theoretical background and principles. Squire (Ref. 128) however, has produced some theoretical background and equations which govern the variation of the film thickness with time. Stanbrook (Ref. 121) also studied theoretically the motion of an oil film. He proposed an expression for the time required to form a typical pattern, and noted that the initial thickness of the oil film did not appear to influence the time taken for pattern development. He considered various forms of oil films and suggested a general procedure for producing suitable oil mixtures. More recently, Tanner and Blows (Ref. 129), have undertaken both experimental and theoretical studies of the motion of a thin oil film on a solid surface. They related the variation of film thickness to the distribution of skin friction. These authors measured the oil film thickness by interferometric techniques, and thus obtained quantitative results for the variation of skin friction over the surface.

These results were in good agreement with previously published data, particularly for comparatively low speed flows. It thus appears possible in the future that the oil film technique could be used to obtain quantitative values for the local heat transfer coefficients by invoking a suitable analogy between skin friction and heat transfer.

The use of an oil film technique however, is sometimes criticised on the grounds that the oil film mixture interferes with the boundary layer flows, and that the streaky deposits of pigment used for visualisation purposes do not necessarily align in the local flow directions. Tanner and Blows have, however, shown that "if the film is thin enough, the dominant force is the skin friction". Thus under most practical conditions, gravitational effects can be regarded as negligible and experience has shown that the oil film method gives useful and reliable information. In this present study, gravitational effects were minimised by ensuring that the photographic paper on which the patterns were formed was in good contact with the flat, horizontal impingement surface.

The oil film technique was used in this work to obtain reasonably accurate locations for the impingement stagnation points, the profiles of the separation lines, and also to observe the general distribution of the flow stream-lines. The effects of nozzle to target spacing, jet inclination, Reynolds number and jet-to-crossflow velocity ratio on these flow patterns were examined. The surface flow patterns were also used to assist in explaining the local heat transfer measurements.

6.3.2 Experimental Apparatus and Procedure used for Flow Visualisation.

The experimental apparatus and arrangement are shown in Fig. 6.1. A copper plate, 508 mm long, 298.5 mm wide, and 1.63 mm in thickness was used as the target plate. This plate was readily removed from the test section at the end of a test, and the flow pattern photographically recorded. Subsequent repositioning of the plate in the test section was possible without alteration of the experimental set-up.

To obtain good photographic contrast, thick white photographic paper was mounted on the copper plate to act as the impingement surface. The copper plate was cleaned and dried prior to application. Strips of double-sided sellotape mounted lengthwise at regular intervals across its surface were then used to mount the photographic paper with its oil-resistant surface uppermost. Gravitational effects were minimised by maintaining good contact between the paper and the plate.

The upper paper surface was then coated with a specially prepared mixture of lampblack, oleic acid, and paraffin as described in Appendix E. Oils commonly employed in the oil film technique have ranged from kerosene to engine oil. Fig. 6.2 presents the viscosity-temperature relationships for many of these oils, and a brief description of their characteristics is also given in Appendix E. Paraffin was most suitable in the present study. It required reasonably short duration tests for the patterns to develop and dry, and moreover, was readily obtained locally.

Titanium dioxide has been extensively used in most previously reported investigations as a pigment in the oil. However, in the present study, lampblack was employed since it provided very good contrast against the background of the photographic paper. The photographs obtained with the use of lampblack gave improved definition for the stream-lines than that obtained using titanium dioxide. The photographs also appeared to be of superior quality to those previously reported in the open literature with titanium dioxide.

After coating of the impingement surface with the oil mixture, the plate was positioned in the test section and a test run at the appropriate flow and geometrical conditions undertaken. Streaky deposits of lampblack marked the local flow directions. A typical pattern forming under the action of an impinging jet in a cross-flow is shown in Fig. 6.1. Approximately 15 to 20 minutes were required (depending on the air flow rates) for the oil film patterns to develop and dry. At the end of each test, the plate was taken to a photographic studio, and photographs of the oil film pattern were obtained. Measurements of the stagnation point location and the separation line profiles were then subsequently made directly from the pattern.

6.4 Techniques for the Visualisation of the Main Flow Structure.

The heat transfer characteristics of impinging jet systems can be understood more readily if details of the associated fluid flows are available. This knowledge of the flow characteristics and the associated fluid mechanics can be obtained by suitable visualisation of the flow field. Surface flow techniques can display details of the surface flow patterns, whereas flow structure techniques reveal the physical shape and associated features of the flow , by an orthogonal representation of the flow field. These latter flow structure techniques may be divided into two classes, namely, optical and non-optical methods.

Optical methods utilise the fact that density gradients can vary considerably within the flow-field. Optical systems enable these gradients to be observed visually. Three main types of optical systems are employed, namely:

(i) the Shadowgraph system

(ii) the Schlieren system, and

(iii) Interferometry systems (such as the Mach-Zehnder Interferometer)

Details of the techniques are discussed by Bradshaw (Ref.-120), Pope and Goin (Ref. 130), Hölder and North (Ref. 131) and in standard fluid mechanics text books. Of these three methods, the Schlieren system is the most widely used, and has been employed in previous jet impingement investigations (e.g. see Refs. 14 & 132).

These optical methods were considered at the initial stage of the present study. However, they were rejected as unsuitable for two main reasons. Firstly, the available space around the experimental set-up was too small to mount the focusing arrangements of the optical systems. Secondly, the air jets used in the investigation were not heated so that the necessary density variations were not present in the flow-field.

Thus non-optical techniques were then considered. The bubble seeding method (Refs. 121 & 134) in which small neutrally buoyant helium-filled 'soap' bubbles are injected into the fluid stream appeared promising. This can show detailed stream-lines for the fluid motion, and is particularly suitable in free jet situations.

Preliminary tests were undertaken with an available bubble generator. The stream-lines and the general path of the jet were clearly defined as far as the end of the free jet region. However, on impact with the impingement surface, the bubbles collapsed and the pattern deteriorated into a general fog. Consequently, important structural features of the flowfield in the impingement and wall jet regions were not visible. This situation was even more pronounced under crossflow conditions so that the technique was abandoned. A smoke technique was thus eventually adopted, and details are presented in the remainder of this chapter.

6.5 Smoke Techniques in Flow Visualisation

6.5.1 General Review with Special Reference to Jet Flows

In this present investigation, a smoke technique was used, and with suitable lighting, the tests revealed important details of the flow structure of impinging jets in crossflows. A typical example of the smoke patterns is shown in Fig. 2.3. The technique has also been used in previous jet flow investigations.

Keffer and Baines (Ref. 36) used an oil-vapour and nitrogen aerosol to generate a smoke which was employed for qualitative visual observations of a free jet in a cross-wind. They investigated jet penetration and discussed the related structural features of the jet flow.

Margason (Ref. 43) employed a mixture of water vapour and compressed air as the tracer to examine the path of a free jet inclined at various angles to a crossflowing air-stream. An analytical expression was proposed for the jet trajectory, and the results were in good agreement with those of previous investigators. Ramsey and Goldstein (Ref. 47) employed another version of the technique in their investigation of the interaction of a heated jet with a deflecting stream. They used a carbon dioxide fog (generated by mixing solid carbon and hot water) as the tracer.

Stoy and Ben-haim (Ref. 49) obtained jet trajectories with yet another modification of the technique. They injected ammonium sulphate as the visualisation tracer, and were able to observe clearly defined jet centre lines and the shape of the jet as it developed in the crossflow.. Zandbergen and Joosen (Ref. 135) also made extensive use of the smoke technique in their investgation of jet trajectories in crossflowing streams.

Popiel et al (Ref. 136) used smoke in their investigation of the flowfield for a round air jet impinging on a rotating disc. They obtained good quality smoke visualisation photograhs, and thus described the structure of the impinging jet at various Reynolds numbers. The flow structure of impinging jets in crossflowing streams was studied by Bouchez (Ref. 81) who again employed a smoke method. Koopman (Ref. 66) attempted to use a similar technique but could not 'discern' the flow pattern. Nevertheless the smoke technique can provide a visual presentation of an entire flowfield, particularly in non-turbulent flows. Turbulent mixing in the smoke injection region, however, can cause rapid diffusion of the smoke so that details of the smoke streams are no longer clearly defined. Consequently, the smoke technique is particularly suitable in low speed flow situations, and may not be too successful in turbulent flows unless elaborate precautions are taken.

The smoke used in flow visualisation work should be dense, and non-toxic and non-corrosive. White smoke is preferable for contrast purposes and it should not clog and condense in the system. Ease and simplicity of generation is a further consideration and moderate injection velocities should be employed to avoid disturbing the flowfield. Successful application of smoke techniques also depends on the quality of lighting, particularly if the smoke pattern is to be permanently recorded by photography.

6.5.2 Smoke Generation

Several methods of generating smoke have been reported e.g. by combustion of rotten wood, or smouldering paper, and by the vaporisation of mineral oils such as kerosene or resins. Smokes can also be generated chemically for example liquid Titanium tetrachloride in the presence of moist air produces dense white fumes consisting of titanium dioxide and liquid Hydrogen Chloride. Injection and susequent atomisation of water in high velocity air-streams can produce a mist which can then be used to trace the paths of jets (see Margason Ref. 43)

Some of the above methods of generating smoke can lead to the formation of solid deposits which may be corrosive or toxic. Furthermore, the quality of smoke produced can require expensive and complicated experimental apparatus. Therefore, in the present investigation, it was decided to obtain smoke from a cheap and simple experimental set-up using chemical smoke made by burning pellets of dichlorodiphenyltrichloroethane.

6.5.3 Experimental Apparatus and Procedure.

The experimental apparatus and arrangement were as shown in Fig. 6.3. The smoke generator system consisted of a metal can (the smoke drum). A hand-operated pump was used to pressurise the drum. This controlled the smoke delivered to the apparatus. The low pressure also ensured that the entry of the smoke into the jet was at such a speed that the flowfield was not significantly disturbed.

Smoke pellets were ignited and dropped into the 'smoke drum' which was connected to the plenum via a flexible connection and a nipple mounted flush with the the interior face of the chamber. The smoke drum lid was replaced and the smoke injected by means of the hand pump. The smoke then passed into the test section. This section, was illuminated by means of a narrow beam (approx. 3 mm wide) of intense light from a 500W Projector lamp. This lighting was sufficient to obtain flow visualisation photographs using a 35 mm single lens reflex camera. All the photographs in the study were taken at an exposure time of 1/15th of a second.

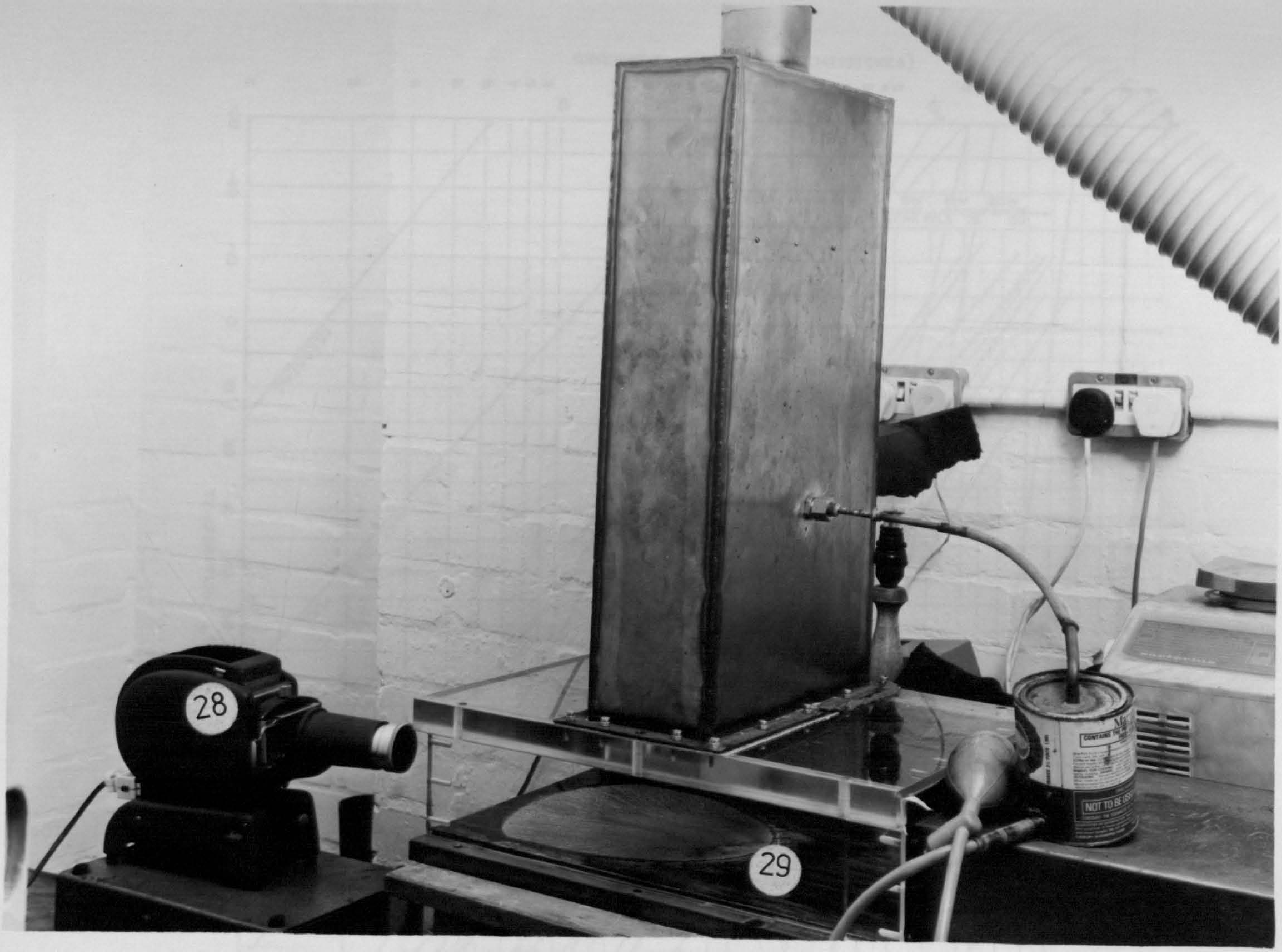

FIG. 6.1. OIL FILM FLOW VISUALISATION

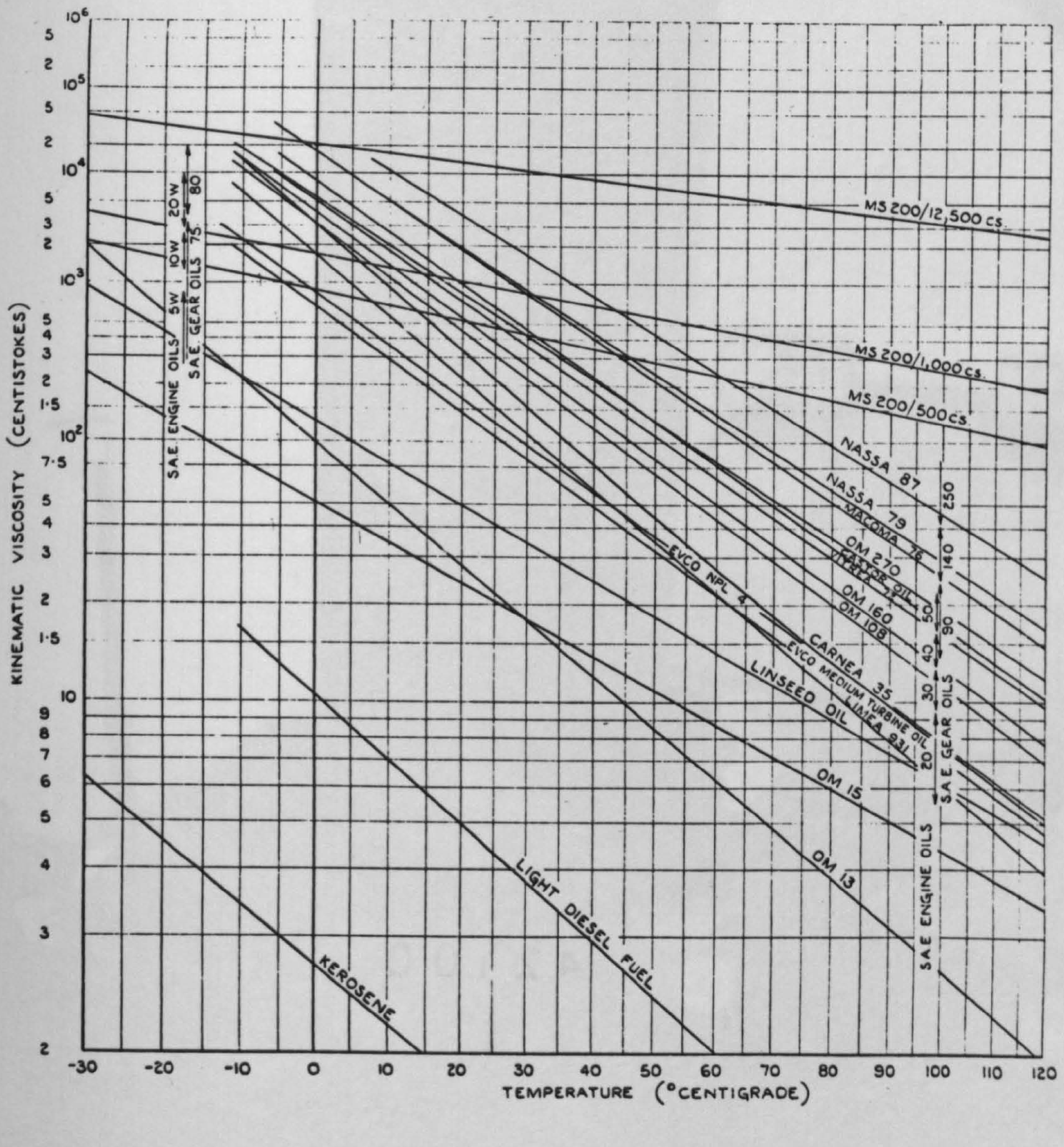

FIG. 6.2. VISCOSITY TEMPERATURE RELATIONSHIP FOR VARIOUS OILS IN USE

FIG. 6.3. EXPERIMENTAL SET-UP FOR SMOKE FLOW VISUALISATION

CHAPTER 7

RESULTS AND DISCUSSION

7.1 General

In this chapter, the results of the flow and heat transfer studies are presented and discussed. The first section of the chapter describes the flow visualisation studies which were undertaken. This is followed by a brief consideration of the jet and crossflow velocity and turbulence intensity profiles. Attention is then paid to the heat transfer results; and finally, the flow and heat transfer results for the present study are compared with those of previously reported investigations.

7.2 Flow Visualisation Studies

7.2.1 Jet Impingement in Stagnant Surroundings

Introduction

As mentioned in previous chapters, two techniques were employed to gain visual information about the flow fields. Smoke tracer techniques were employed to investigate the flow structure, and oil film surface flow visualisation was used to determine the surface flow patterns. Detailed descriptions of the test apparatus and experimental procedure were presented in chapter 6.

Flow Structure Studies

For the jets exiting into stagnant surroundings, the flow structure tests were conducted for impingement angles of 70° and 90°, nozzle-to-target spacings of 2 and 4 jet diameters, and Reynolds numbers of 32,700 and 55,100. A typical flow structure for such a jet is shown in Fig. 7.1. The photograph reveals a well-defined pattern of flow at exit from the nozzle. In the free jet region, before impingement, considerable mixing and entrainment occurs, and the jet spreads into the observed conical shape.

After impingement, a well-defined 'wall-jet' can be seen on each side of the impingement zone, and this jet, thickens quite rapidly with increasing radial distance from the stagnation region. These observations are in accordance with the generally accepted behaviour of a turbulent jet, as discussed in section 2.2.

Orthogonal and inclined impinging jets are compared in Fig. 7.2. The inclined jet exhibits the same general flow structure as in the orthogonal case, i.e. free jet spread followed by the establishment of a wall jet region. However, in the inclined jet situation, the wall jet flow is predominantly in the direction of inclination. Observation of Fig. 7.2 also indicates that for particular geometrical conditions the general jet flow structure is independent of the Reynolds number. Thus similar flow structures were observed at Reynolds' numbers of 32,700 and 55,100.

The flow visualisation findings together with previous descriptions are illustrated schematically in Fig. 7.3 In both the orthogonal and inclined cases, the flowfield is consistent with the description in section 2.2, namely, that the flowfield consists of three regions:-

(a) the free jet region in which the jet spreads due to viscous mixing and entrainment of the surrounding fluid

(b) the impingement region in which the flow changes direction, and

(c) the wall jet region in which the jet flows radially over the impingement surface.

Surface Flow Studies

The surface flow patterns associated with impinging jets can provide information for the impingement and wall jet regions. Surface flow tests were thus conducted for impingement angles of 45°, 70°, and 90°, nozzle-to-target spacings of 2, 4, and 8 nozzle diameters, and Reynolds numbers of 30,200, 32,700 and 55,100. Fig. 7.4 shows the effect of Reynolds number on these surface flow patterns. Once again, it can be seen that for particular geometrical conditions, the patterns are independent of Reynolds number.

Generally, the patterns are characterised by a small central patch of deposited lampblack. This corresponds to the stagnation point. Consequently, concentric rings (which can be seen in detail during the test) of lampblack are left in this area indicating the 'zero centre-line velocity' condition at the stagnation point. Surrounding this point, is a 'clean or swept' region which corresponds to the so-called impingement region. As was discussed in section 2.2, the centre-line velocity of the jet accelerates over this impingement region. The 'clean or swept' area corresponds to this region where the flow is accelerating, and the oil film is swept away in the process. This 'clean' area is surrounded by the wall jet region in which clearly-defined streamlines can be seen to radiate outwards from the jet axis. The surface flow patterns are also independent of Reynolds number at a lower nozzle to target spacing (Z/d), see Fig. 7.5. In addition to the 'clean or swept' impingement region pattern, small localised 'clean' spots also ensue at the low nozzle to target spacings. The impingement region is also distorted at these geometries. These effects are caused by the interaction between the outward flowing wall jet fluid and the re-circulating fluid returning due to the proximity of the walls and roof. This interaction is referred to as a "wall effect at low Z/d".

Fig. 7.6 illustrates the effect of impingement angle on the surface flow patterns. It may be seen that as the impingement angle is decreased from 90°, the impingement and wall jet regions are shifted in the direction of inclination thus confirming the smoke test observations.

Fig. 7.7 shows the effects of impingement angle and Reynolds number on the surface flow patterns. Once again, it can be seen that for fixed geometrical configurations, the patterns for various Reynolds numbers are similar. Fig. 7.8 shows the effects of Reynolds number and nozzle to target spacing on surface flow patterns. It can be seen that at a nozzle to target spacing of two jet diameters, the pattern is distorted due to the wall effect and the exhaust flow.

7.2.2 Jet Impingement in Crossflows.

Fundamental Concepts.

It may be recalled from the discussion in section 2.2 that a crossflowing stream of even comparatively low velocity relative to that of the jet can produce considerable changes in the flowfield. For jet impingement in crosslows, two general conditions exist. The first is a situation of high blowing rate (mass velocity ratio) in which vortex formation ensues. The second is that of a low blowing rate in which the jet is simply swept directly downstream. At larger nozzle to target spacings, impingement does not occur. Even at closer spacings it is often difficult to detect a clearly-defined stagnation point.

The present investigation has shown that vortex formation depends on mass velocity ratio as well as on the nozzle to target spacing. Vortices were observed subject to the following limiting conditions:-

At $Z/d = 2$ and $M \geqslant 2.0$

$Z/d = 4$ and $M \geqslant 4.0$

$Z/d = 8$ and $M \geqslant 8.1$

Conversely, the jets were swept out of the test section under the following conditions (see Fig. 7.15):-

$Z/d = 2$ and $M \leqslant 1.96$

$Z/d = 4$ and $M \leqslant 3.94$

$Z/d = 8$ and $M \leqslant 7.88$

Flow-field at High Blowing Rates

Fig. 7.9 shows the flow structure of an impinging jet in a crossflow. This pattern corresponds to a situation of high blowing rate, and the interaction between the jet and the crossflowing stream may be seen clearly. The crossflowing stream decelerates, as it nears the jet boundary. The flow at the nozzle exit is considerably influenced by extensive mixing and entrainment. These effects are partly responsible for the deflection of the jet downstream in the direction of the crossflow. After impingement, part of the wall-jet flow penetrates upstream of the axis of the jet. This flow then separates from the surface, and rolls up into a vortex. This vortex region (denoted by V in Fig. 2.3) can be clearly seen in Fig. 7.9. This flow which has travelled against the crossflowing stream, is subsequently flushed downstream around the central core of the jet and spreads laterally.

Fig. 7.10 (due to Tyler and Williamson (Ref. 39)) presents a schematic representation of the flowfield described above, and illustrates the vortex formation and its subsequent spread into a horse-shoe shape. A surface flow pattern, see Fig. 7.11, clearly indicates the path associated with the spread of the vortex. The rapid lateral spread of the jet fluid, limits the effective width of the crossflowing stream.

The impinging jet presents a 'bluff-body' style of blockage to the crossflowing stream. The resultant deceleration of the crossflowing stream as it approaches the jet is indicated by the deposits of lampblack which can be seen in the region denoted by (a) in Fig. 7.11 However, subsequent acceleration of the crossflowing stream occurs as it flows past the sides of the jet flow. Thus the region denoted by (b) shows clearly-defined local flow directions. These streamlines indicate the direction of motion of the crossflow.

An important feature of the surface flow patterns is the impingement stagnation ring, i.e. dark concentric circles denoted by (d) in Fig. 7.11. The jet velocity is essentially zero at this region of stagnation so that lampblack is deposited in concentric rings. Previous investigations have shown that this stagnation ring is coincident with the position of maximum static pressure.

The local flow directions reveal that the flow is directed radially outwards from the stagnation ring. The 'clean or swept' area once again, indicates the so-called impingement region. The variously described 'dome', 'elliptical' or 'horse-shoe' shaped vortex separation line is indicated by (c). This line defines the maximum upstream and lateral penetration of the jet flow. The location and shape of this separation line is a function of the blowing rate, nozzle to target spacing and jet inclination, as described later in the chapter.

The smoke tests provide evidence for the existence of the vortex, but do not give detailed information about its nature, or geometry. However, this may be obtained from oil-film patterns. During the tests, it was observed that fluid from the impinging jet was drawn into the vortex in ripples originating in the impingement region. The vortex rotated so that the fluid motion was compatible with the crossflow. This could be seen from the movement of the oil film as the blowers were switched on.

The local flow direction-lines as shown by the lace-like streaks of lampblack radiate from the stagnation region and end on the inside edge of the vortex band. This clearly indicates that part of the impinging jet fluid on impact, is drawn into the vortex. However, the remainder of the flow exits directly downstream as shown by the clearly defined wall-jet streaklines (region(e)).

The oil film pattern also reveals entrainment of the crossflowing stream into the vortex regions. White streaks can be seen starting from zones (a) and (b) and ending on the periphery of the horse-shoe shaped separation band. In particular, a 'clean' area can be seen near the apex of the vortex band (c). This confirms the observation of Wooler et al (Ref. 46) that a fluid particle approaching the jet near the plane of symmetry is more readily entrained than those moving away from the jet. The results of this present visualisation substantiate the findings of previous investigators as given earlier (see section 2.2).

Flow-fields at Low Blowing Rates.

Fig. 7.12 presents a typical oil film pattern corresponding to this situation. The dark central zone denoted by (a) indicates the region where the flow is, as previously described, decelerated due to blockage by the jet. Subsequent to this, the crossflowing fluid accelerates around the sides of the jet. Further downstream can be seen a pair of 'lobes', see areas (b). These light areas are often associated with a pair of 'counter-rotating vortices' (see Refs. 127 and 135) arising from interaction between the jet and the crossflowing stream. Some of the approaching streamlines can be observed to bend towards the jet and terminate on its periphery. It can also be seen that there is no clearly defined impingement stagnation region for this situation. However, clearly defined wall-jet streaklines can be observed in region (c). At these low blowing rates there is thus no upstream penetration zone, and reduced lateral spread of the jet, The jet fluid is simply blown downstrem.

Effects of Changes in Flow and Geometrical Parameters.

Fig. 7.13 illustrates the effects of blowing rate and nozzle to target spacing on the flow structure of impinging jets for the extreme conditions of high and low blowing rates. It is apparent that blowing rate alone does not determine whether a vortex is formed or not. The nozzle to target spacing is also a significant parameter. Thus an orthogonal jet at a blowing rate of 7.88 is deflected downstream without vortex formation at a dimensionless nozzle to target spacing of 8, whereas a vortex is formed for a comparatively low blowing rate of 2.2 at a nozzle to target spacing of 2 jet diameters. At a fixed nozzle to target spacing the type of flowfield is dictated by the blowing rate as described in section 7.2.2

Fig. 7.14 provides further evidence of the effect of blowing rates. It may be noticed that at the higher blowing rate, the jet is not deflected downstream as sharply as it is in the lower blowing rate case. This is in agreement with Ramsey (Ref. 140) who reported a similar effect, although he studied only free jets. Thus it may be stated that jet deflection decreases as the blowing rate is increased for both free and impinging jets. It may also be observed from Fig. 7.14 that there is a difference in the rate of entrainment as the jet exits into the crossflowing stream. Entrainment is indicated by an irregular boundary definition, e.g. a well-defined jet boundary indicates lower entrainment. Furthermore, it may be noticed that with increasing blowing rate, the extent and size of the upstream recirculation zone increases. Thus the upstream penetration is very much reduced at a low blowing rate. This again, is in good agreement with Ramsey's result.

Fig. 7.15 shows the effects of nozzle to target spacing at the limiting blowing rate conditions previously stated. It may also be noticed that entrainment is more prominent at the higher nozzle to target spacings.

Fig. 7.16 illustrates the effects of jet inclination at two nozzle to target spacings under low blowing rate situations. Jet inclination into the crossflow results in a greater penetration upstream. There is also some evidence of greater entrainment in the inclined jet situation for the same blowing rate. At a reduced nozzle to target spacing, there is still no evidence of vortex formation. The jet is flushed out of the test section for all angles of inclination. Once again, entrainment is more pronounced for the inclined jets.

It may be noticed that in the high blowing rate case of Fig. 7.17 for all angles of inclination, the upstream penetration distance decreases as the nozzle to target spacing decreases. The upstream penetration distance however, increases with simultaneously increased blowing rates and jet inclinations.

Fig. 7.18 illustrates the effects of impingement angle at two nozzle to target spacings. Again, there is reduced upstream penetration at the lower nozzle to target spacing and blowing rate. Greater upstream penetration occurs with the jet inclined at 45^o to the flow. Figs. 7.19 to 7.21 show the effects of jet inclination on surface flow patterns for impingement at particular nozzle to target spacings (Z/d in the range 2 to 8 nozzle diameters), and blowing rates (mass velocity ratios in the range 2.0 to 14.6). The features of oil film patterns described earlier can be observed in all cases. The effect of impingement angle may be observed by considering each vertical column of photographs in which the only variable is this angle e.g. the left hand column of Fig. 7.19 presents the patterns for Z/d = 2 and M = 3.7 at impingement angles of 90^o, 70^o, and 45^o. At a fixed nozzle to target spacing and blowing rate, the horse-shoe shaped vortex band spreads as the jet inclination is decreased from 90^o to 45^o. In all cases, there is a significant difference between the extent and shape of the area enclosed by these separation lines for 90^o and 45^o impingement. The separation line opens out more and extends over a greater area of the target surface at an impingement angle of 45^o. The differences, however, are not so pronounced for impingement angles in the range 60^o to 90^o under this condition. Within the range of impingement angles studied, a jet inclined at 45^o can be seen to have generally the largest area enclosed by the separation line.

Figs. 7.22 to 7.24 present the effects of blowing rate (expressed as the mass velocity ratio) on oil film patterns at fixed nozzle to target spacings (Z/d in the range 2 to 4 nozzle diameters), and at fixed impingement angles in the range 90^o to 45^o. The effect of blowing rate may be observed by considering the patterns along each horizontal row of photographs in which the only variable is the mass velocity ratio, e.g. the top row of Fig. 7.22 presents the patterns for Z/d of 8 and $\alpha = 90^o$ at mass velocity ratios of 14.6, 8.8, and 8.1. As the blowing rate is decreased, i.e. the ratio of crossflow to jet increases, the profile of the separation band narrows. However, this effect is much less marked than the impingement angle effect discussed previously.

Consideration of the vertical columns of Figs. 7.22 to 7.24 can also be used to study the effect of changing Z/d on the oil film patterns. In these photographs, the total cross-stream flow rate is maintained constant as the nozzle to target spacing is reduced. This is similar to the behaviour of practical systems in which the total upstream flow is only a function of the number of upstream nozzles, and not the spacing. The effect of reducing Z/d whilst maintaining a constant total cross stream air flow rate is to greatly diminish the area enclosed by the separation lines. This reduction is too great to be explained by the variation in blowing rate. Thus it may be concluded that providing all other variables are fixed, an increase in nozzle to target spacing causes the separation line to open out and enclose a greater area of the target surface. Within the range of flow variables studied, the extent of these separation bands is greatest for the highest blowing rate (i.e. mass velocity ratio) of 14.6 and greatest Z/d of 8.

Figs. 7.25 to 7.28 show the effect of impingement angle on the separation line profiles at constant cross-flows (i.e. fixed blowing rates), and spacings. These profiles were obtained by direct measurements from the surface patterns at the end of each test.
Fig. 7.25 is for M = 2.2 and Z/d = 2, Fig. 7.26 is for M = 4.4 and Z/d = 4, Fig. 7.27 is for M = 8.8 and Z/d = 8, and Fig. 7.28 is for M = 14.6 and Z/d = 8. Thus in these figures, the only variable is the impingement angle.
It can be observed that in general the greater the inclination, the greater the range and size of the horse-shoe shaped area enclosed by the separation lines. Thus an inclined jet spreads more than an orthogonal one. Moreover the effect of increasing the angle of impingement is to move the vertex of the separation line further upstream at constant blowing rate and spacing. Thus the upstream penetration is greater in the inclined cases, and an orthogonal jet is deflected more than an inclined jet. Within the range of impingement angles considered in this investigation, a jet inclined at 45^o can be seen to have generally the largest area within the separation lines. The results also show that at all blowing rates, a jet inclined at 45^o has the greatest upstream penetration.

Figs. 7.29 and 7.30 show the effect of blowing rate on the separation line profiles at constant angles of $90^o$and 45^o respectively, and a fixed Z/d of 8. It can be observed that for a fixed impingement angle, the lateral spread of the jet is relatively unaffected by blowing rate. However, the upstream penetration i.e. the axial spread is much greater for the higher blowing rate jet than for the lower blowing rate case. Within the range of flow parameters studied, a jet of high blowing rate can be seen to have generally a much greater axial penetration.

7.3 Heat Transfers

7.3.1 Velocity and Turbulence Profiles

As previously mentioned, the shape of the velocity profile at the nozzle exit can affect the heat transfers associated with impinging jets (see Sparrow and Lee (Ref. 116)). These authors analysed the flow and heat transfer characteristics associated with the impingement of a slot jet of initially non-uniform velocity distribution. They found that the non-uniformity could increase the stagnation point heat (or mass) transfer coefficients by a factor of two. Moreover, Gardon and Akfirat (Ref. 68), found that the turbulence intensity of the impinging jet is also an important factor in determining the heat transfer characteristics of impinging jets. Hence in this investigation, velocity profiles of the jet and crossflowing stream together with the turbulence intensity of the jet were measured to establish the characteristics of the flows. As discussed previously, the reported velocities and turbulence intensities are for free jets.

Figs. 7.31 to 7.33 show radial variations of velocity and turbulence intensity at the nozzle exits for both orthogonal and inclined jets. These measurements were made at a Reynolds number of 32,700. The exit velocity distributions change from an approximately flat profile for impingement angles of 90^o and 60^o to a partially developed profile in the 45^o case. This effect is probably mainly due to the nozzle geometry in the inclined case. For orthogonal impingement the nozzle has a circular exit whereas an inclined nozzle has an elliptical cross-section at the exit plane. With the inclined jets, the velocity profiles were measured across the minor axis of the ellipse. The effect of these elliptical exit is apparently more pronounced in the 45^o situation. The radial turbulence distribution for all the nozzles show similar trends to the previously reported investigations of Corrsin (Ref. 34) although he used larger diameter nozzles.

Similar profiles were observed at the other Reynolds numbers of 30,200 and 55,100 employed in this present study. The velocity profiles were basically uniform for the 90^o and 60^o impingement angles with a more partially developed profile for $= 45^o$ situation. The radial variations of turbulence intensity exhibited minima at the jet axis as in the Figs. 7.31 to 7.33.

Typical axial variations of turbulence intensity along the centre lines of the jets are presented in Figs. 7.34 and 7.35 for the range of conditions employed in the present tests. The intensities increase with axial distance from the nozzle exit. This is in agreement with the results of Corrsin (Ref. 34) which are also included on the diagrams for comparison purposes. A detailed discussion of this comparison is provided later in the chapter. However, it should be noted that Corrsin used larger diameter nozzles and that the present author could not find any details of the Reynolds number employed in Corrsin's investigation. However, Corrsin's velocity and turbulence profile distributions exhibit similar trends to the measurements presented in this thesis. The present turbulence intensities are based on the maximum velocity (U_{max}) at the appropriate axial section.

Fig. 7.36 presents the velocity profiles across the section at the exits of the crossflow duct (i.e. at x/d = -20) for various heights (Z) of the duct. For the range of nozzle to target spacings investigated, the crossflow exit profiles were approximately flat in all cases.

7.3.2 General Features of Heat Transfer Tests

The major portion of the work undertaken in this experimental investgation was concerned with the combined effects of jet inclination and crossflows on the heat transfers. The ranges of flow and geometrical parameters were chosen as being of interest in many practical applications of jet impingement. Jet inclinations of 45°, 60° and 90°, nozzle to target spacings of 2, 4, and 8 jet diameters, and Reynolds numbers of 30,200, 32,700 and 55,100 were employed. The flows were adjusted to give mass velocity ratios in the range 4.0 to 8.8.

7.3.3 Effects of Flow and Geometrical Parameters on Heat Transfers for Jet Impingement in Stagnant Surroundings.

(a) Effect of Inclination

Figs. 7.37 to 7.39 show the effects of jet inclination on the 'axial' variation of heat transfer i.e. the distribution along the central axis of the test duct. The nozzle to target spacing is fixed at 8 jet diameters and no cross-flow is applied in these cases. Fig. 7.37 applies for a fixed Reynolds number of 30.200 whilst Reynolds numbers of 32,700 and 55,100 are associated with Figs. 7.38 and 7.39 respectively. At this nozzle to target spacing, the heat transfer distribution for the orthogonal jet has a characteristic 'bell-shape'. This is similar to the patterns observed by Gardon and Cobonpue

(Ref. 59) in a previously reported study of impingement of a single circular jet. For the inclined jets, the local heat transfer coefficients in the upstream direction (i.e. the direction of inclination) are greater than those due to orthogonal impingement. In the downstream direction however, the heat transfers decay very rapidly so that the local heat transfer coefficients for the orthogonal case are higher than those for inclined impingement.

A further feature worthy of notice, is that the stagnation point heat transfers for the jet inclined at 60° to the horizontal are only slightly lower than those for the orthogonal impingement case. This confirms the comments of Thurlow (Ref. 57) who suggested that the maximum heat transfer was relatively insensitive to the impingement angle (for inclinations up to 60° with the vertical). No experimental evidence however was produced by Thurlow.

For inclinations of 45°, however, there is, clearly, a significant difference between stagnation heat transfers for the orthogonal and inclined cases. The effect of inclination thus appears to be a reduction in maximum heat transfer. At this nozzle to target spacing of 8 jet diameters also, secondary heat transfer peaks are generally absent for all Reynolds numbers and impingement angles. This agrees with the observations of Gardon and co-workers (Refs. 59, 68, and 75), although their results were mainly confined to orthogonal impingement.

Figs. 7.40 to 7.42 present the effect of impingement angle on the axial variation of heat transfer for a lower nozzle to target spacing of 4 jet diameters. Once again, no crossflow is applied and the Reynolds numbers are as in the previous figures. For the jets impinging normally to the surface, the distributions of local heat transfers have the characteristic 'bell-shape' previously observed. However, at this reduced nozzle to target spacing, at the highest Reynolds number (see Fig. 7.42), secondary peaks can be observed at approximately 7 jet diameters on either side of the stagnation point. These may be attributed to a transition from laminar to turbulent flow in the boundary layers as suggested by Gardon and co-workers (Refs. 59 & 75).

For the inclined impingement cases at this nozzle to target spacing, these secondary peaks are particularly pronounced in the wall jet associated with the main flow (i.e. the upstream test duct direction). Once again, these can be attributed to the transition from laminar to turbulent boundary layer flow as previously discussed.

These peaks appear to occur at all Reynolds numbers (their absence in Fig. 7.41 is probably due to the interval between the measurements), and this is due to higher flow velocities in the boundary layers.

At this lower nozzle to target spacing, higher heat transfers are associated with the upstream zone of the impingement surface. The peak heat transfer coefficients for the 60° and 45° cases are again lower than the orthogonal values. This reduction is particularly pronounced for the 45° geometry. The effect of jet inclination on local heat transfers at the lowest nozzle to target spacing studied ($Z/d = 2$) is presented in Figs. 7.43 and 7.44. At this lowest nozzle to target spacing, clearly defined secondary peaks can be seen. Symmetrical distributions are apparent for the orthogonal jet.However, the results of flow visualisation tests conducted at this nozzle to target spacing, suggest that interaction between the wall and the jet can also be partly responsible for the existence of these peaks. These well-defined secondary peaks are also observed at all angles of inclination at this low nozzle to target spacing. The reduction in stagnation point heat transfers for the 60° and 45° angles are similar to the results for the higher nozzle to target spacings. Thus there is comparatively little difference between the 60° and orthogonal values, and a much greater reduction for the 45° inclination.

The overall effect of the angle of inclination of the jet on stagnation point heat transfers can be clearly seen from Fig. 7.45. This confirms that inclining the jet at 60° to the horizontal has comparatively little effect whilst the 45° inclination results in a significant reduction in maximum heat transfer coefficient. Considerable scatter is apparent however, and this may partly be due to the difference in turbulence levels in the jets since stagnation heat transfer values are particularly sensitive to this parameter. The stagnation heat transfer coefficient is reduced to a mean level of 97% of the orthogonal result for 60° inclination, and to a mean of 82% for the 45° geometry.

(b) Effect of Nozzle to Target Spacing

The effect of nozzle to target spacing on the stagnation point heat transfer coefficients are presented in Figs. 7.46 to 7.48. These curves suggest that the maximum stagnation point heat transfer occurs for Z/d between 2 and 4. In general, nozzle to target spacing of three jet diameters appears to be the most likely configuration for maximum heat transfer. However, due to the comparatively few geometries studied in this present investigation, the conclusion should be treated with caution. This spacing is approximately co-incident with the end of the potential core flow region. (Hinze (Ref. 147) suggests a potential core of 3 to 5 jet diameters). Gauntner and Livingwood (Ref. 31) have attributed the maximum heat transfer to turbulence effects at the apex of the potential core. Gardon and Cobonpue (Ref. 59) found maximum heat transfers at Z/d = 6. This discrepancy with the present study may be due to differences in the geometry of the nozzles and in the flow structure of the jets (i.e. turbulence and velocity profile differences) in the two investigations.

(c) Effect of Reynolds Number

The heat transfers (at the stagnation points) are reduced for all nozzle to target spacings as the Reynolds number is decreased, see Fig. 7.48. However, the range of Reynolds number is not sufficient to draw general quantitative conclusions. Nevertheless, the effect of jet Reynolds number is discussed in greater detail later in this chapter when comparisons are drawn with other published data.

7.3.4 Effects of Flow and Geometrical Parameters on Heat Transfers for Jet Impingement in Crossflows.

(a) Effect of Blowing Rate.

Figs. 7.49 to 7.51 show the effect of blowing rate i.e. the ratio $(\rho_j U_j)/(\rho_c U_c)$, on the 'axial' variations of heat transfer coefficient for jets impinging at a fixed nozzle to target spacing of 8 nozzle diameters. These diagrams are respectively for the orthogonal case, and for inclined impingement at angles of 60° and 45°. For comparison purposes, the axial heat transfer distributions in the absence of crossflow are included in the figures. It may be observed that for the fixed blowing rates of 8.1 and 8.8, for all impingement angles, crossflows generally decrease the stagnation value as well as the local heat transfer coefficients in the upstream crossflow region. However, local heat transfer coefficients in the downstream crossflow region are augmented for both inclined and orthogonal configurations. Similar trends (i.e. an upstream degradation and a downstream enhancement) were reported by Metzger and Korstad (Ref. 78) who studied initially orthogonal jets.

Consideration of Fig. 7.49 indicates that for the orthogonal impingement case under crossflow, the local heat transfers are relatively constant in the upstream region before increasing sharply as the impingement point is approached. The heat transfer coefficients thus rise steeply to a peak value at around 2 jet diameters downstream from the centre line of the jet nozzle. A gradual decrease in coefficients subsequently ensues although the local values in this downstream region are higher than those for impingement without crossflows. This behaviour may be understood by reference to the flow visualisation tests. The low upstream values of heat transfer correspond to the regions where the crossflowing stream is decelerated due to the blockage presented by the jet (e.g. see Fig. 7.11). The subsequent steep rise as the stagnation point is approached corresponds to the high speed vortex region arising from the interaction between the upstream penetration of the jet fluid and the crossflowing stream. Thus the low heat transfer region corresponds to the deceleration zone prior to the vortex of curve (c) in Fig. 7.11. The region of steeply rising heat transfer corresponds to the zone between (c) and (d) in this figure.

Sparrow et al (Ref. 82) concluded that the deflection of jet by the crossflow is small for large mass velocity ratios ($M \geqslant 8$). This is substantiated in this present investigation (see the smoke test studies in Figs. 7.14, 7.17 and 7.18). It can thus be concluded that a jet of high blowing rate can penetrate farther upstream than one of a low blowing rate. This conclusion is corroborated by observation of Fig. 7.49. The deceleration region associated with the low heat transfer coefficient extends farther downstream for the lower blowing rate jet, i.e. $M = 8.1$.

For the inclined impingement cases (see Figs. 7.50 and 7.51) it is interesting to note that local heat transfers under crossflows are at every point higher than the corresponding orthogonal values in the upstream region. In the downstream region, the situation is, however, reversed. An interesting feature in the local heat transfer curves is that for both orthogonal and inclined impingement situations, the local heat transfers in the upstream regions under crossflow are generally lower than corresponding values in the absence of crossflow. In these inclined impingement cases, the effect of blowing rate is again to displace the curve farther downstream at the lower blowing rates; thus resulting in lower heat transfers over a greater length upstream of the stagnation region for a jet of lower blowing rate. Also the stagnation point heat transfers can be observed to decrease as the blowing rate is decreased although for the limited range studied at present the decrease does not appear to be very significant.

Figs. 7.52 to 7.54 illustrate the effect of blowing rate on axial heat transfer variations for both orthogonal and inclined impingement at a lower nozzle to target spacing of 4 jet diameters. The total crossflow mass flow rate was maintained constant so that the reduced spacing results in lower jet blowing rates of 4.4 and 4.0. Once again, for comparison purpose the heat transfers in the absence of crossflows (i.e. $M = \infty$) are also presented. At this lower nozzle to target spacing, the effects of crossflows are similar to those at $Z/d = 8$. Thus for orthogonal impingement, the local heat transfer once again, starts from a low (almost constant) value in the upstream region, and rises steeply as the stagnation region is approached; subsequently falling gradually in the downstream direction. The effect of a lower jet blowing rate is once again, to decrease stagnation point heat transfers and displace the distribution curves downstream. However, at this lower nozzle to target spacing, for the range of blowing rates studied the displacement of the distribution curve downstream as well as the reduction in stagnation point heat transfer do not appear to be pronounced as the blowing rates are varied, regardless of the impingement angle. Apart from this, the characteristics of the heat transfer curves are exactly similar to those previously described for the nozzle to target spacing of 8 jet diameters. Virtually identical effects were observed at a $Z/d = 2$ so that to improve the clarity of the figures, the results are presented for only a limited number of cases, see figures 7.55 to 7.57. The jet blowing rate has again decreased due to the maintenance of a constant crossflow mass flow rate and the reduced spacing. The diagrams present the results for the no crossflow case and those for $M = 2$ at all angles.

At this lowest nozzle to target spacing the curves exhibit generally similar features to those previously discussed; although a number of differences can also be identified. There is generally reduced upstream heat transfer. A further interesting effect of the crossflow at this low nozzle to target spacing is the elimination of the secondary peaks which occur in the absence of crossflow at all impingement angles. Thus at low blowing rates, secondary peak heat transfers do not arise in the presence of crossflows. Sparrow et al (Ref. 82) however noticed these secondary maxima under crossflows for $M = 12.1$ at $Z/d = 3$. These are probably due to the extremely high blowing rate of 12.1 which they used at this low nozzle to target spacing.

A further interesting feature which can be noticed at this nozzle to target spacing is that the downstream displacement of the stagnation point is greatly reduced. However, the high crossflows ($M = 2.0$) reduce the stagnation heat transfer coefficients when compared with the results for initially stagnant surroundings.

Figs. 7.58 to 7.60 show the normalised variation of heat transfers as functions of the jet blowing rates for fixed impingement angles of 90°, 60°, and 45° respectively. It may be noticed that at a fixed nozzle to target spacing of 8 jet diameters, dimensionless stagnation point heat transfers generally decrease as the blowing rate decreases, i.e. stagnation heat transfers generally decrease as crossflow is applied. A similar effect was observed by Sparrow et al (Ref. 82) and the approximate reductions observed by these investigators at $Z/d = 8$ are also included. It should be emphasised that Sparrows results are higher than the present data since they did not conduct tests in the absence of crossflow. Thus the stagnation heat transfer at a high blowing rate of 12 has been used as the datum.

As the nozzle to target spacing is increased to 4 jet diameters, relative stagnation heat transfers continue to decrease as crossflow is increased (but less steeply than at $Z/d = 8$). At the nozzle to target spacing of 2 jet diameters, the decrease in stagnation point heat transfers is much less pronounced. Bouchez (Ref. 81) recorded slightly higher stagnation point heat transfers at lower nozzle to target spacings under crossflows. At the lowest nozzle to target spacing this investigation has shown that the stagnation point heat transfers in crossflows are generally of about the same order as those obtained in the absence of crossflows. Apart from this, the local heat transfer variations show similar trends to those observed by Sparrow et al (Ref. 82). These general effects are similar for all three impingement angles.

(b) Effect of Impingement Angle

Figs. 7.61 and 7.62 show the effect of jet inclination on the 'axial' variations of local heat transfer for a nozzle to target spacing Z/d = 8. The first diagram applies at a jet blowing rate of 8.8 and Fig. 7.62 is at the lower M of 8.1. For comparison purposes, the distributions in the absence of crossflow are also presented. It may be recalled that for jet impingement in initially quiescent surroundings, the stagnation heat transfersfor impingement at 60° were only slightly less than that for the orthogonal case, whereas the difference at 45° was much more marked. In the case of crossflow however, at Z/d = 8 the differences between orthogonal and angled impingement is less (see Figs. 7.61 and 7.62). As in the previous situation of impingement in stagnant surroundings, the local upstream heat transfer coefficients for inclined impingement are everywhere higher than corresponding values with the reverse occurring downstream. The 60° stagnation values are intermediate between the other two.

Figs. 7.63 and 7.64 illustrate the influence of jet inclination on the axial variations of heat transfer coefficients at a nozzle to target spacing of 4 jet diameters. Because of the constancy of crossflow mass flow rate, the jet blowing rates are reduced to 4.4 and 4.0. In general the effects of inclining the impinging jet against the crossflow are broadly similar to those at the higher Z/d just discussed. Fig. 7.64 in particular shows the complete absence of secondary peaks under crossflows at this nozzle to target spacing. An interesting feature of the distribution curves which may be noticed at this stage, is the effect of nozzle to target spacing on the peak as well as local values. Direct comparison between Figs. 7.61 - 7.62 and 7.63 - 7.64 shows that under inclined impingement, the effective heat transfer area appears to increase at the higher Z/d although the intensity or magnitude is everywhere lower than at corresponding points for the lower Z/d. The latter effect is particularly true of the crossflow cases.

Fig. 7.65 shows the influence of impingement angle for the lowest nozzle to target spacing studied (i.e. Z/d = 2). Once again, it can be seen that there is a consistent variation, with impingement angle, with the local heat transfer coefficients for 60° inclination being intermediate between the other two cases. At this nozzle to target spacing, and for this low blowing rate, the stagnation point heat transfer for orthogonal impingement is, clearly, higher than that for the inclined impingement cases.

The overall effect of impingement angle on the dimensionless stagnation point heat transfers for the range of blowing rates studied is presented in Fig. 7.66. Also included in this diagram is the mean effect of the impingement angle in the absence of crossflow. Broadly speaking, the present results can be split into two categories, namely, those at high jet blowing rates, $M > 4.0$ (i.e. high Z/d) and the lower blowing rate cases (i.e. low nozzle to target spacings). At the higher spacings, the reduction in stagnation heat transfer due to jet inclination is much less in the presence of crossflows than in the case of initially quiescent surroundings. At these high jet blowing rates, the stagnation point heat transfer is virtually unaffected by the impingement angle.

(c) Heat Transfer Distributions due to Crossflow Alone

Figs. 7.67 presents the variations of the heat transfer coefficients along the test section under crossflow conditions. These variations are for nozzle to target spacings of 2 and 8 jet diameters, and are typical of the heat transfer variations over the impingement surface due to crossflow alone. It should be noted that the crossflow mass flow rate was maintained constant in this study. Sparrow et at (Ref. 82) obtained similar variations which are typical of developing flow in a duct. These local crossflow coefficients are presented so that the separate effects of impingement and crossflow may be distinquished.

7.3.5 Contours of Local Heat Transfer

Contour plots of the local heat transfer coefficients for impingement angles of 90^o, 60^o, and 45^o are shown in Figs. 7.68, 7.69, and 7.70 respectively. These results apply for a Reynolds number of 32,700 at a nozzle to target spacing of 8 jet diameters, and were obtained in the absence of crossflow. Figs. 7.68 to 7.70 are typical of the contour plots obtained in this present study for jet impingement in initially quiescent surroundings. They are presented to give some insight into the complex flow and heat transfer fields arising from the interaction between an impinging jet and a flat surface. Only 'contour maps' for the orthogonal case have been reported previously e.g. see Gardon and Cobonpue (Ref. 59). Local heat transfer contour maps for impingements of inclined jets have not been reported in the literature.

In this section, contour plots for both the inclined and orthogonal jets are discussed. Comparisons are then made with the associated surface flow patterns to assist in understanding the heat transfer results.

These 'contour maps' were obtained by assuming symmetry about the axial centre-line of the test duct. Average values were then calculated for positions equi-distant from this centre line and the contour curves were then smoothed. In fig. 7.68, the heat transfer coefficients are highest in the region directly under the nozzle. In this 'impingement region' the contour lines are concentric and closely spaced. The slight asymmetry of the contours is probably due to the effect of exhausting the air from one end of the test duct. Nevertheless, the impingement and wall jet regions are indicated. High heat transfer regions correspond to the impingement stagnation region. Farther outwards, the heat transfers generally decrease from the impingement to the wall jet regions as discussed previously.

The effects of jet inclination can be observed from Figs. 7.68 to 7.70. For the orthogonal impingement the heat transfers in the downstream region towards the exit are everywhere higher than those for the inclined impingement cases. Thus for orthogonal impingement, the 50 $Wm^{-2}K^{-1}$ contour can be seen to extend downstream over the entire length of the target surface. In the 60° impingement case of Fig. 7.69 however, lower heat transfers are observed in this downstream region, with a 25 $Wm^{-2}K^{-1}$ contour ensuing. In the 45° impingement situation however, this 25 $Wm^{-2}K^{-1}$ contour ensues at a position much closer to the impingement region.

Heat transfers around the impingement stagnation point are of about the same magnitudes for orthogonal and 60° impingement as previously discussed. For the 45° impingement case, the values near the stagnation zone are significantly lower than those for the 90° and 60° jets.

Fig. 7.71 presents comparisons of the heat transfer distributions with the oil film patterns of the surface flows. The effect of jet inclination on the heat transfers can also be clearly seen. The location of the stagnation regions as indicated by the contour plots and the oil film patterns appear to be in good agreement. This region is displaced further upstream as the inclination and hence jet penetration increases.

Figs. 7.72 to 7.74 present typical results for the heat transfer distributions at Z/d = 8 and at a jet to crossflow blowing rate of 8.8. Within the knowledge of the author, local contours for impinging jets (whether inclined or orthogonal) in crossflows have not been reported in the published literature. The heat transfer contour plots presented are for both orthogonal and inclined impinging jets.

Fig. 7.72 illustrates the local heat transfer 'map' for an impinging orthogonal jet of mass velocity ratio 8.8, and Fig. 711 (described earlier) will assist in explaining the distribution of heat transfers. Region (a) of Fig. 7.11 corresponds to the upstream zone with low heat transfer coefficients (the upstream 'degradation' zone). It is this region which is bounded by the 25 $Wm^{-2}K^{-1}$ contours in Fig. 7.72. As was described earlier, this is the region where the crossflowing stream is decelerated as a result of the blockage presented by the jet. Accordingly, this region has low (almost constant) heat transfer coefficients. Just downstream of this region the contours are closely spaced and this corresponds to the vortex region (referred to as a 'highly turbulent recirculation zone' in Refs. 16, 81, and 82). The contours represent a steep rise in the heat transfer coefficients as the impingement point is approached. The 50 $Wm^{-2}K^{-1}$ contour appears to provide a rough indication of jet spread prior to separation. The higher heat transfers are in regions under the jet flow whilst the outer region is associated with the crossflow. The heat transfer coefficients in this region are thus lower than in that mainly influenced by the jet fluid.

Fig. 7.73 presents the contours for impingement at a jet inclination of 60° to the horizontal. It may be noticed that the heat transfer coefficients in the region around the stagnation point for this value of crossflow are approximately similar to those for orthogonal impingement previously discussed. In fig. 7.74 the slightly lower heat transfers near the stagnation region of the 45° jet are apparent. The greater spread and upstream penetration of the inclined jets can also be observed.

In summary, it may be stated that as a crossflowing stream approaches an impinging jet, it is decelerated. Accordingly, the heat transfer coefficients in this zone are low and of almost constant values. This is the 'upstream degradation' in heat transfer described by Metzger and Korstad (Ref. 78) and also reported by Bouchez (Ref. 81), Sparrow et al (Ref. 82) and can be clearly seen in the present results. In the impingement zone, the jet fluid accelerates and higher heat transfer coefficients are observed with a maximum at the stagnation point. Downstream of the impingement zone, the wall jet develops along the surface, and in this region, lower heat transfer coefficients can be observed, decreasing to an almost constant value at large distances from the impingement point. Evidence of a 'highly turbulent upstream recirculation zone' i.e. the vortex region is indicated by the steep rise in heat transfer which follows immediately afterwards, eventually attaining a peak value at the stagnation point. A crossflowing stream thus results in a more complicated distribution of heat transfers over the target or impingement surface.

Fig. 7.75 summarises the effects of impingement angle and crossflows on the heat transfer distributions. It can be noticed that a crossflowing stream results in a modified and more complicated heat transfer distribution. Not only do they increase the downstream heat transfer coefficients but also the peak point heat transfers are decreased for all angles of impingement. The reduction in stagnation point heat transfers due to jet inclinations is less in crossflow conditions.

Fig. 7.76 presents direct comparisons between the surface flow visualisation and heat transfer results. once again, the features of the surface flows are in good correlation with the heat transfer distributions. In particular, the displacement of the impingement point and the increased spread and jet penetration due to inclination can be observed in both the flow and heat transfer patterns.

7.4 Comparison of Present Results with those of Previously Reported Studies.

In this section of the discussion, a comparison will be presented between the experimental data of the present investigation and the results of previously reported studies for flow and heat transfers in jet-impingement systems. A number of comparisons have already been drawn but it is nevertheless useful to group further comparisons into a single compact section.

(a) Flow Studies

It can be observed from the smoke test photographs in Figs. 7.1 and 7.2 that in common with previously reported studies, the flowfield under impinging jets may be divided into three regions, namely, the free jet, impingement and wall jet regions. Popiel et al. (Ref. 136) reported results obtained using the smoke technique, and their flow structure photographs reveal similar features to those obtained in this investigation.

The surface flow patterns for jet impingement in crossflows obtained in this investigation are also similar to those previously reported, see for example Tyler and Williamson (Refs. 38 & 39) and Colin and Olivari (Ref. 16).

The location of the centre-line of a free jet in crossflows has been the subject of a number of previously reported investigations. These results together with those of studies of impingement in crossflows, see Refs. 16, 38 and 39 are of interest. The jet centre line may be used to estimate the impingement point, and comparisons can be made with the oil film patterns in this investigation, since the impingement point was determined using the oil film technique. Previous investigators have employed different parameters to define the centre-line of a jet e.g. the highest dynamic pressure line was employed in Refs. 16 and 50, and Ramsey (Ref. 140) and Kamotani and Greber (Ref. 48) used the maximum temperature line of a heated jet.

Shetz and Billig (Ref. 41) presented analytical studies of the location of the centre-line of a jet for $\alpha = 90^\circ$ and obtained fair agreement with the data of Shandorov (Ref. 44). The analytical expression is of the general form:-

$$x/d = (A.(Z/d)^a)/I^b$$

TABLE 1

CORRELATION CONSTANTS FOR THE LOCATION OF JET CENTRE-LINE

INVESTIGATOR		A	a	b
1. SHETZ & BILLIG (Ref. 41)		1	2.3	1
2. MARGASON (Ref. 43)		0.25	3	1
3. SHANDOROV (Ref. 44)	(i)	1	3	1.3
	(ii)	1	2.55	1

where I is the ratio of momentum flux for jet and crossflowing stream$[I = (\rho_j U_j^2)/(\rho_c U_c^2)]$ and Z is the vertical distance from jet exit plane. Empirical equations for the location of the jet centre-line derived from investigations are generally in this form. The constants proposed in these previous investigations are tabulated in Table 1 and the resultant relationships are plotted in Fig. 7.77. In this diagram, the present results for the location of the jet centre-line are also presented. These were obtained from measurements of the impingement point as determined by the position of the stagnation point (d) of Fig. 7.11. This point was measured from the oil film tests. These present measurements are in good agreement with those of previous studies.

Colin and Olivari (Ref. 16) found that for jet impingement in crossflow, separation of the radial wall jet occurs along a horse-shoe shaped line. The area enclosed by this line may be large compared to the jet diameter, for high values of the jet to free stream velocity ratio. This phenomenon is confirmed by the present work (see Figs. 7.11 and 7.14). It also shows that for a fixed Z/d, the size of this recirculation region (vortex region) and therefore the upstream penetration distance is a function of the mass velocity ratio as well as the impingement angle. Colin and Olivari also found that for a high momentum ratio and a high nozzle to target spacing of 4 jet diameters, the jet was not as deflected as the same jet in an unbounded space.

(b) Jet Axial Turbulence Measurements

Gardon and Akfirat (Ref. 75) showed that the stagnation point heat transfer reaches a maximum at a nozzle to target spacing between 6 and 7 jet diameters. This is the distance at which the apex of the potential core is formed. The centre-line velocity is constant within the potential core, so that the observed increase in heat transfer is generally agreed to be due to an increase in the turbulence level (see Gauntner and Livingwood (Ref. 31)).

Typical results of the axial turbulence variations obtained for the 60° and 45° jets in the present study are compared with Corrsin's results in Figs. 7.34 and 7.35. Corrsin showed that the turbulence level in the jet centre-line is a function of nozzle diameter. This is confirmed by the present investigation. Corrsin's results are for nozzle diameters of 76.2 and 25.4 mm respectively. This investigation employed 12.7 mm diameter jets. The axial turbulence intensity variations increase with decreasing nozzle diameter. Thus the results of the present investigation are in good agreement with the trends suggested by Corrsin's earlier measurements, although this investigation did not state his Reynolds number.

The present results further suggest that for a fixed nozzle geometry, the turbulence intensity at nozzle exit is independent of the Reynolds number (see Fig. 7.34). The differences in the values of nozzle exit turbulence intensities between the 60^{o} and 45^{o} nozzles for the various Reynolds numbers are thus due mainly to the nozzle exit geometry as previously discussed. The radial distribution of turbulence intensity at the nozzle exits see Figs 7.31 to 7.33 also exhibit similar trends to Corrsin's reported measurements. Thus the turbulence intensity results of the present studies generally exhibit similar trends to the limited previously reported data.

(c) Stagnation Point Heat Transfer Coefficients

Fig. 7.78 shows the effects of Reynolds number and nozzle to target spacing on heat transfer for orthogonal impingement in stagnant surrounding. Within the range of flow and geometrical parameters investigated, the experimental results show fair agreement with Gardon and Cobonpue's results, particularly since the stagnation heat transfers are particularly sensitive to the turbulence level. The heat transfer results of the present work however suggest that the stagnation point maxima are at a nozzle to target spacing (Z/d) of approximately 3.5 as discussed previously. The difference between the nozzle to target spacing for maximum heat transfers in this study and that reported by Gardon and Cobonpue may be due to differences in the turbulence levels and test conditions.

Fig. 7.79 presents previous correlations for stagnation point heat transfers for a nozzle to target spacing of 4 jet diameters. The present results are in good agreement with them. Huang's results (Ref. 60) are considerably lower than those of Gardon (Ref. 59) and the present test. It may be recalled that Huang did not take into account the influence of nozzle to target spacing in his correlation. This investigation suggests that the nozzle to target spacing is an important parameter for an accurate and reliable heat transfer correlation.

TABLE 2

TABULAR PRESENTATION OF EXPERIMENTAL AND PREVIOUSLY CORRELATED STAGNATION POINT HEAT TRANSFERS FOR ORTHOGONAL IMPINGEMENT AT $Z/d = 8$

Re_d	EXPERIMENTAL		HUANG (REF. 60)
	h_o	Nu_o	$Nu_o = 0.0233Re_d^{0.87}Pr^{0.33}$
32,700	320	160	176
30,200	310	156	164

Table 2 shows a comparison between the stagnation point heat transfer of the present studies and Huang's correlation for a nozzle to target spacing of 8 jet diameters. It can be noticed that agreement is quite good in this case. Huang's correlation should thus be used with caution for nozzle to target spacings less than 4, since the influence of nozzle to target spacing is apparently important in this region (e.g. see Ref. 59). However, there is no adequate correlation for this low range of Z/d as pointed out by Gardon and Cobonpue (Ref. 59).

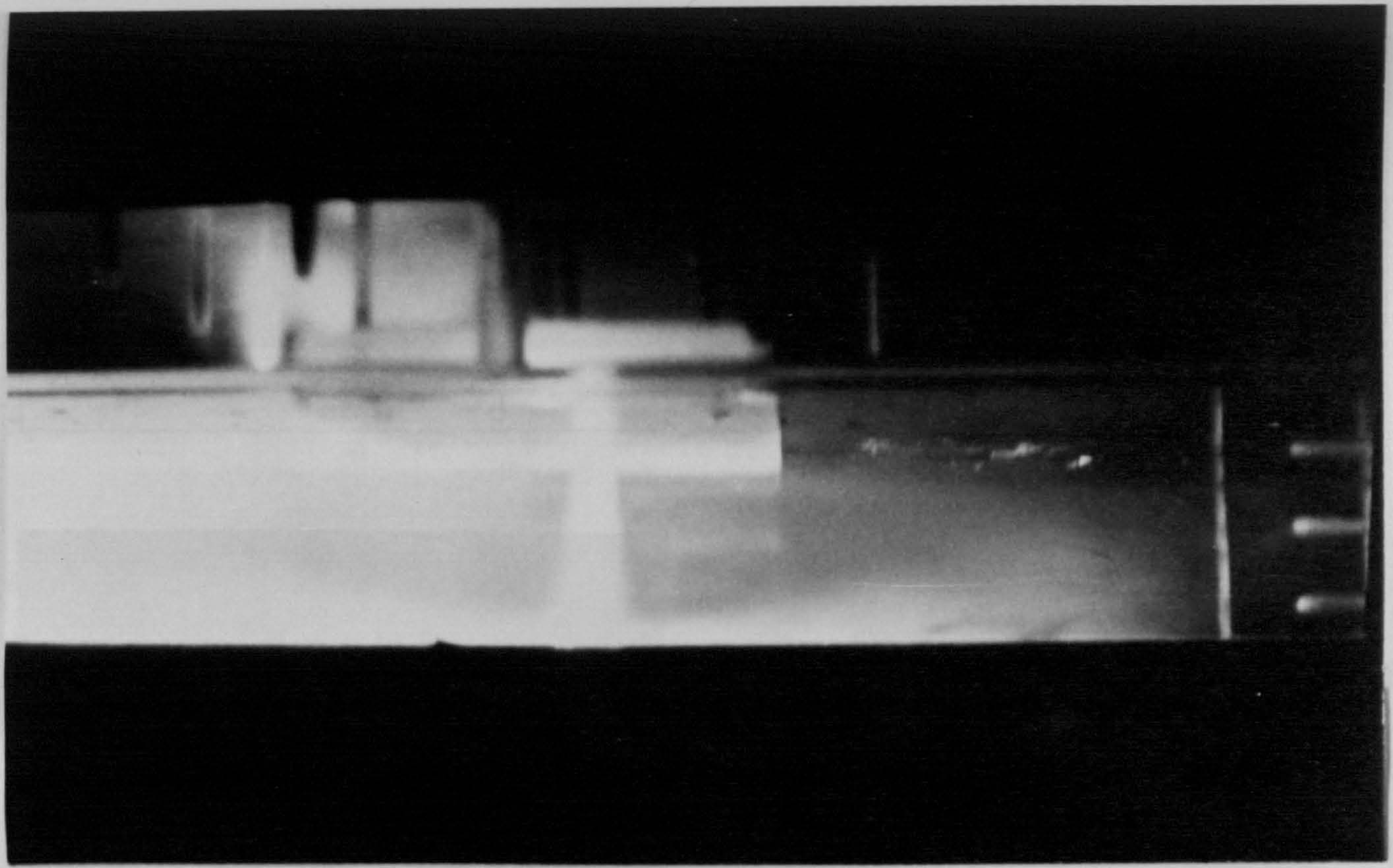

FIG. 7. 1. FLOW STRUCTURE OF AN ORTHOGONALLY IMPINGING JET IN STAGNANT SURROUNDINGS

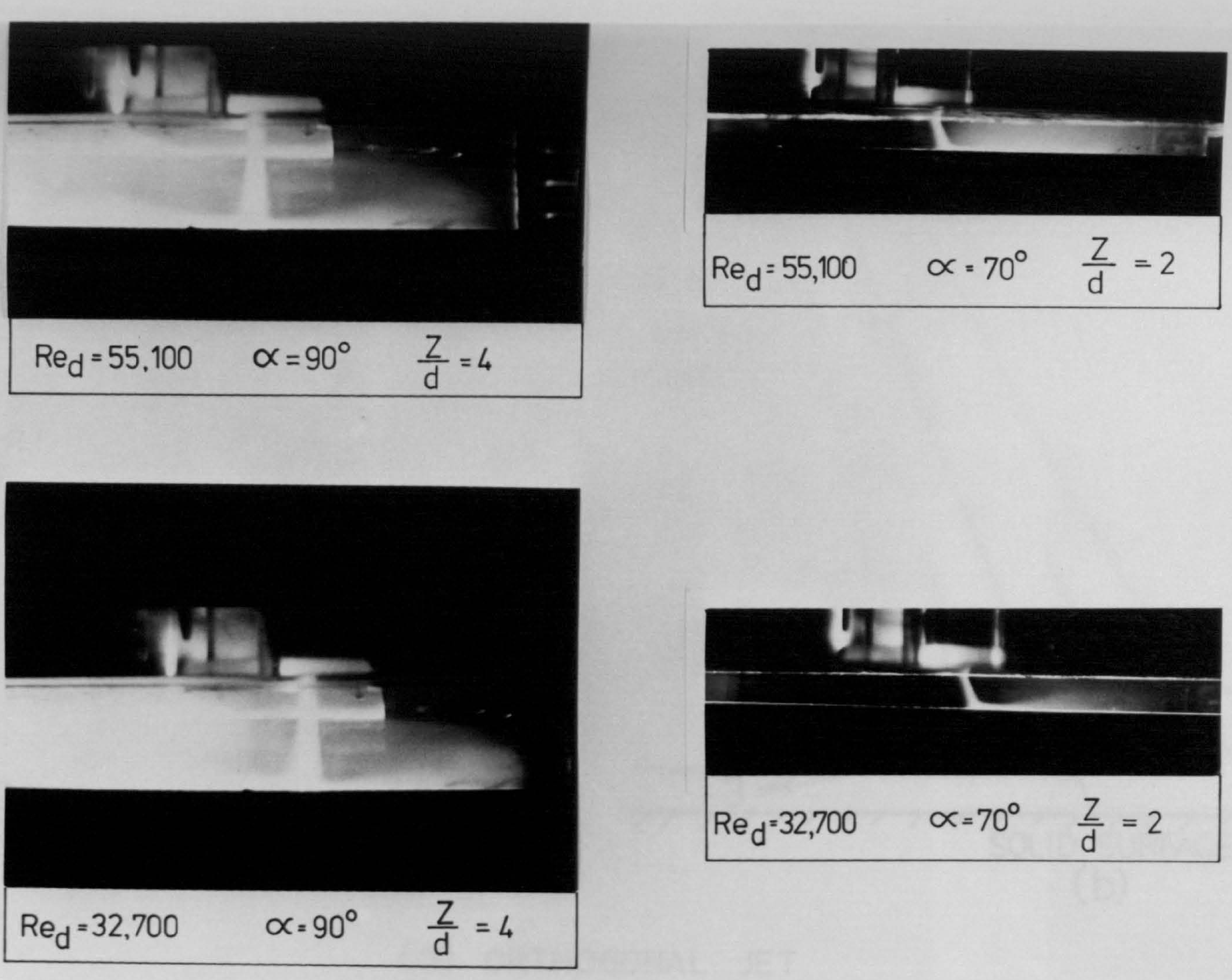

$Re_d = 55,100$ $\alpha = 90°$ $\frac{Z}{d} = 4$

$Re_d = 55,100$ $\alpha = 70°$ $\frac{Z}{d} = 2$

$Re_d = 32,700$ $\alpha = 90°$ $\frac{Z}{d} = 4$

$Re_d = 32,700$ $\alpha = 70°$ $\frac{Z}{d} = 2$

FIG. 7. 2. EFFECTS OF REYNOLDS NUMBER AND IMPINGEMENT ANGLE ON THE FLOW STRUCTURE OF IMPINGING JETS IN QUIESCENT MEDIA

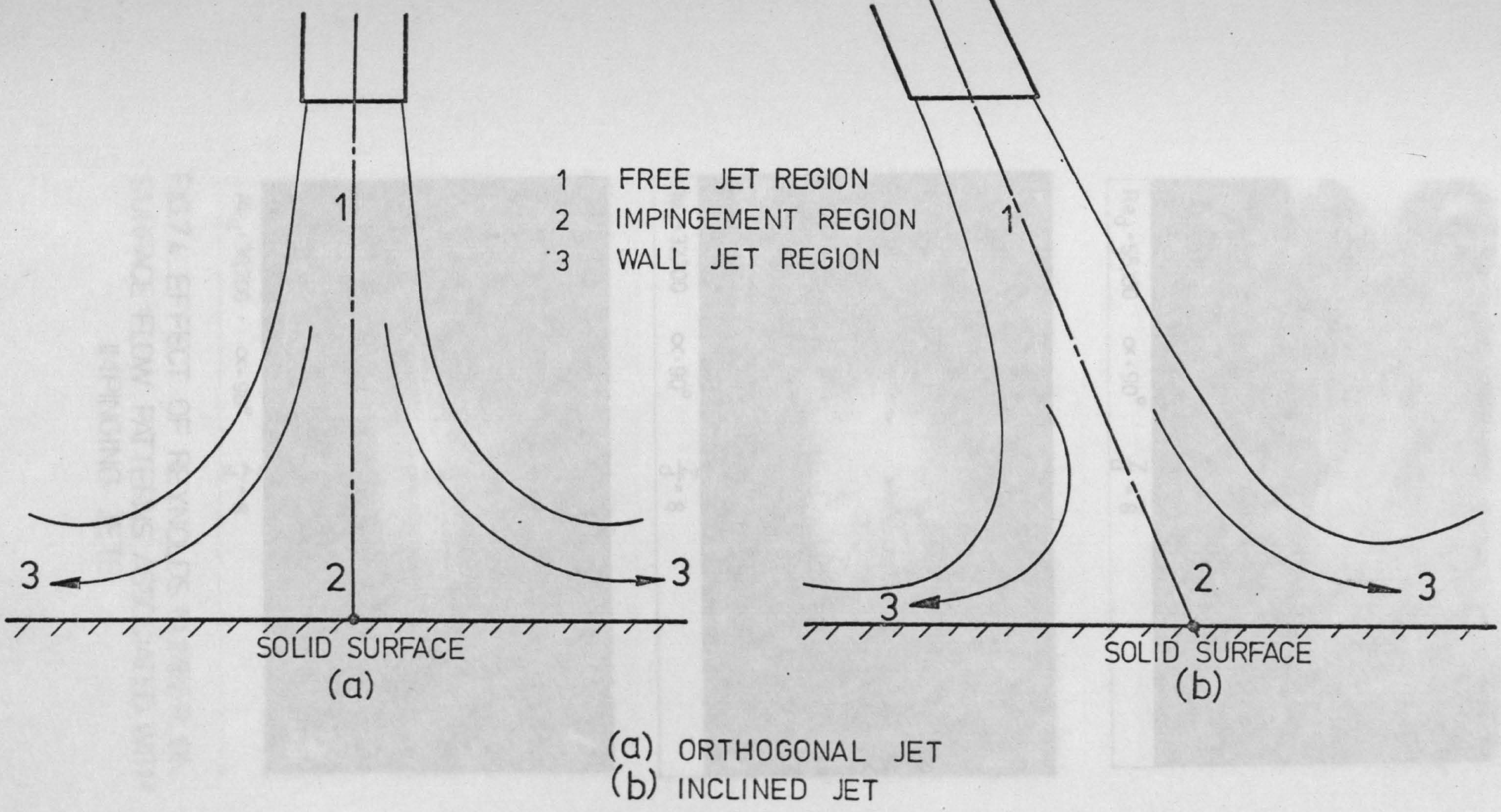

FIG. 7.3. SCHEMATIC REPRESENTATION OF FLOW STRUCTURE PATTERNS ASSOCIATED WITH IMPINGING JETS IN STAGNANT SURROUNDINGS

$Re_d = 55{,}100$ $\alpha = 90^\circ$ $\frac{Z}{d} = 8$

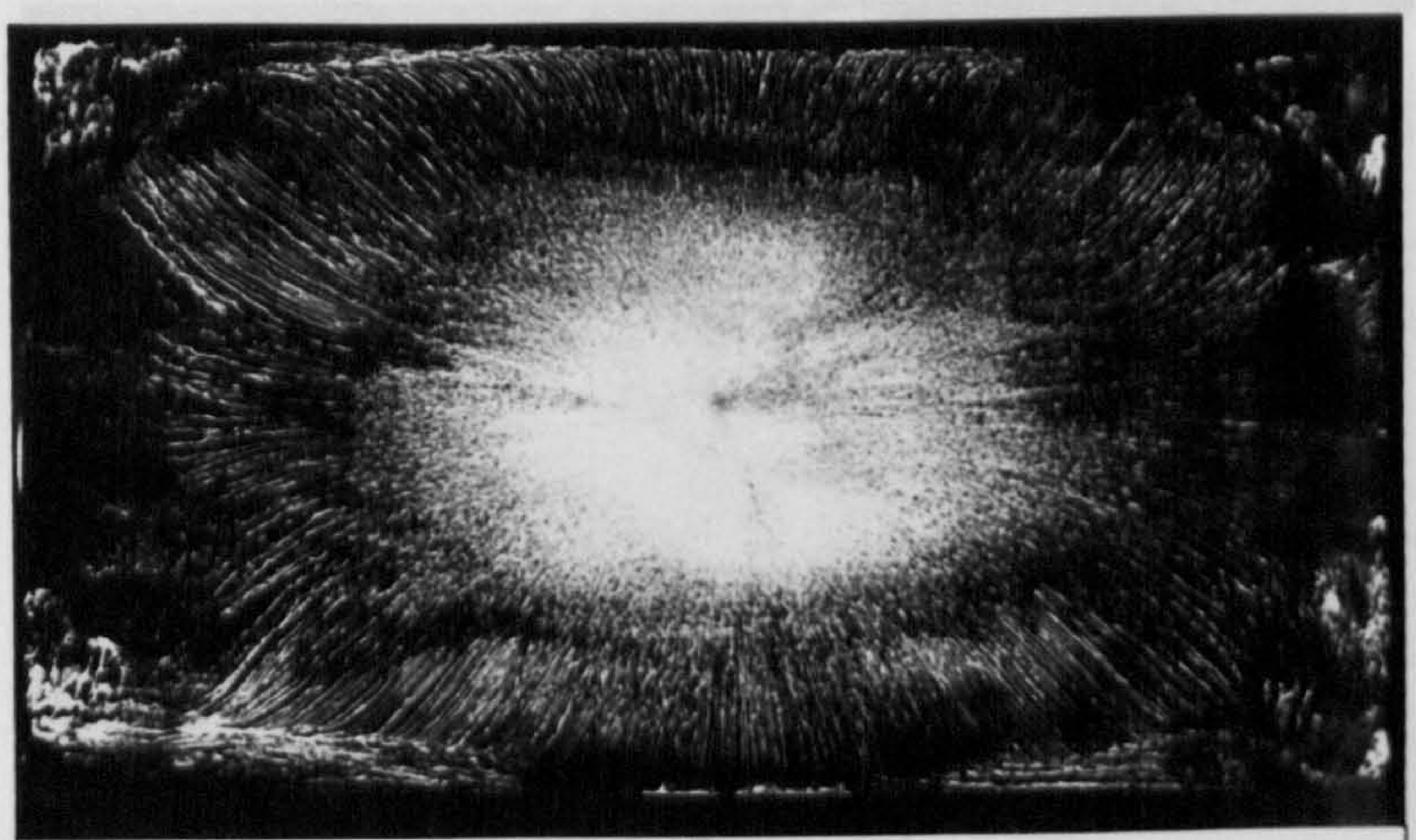

$Re_d = 32{,}700$ $\alpha = 90^\circ$ $\frac{Z}{d} = 8$

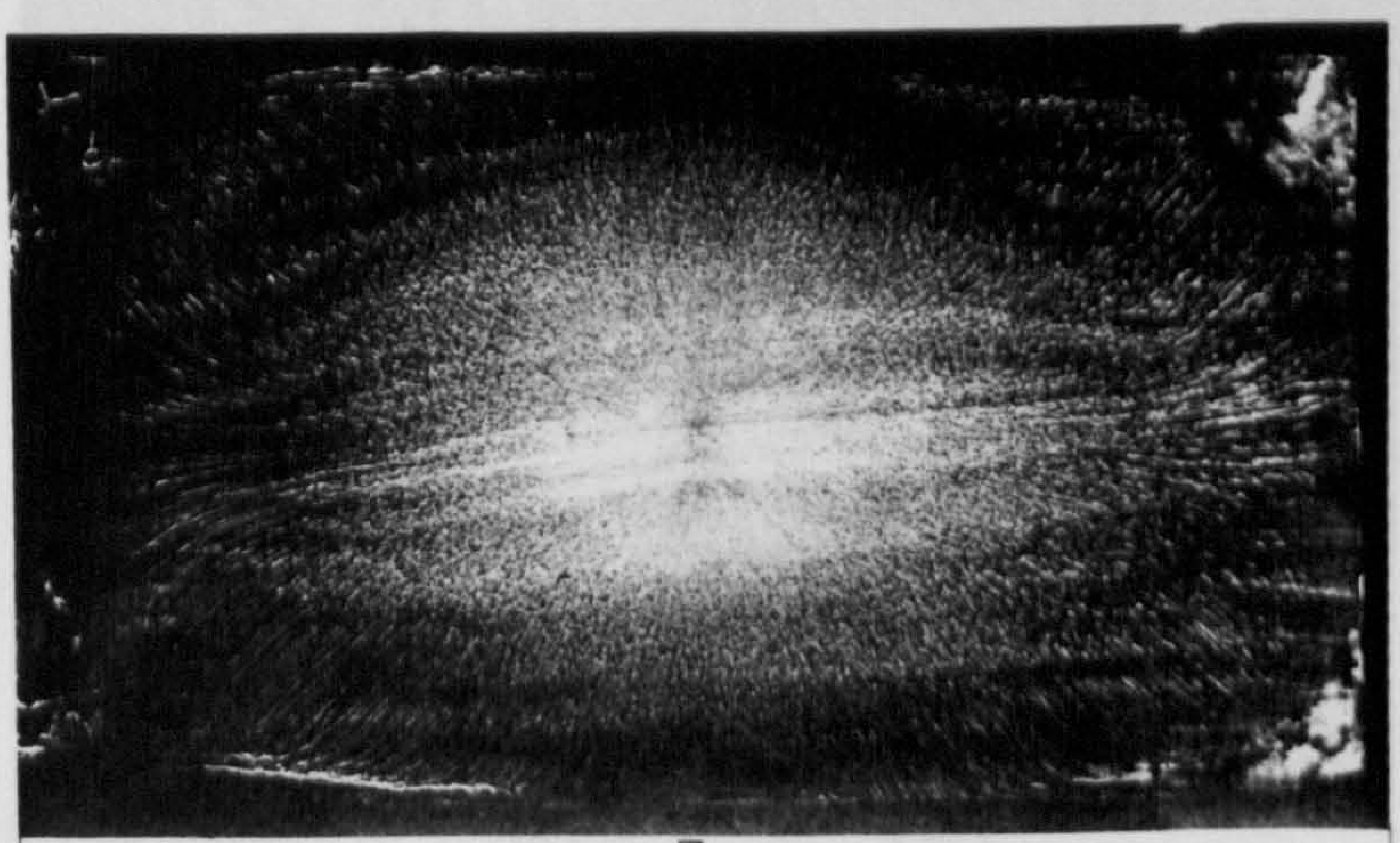

$Re_d = 30{,}200$ $\alpha = 90^\circ$ $\frac{Z}{d} = 8$

FIG.7.4. EFFECT OF REYNOLDS NUMBER ON SURFACE FLOW PATTERNS ASSOCIATED WITH IMPINGING JETS

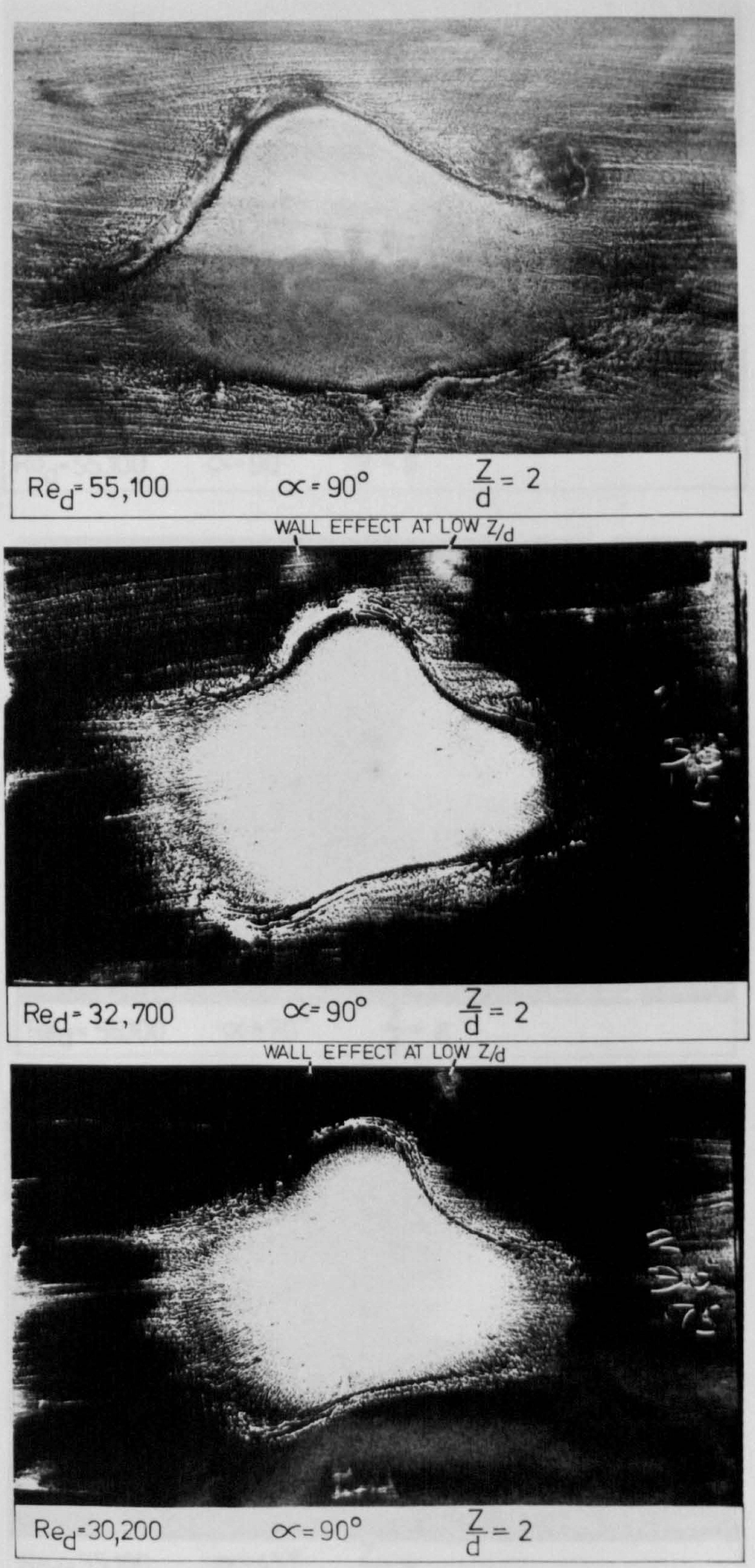

FIG. 7.5. EFFECT OF REYNOLDS NUMBER ON SURFACE FLOW PATTERNS ASSOCIATED WITH IMPINGING JETS

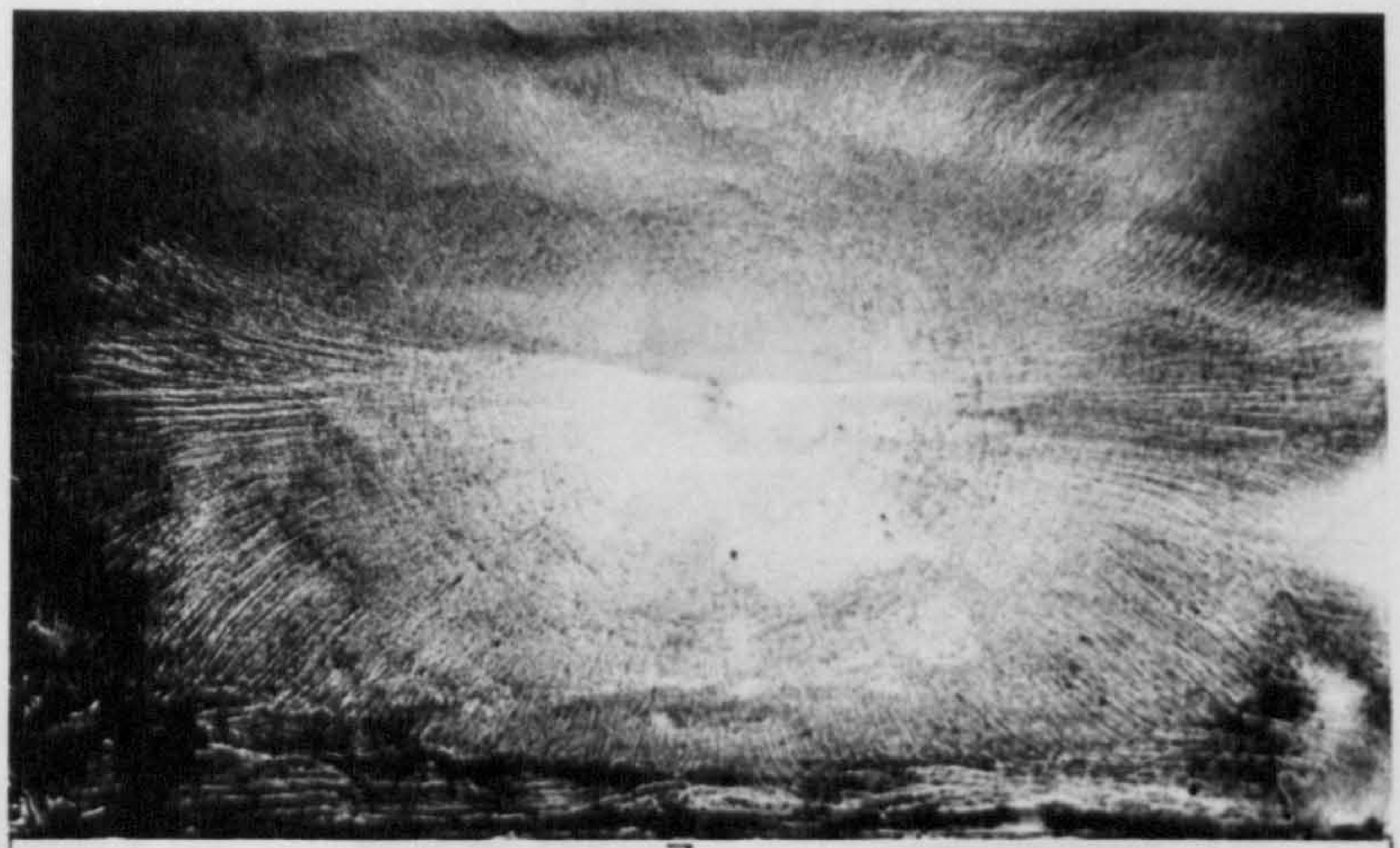

$Re_d = 55{,}100$ $\alpha = 90°$ $\frac{Z}{d} = 8$

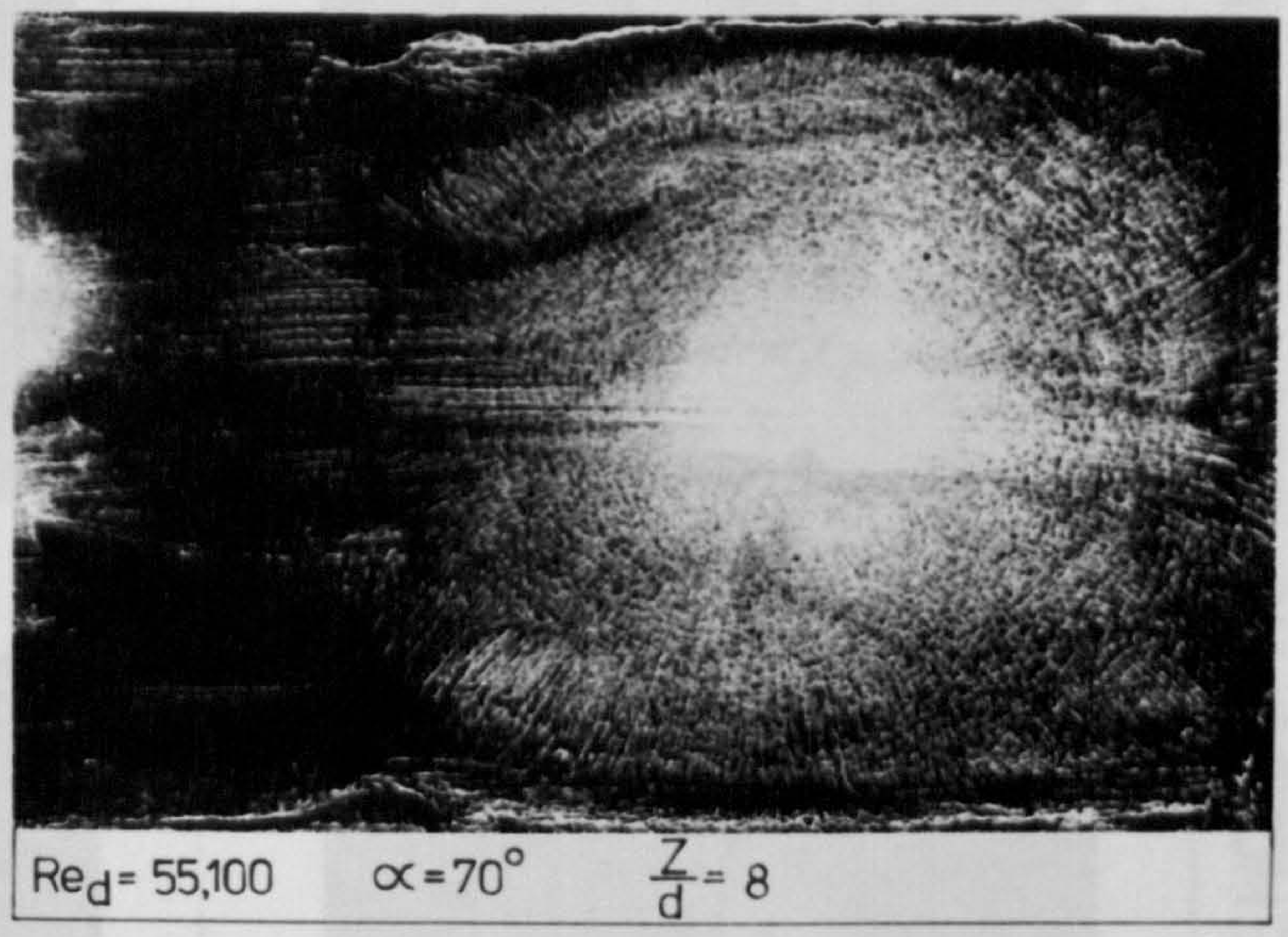

$Re_d = 55{,}100$ $\alpha = 70°$ $\frac{Z}{d} = 8$

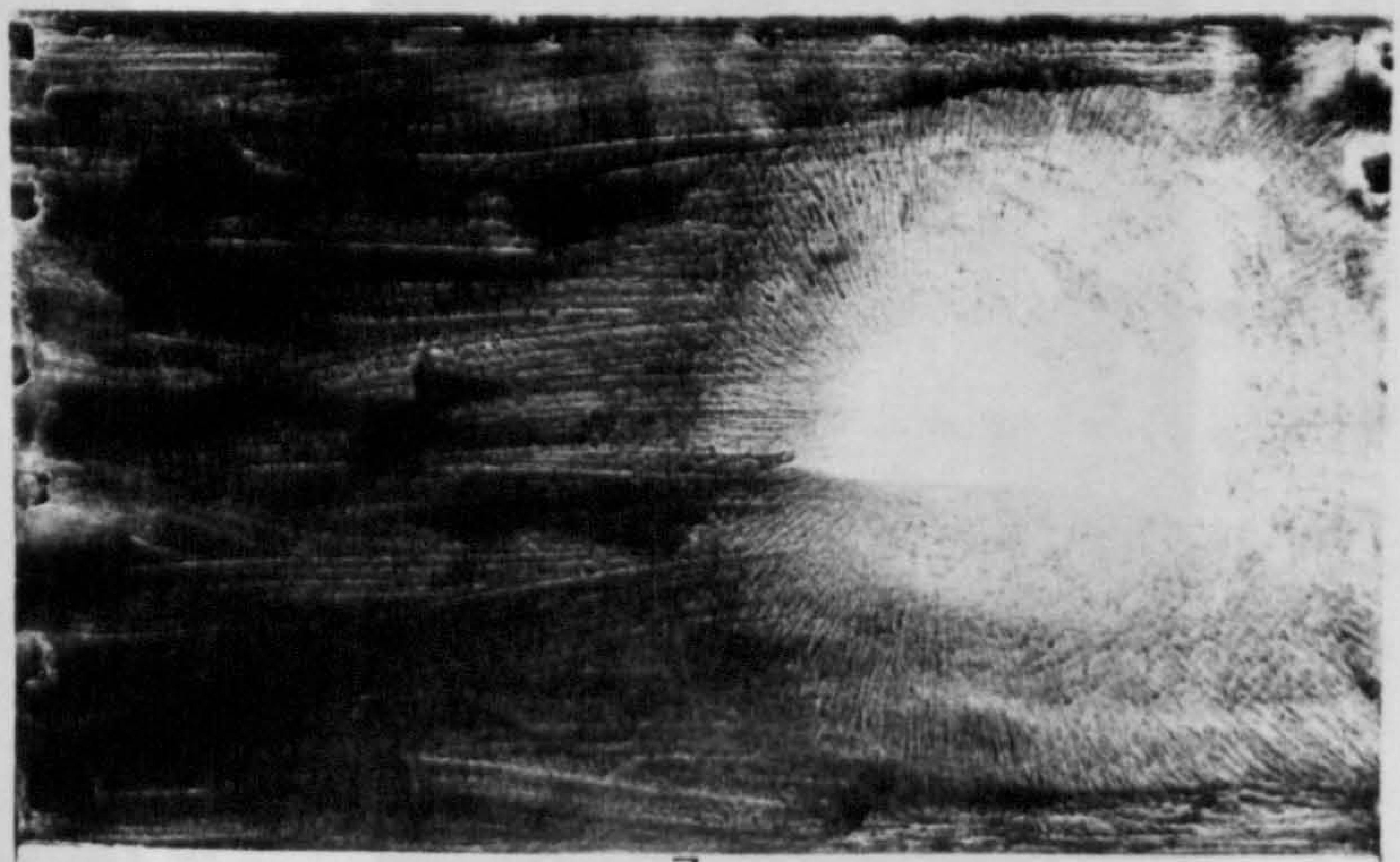

$Re_d = 55{,}100$ $\alpha = 45°$ $\frac{Z}{d} = 8$

FIG.7.6. EFFECT OF JET INCLINATION ON SURFACE FLOW PATTERNS ASSOCIATED WITH IMPINGING JETS

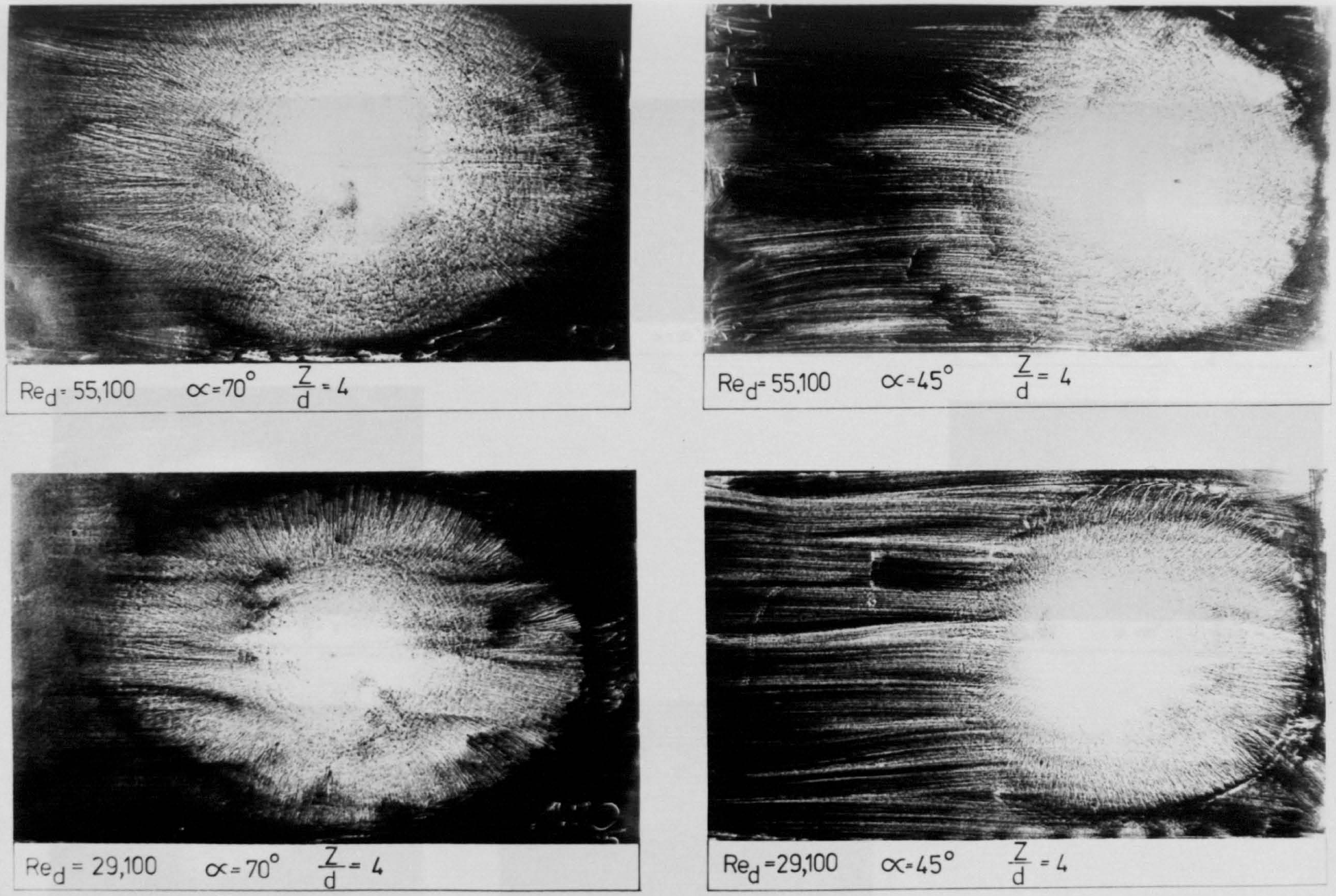

$Re_d = 55{,}100$ $\alpha = 70°$ $\frac{Z}{d} = 4$

$Re_d = 55{,}100$ $\alpha = 45°$ $\frac{Z}{d} = 4$

$Re_d = 29{,}100$ $\alpha = 70°$ $\frac{Z}{d} = 4$

$Re_d = 29{,}100$ $\alpha = 45°$ $\frac{Z}{d} = 4$

FIG. 7.7. EFFECT OF RENOLDS NUMBER AND JET INCLINATION ON SURFACE FLOW PATTERNS

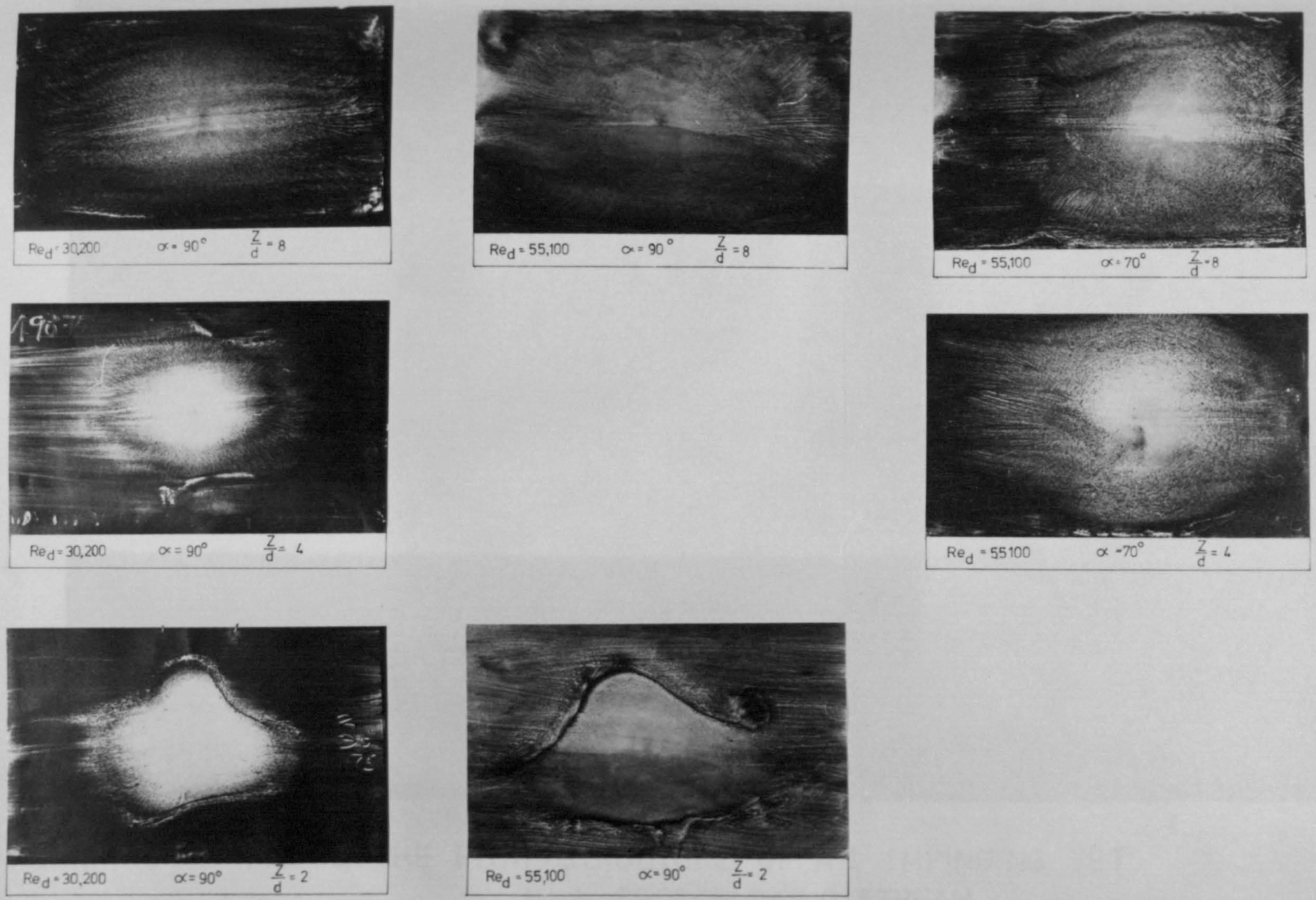

FIG. 7. 8. EFFECTS OF REYNOLDS NUMBER AND NOZZLE TO TARGET SPACING ON SURFACE FLOW PATTERNS ASSOCIATED WITH IMPINGING JETS IN STAGNANT SURROUNDINGS

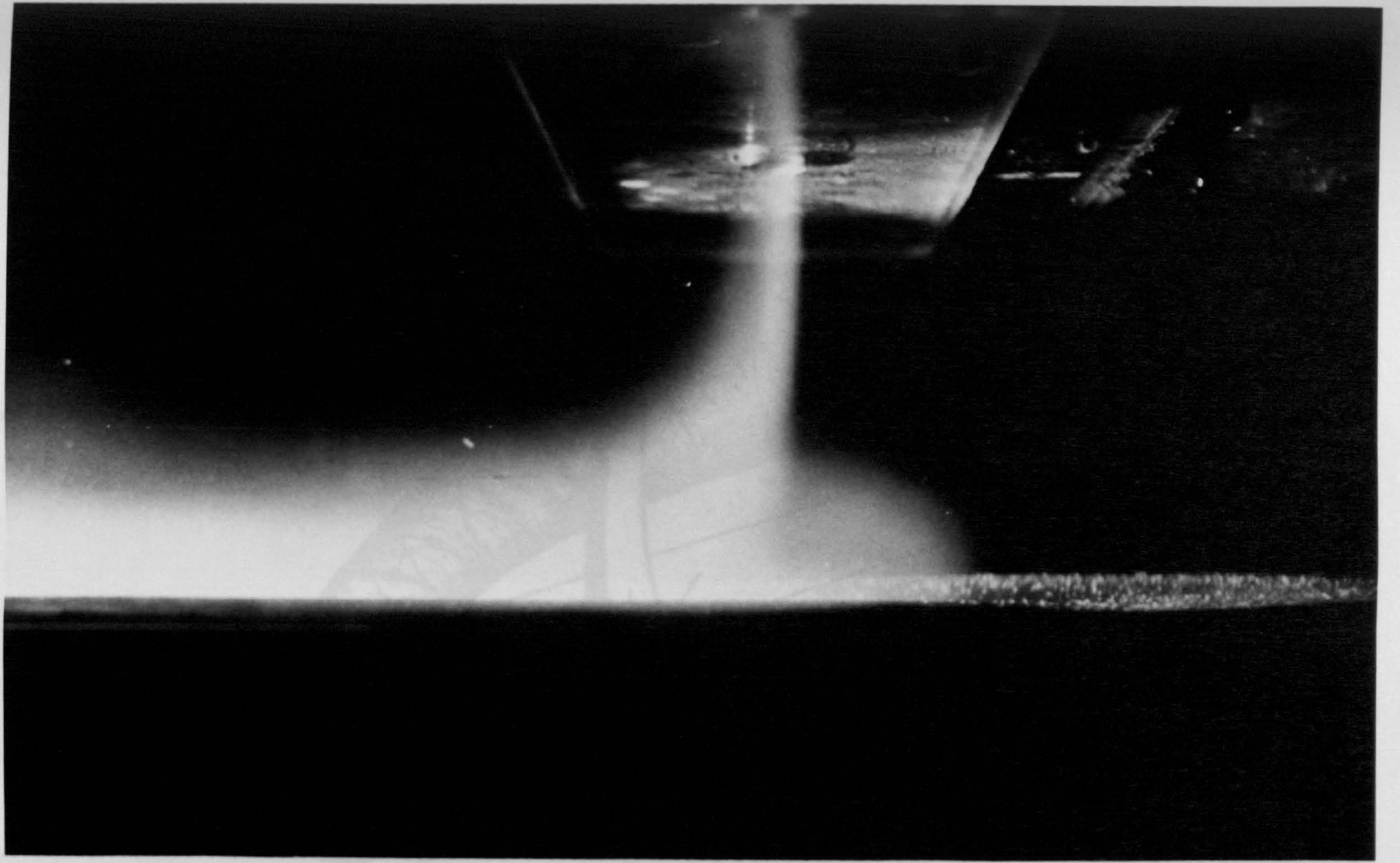

FIG. 7. 9. THE FLOW STRUCTURE OF AN IMPINGING JET IN A CROSSFLOWING STREAM

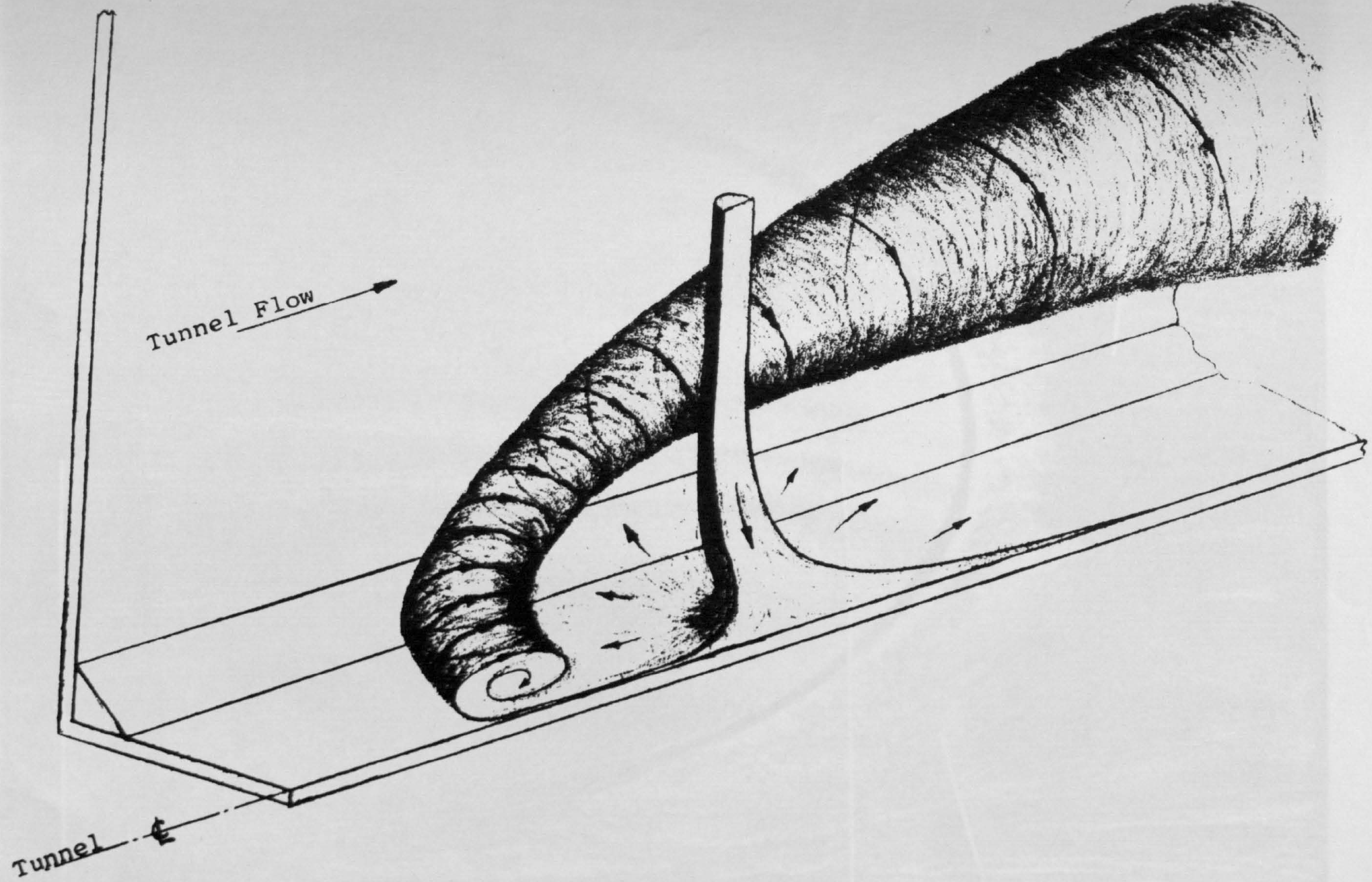

FIG. 7.10. SCHEMATIC REPRESENTATION OF THE FLOW STRUCTURE OF AN IMPINGING JET IN A CROSSFLOWING STREAM — SITUATION WITH VORTEX FORMATION.

FIG. 7.11. SURFACE FLOW PATTERN ASSOCIATED WITH AN IMPINGING JET IN A CROSSFLOWING STREAM
SITUATION WITH VORTEX FORMATION

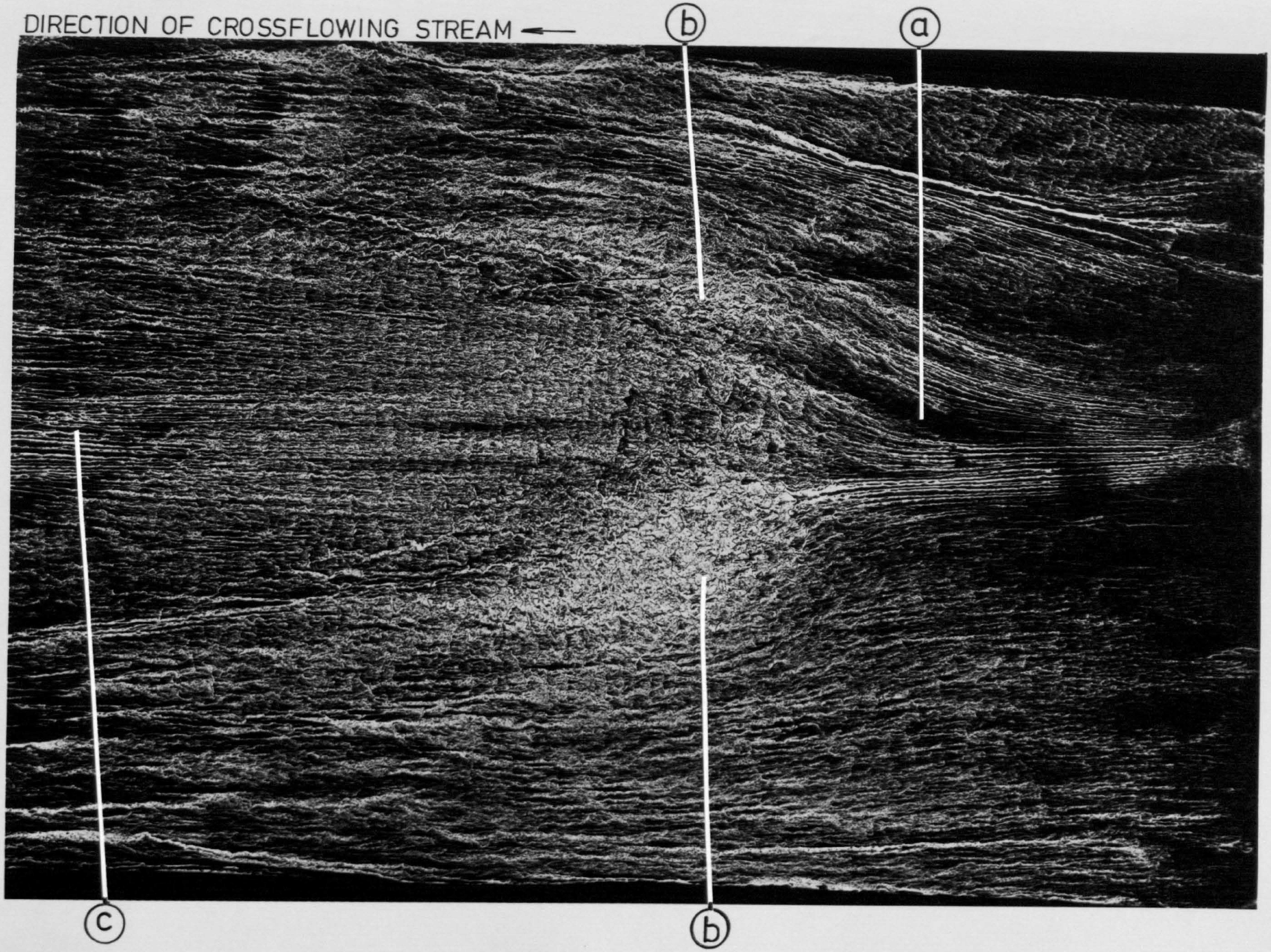

FIG. 7. 12. SURFACE FLOW PATTERN ASSOCIATED WITH AN IMPINGING JET IN A CROSSFLOWING STREAM
SITUATION WITHOUT VORTEX FORMATION

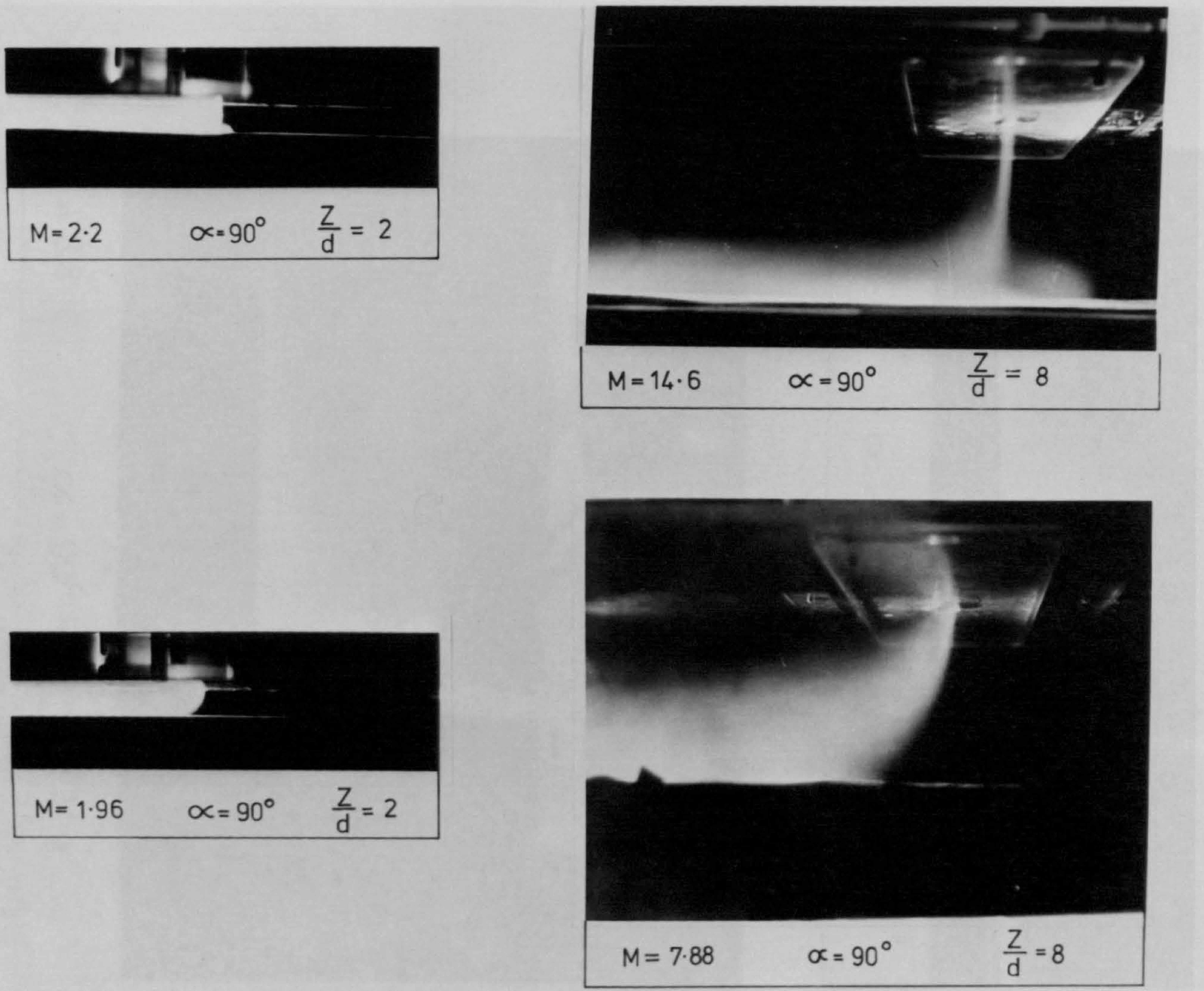

$M = 2{\cdot}2$ $\alpha = 90^\circ$ $\frac{Z}{d} = 2$

$M = 14{\cdot}6$ $\alpha = 90^\circ$ $\frac{Z}{d} = 8$

$M = 1{\cdot}96$ $\alpha = 90^\circ$ $\frac{Z}{d} = 2$

$M = 7{\cdot}88$ $\alpha = 90^\circ$ $\frac{Z}{d} = 8$

FIG.7.13. EFFECT OF MASS VELOCITY RATIO AND NOZZLE TO TARGET SPACING ON AN IMPINGING JET IN CROSSFLOWS

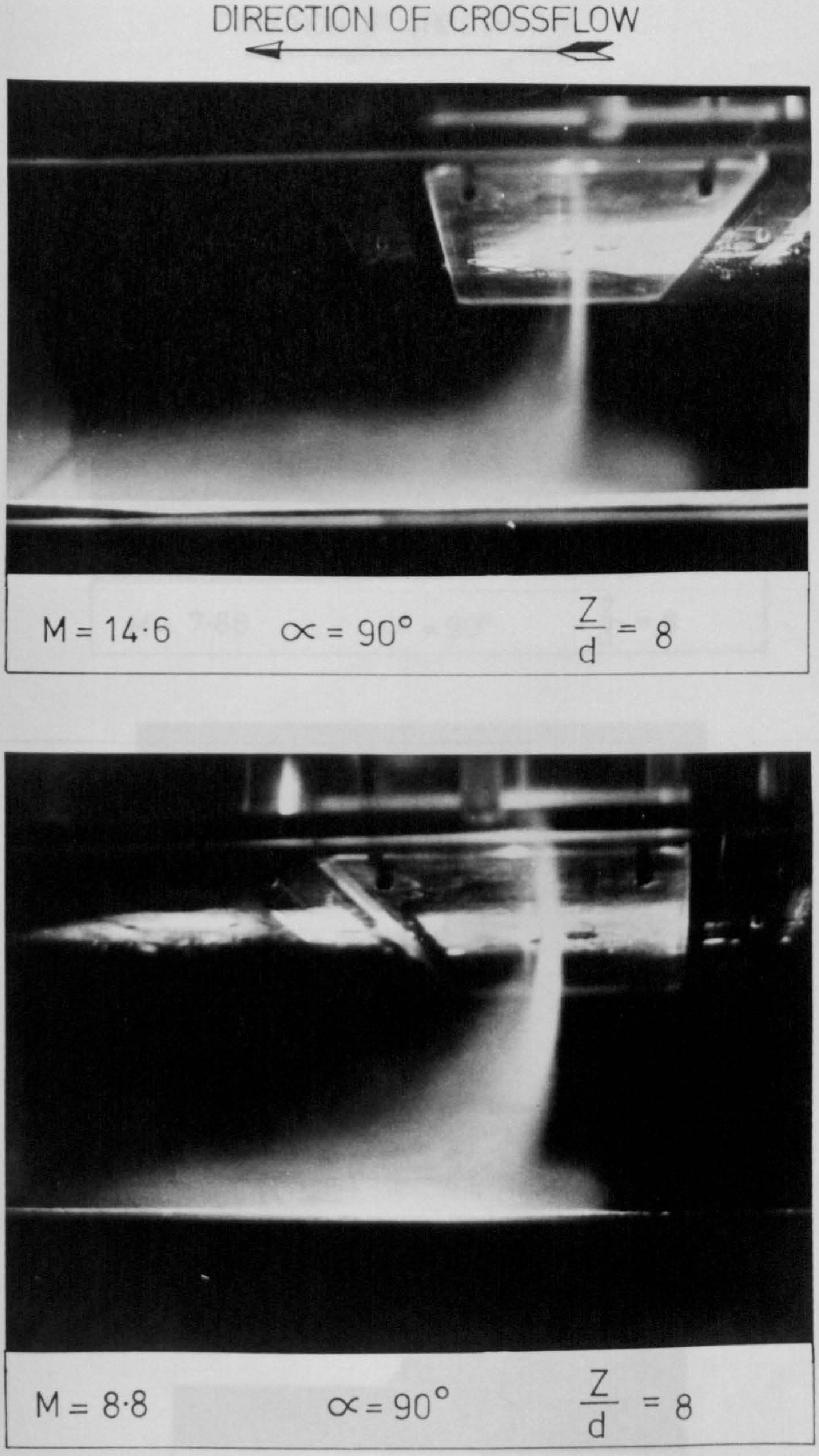

FIG. 7.14. EFFECT OF MASS VELOCITY RATIO ON THE FLOW STRUCTURE OF AN IMPINGING JET IN CROSSFLOWS

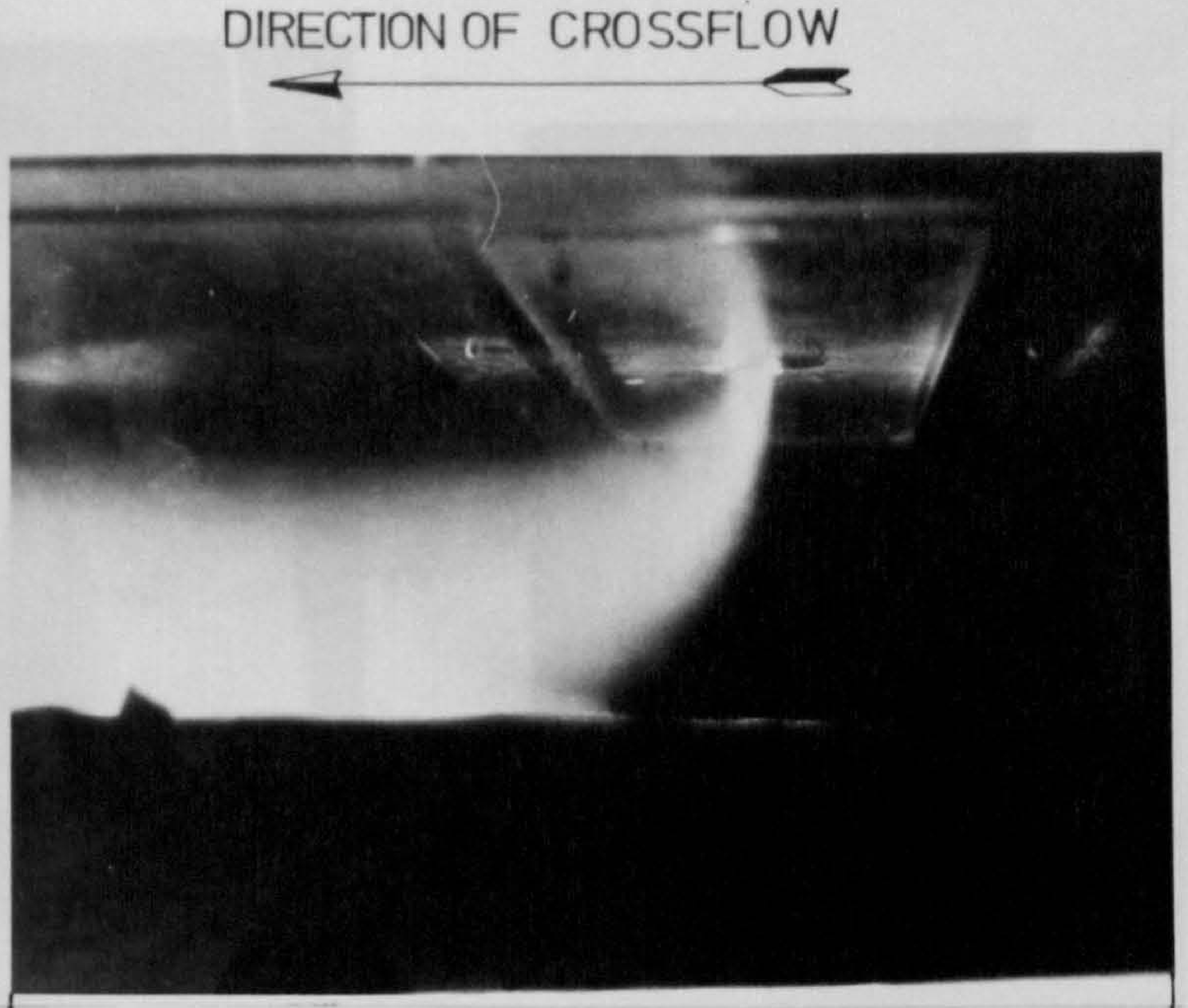

$M = 7{\cdot}88 \quad \alpha = 90° \quad \frac{Z}{d} = 8$

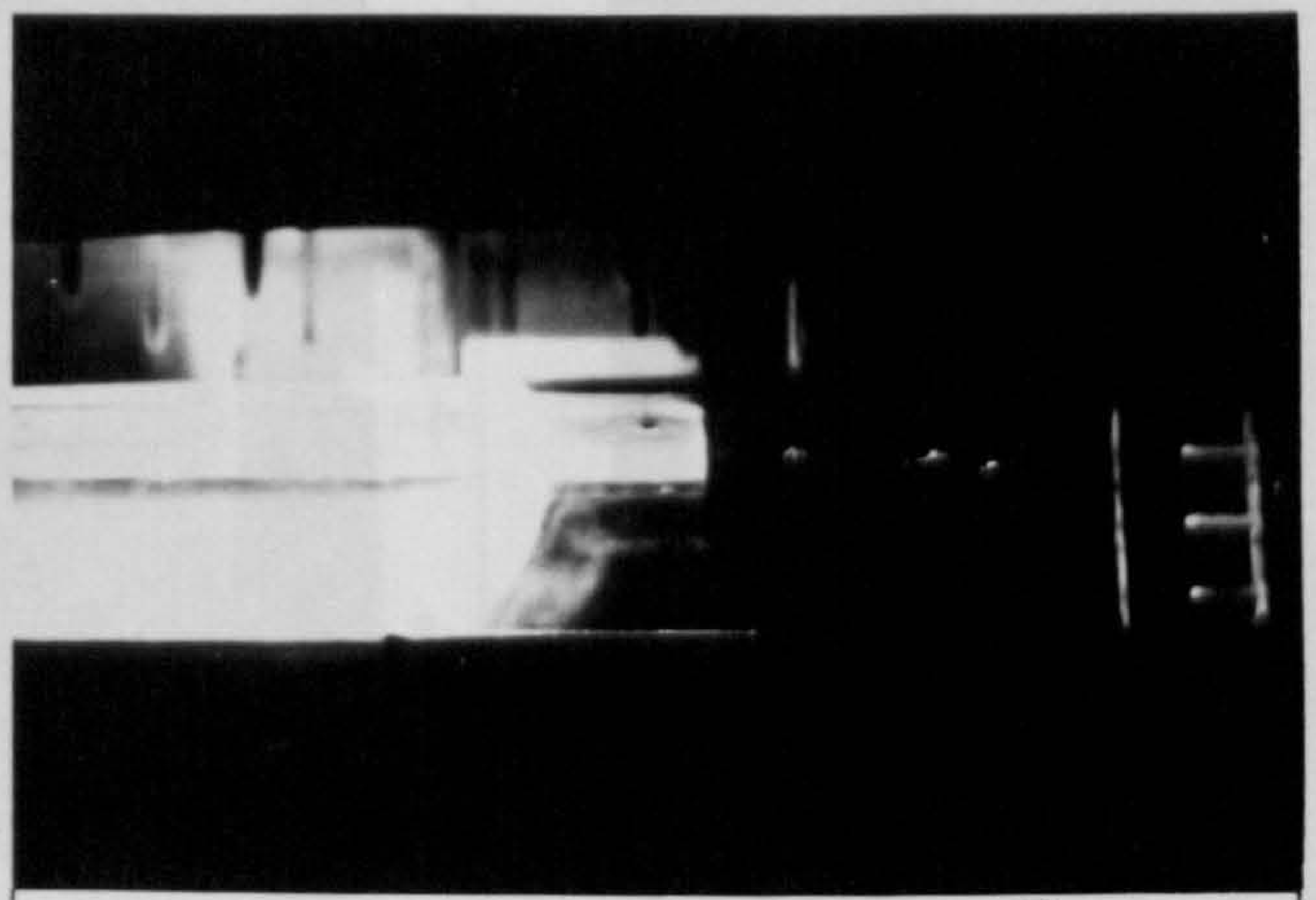

$M = 3{\cdot}94 \quad \alpha = 90° \quad \frac{Z}{d} = 4$

$M = 1{\cdot}96 \quad \alpha = 90° \quad \frac{Z}{d} = 2$

FIG. 7.15. EFFECT OF NOZZLE TO TARGET SPACING

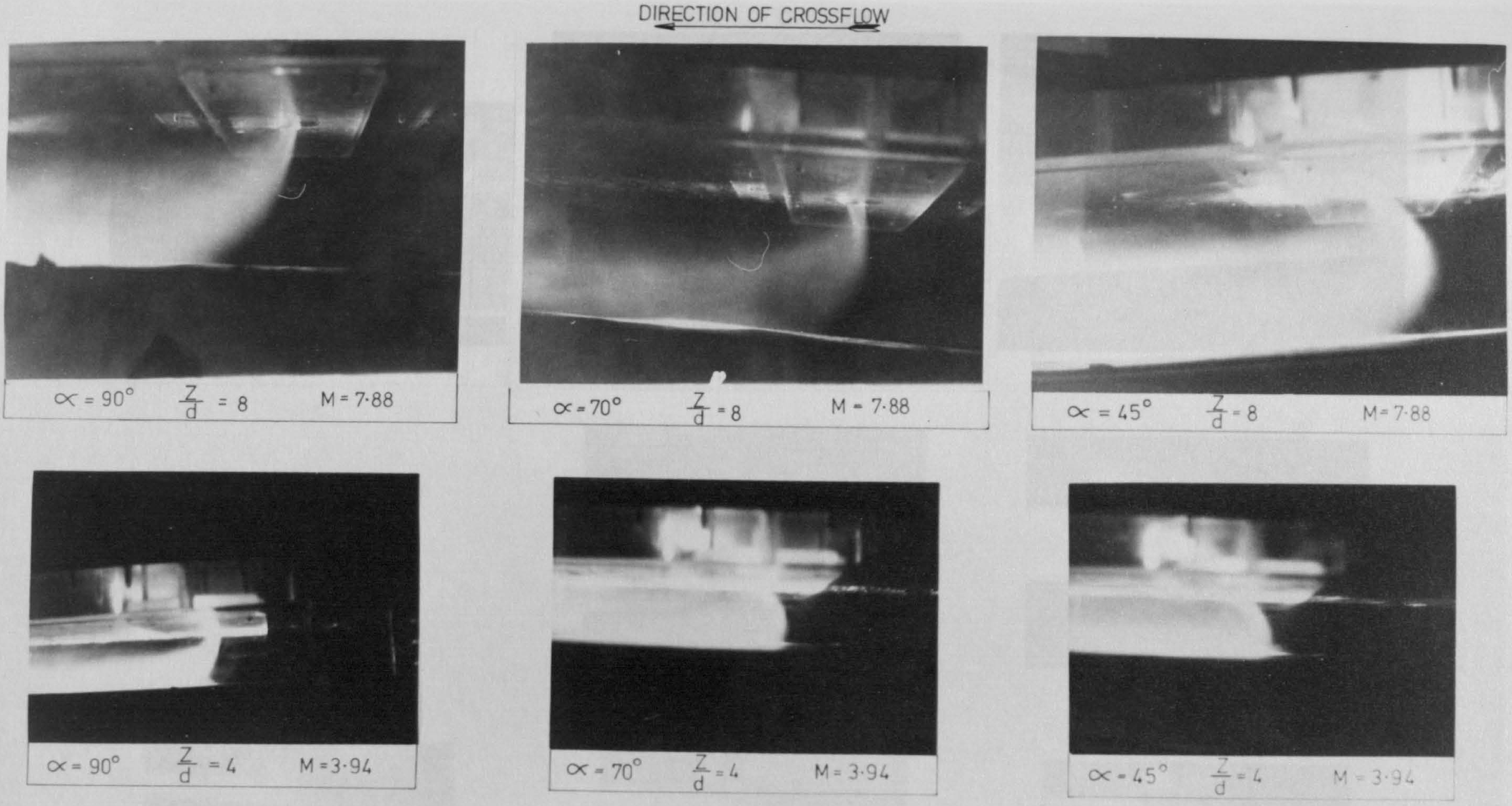

$\alpha = 90°$ $\frac{Z}{d} = 8$ $M = 7{\cdot}88$

$\alpha = 70°$ $\frac{Z}{d} = 8$ $M = 7{\cdot}88$

$\alpha = 45°$ $\frac{Z}{d} = 8$ $M = 7{\cdot}88$

$\alpha = 90°$ $\frac{Z}{d} = 4$ $M = 3{\cdot}94$

$\alpha = 70°$ $\frac{Z}{d} = 4$ $M = 3{\cdot}94$

$\alpha = 45°$ $\frac{Z}{d} = 4$ $M = 3{\cdot}94$

FIG. 7. 16. EFFECT OF JET INCLINATION ON FLOW STRUCTURE OF JETS IN CROSSFLOWS

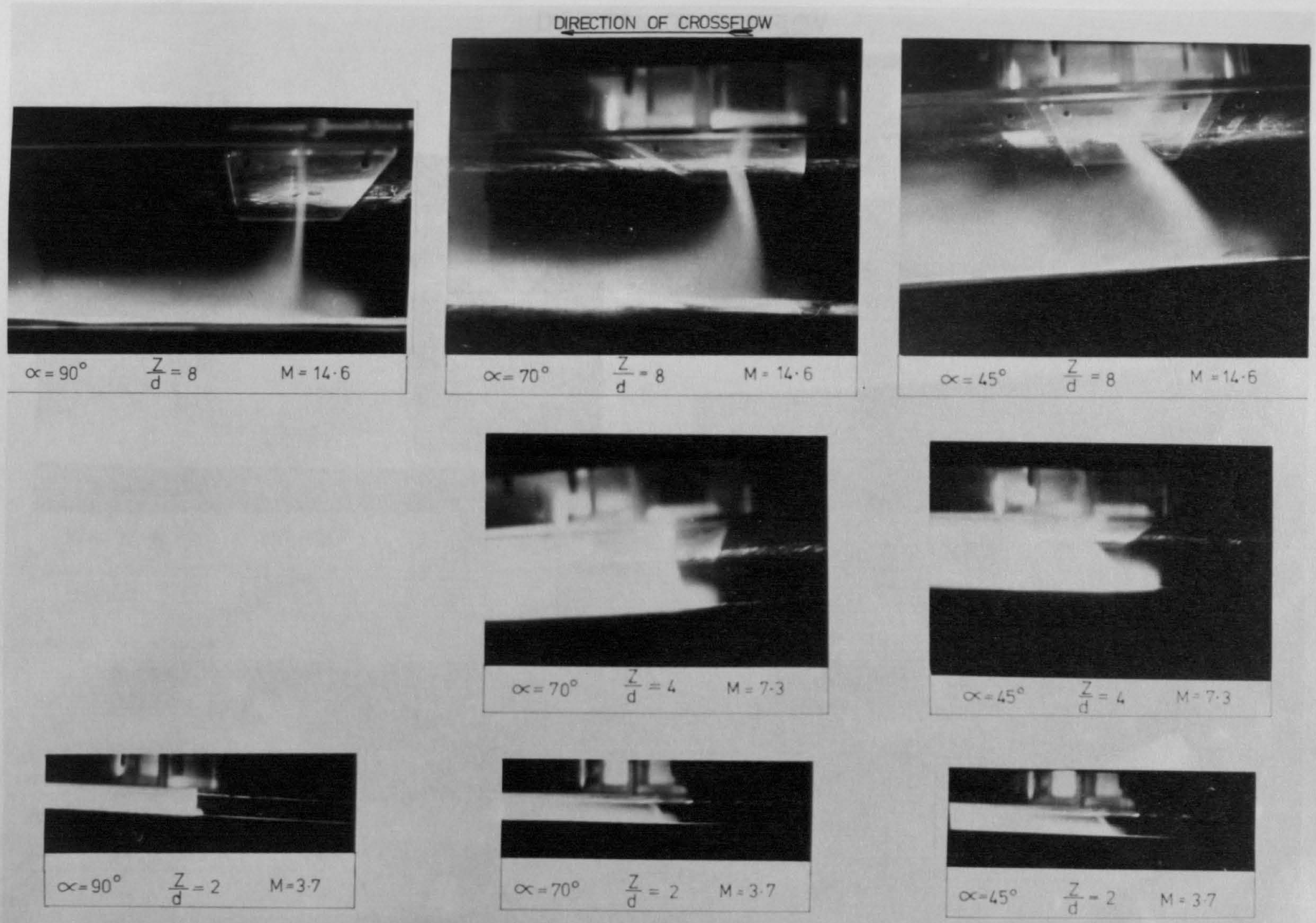

$\alpha = 90°$ $\frac{Z}{d} = 8$ $M = 14{\cdot}6$

$\alpha = 70°$ $\frac{Z}{d} = 8$ $M = 14{\cdot}6$

$\alpha = 45°$ $\frac{Z}{d} = 8$ $M = 14{\cdot}6$

$\alpha = 70°$ $\frac{Z}{d} = 4$ $M = 7{\cdot}3$

$\alpha = 45°$ $\frac{Z}{d} = 4$ $M = 7{\cdot}3$

$\alpha = 90°$ $\frac{Z}{d} = 2$ $M = 3{\cdot}7$

$\alpha = 70°$ $\frac{Z}{d} = 2$ $M = 3{\cdot}7$

$\alpha = 45°$ $\frac{Z}{d} = 2$ $M = 3{\cdot}7$

FIG. 7. 17. EFFECT OF IMPINGEMENT ANGLE AND NOZZLE TO TARGET SPACING

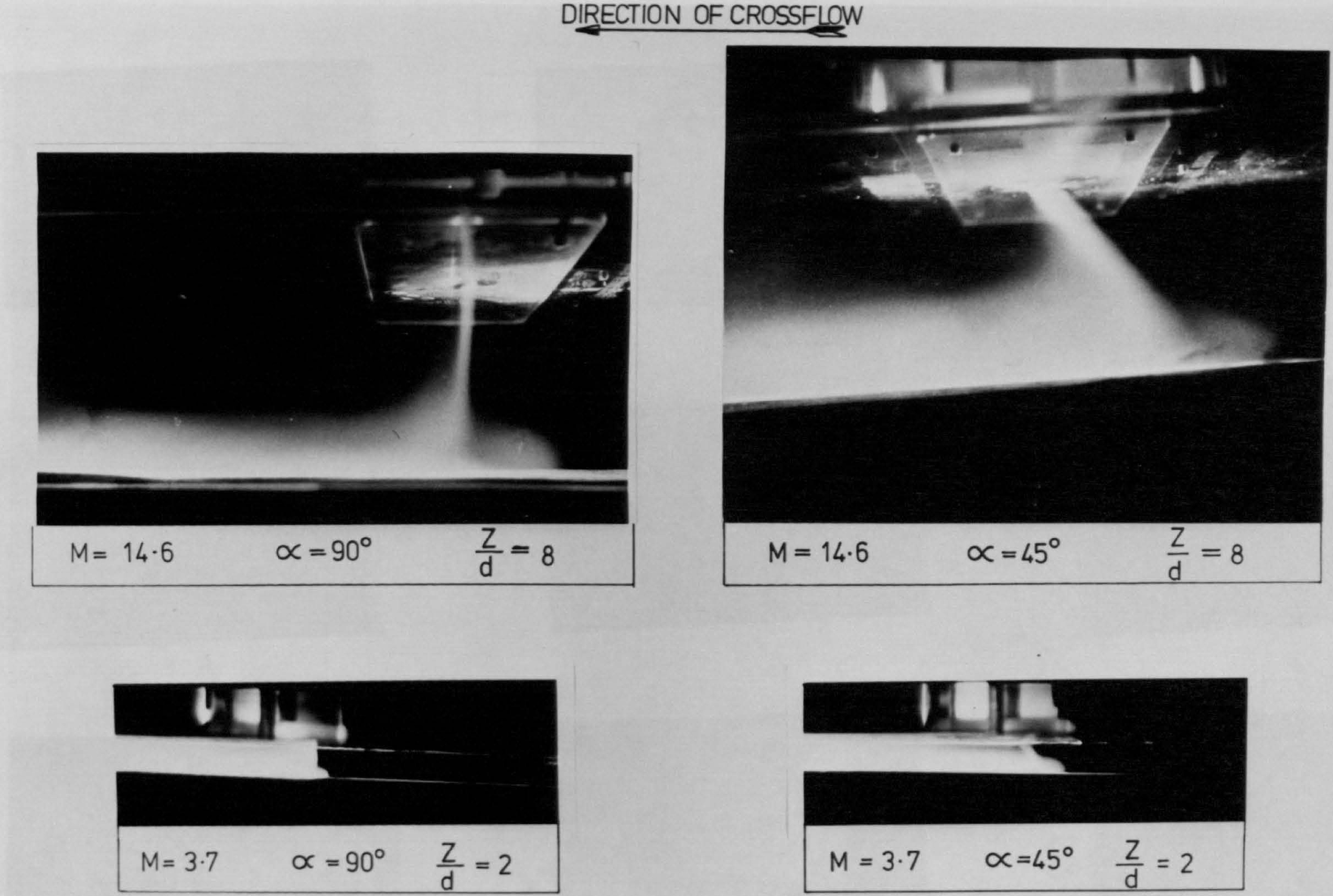

M = 14·6 $\alpha = 90°$ $\frac{Z}{d} = 8$

M = 14·6 $\alpha = 45°$ $\frac{Z}{d} = 8$

M = 3·7 $\alpha = 90°$ $\frac{Z}{d} = 2$

M = 3·7 $\alpha = 45°$ $\frac{Z}{d} = 2$

FIG. 7. 18. EFFECT OF IMPINGEMENT ANGLE AND NOZZLE TO TARGET SPACING

$\frac{Z}{d} = 2$ $M = 3{\cdot}7$ $\alpha = 90°$

$\frac{Z}{d} = 4$ $M = 7{\cdot}3$ $\alpha = 90°$

$\frac{Z}{d} = 8$ $M = 14{\cdot}6$ $\alpha = 90°$

$\frac{Z}{d} = 2$ $M = 3{\cdot}7$ $\alpha = 70°$

$\frac{Z}{d} = 4$ $M = 7{\cdot}3$ $\alpha = 70°$

$\frac{Z}{d} = 8$ $M = 14{\cdot}6$ $\alpha = 70°$

$\frac{Z}{d} = 2$ $M = 3{\cdot}7$ $\alpha = 45°$

$\frac{Z}{d} = 4$ $M = 7{\cdot}3$ $\alpha = 45°$

$\frac{Z}{d} = 8$ $M = 14{\cdot}6$ $\alpha = 45°$

FIG.7.19. EFFECTS OF NOZZLE TO TARGET SPACING AND JET INCLINATION ON OIL FILM PATTERNS FOR IMPINGING JETS IN CROSSFLOWING AIR STREAMS

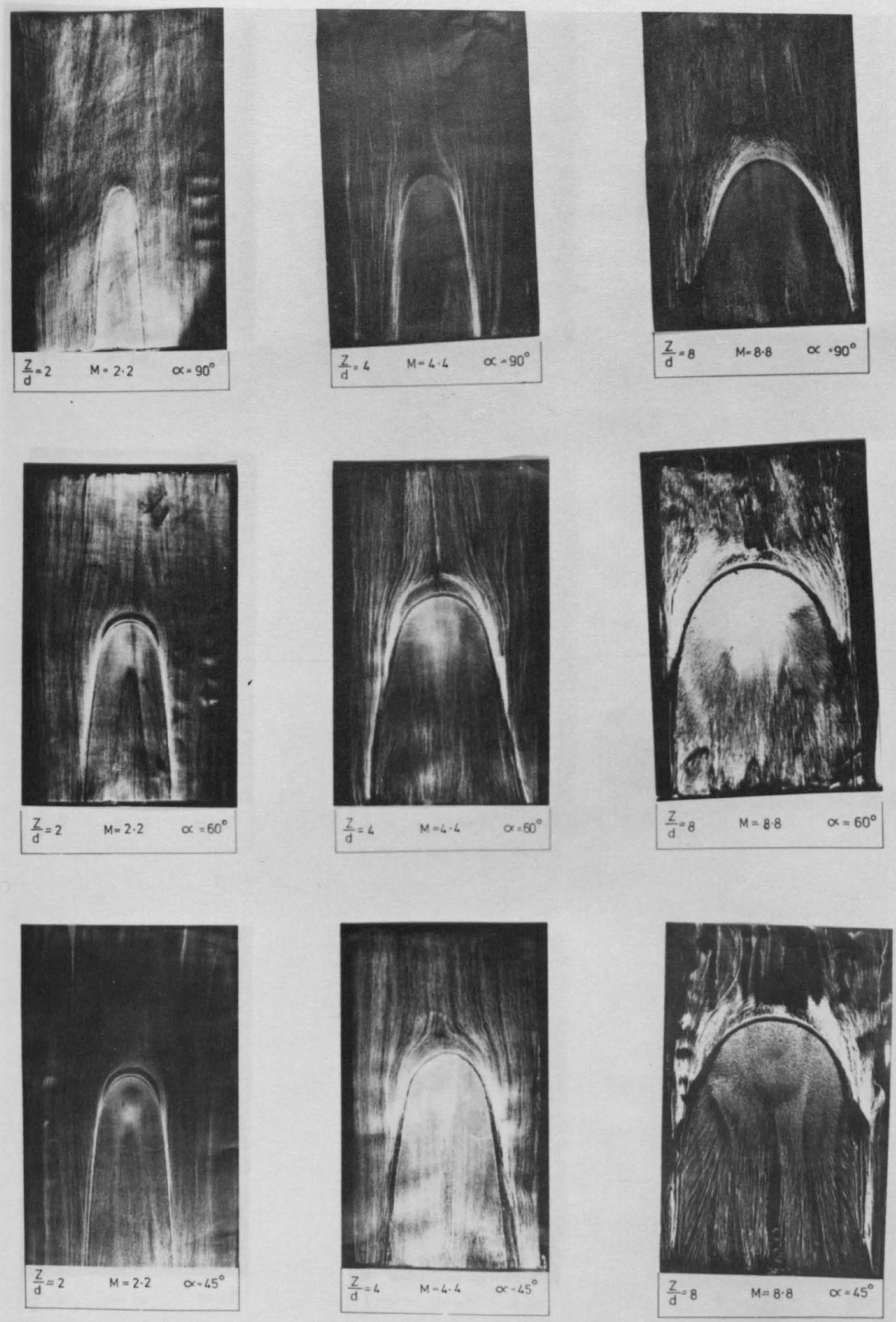

$\frac{Z}{d} = 2$ $M = 2{\cdot}2$ $\alpha = 90^\circ$

$\frac{Z}{d} = 4$ $M = 4{\cdot}4$ $\alpha = 90^\circ$

$\frac{Z}{d} = 8$ $M = 8{\cdot}8$ $\alpha = 90^\circ$

$\frac{Z}{d} = 2$ $M = 2{\cdot}2$ $\alpha = 60^\circ$

$\frac{Z}{d} = 4$ $M = 4{\cdot}4$ $\alpha = 60^\circ$

$\frac{Z}{d} = 8$ $M = 8{\cdot}8$ $\alpha = 60^\circ$

$\frac{Z}{d} = 2$ $M = 2{\cdot}2$ $\alpha = 45^\circ$

$\frac{Z}{d} = 4$ $M = 4{\cdot}4$ $\alpha = 45^\circ$

$\frac{Z}{d} = 8$ $M = 8{\cdot}8$ $\alpha = 45^\circ$

FIG. 7.20. EFFECTS OF NOZZLE TO TARGET SPACING AND JET INCLINATION ON OIL FILM PATTERNS FOR IMPINGING JETS IN CROSSFLOWING AIR STREAMS

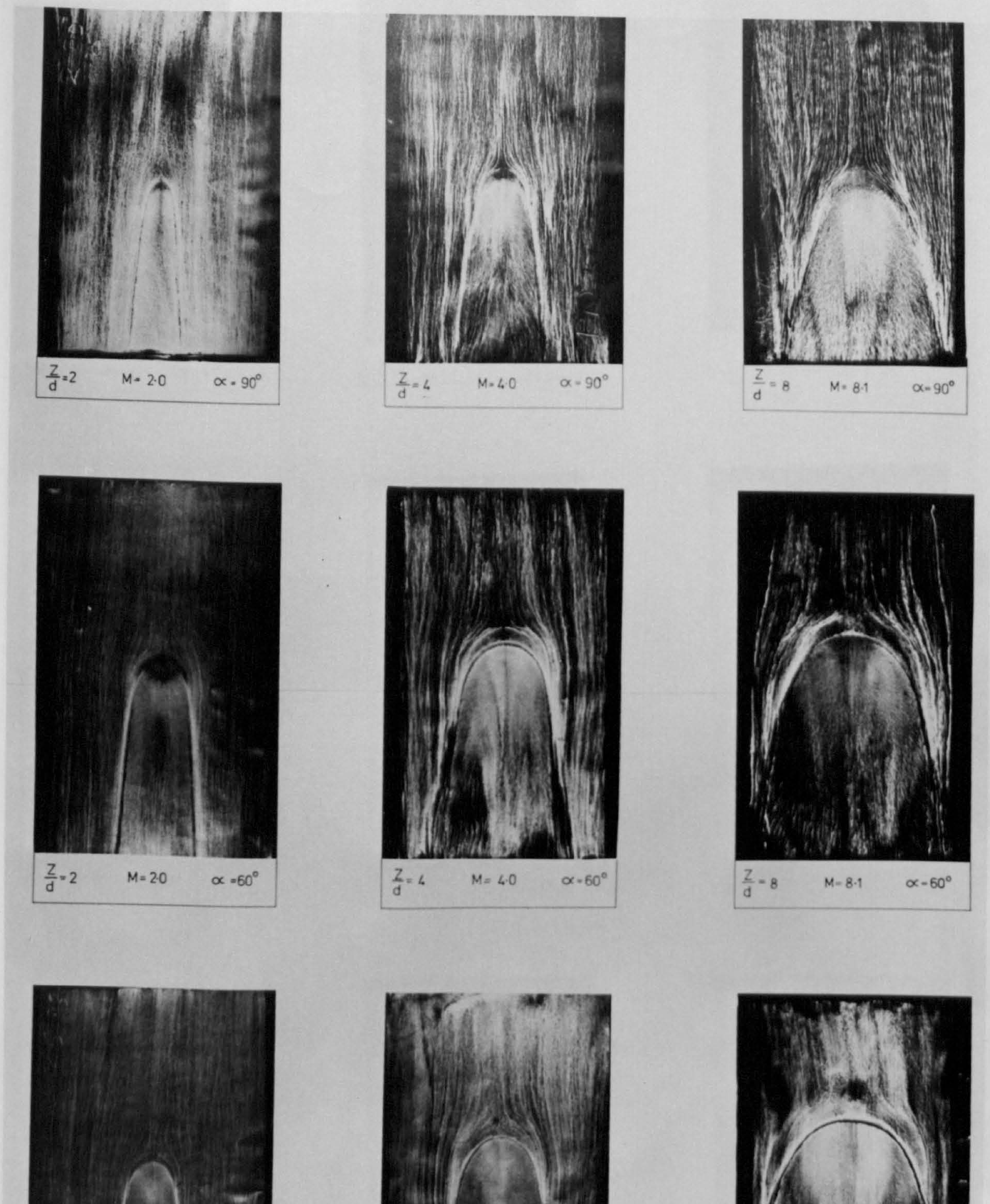

$\frac{Z}{d} = 2$ M = 2·0 α = 90°

$\frac{Z}{d} = 4$ M = 4·0 α = 90°

$\frac{Z}{d} = 8$ M = 8·1 α = 90°

$\frac{Z}{d} = 2$ M = 2·0 α = 60°

$\frac{Z}{d} = 4$ M = 4·0 α = 60°

$\frac{Z}{d} = 8$ M = 8·1 α = 60°

$\frac{Z}{d} = 2$ M = 2·0 α = 45°

$\frac{Z}{d} = 4$ M = 4·0 α = 45°

$\frac{Z}{d} = 8$ M = 8·1 α = 45°

FIG. 7.21. EFFECTS OF NOZZLE TO TARGET SPACING AND JET INCLINATION ON OIL FILM PATTERNS FOR IMPINGING JETS IN CROSSFLOWING AIR STREAMS

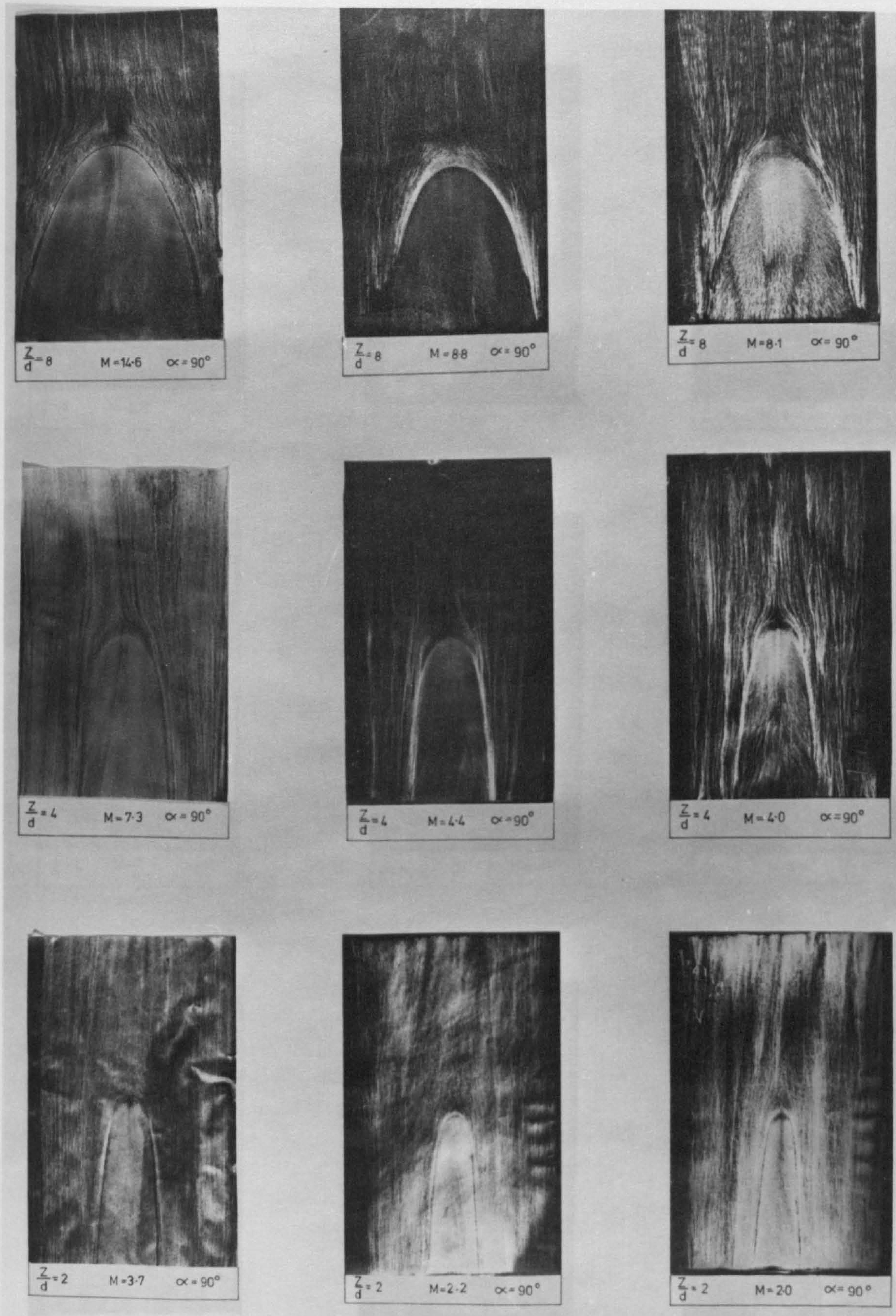

$\frac{Z}{d} = 8$ M = 14·6 ∝ = 90°

$\frac{Z}{d} = 8$ M = 8·8 ∝ = 90°

$\frac{Z}{d} = 8$ M = 8·1 ∝ = 90°

$\frac{Z}{d} = 4$ M = 7·3 ∝ = 90°

$\frac{Z}{d} = 4$ M = 4·4 ∝ = 90°

$\frac{Z}{d} = 4$ M = 4·0 ∝ = 90°

$\frac{Z}{d} = 2$ M = 3·7 ∝ = 90°

$\frac{Z}{d} = 2$ M = 2·2 ∝ = 90°

$\frac{Z}{d} = 2$ M = 2·0 ∝ = 90°

FIG. 7.22. EFFECTS OF MASS VELOCITY RATIOS AND NOZZLE TO TARGET SPACING ON SURFACE FLOW PATTERNS ASSOCIATED WITH IMPINGING JETS IN CROSSFLOWS

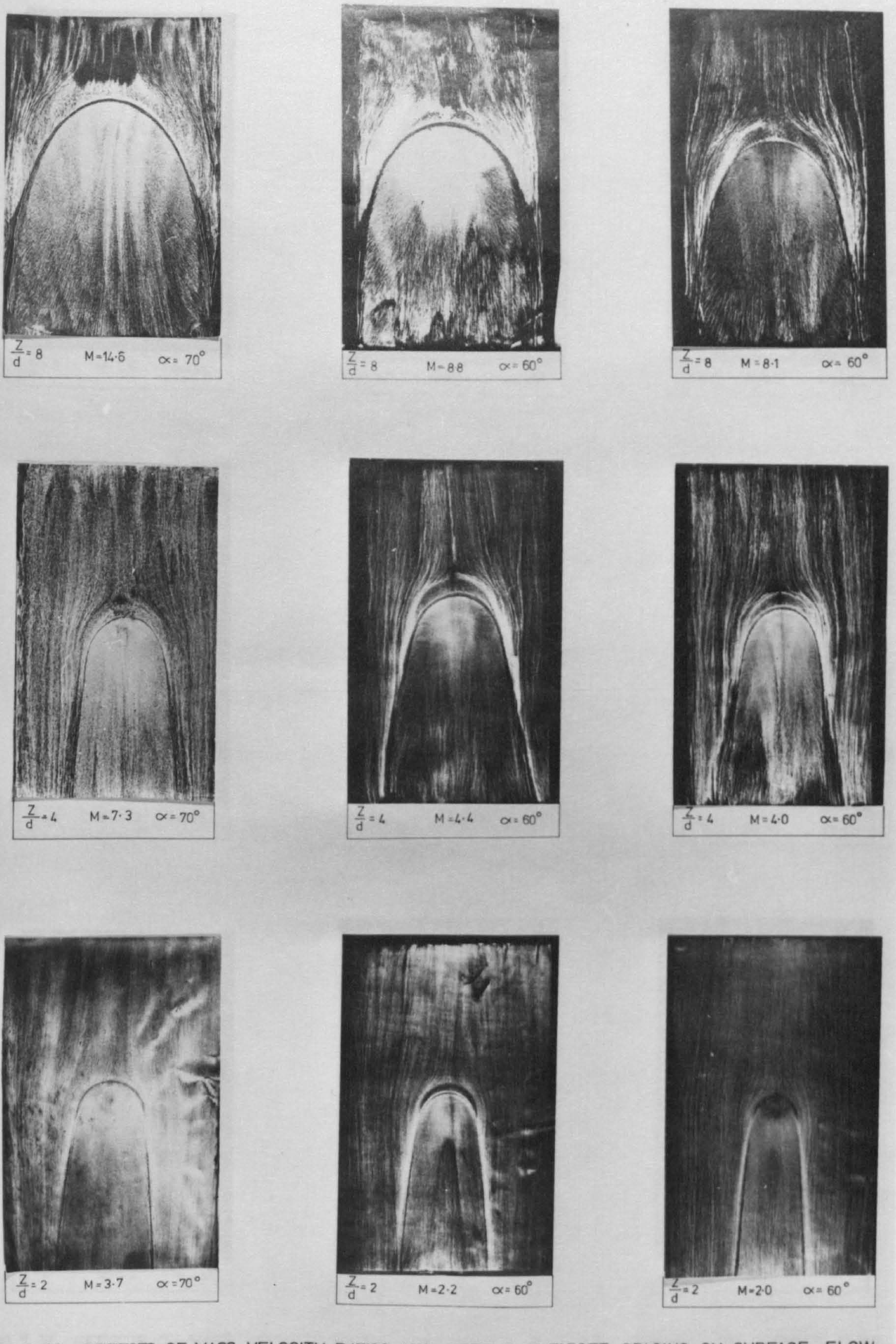

$\frac{Z}{d} = 8$ M = 14·6 $\alpha = 70°$

$\frac{Z}{d} = 8$ M = 8·8 $\alpha = 60°$

$\frac{Z}{d} = 8$ M = 8·1 $\alpha = 60°$

$\frac{Z}{d} = 4$ M = 7·3 $\alpha = 70°$

$\frac{Z}{d} = 4$ M = 4·4 $\alpha = 60°$

$\frac{Z}{d} = 4$ M = 4·0 $\alpha = 60°$

$\frac{Z}{d} = 2$ M = 3·7 $\alpha = 70°$

$\frac{Z}{d} = 2$ M = 2·2 $\alpha = 60°$

$\frac{Z}{d} = 2$ M = 2·0 $\alpha = 60°$

FIG. 7. 23. EFFECTS OF MASS VELOCITY RATIOS AND NOZZLE TO TARGET SPACING ON SURFACE FLOW PATTERNS ASSOCIATED WITH IMPINGING JETS IN CROSSFLOWS

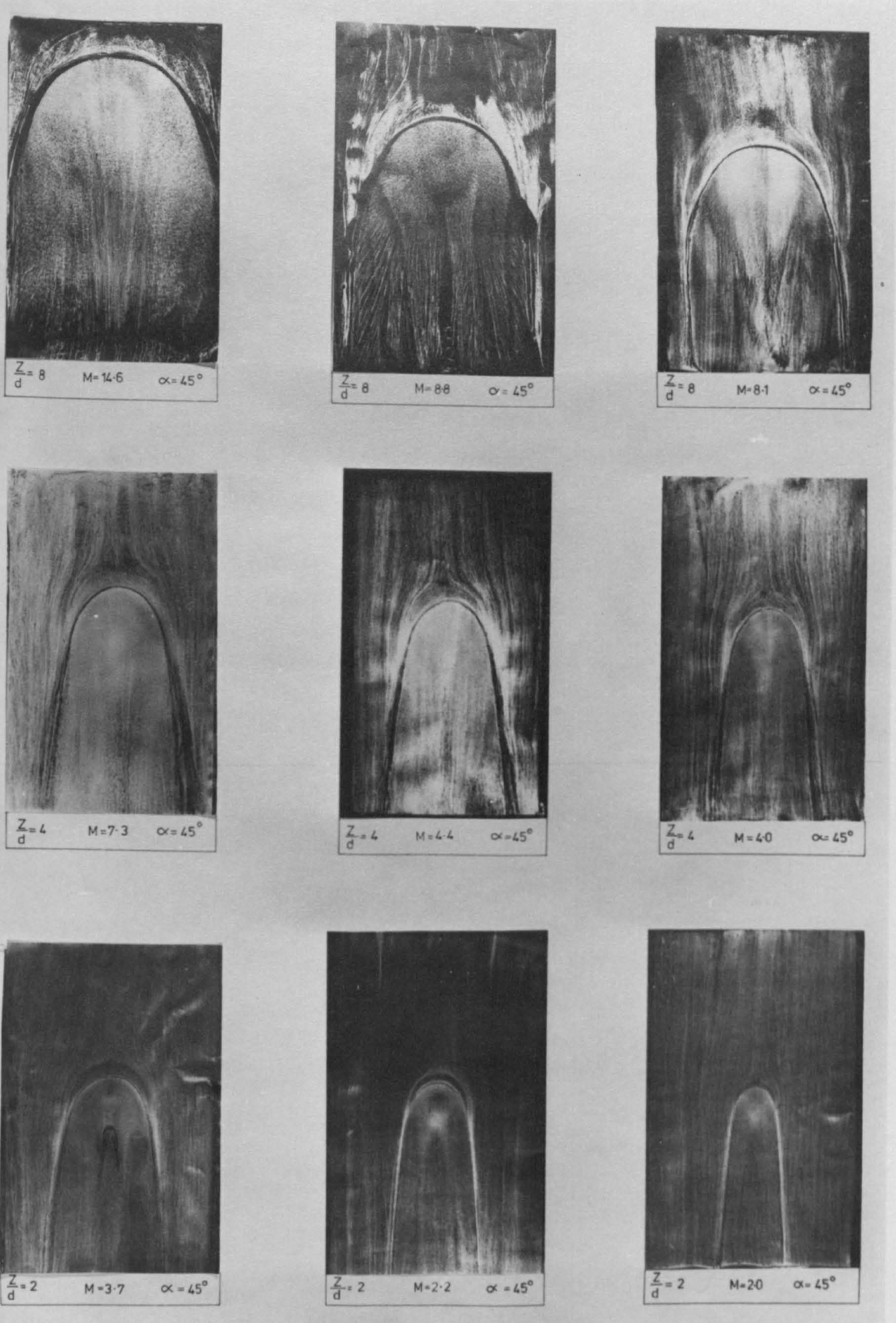

$\frac{Z}{d}=8$ $M=14{\cdot}6$ $\alpha=45^\circ$

$\frac{Z}{d}=8$ $M=8{\cdot}8$ $\alpha=45^\circ$

$\frac{Z}{d}=8$ $M=8{\cdot}1$ $\alpha=45^\circ$

$\frac{Z}{d}=4$ $M=7{\cdot}3$ $\alpha=45^\circ$

$\frac{Z}{d}=4$ $M=4{\cdot}4$ $\alpha=45^\circ$

$\frac{Z}{d}=4$ $M=4{\cdot}0$ $\alpha=45^\circ$

$\frac{Z}{d}=2$ $M=3{\cdot}7$ $\alpha=45^\circ$

$\frac{Z}{d}=2$ $M=2{\cdot}2$ $\alpha=45^\circ$

$\frac{Z}{d}=2$ $M=2{\cdot}0$ $\alpha=45^\circ$

FIG. 7. 24. EFFECTS OF MASS VELOCITY RATIOS AND NOZZLE TO TARGET SPACING ON SURFACE FLOW PATTERNS ASSOCIATED WITH IMPINGING JETS IN CROSSFLOWS

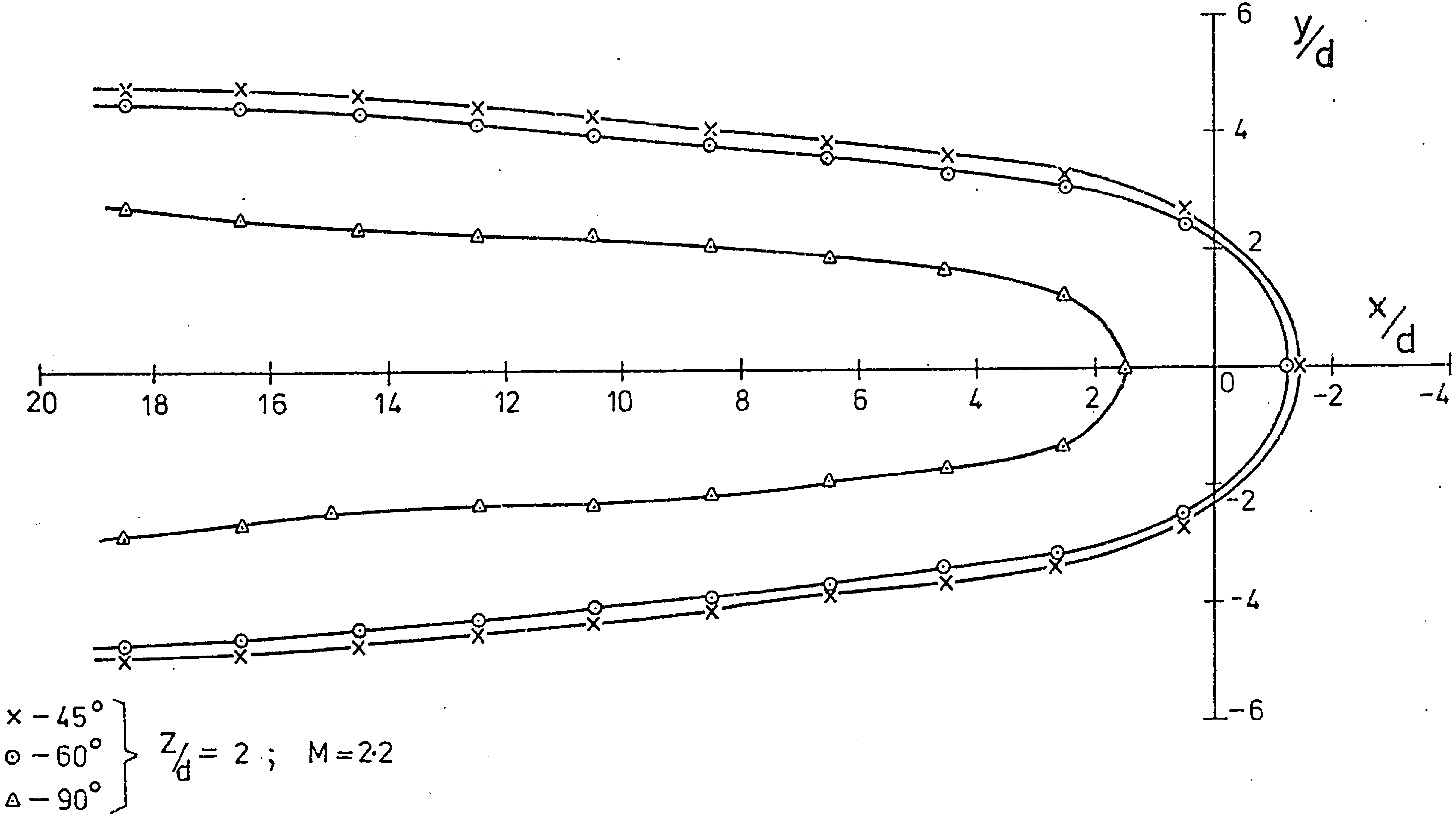

FIG. 7. 25. EFFECT OF IMPINGEMENT ANGLE ON SEPARATION LINE PROFILES FOR M=2·2

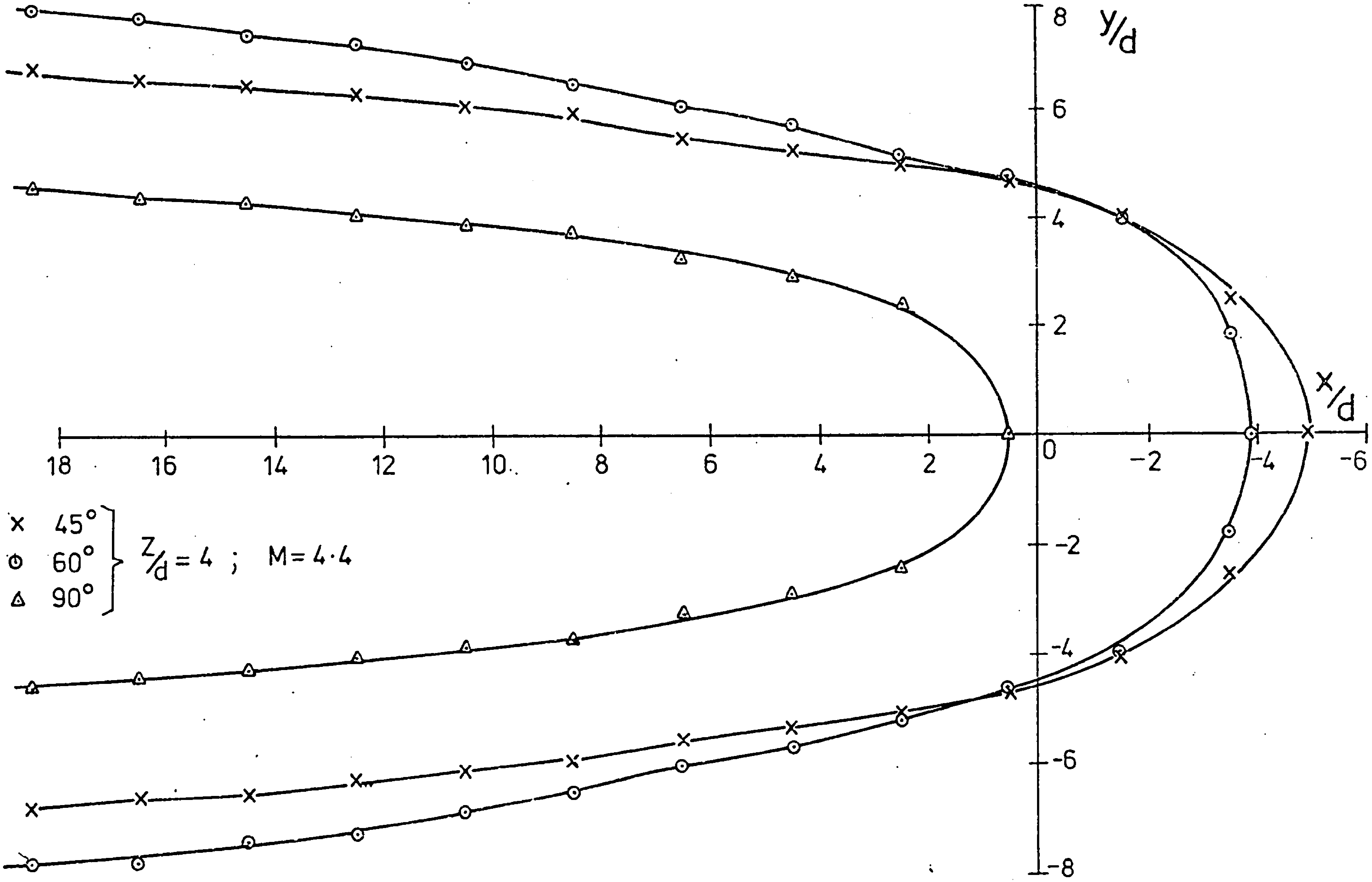

FIG. 7. 26. EFFECT OF IMPINGEMENT ANGLE ON SEPARATION LINE PROFILES FOR M= 4·4

FIG. 7. 27. EFFECT OF IMPINGEMENT ANGLE ON SEPARATION LINE PROFILES FOR M = 8·8

FIG. 7. 28. EFFECT OF IMPINGEMENT ANGLE ON SEPARATION LINE PROFILES FOR M = 14·6

FIG. 7. 29. EFFECT OF BLOWING RATE ON SEPARATION LINE PROFILES

FIG. 7.30. EFFECT OF BLOWING RATE ON SEPARATION LINE PROFILES

FIG.7.31. VELOCITY TRAVERSE AND RADIAL TURBULENCE INTENSITY PROFILES

FIG. 7.32. VELOCITY TRAVERSE AND RADIAL TURBULENCE INTENSITY PROFILES

FIG. 7.33. VELOCITY TRAVERSE AND RADIAL TURBULENCE INTENSITY PROFILES

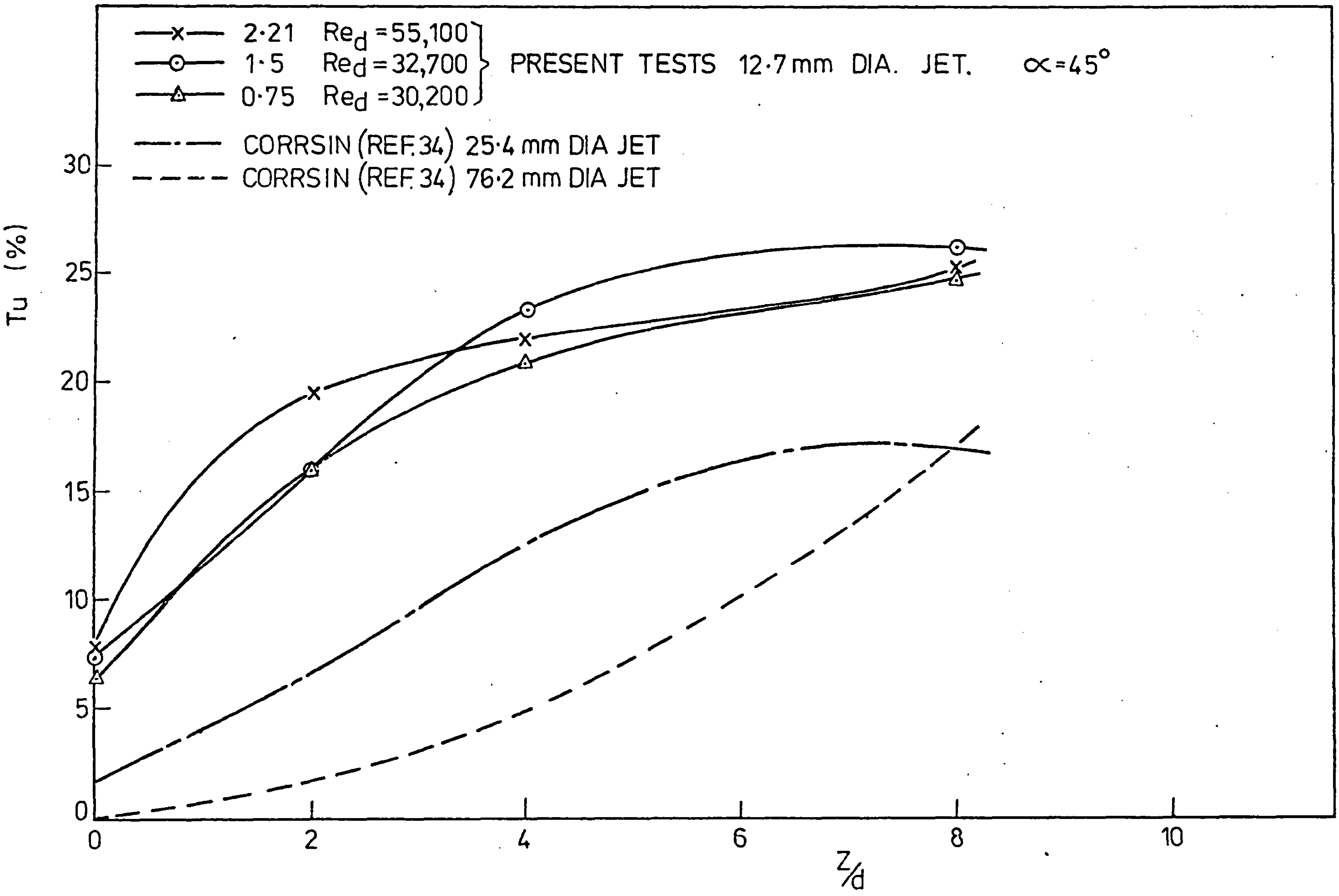

FIG. 7.34. AXIAL TURBULENCE VARIATION – COMPARISON WITH PREVIOUS STUDIES

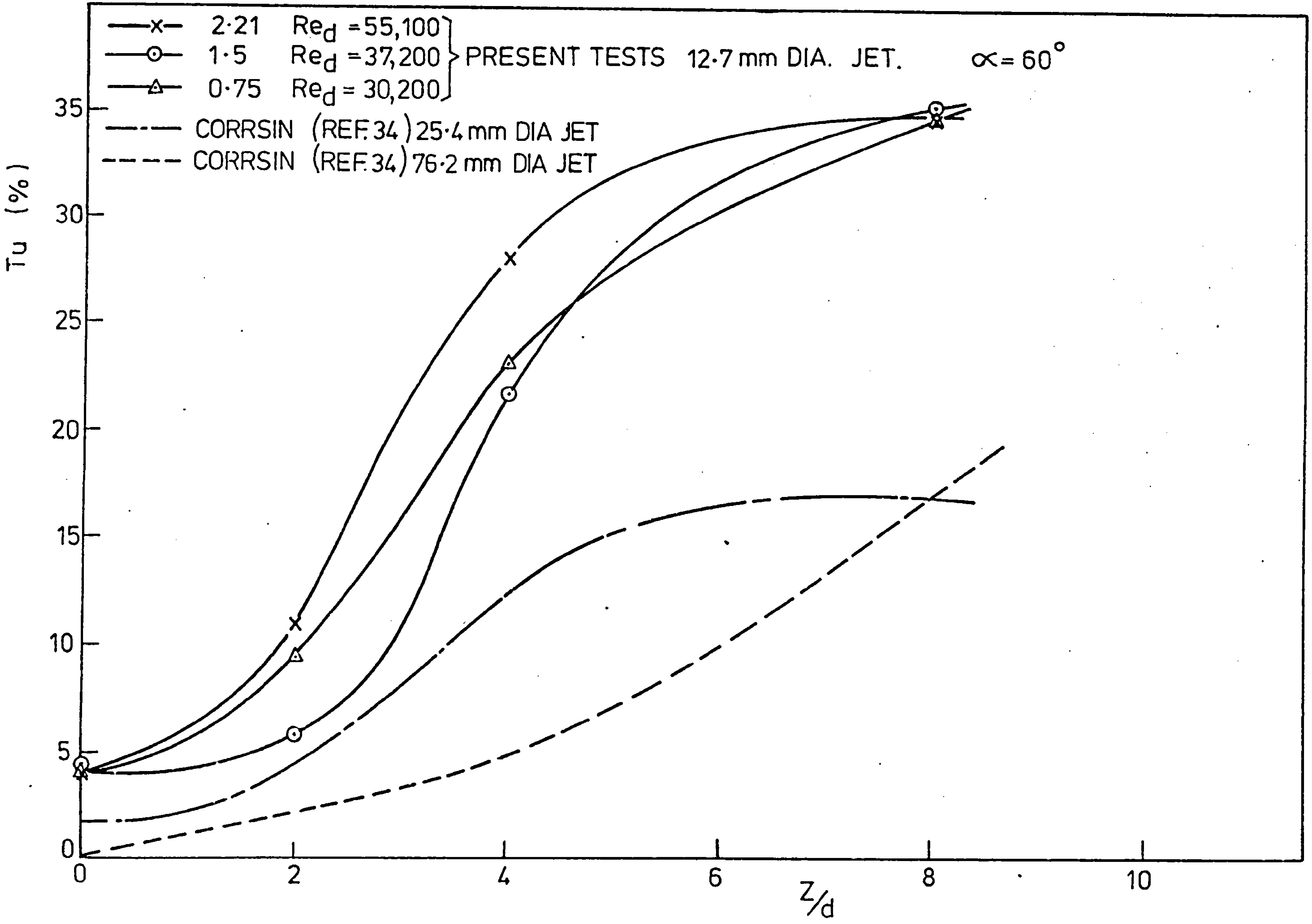

FIG. 7.35. AXIAL TURBULENCE VARIATION - COMPARISON WITH PREVIOUS STUDIES

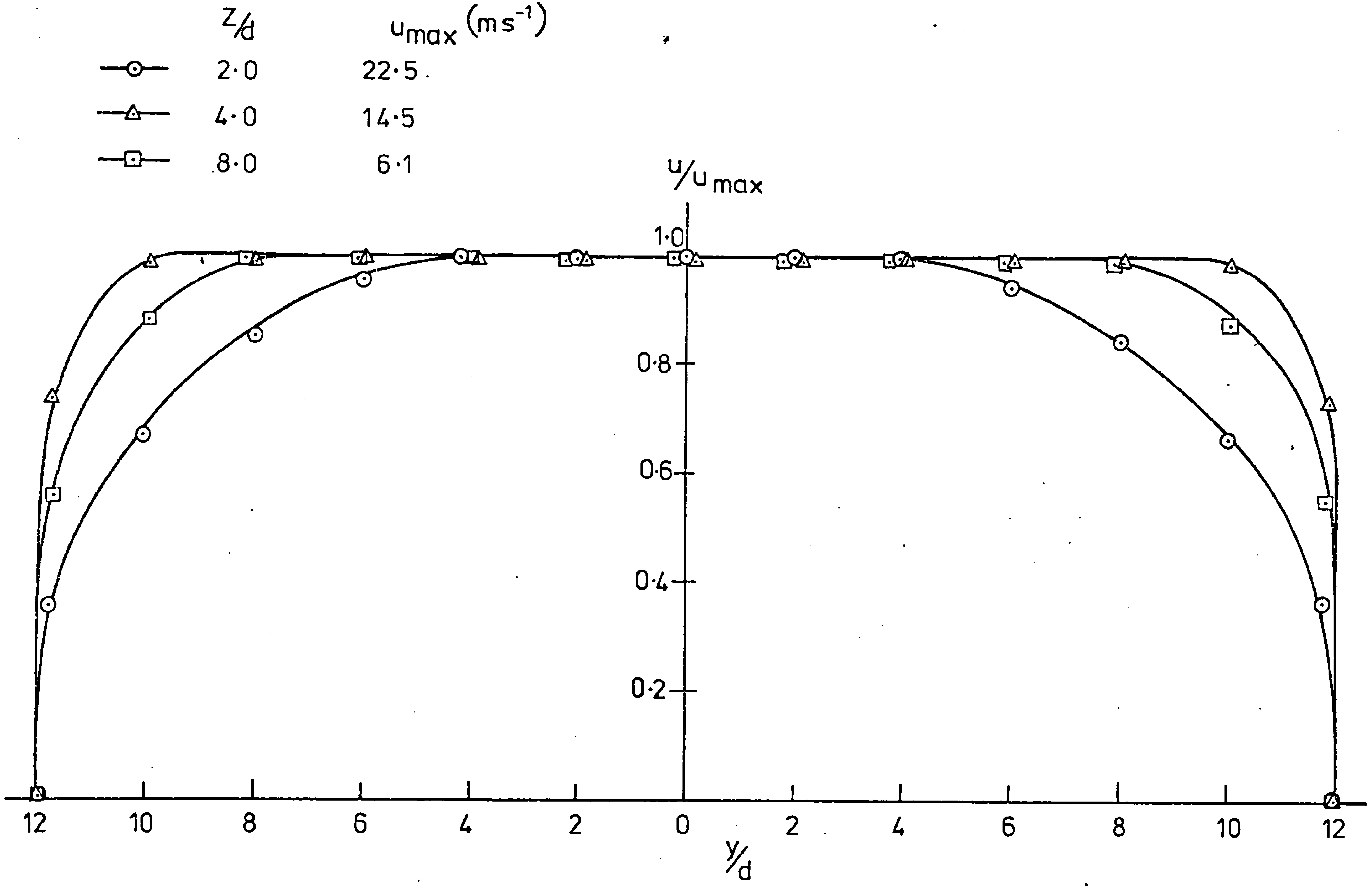

FIG.7.36. CROSSFLOW TRAVERSE VELOCITY PROFILES $(x/d = -20)$

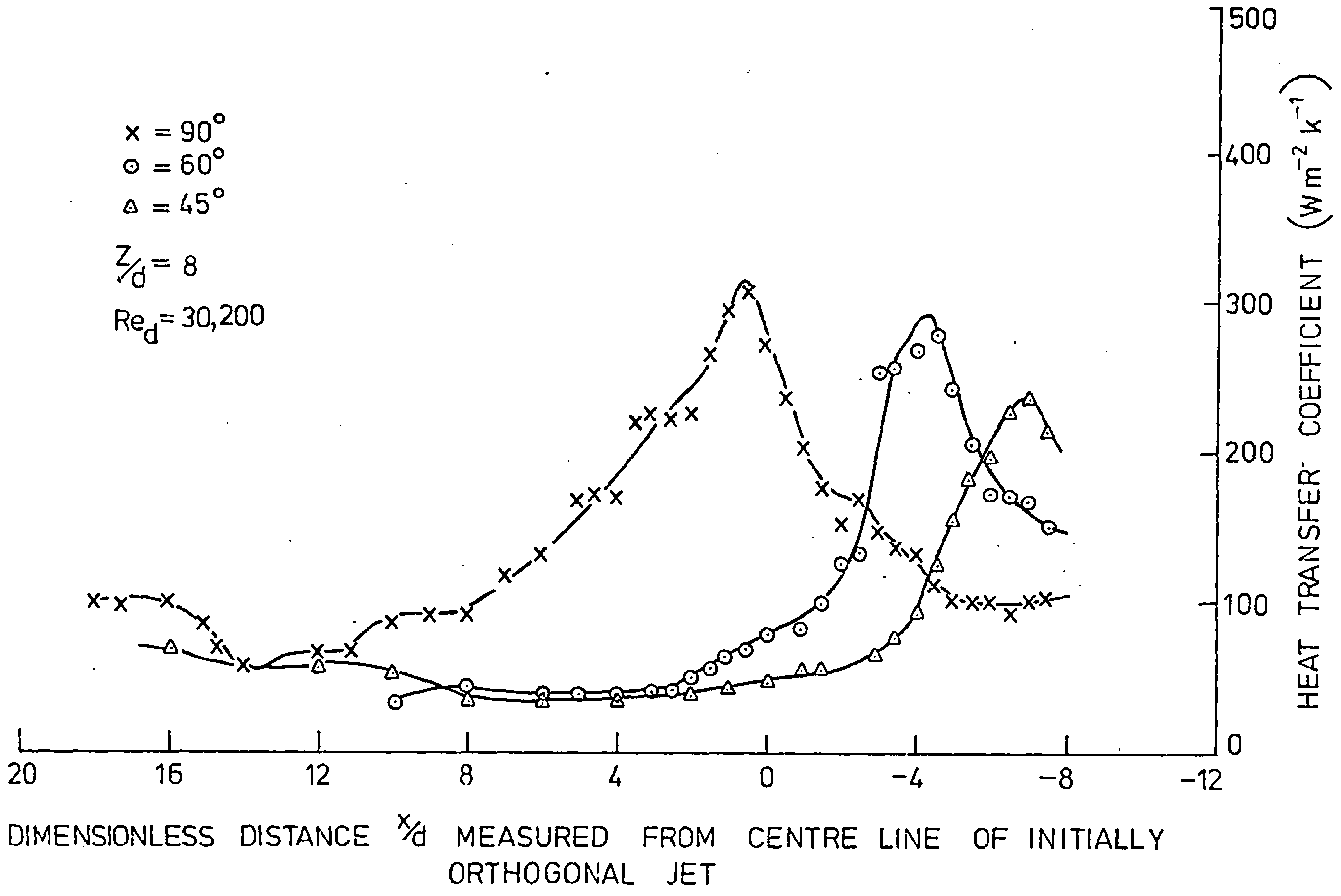

FIG.7.37 EFFECT OF INCLINATION ON AXIAL VARIATION OF HEAT TRANSFER $(Y/d = 0)$
IN THE ABSENCE OF CROSSFLOW

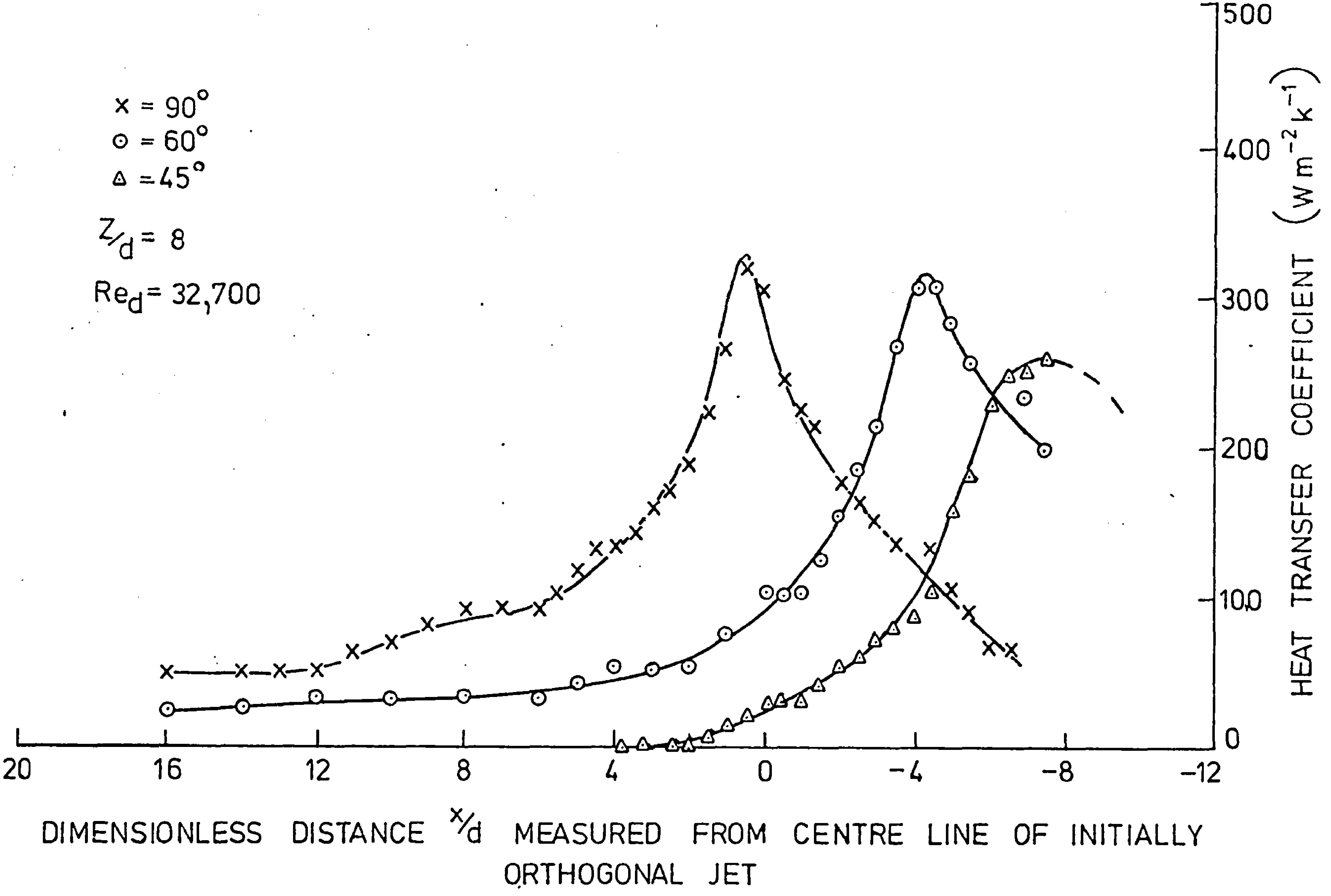

FIG.7.38 EFFECT OF INCLINATION ON AXIAL VARIATION OF HEAT TRANSFER ($y/d = 0$) IN THE ABSENCE OF CROSSFLOW

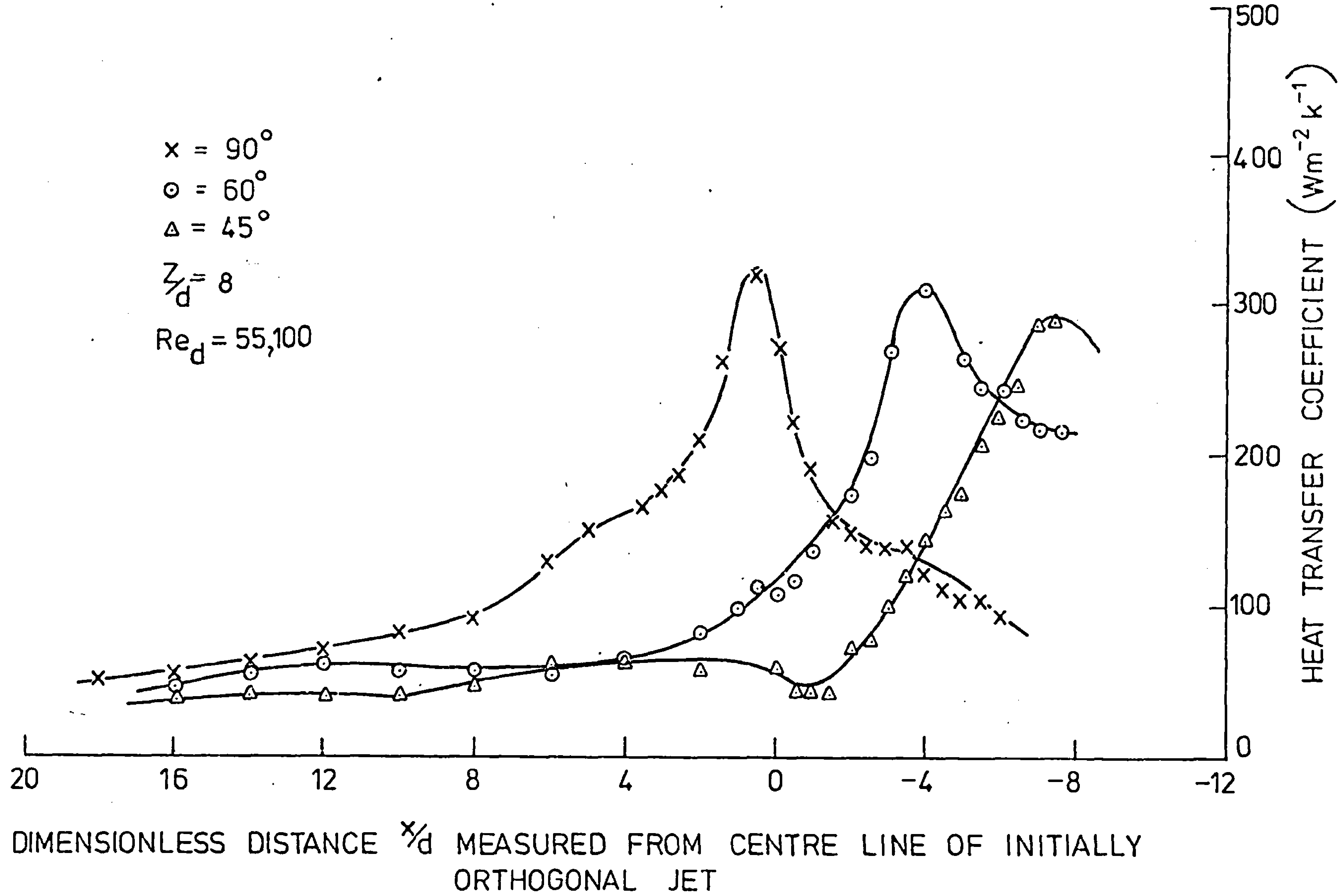

FIG.7.39. EFFECT OF INCLINATION ON AXIAL VARIATION OF HEAT TRANSFER $(y/d = 0)$ IN THE ABSENCE OF CROSSFLOW

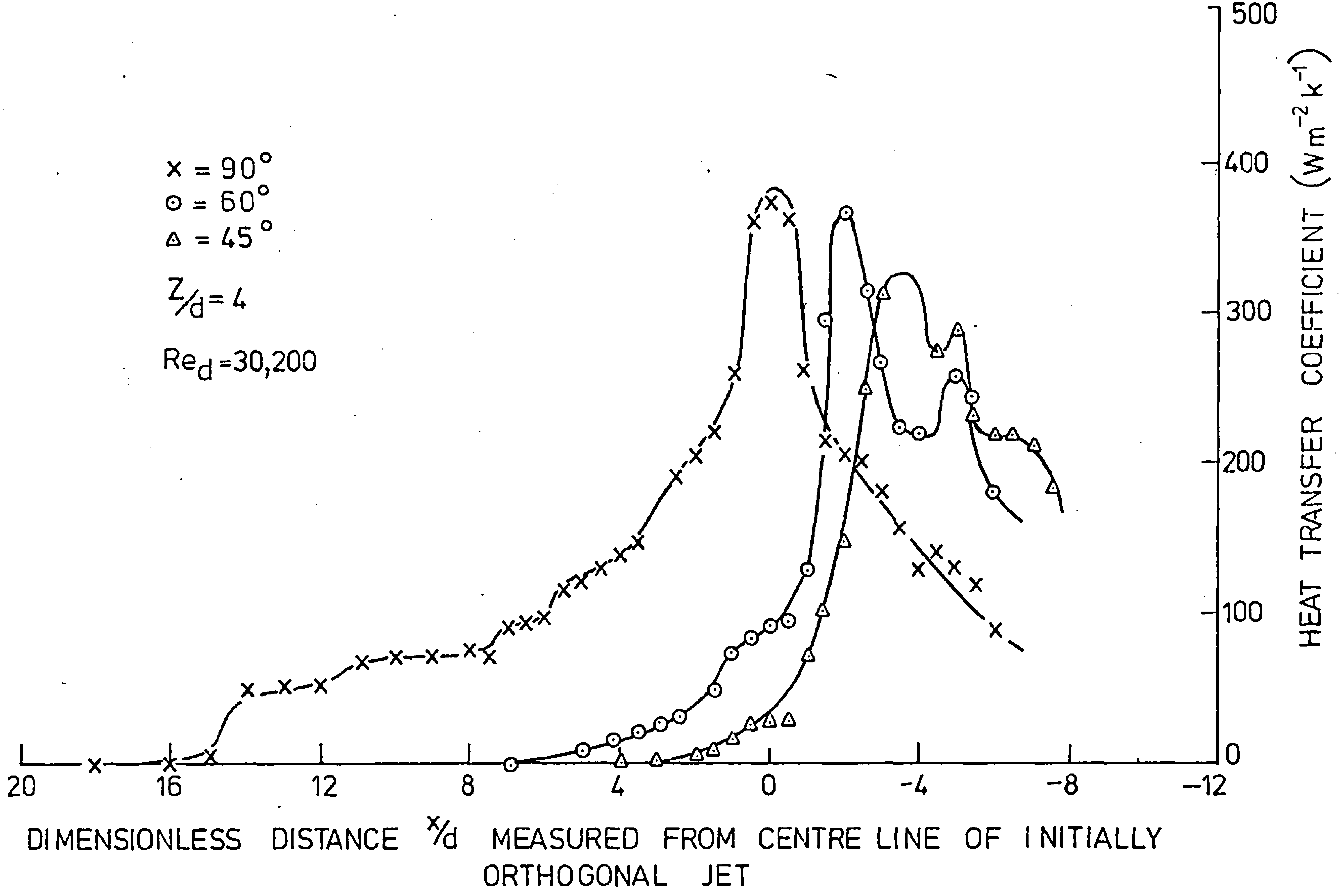

FIG.7.40. EFFECT OF INCLINATION ON AXIAL VARIATION OF HEAT TRANSFER $(y/d = 0)$ IN THE ABSENCE OF CROSSFLOW

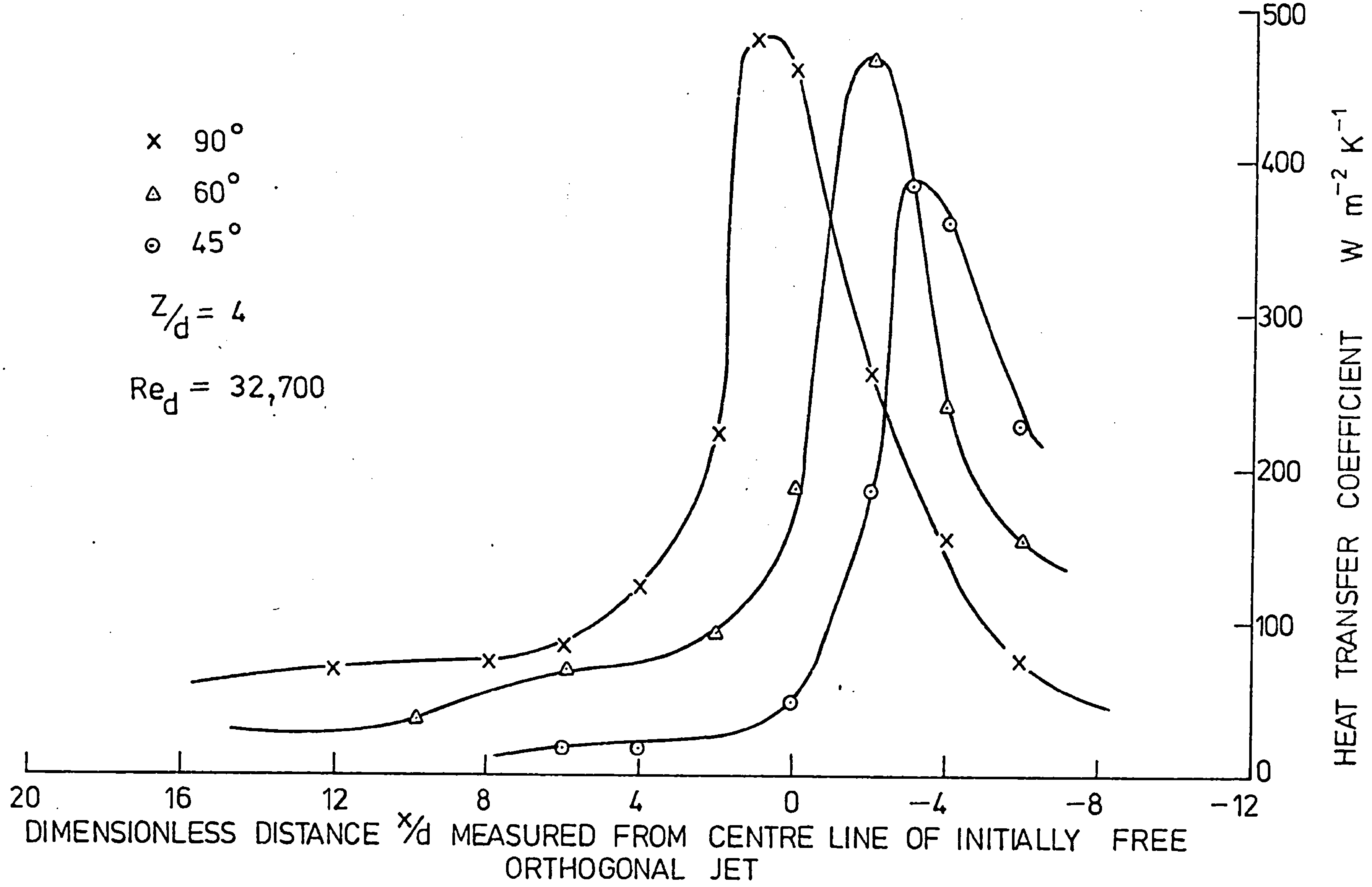

FIG. 7. 41. EFFECT OF INCLINATION ON AXIAL VARIATION OF HEAT TRANSFER $(Y/d = 0)$ IN THE ABSENCE OF CROSSFLOW

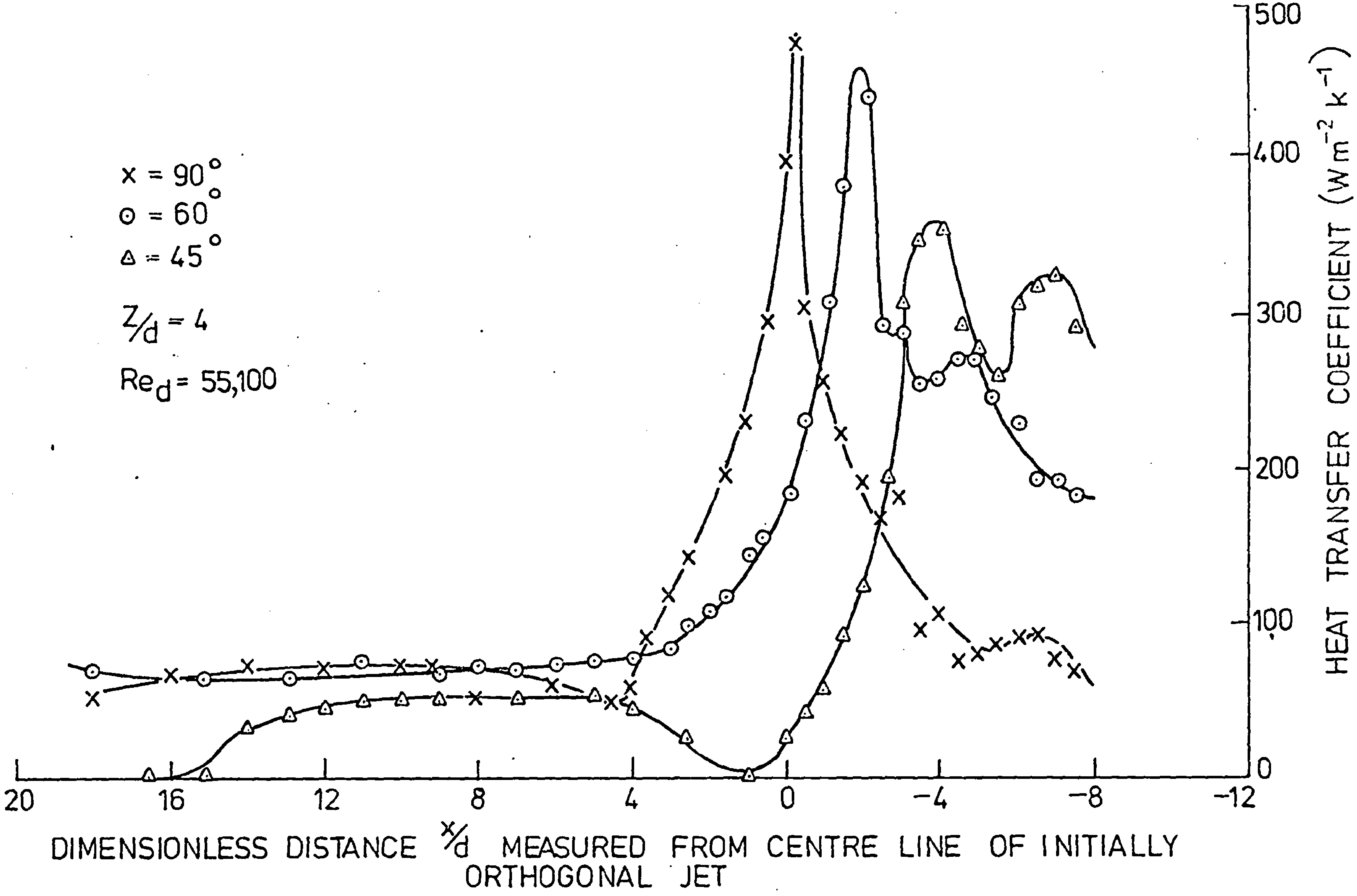

FIG.7.42. EFFECT OF INCLINATION ON AXIAL VARIATION OF HEAT TRANSFER ($y/d = 0$) IN THE ABSENCE OF CROSSFLOW

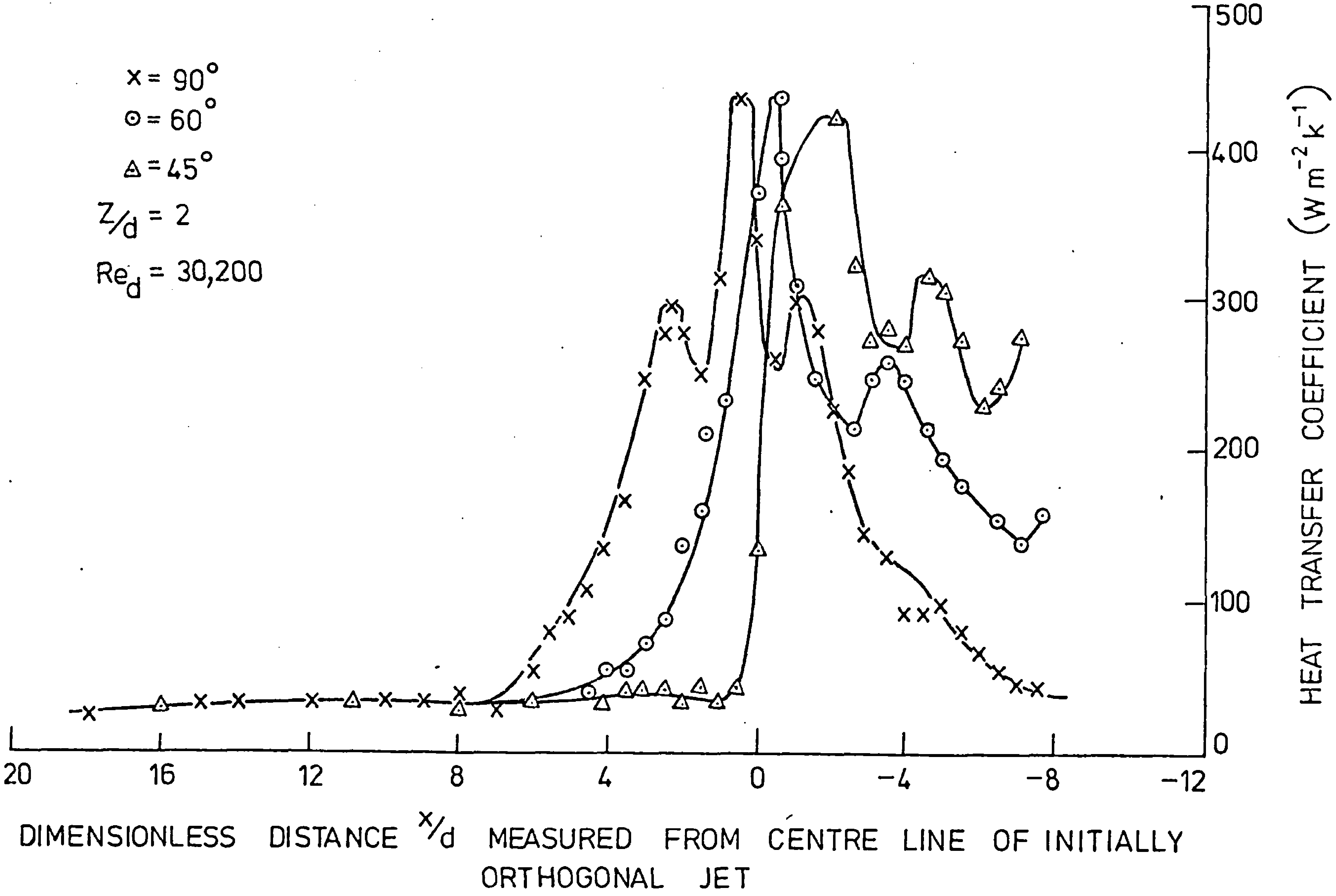

FIG.7.43. EFFECT OF INCLINATION ON AXIAL VARIATION OF HEAT TRANSFER $(y/d = 0)$ IN THE ABSENCE OF CROSSFLOW

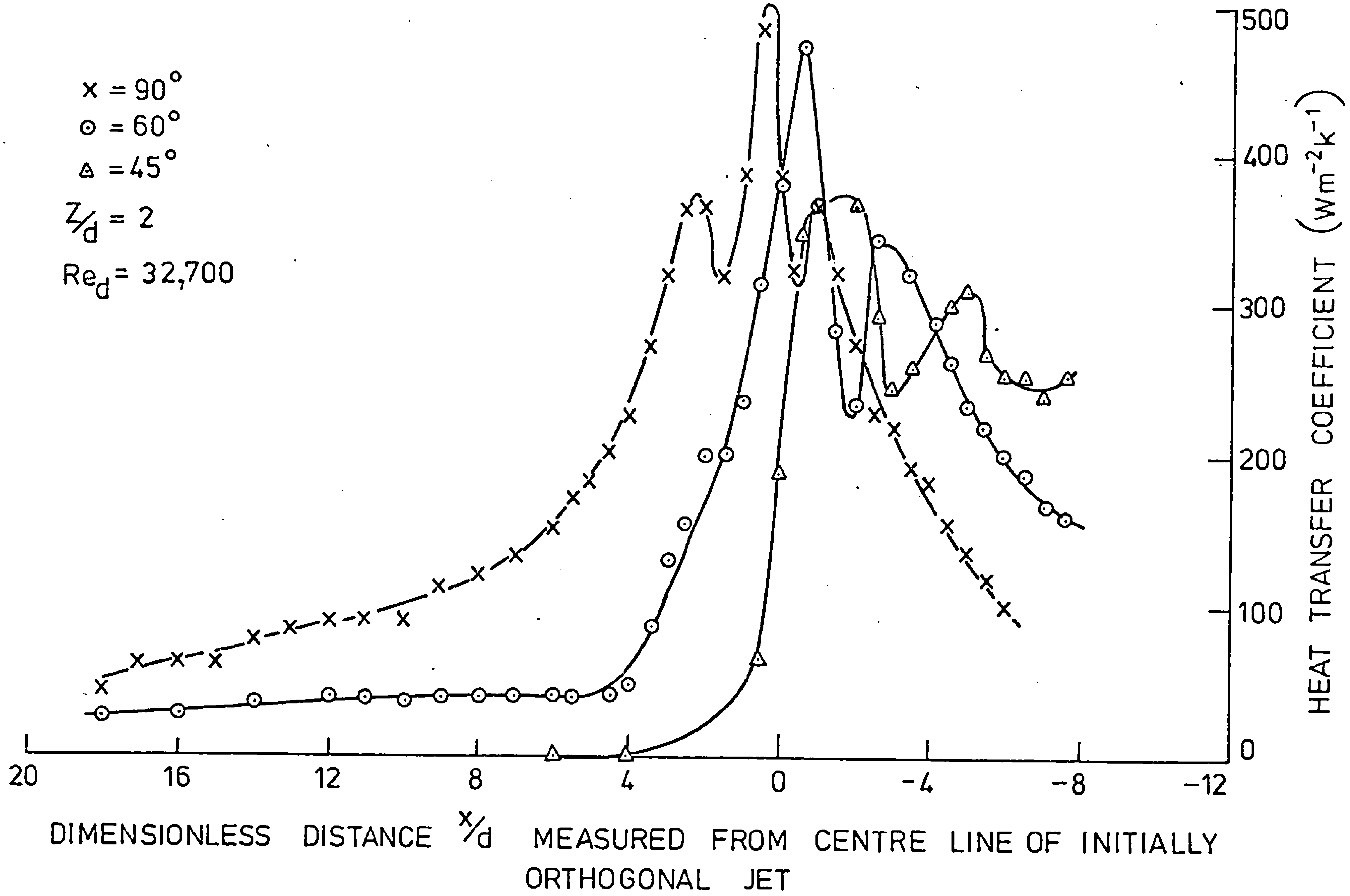

FIG.7.44. EFFECT OF INCLINATION ON AXIAL VARIATION OF HEAT TRANSFER $(y/d = 0)$ IN THE ABSENCE OF CROSSFLOW

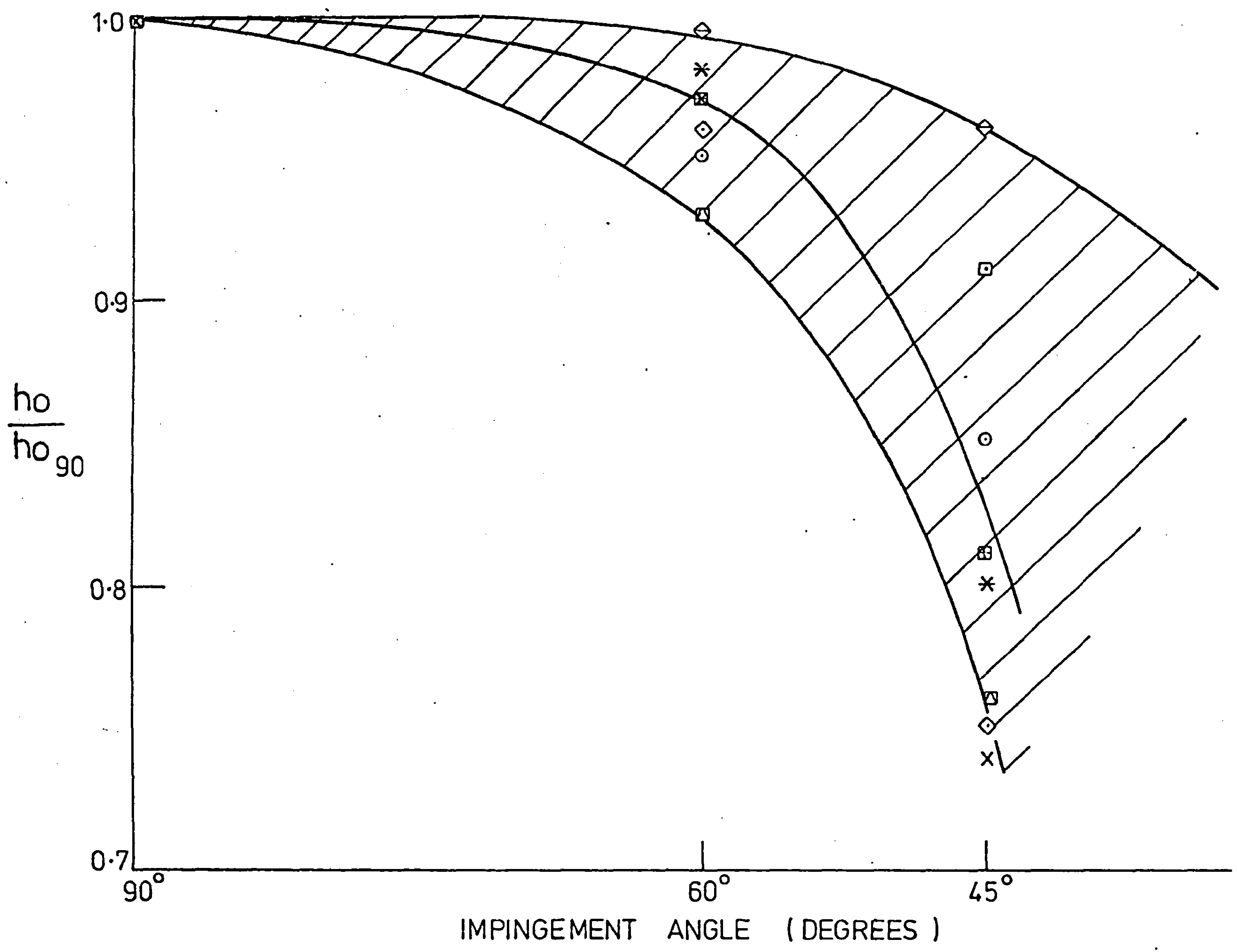

FIG. 7. 45. EFFECT OF IMPINGEMENT ANGLE ON DIMENSIONLESS STAGNATION POINT HEAT TRANSFERS

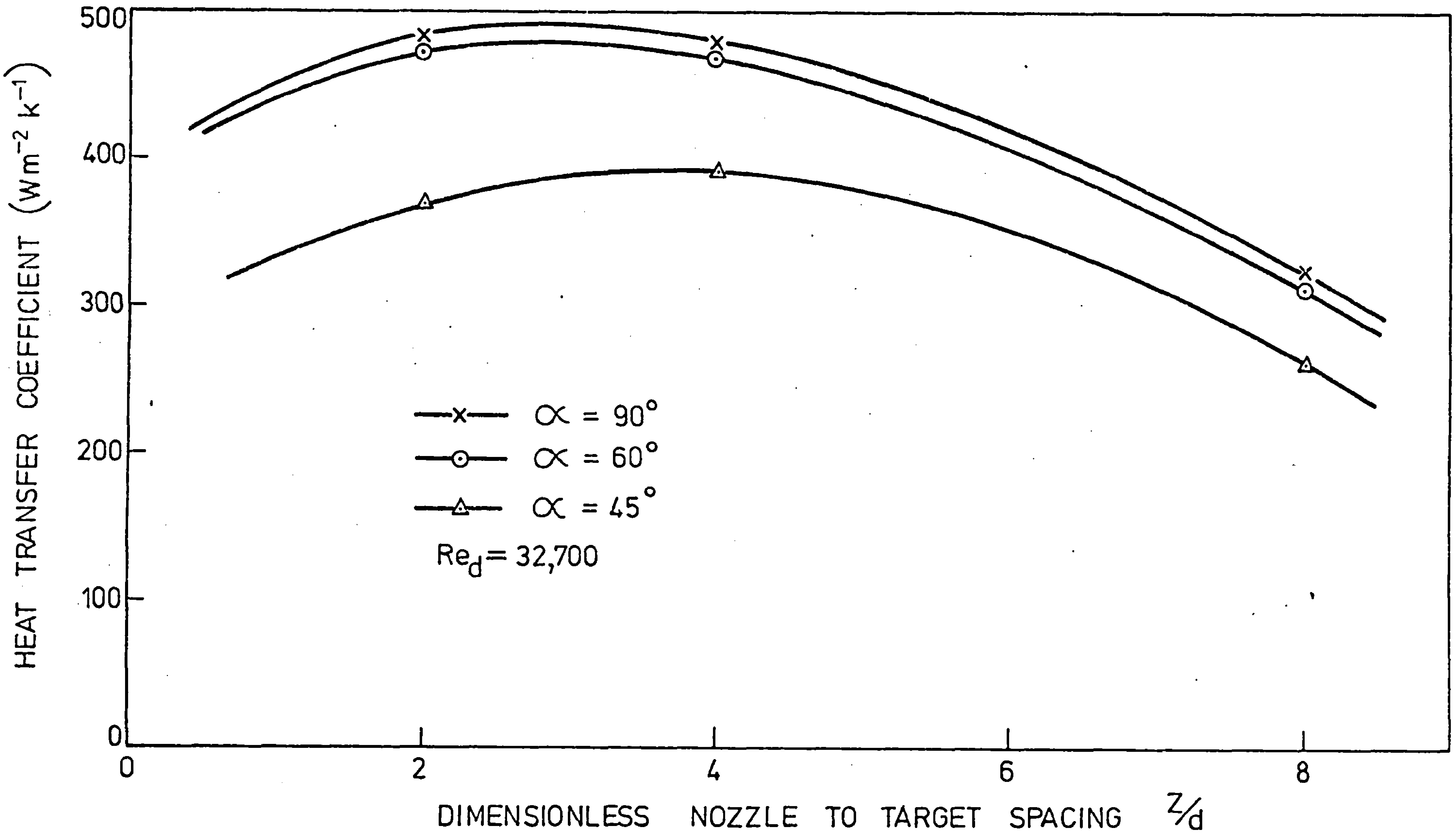

FIG. 7.46. EFFECTS OF NOZZLE TO TARGET SPACING AND JET INCLINATION ON STAGNATION POINT HEAT TRANSFER

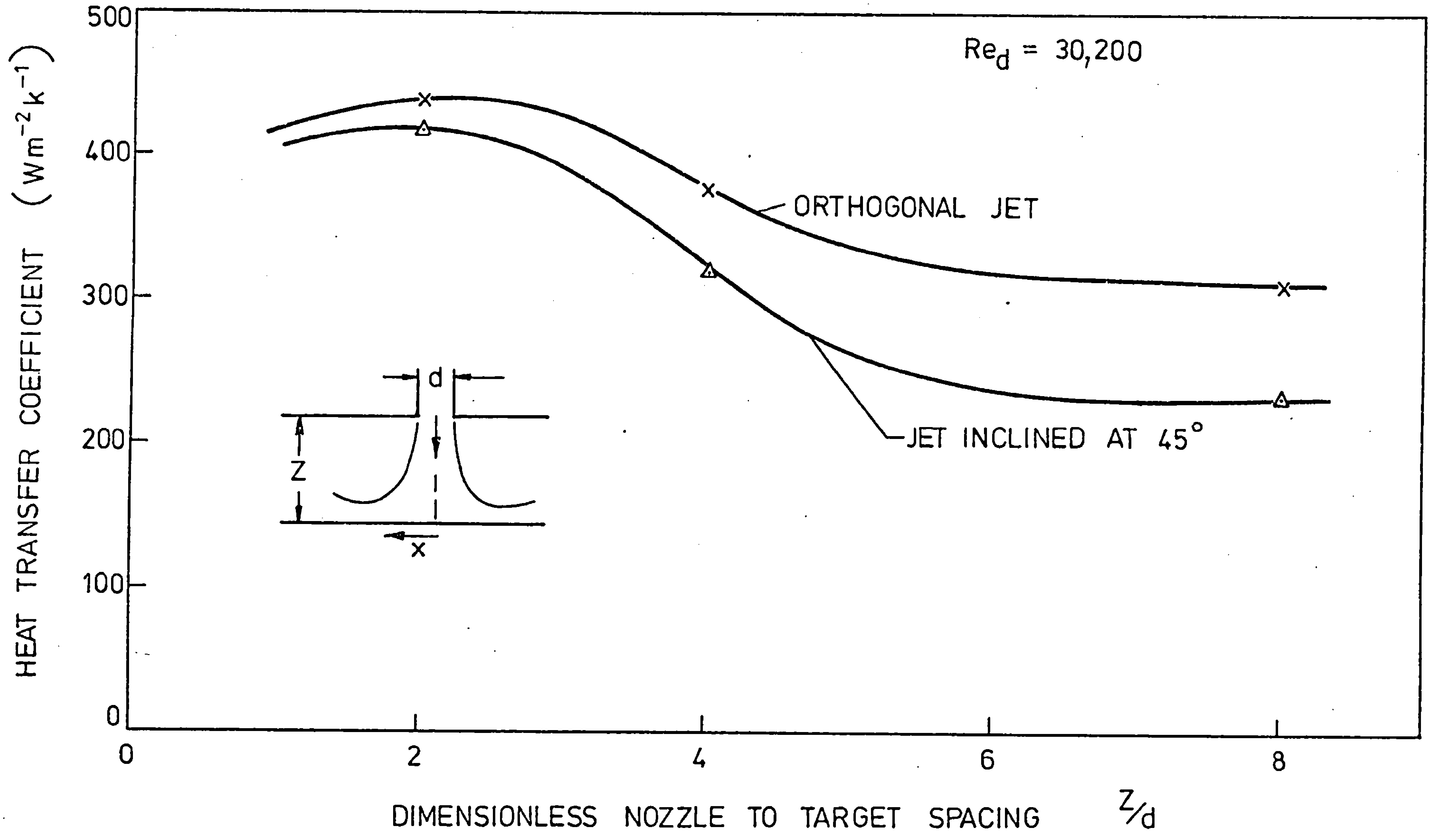

FIG.7.47. EFFECTS OF NOZZLE TO TARGET SPACING AND JET INCLINATION ON STAGNATION POINT HEAT TRANSFER

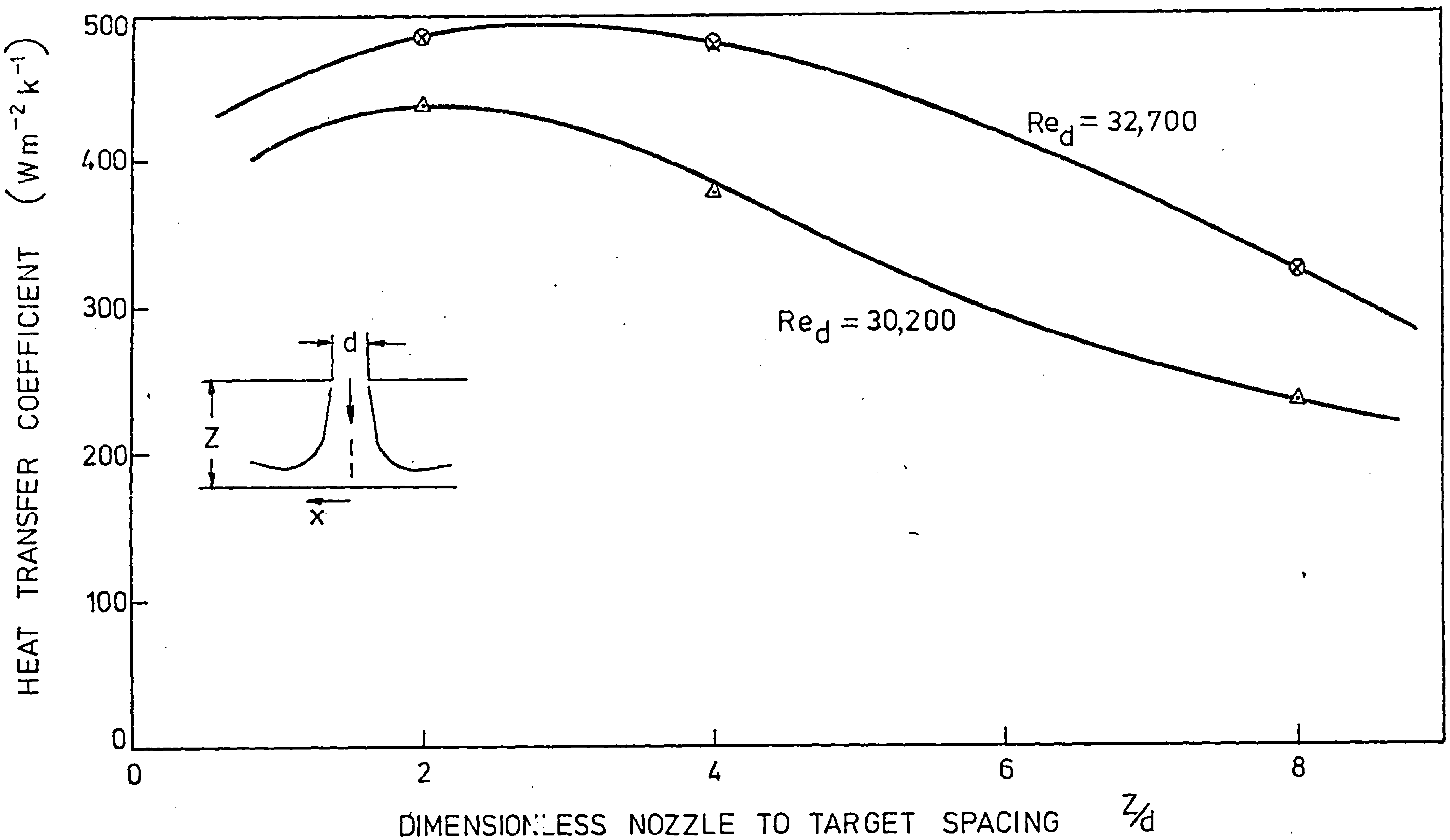

FIG.7.48. EFFECT OF REYNOLDS NUMBER AND NOZZLE TO TARGET SPACING ON STAGNATION POINT HEAT TRANSFER

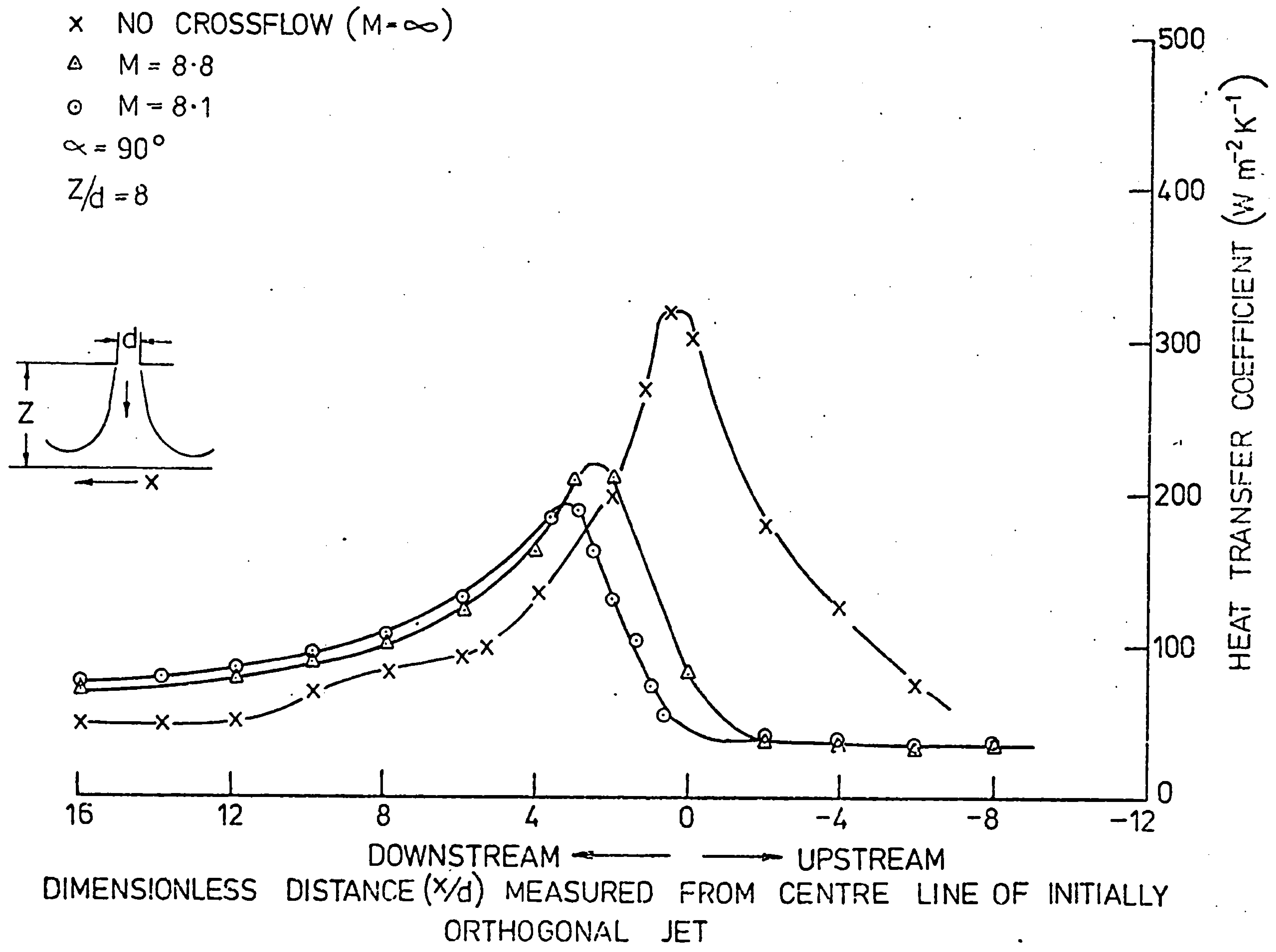

FIG. 7.49. EFFECT OF CROSSFLOWS ON JET IMPINGEMENT HEAT TRANSFERS (ORTHOGONAL JETS AT $Z/d=8$)

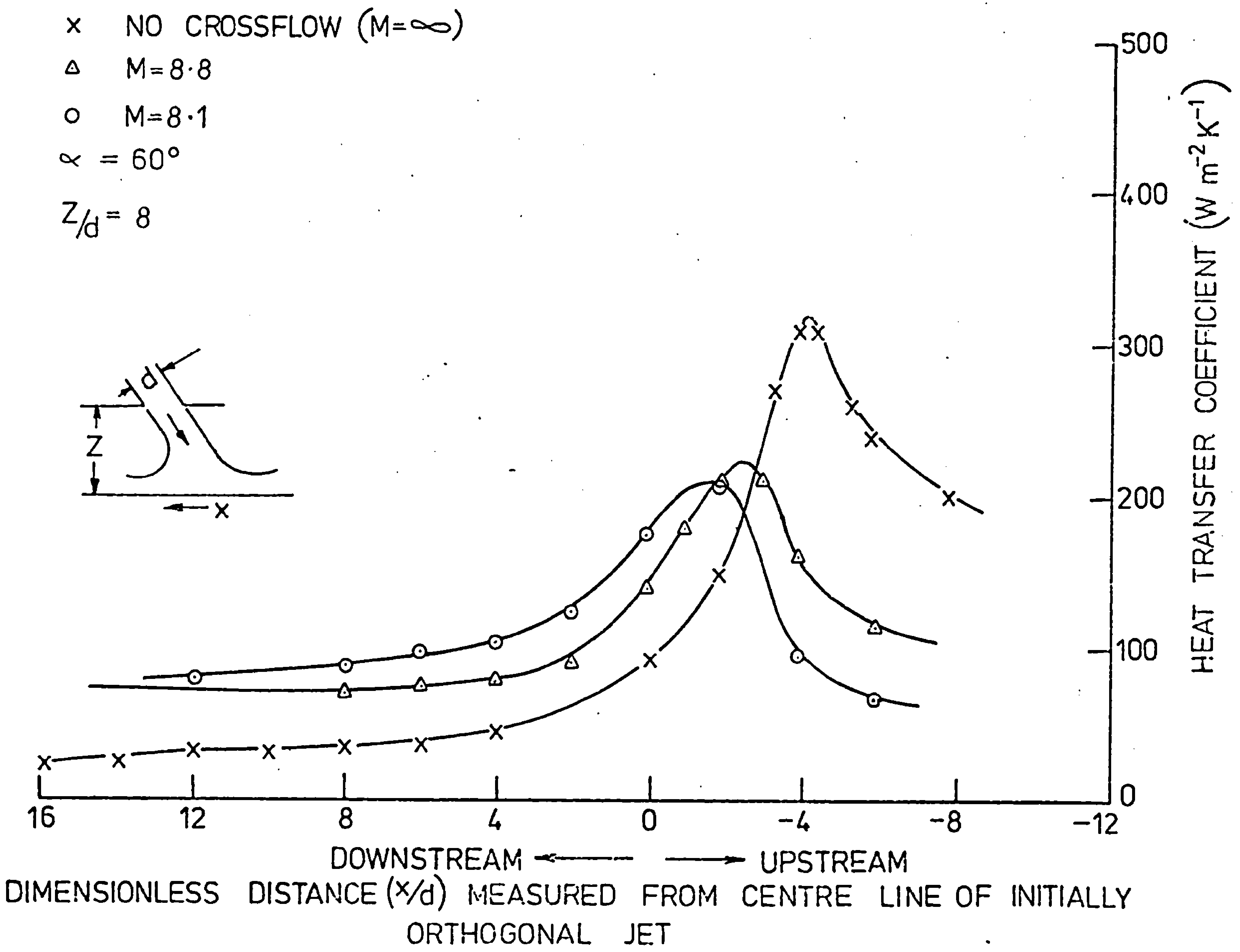

FIG. 7.50. EFFECT OF CROSSFLOWS ON JET IMPINGEMENT HEAT TRANSFERS (JETS IN CLINED AT 60° TOWARDS CROSSFLOW DIRECTION; Z/d = 8)

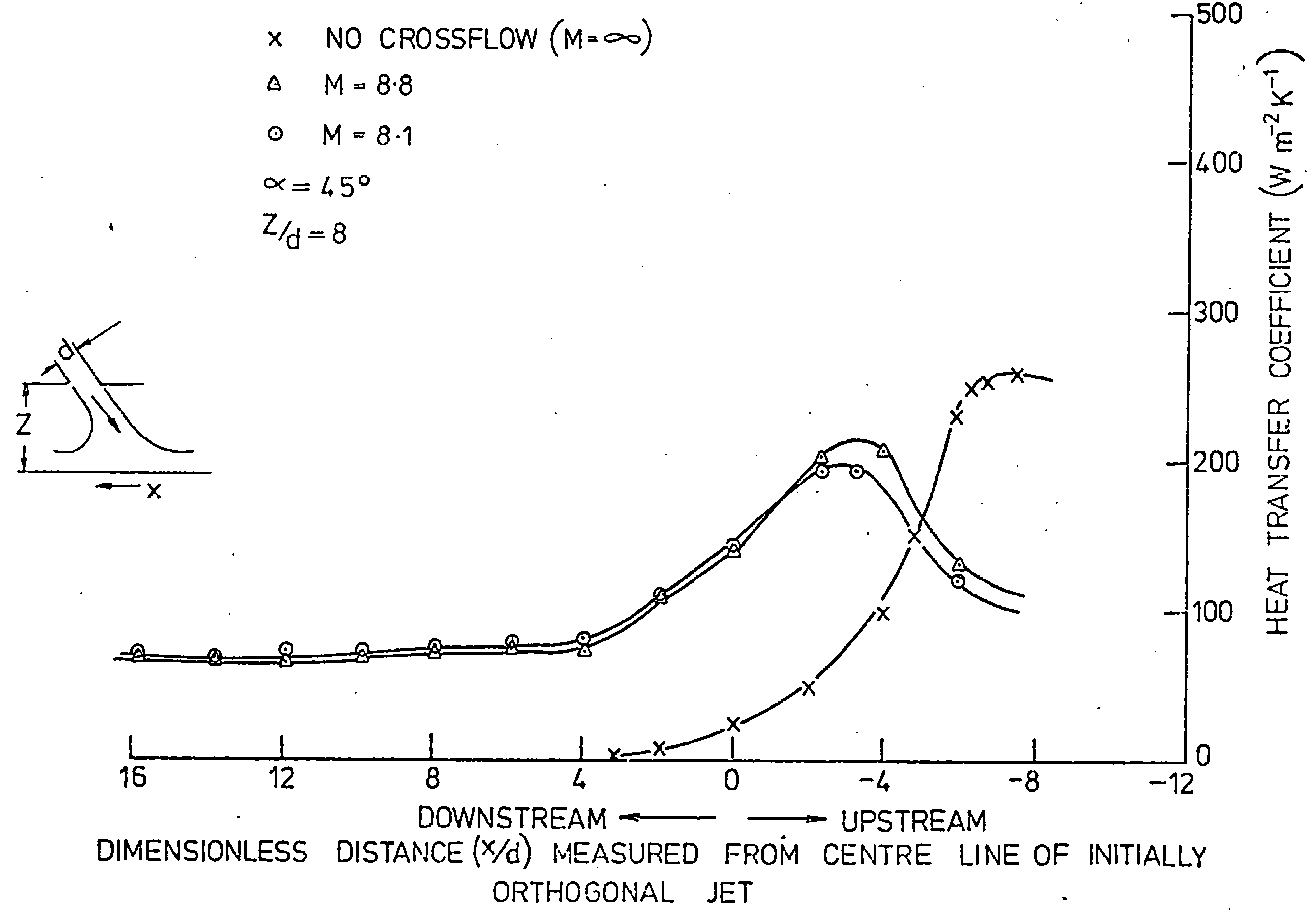

FIG. 7.51. EFFECT OF CROSSFLOWS ON JET IMPINGEMENT HEAT TRANSFERS (JETS INCLINED AT 45° TOWARDS CROSSFLOW DIRECTION; $Z/d = 8$).

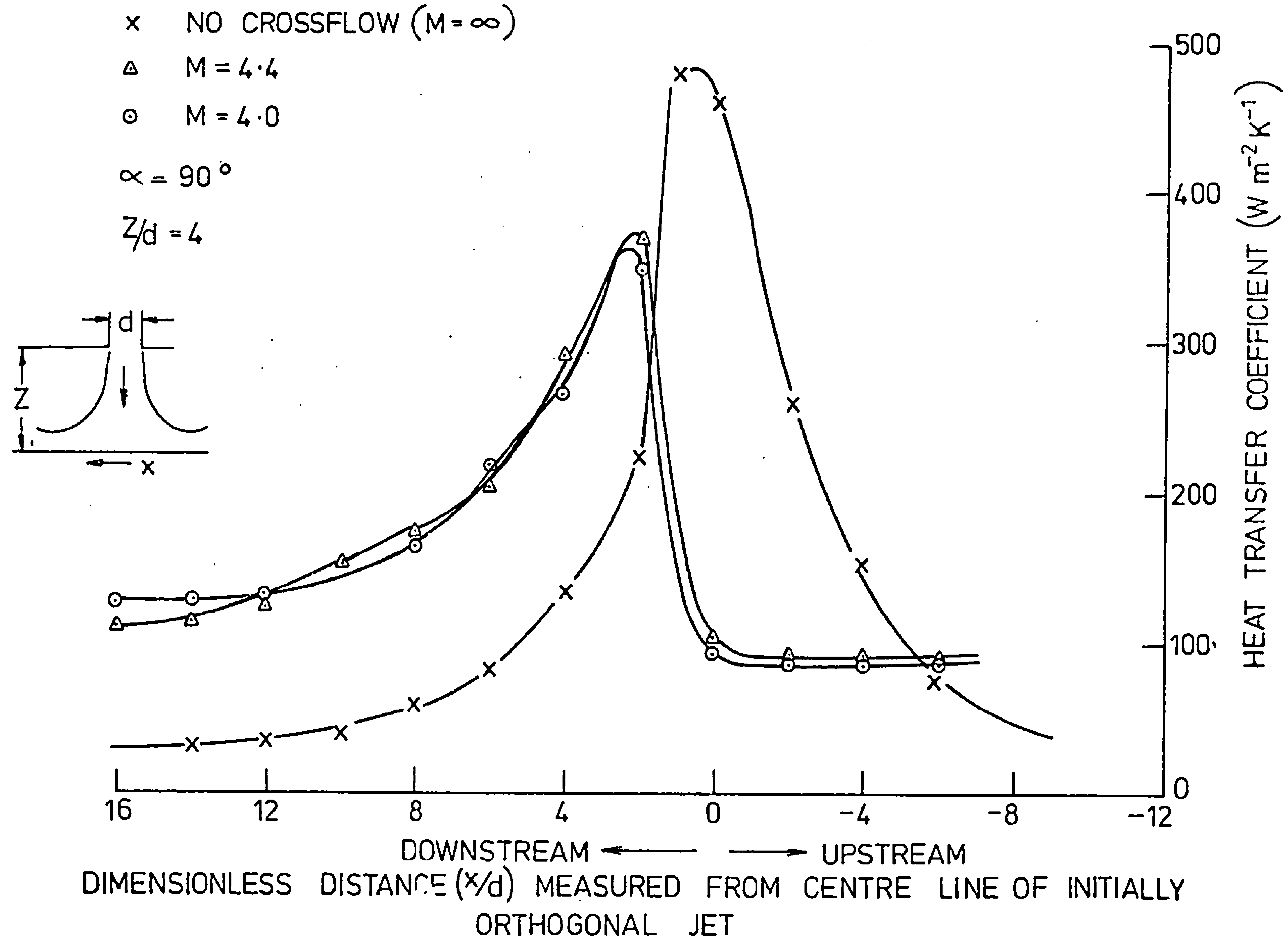

FIG. 7.52. EFFECT OF CROSSFLOWS ON JET IMPINGEMENT HEAT TRANSFERS (ORTHOGONAL JETS AT Z/d = 4)

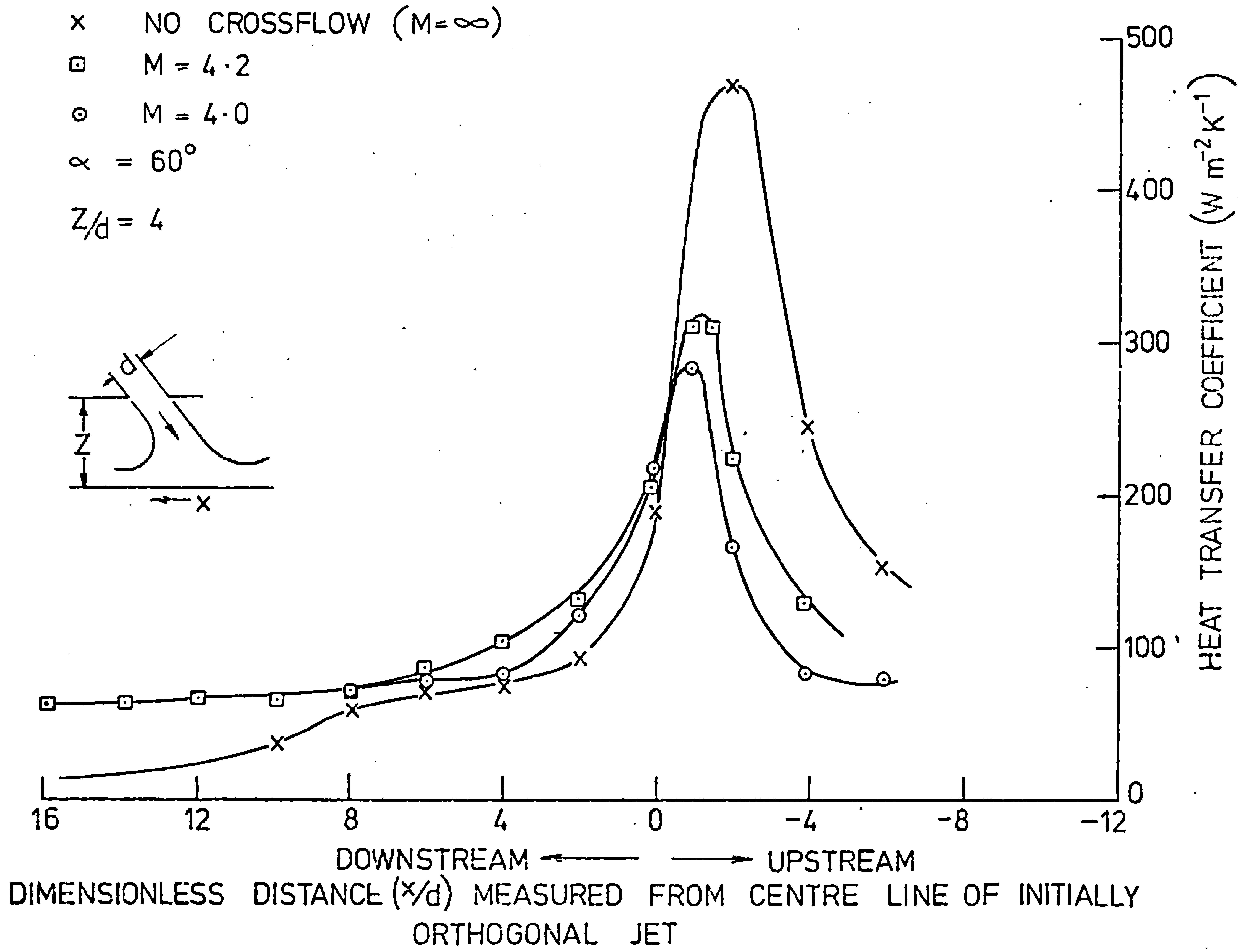

FIG. 7.53. EFFECT OF CROSSFLOWS ON JET IMPINGEMENT HEAT TRANSFERS (JETS INCLINED AT 60° TOWARDS CROSSFLOW DIRECTION $Z/d=4$)

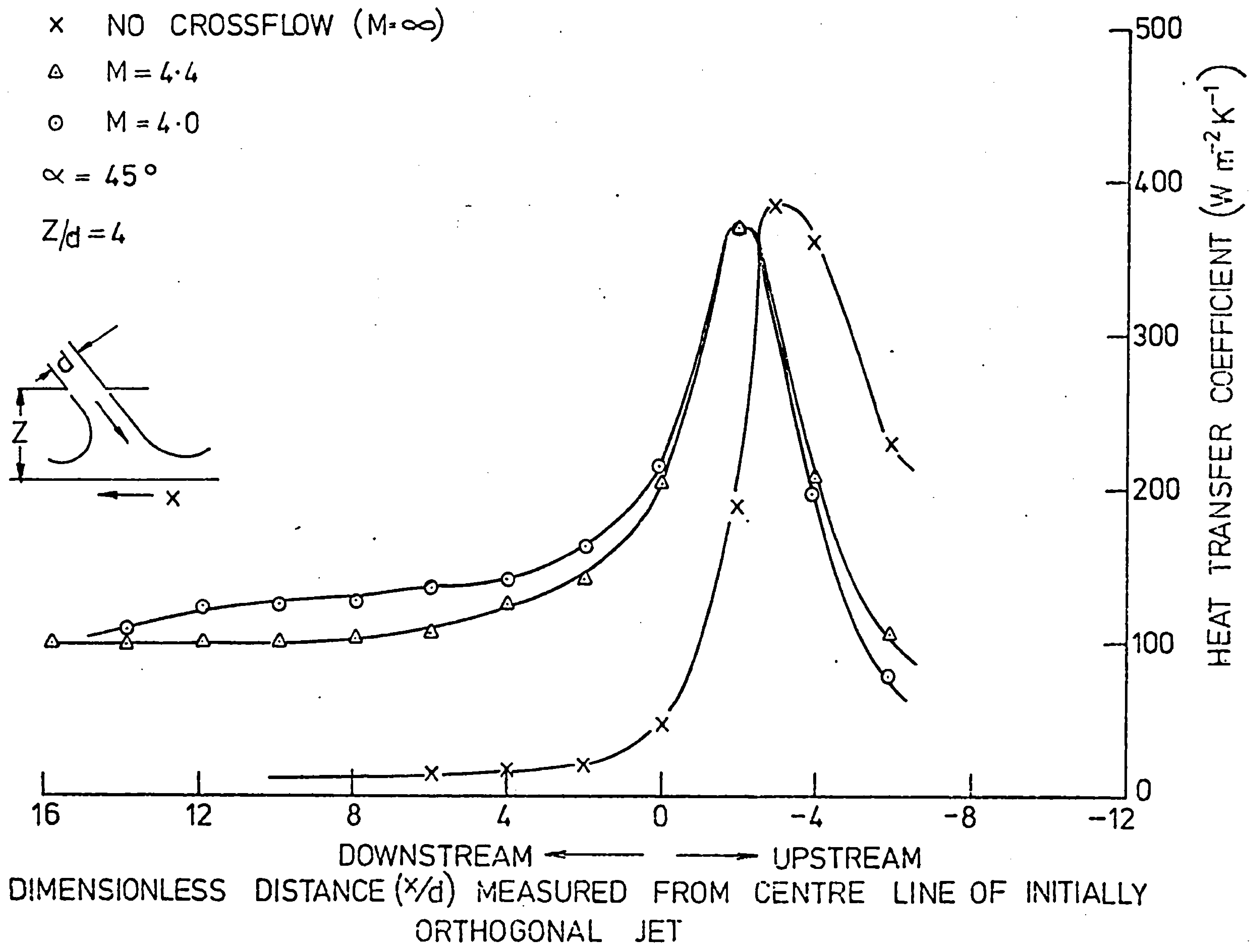

FIG. 7.54. EFFECT OF CROSSFLOWS ON JET IMPINGEMENT HEAT TRANSFERS (JETS INCLINED AT 45° TOWARDS CROSSFLOW DIRECTION $Z/d=4$)

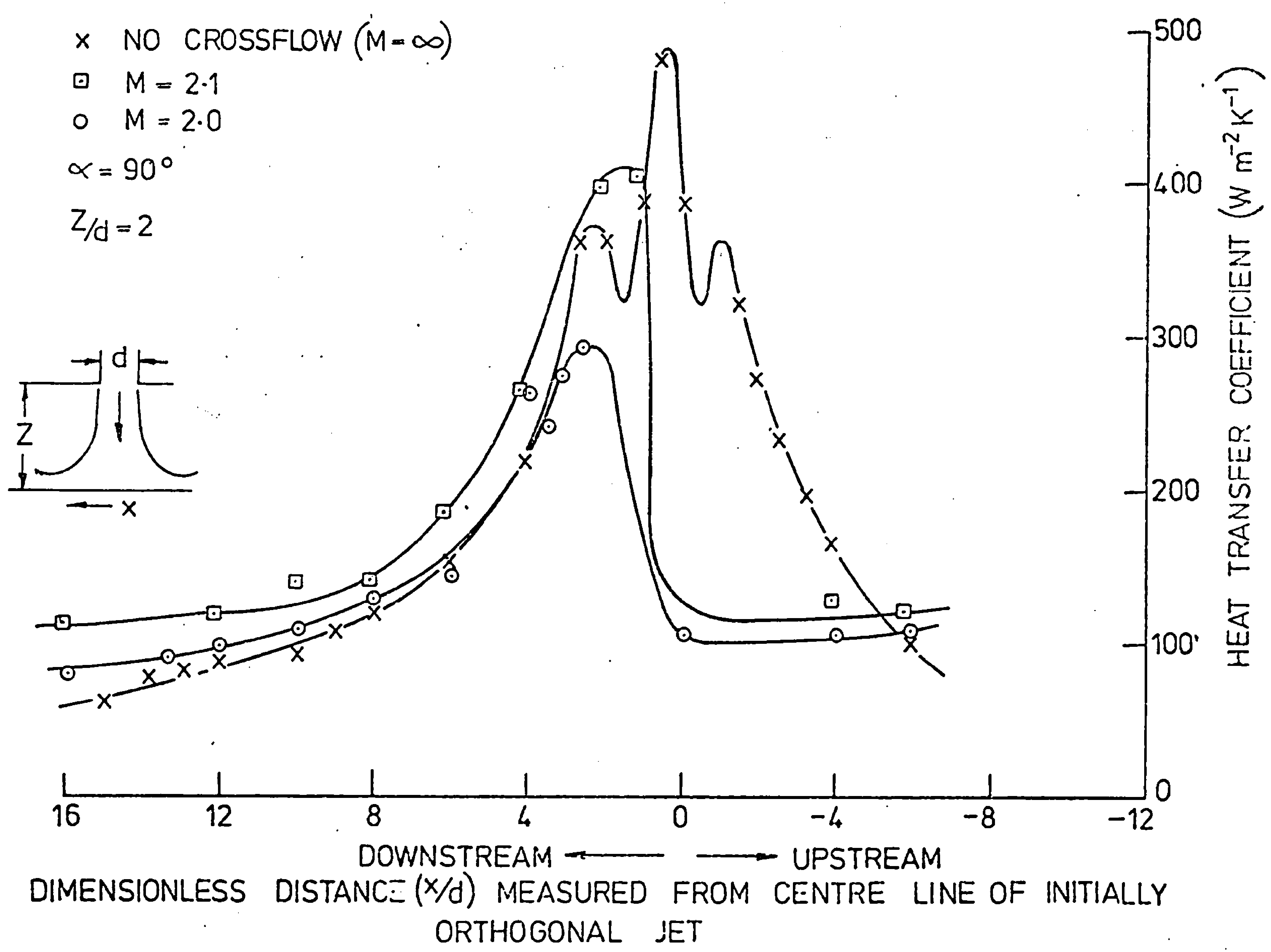

FIG. 7. 55. EFFECT OF CROSSFLOWS ON JET IMPINGEMENT HEAT TRANSFERS (ORTHOGONAL JETS AT $Z/d=2$)

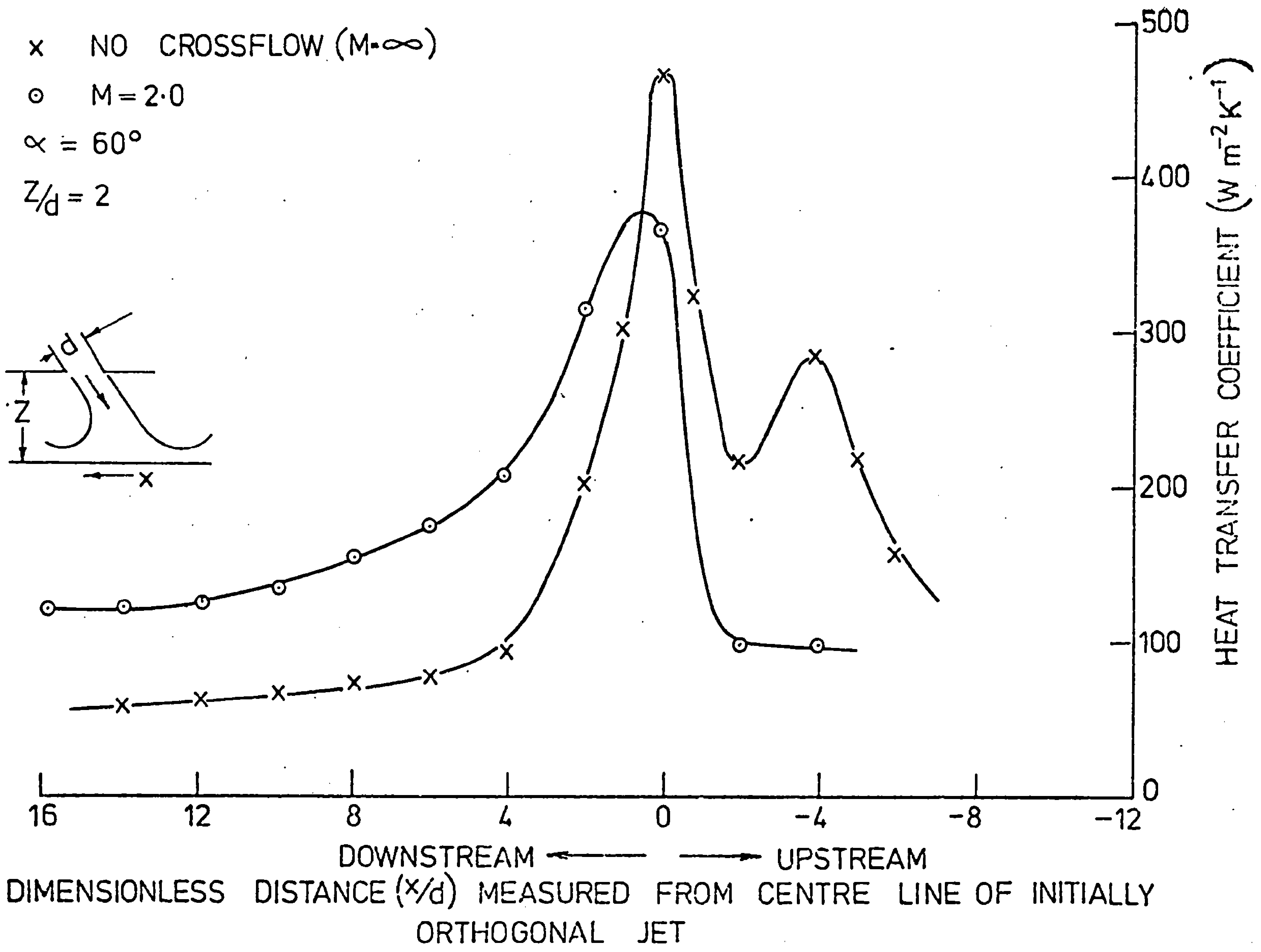

FIG. 7. 56. EFFECT OF CROSSFLOWS ON JET IMPINGEMENT HEAT TRANSFERS (JETS INCLINED AT 60° TOWARDS CROSSFLOW DIRECTION $Z/d = 2$)

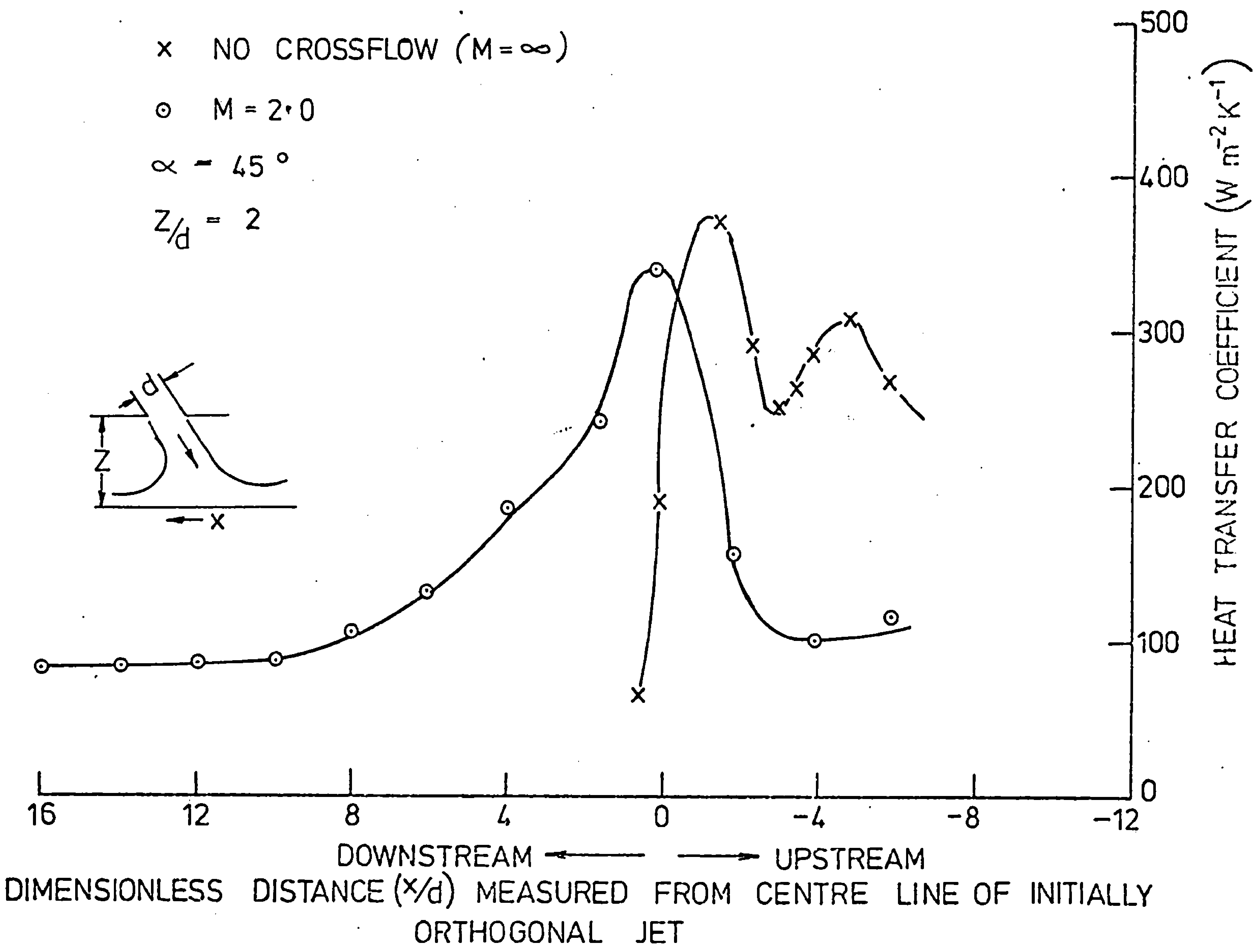

FIG. 7. 57. EFFECT OF CROSSFLOWS ON JET IMPINGEMENT HEAT TRANSFERS (JETS INCLINED AT 45° TOWARDS CROSSFLOW DIRECTION; $Z/d = 2$)

FIG. 7.58. EFFECT OF CROSSFLOWS ON DIMENSIONLESS STAGNATION POINT HEAT TRANSFERS FOR IMPINGING ORTHOGONAL JETS

FIG. 7.59. EFFECT OF CROSSFLOWS ON DIMENSIONLESS STAGNATION HEAT TRANSFERS FOR JETS INCLINED AT 60° TOWARDS CROSSFLOW DIRECTION

FIG. 7. 60. EFFECT OF CROSSFLOWS ON DIMENSIONLESS STAGNATION POINT HEAT TRANSFERS FOR JETS INCLINED AT 45° TOWARDS CROSSFLOW DIRECTION

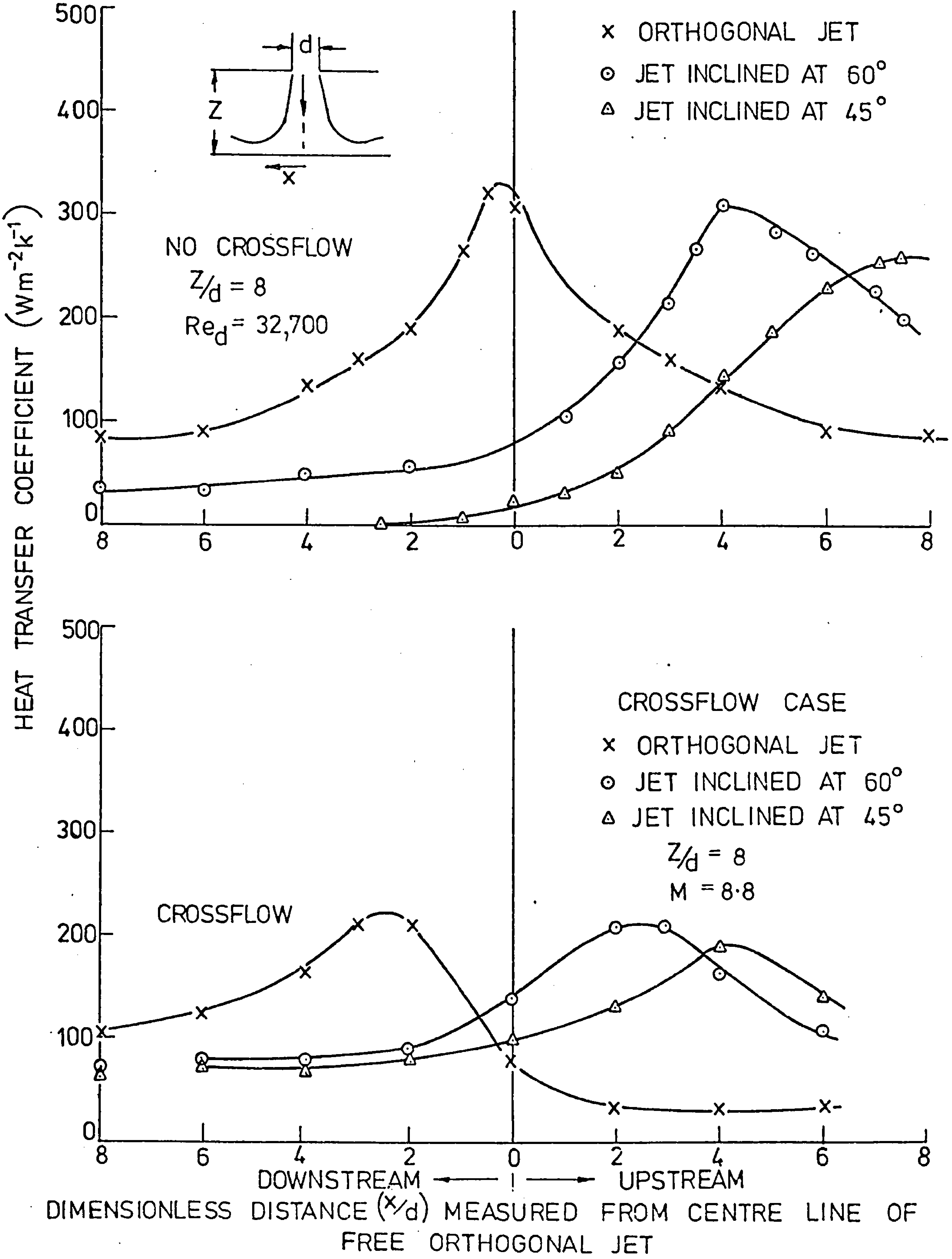

FIG. 7.61. EFFECT OF JET INCLINATION ON JET IMPINGEMENT HEAT TRANSFER FOR M=8·8

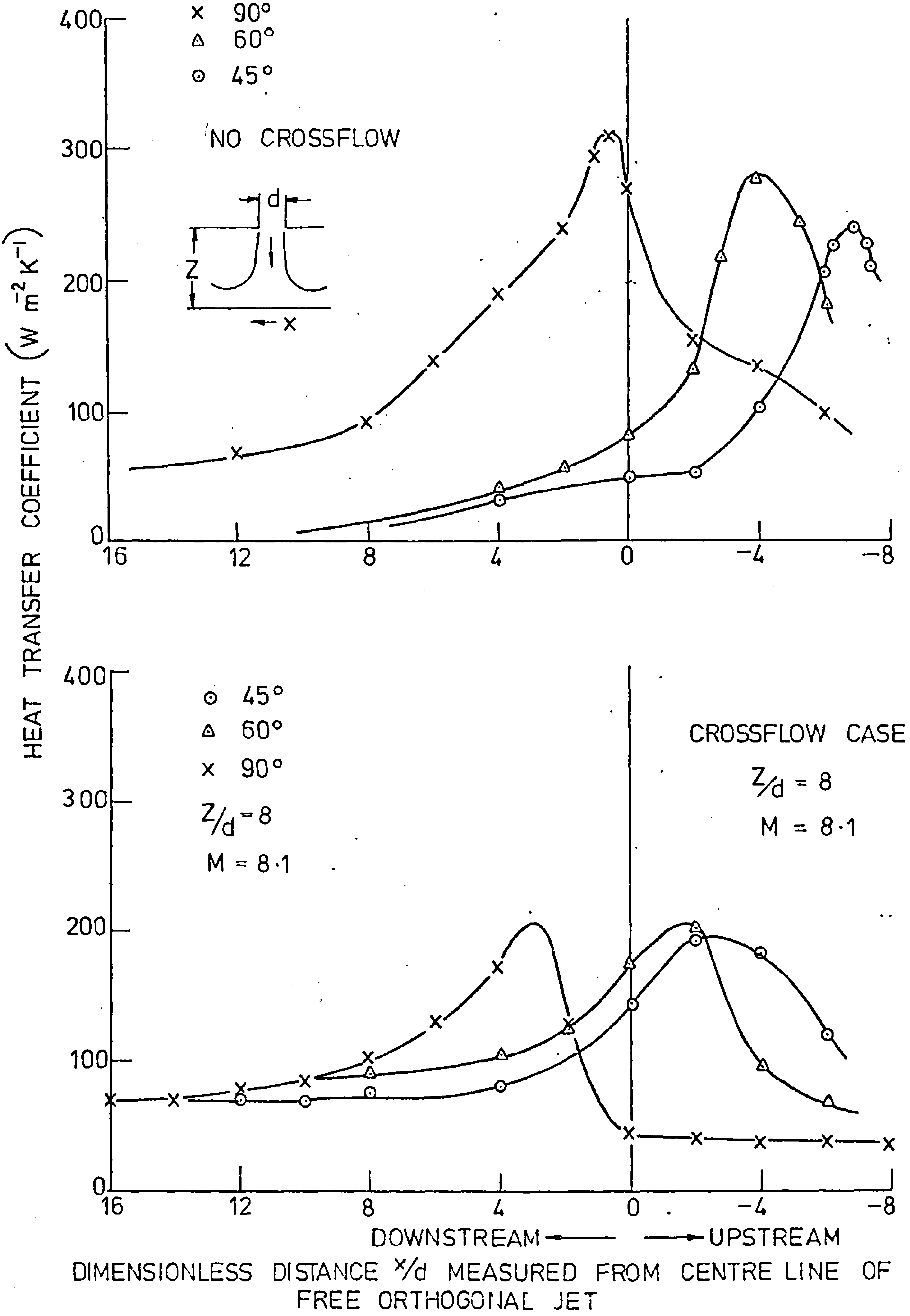

FIG. 7.62. EFFECT OF JET INCLINATION ON JET IMPINGEMENT HEAT TRANSFER FOR M = 8·1

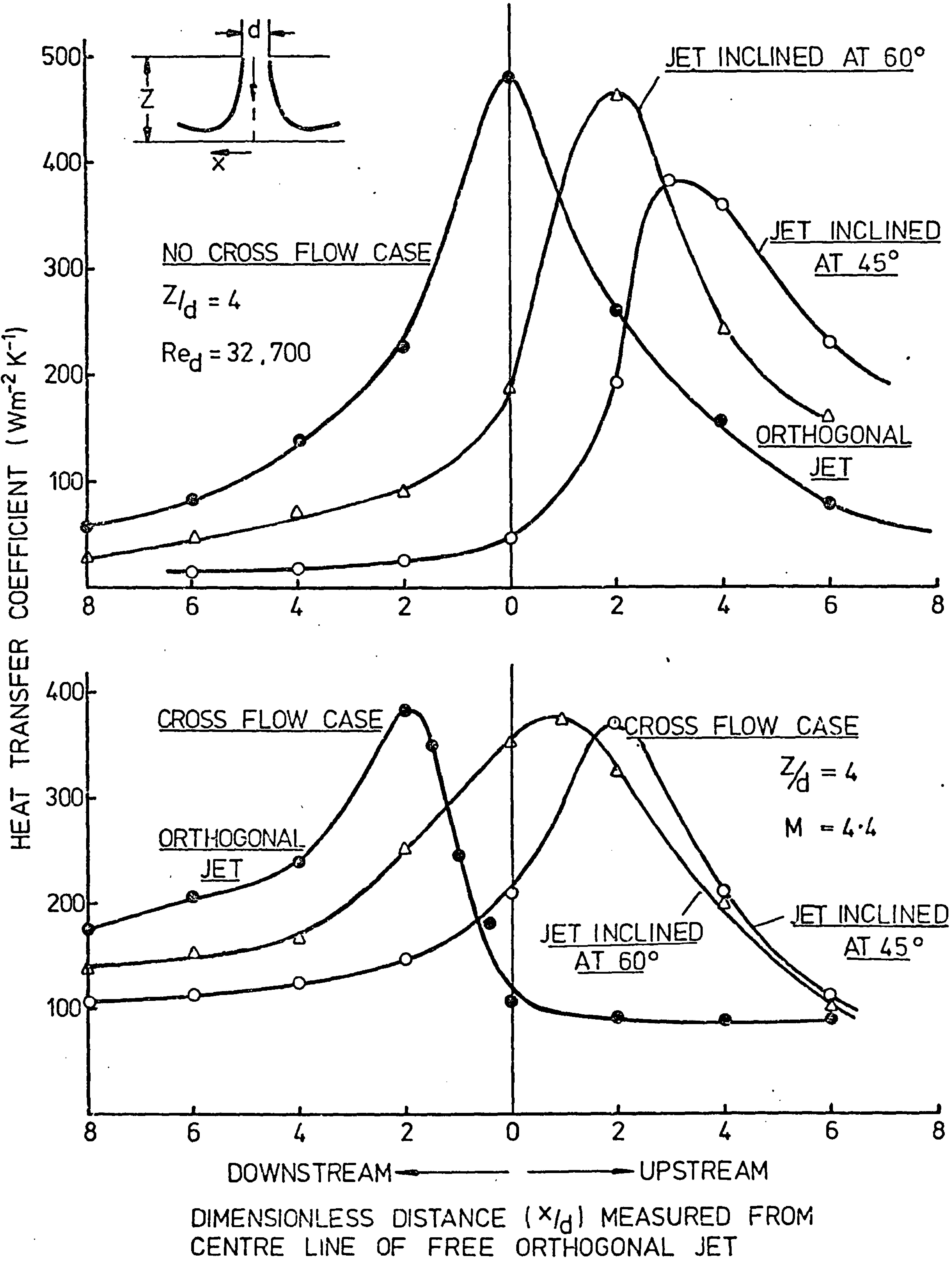

FIG. 7.63. EFFECT OF INCLINATION ON JET IMPINGEMENT HEAT TRANSFER FOR M = 4·4

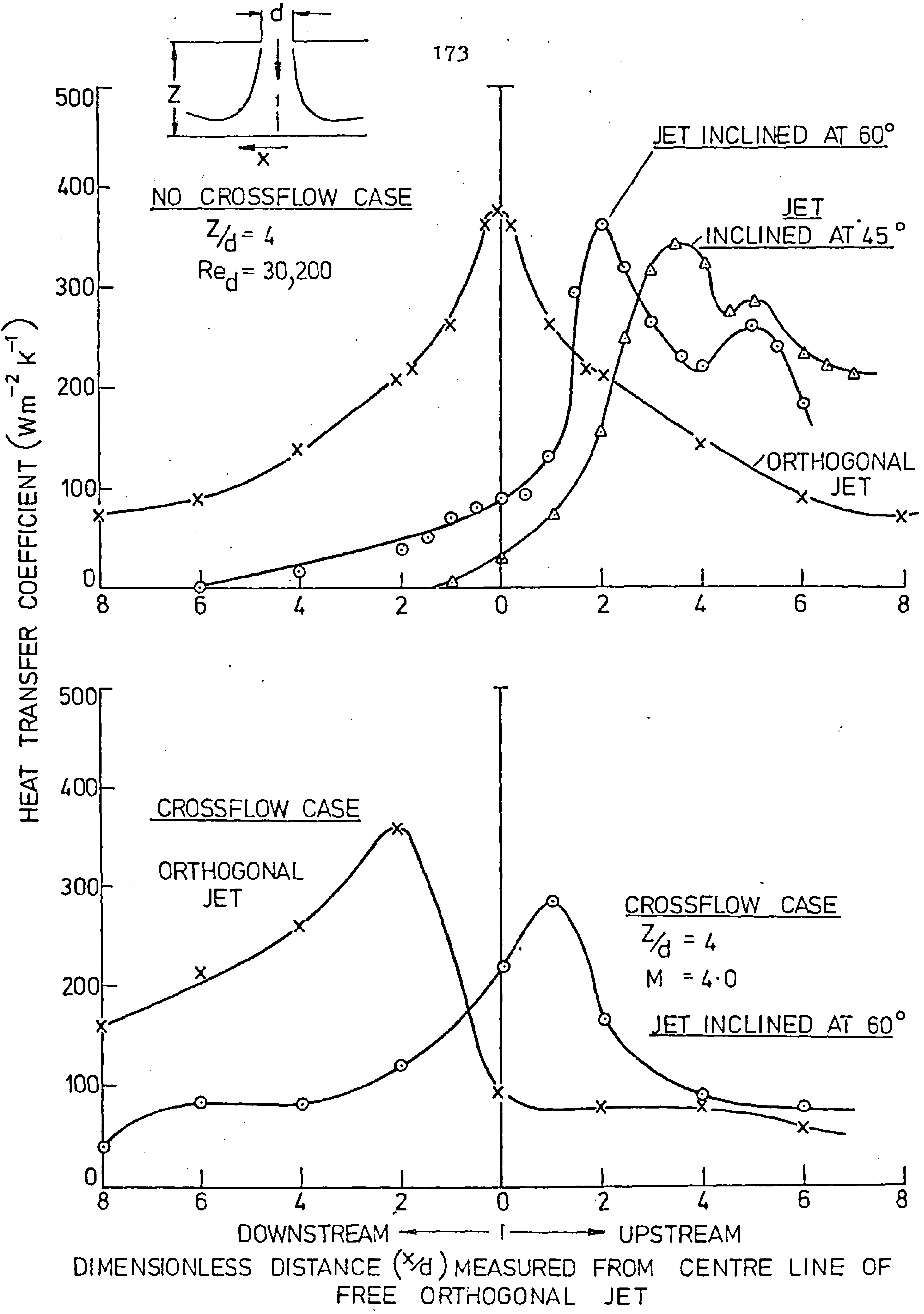

FIG.7.64. EFFECT OF JET INCLINATION ON JET IMPINGEMENT HEAT TRANSFER FOR M = 4·0

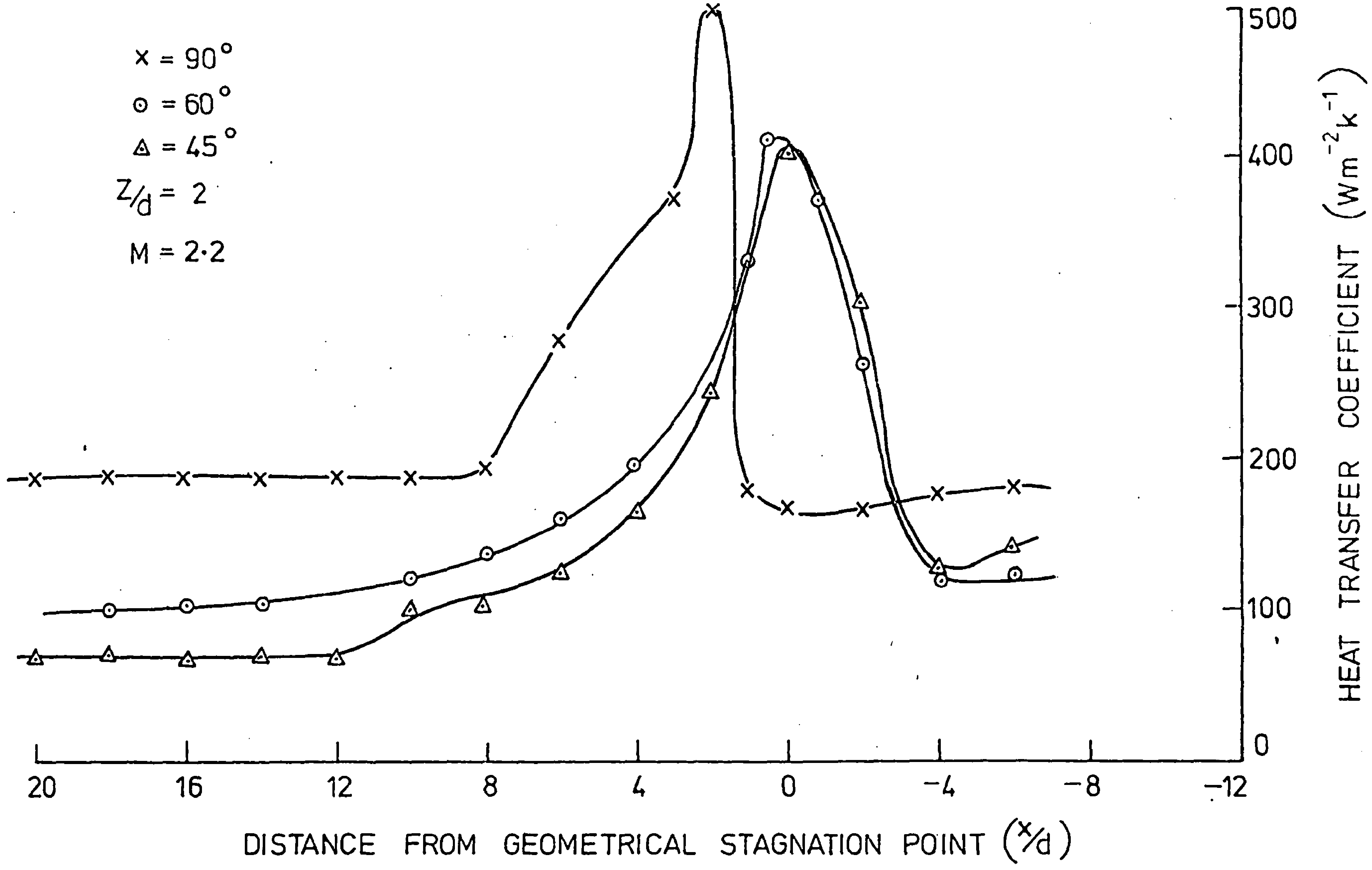

FIG.7.65. EFFECT OF CROSSFLOW AND IMPINGEMENT ANGLE ON AXIAL VARIATION OF HEAT TRANSFER ($Y/d = 0$).

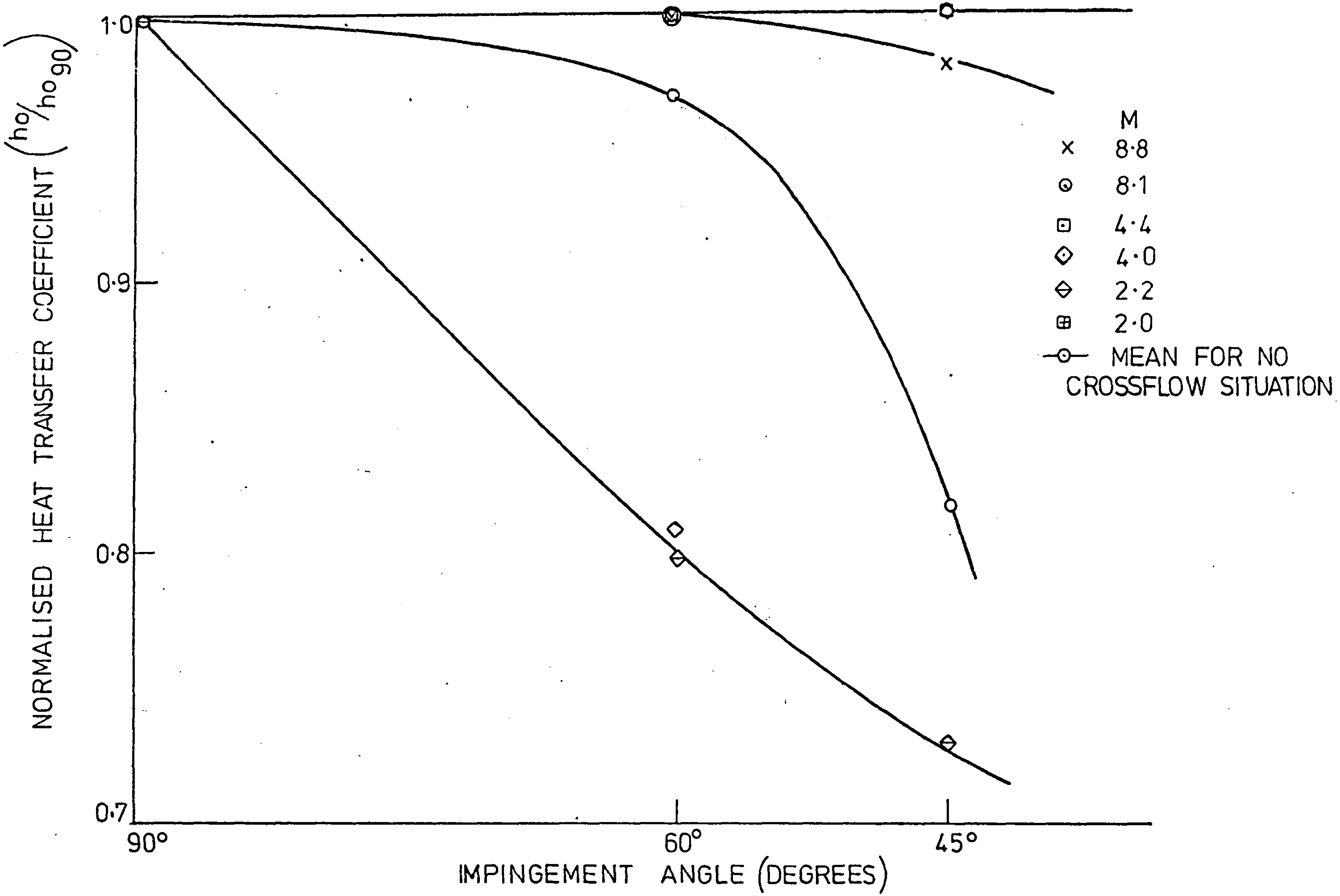

FIG. 7. 66. EFFECT OF IMPINGEMENT ANGLE ON DIMENSIONLESS STAGNATION HEAT TRANSFERS FOR JET IMPINGEMENT IN CROSSFLOWS

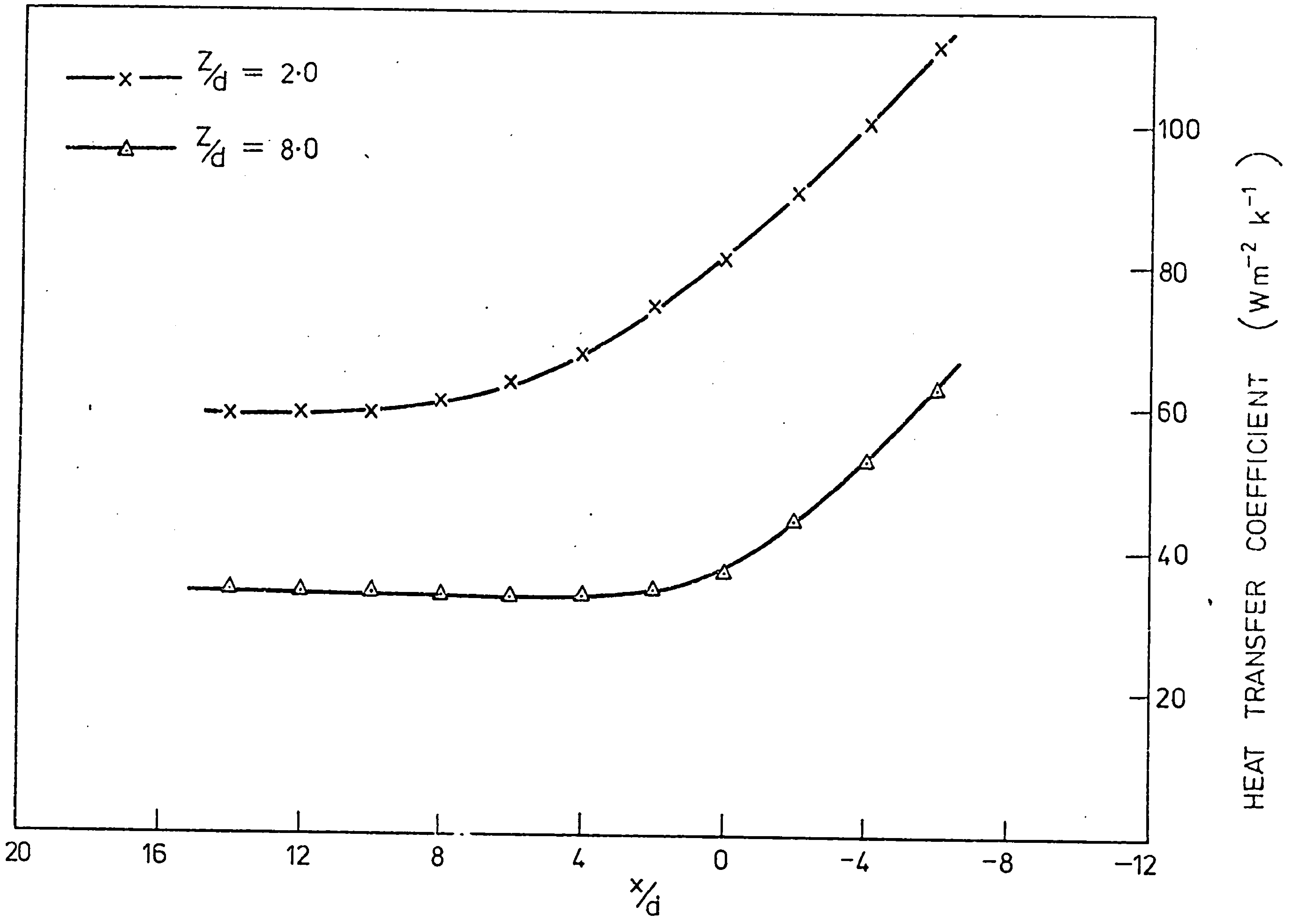

FIG.7.67. LOCAL HEAT TRANSFER COEFFICIENTS FOR CROSSFLOW WITHOUT JET IMPINGEMENT

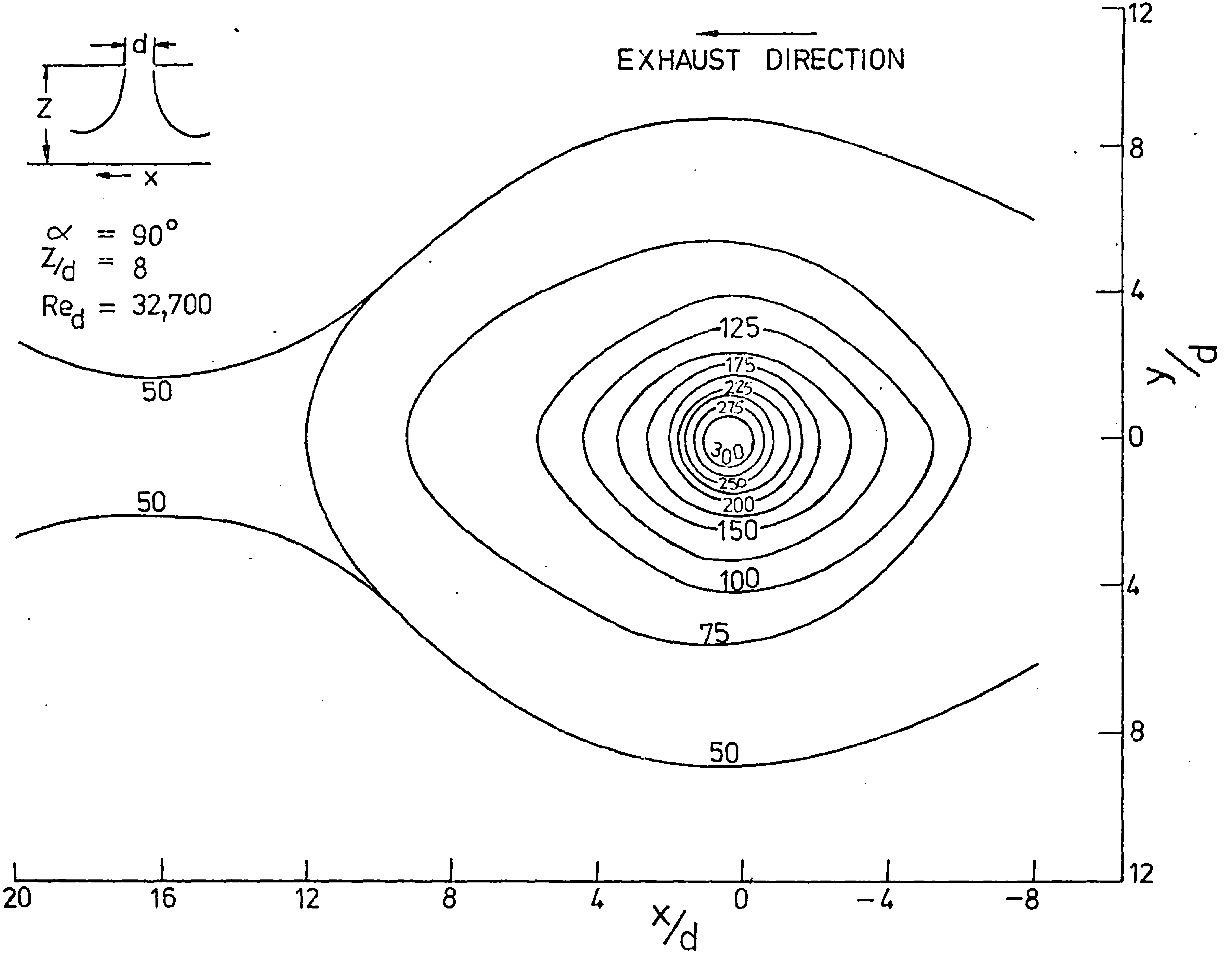

FIG. 7. 68. VARIATION OF LOCAL CONVECTIVE HEAT TRANSFER ON TARGET PLATE FOR JET IMPINGEMENT IN STAGNANT SURROUNDINGS ($\alpha = 90°$)

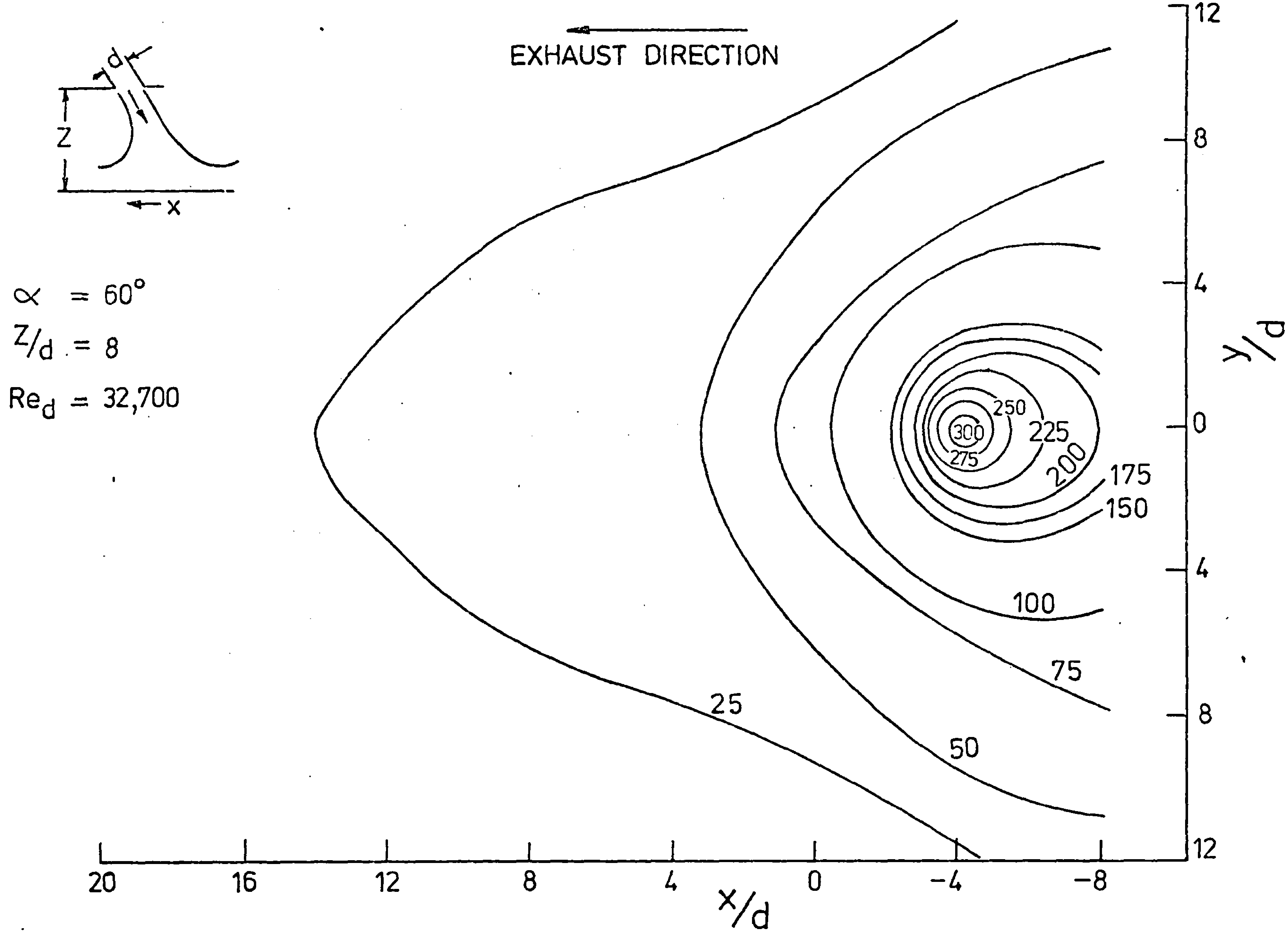

FIG. 7. 69. VARIATION OF LOCAL CONVECTIVE HEAT TRANSFER ON TARGET PLATE FOR JET IMPINGEMENT IN STAGNANT SURROUNDINGS ($\alpha = 60°$)

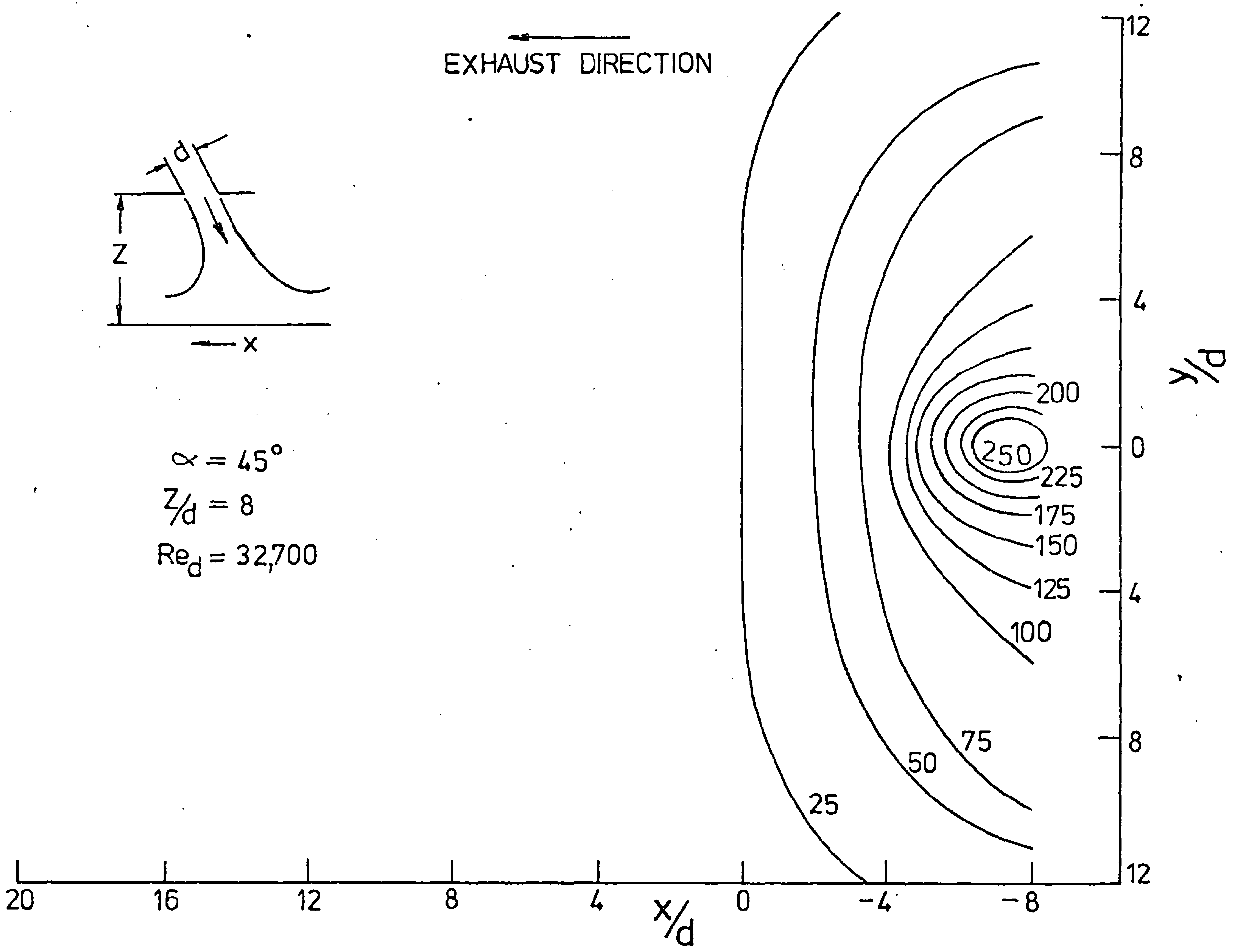

FIG. 7. 70. VARIATION OF LOCAL CONVECTIVE HEAT TRANSFER ON TARGET PLATE FOR JET IMPINGEMENT IN STAGNANT SURROUNDINGS (α-45°)

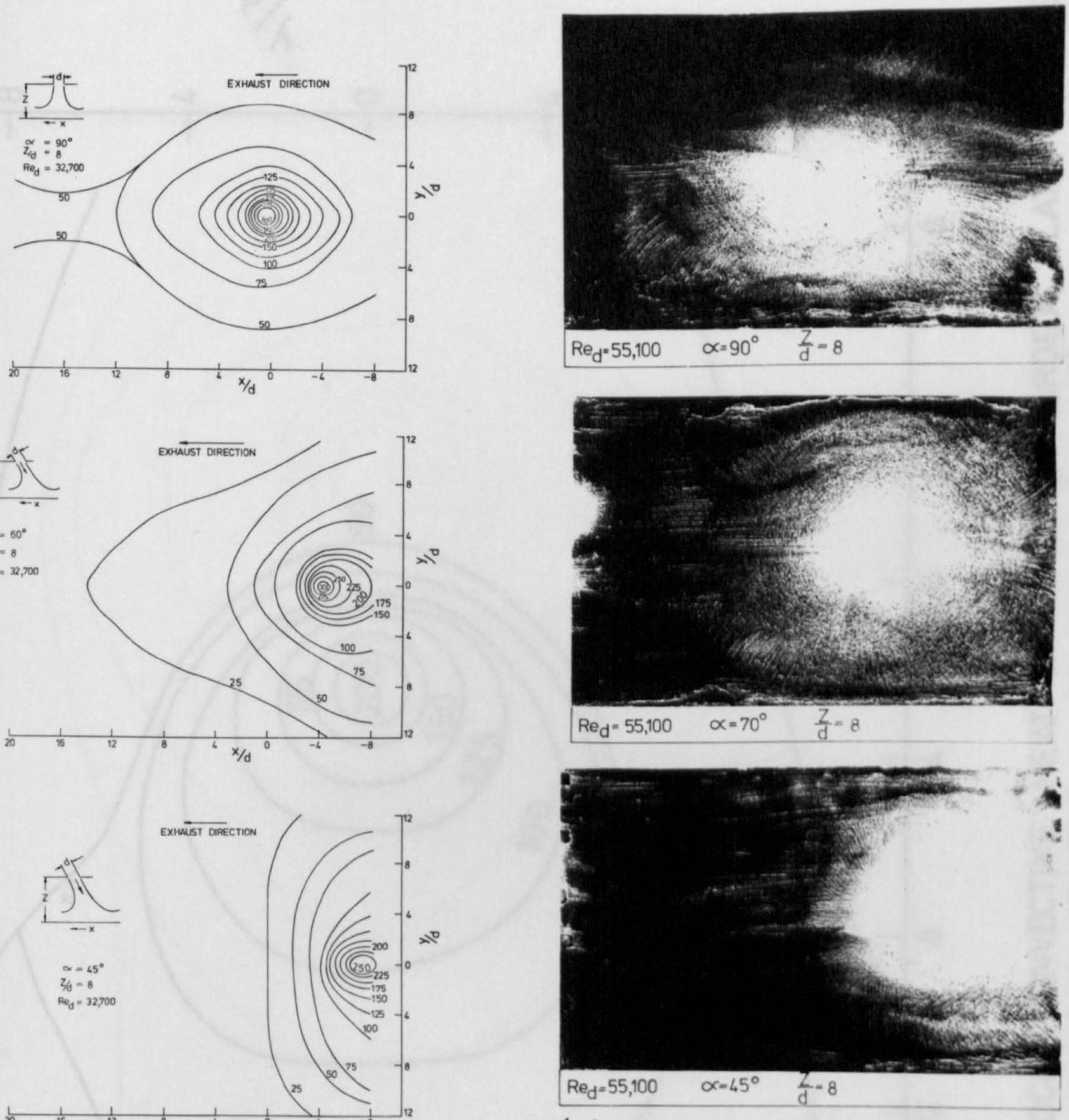

(a) EFFECT OF IMPINGEMENT ANGLE ON THE DISTRIBUTION OF LOCAL CONVECTIVE HEAT TRANSFER FOR JET IMPINGEMENT IN STAGNANT SURROUNDINGS.

(b) EFFECT OF JET INCLINATION ON SURFACE FLOW PATTERNS ASSOCIATED WITH IMPINGING JETS

FIG. 7. 71. EFFECT OF IMPINGEMENT ANGLE ON THE DISTRIBUTION OF LOCAL CONVECTIVE HEAT TRANSFER FOR JET IMPINGEMENT IN STAGNANT SURROUNDINGS — DIRECT COMPARISON WITH ASSOCIATED SURFACE FLOW PATTERNS

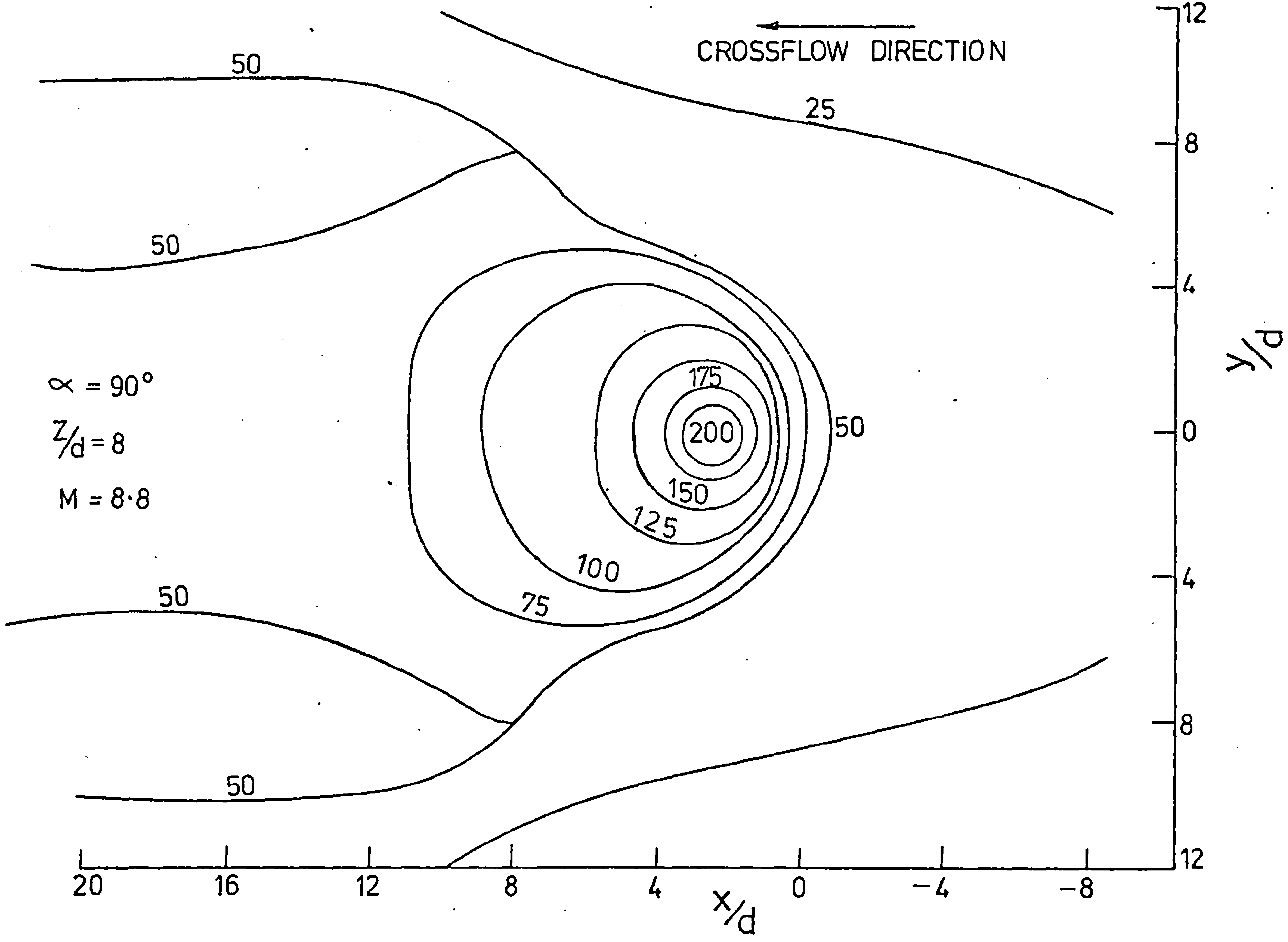

FIG. 7. 72. VARIATION OF LOCAL CONVECTIVE HEAT TRANSFER ON TARGET PLATE FOR JET IMPINGEMENT IN CROSSFLOW ($\alpha = 90°$)

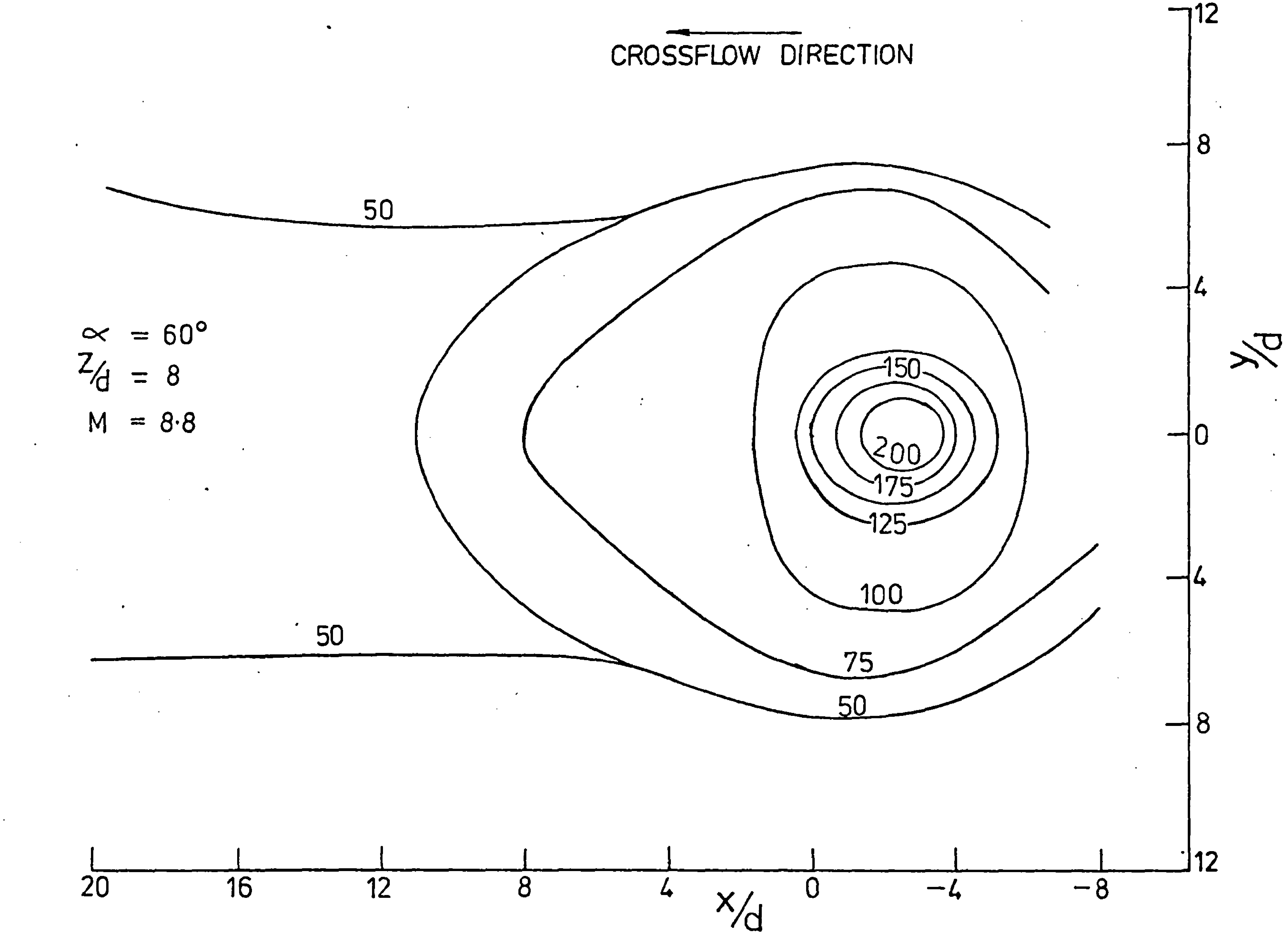

FIG. 7. 73. VARIATION OF LOCAL CONVECTIVE HEAT TRANSFER ON TARGET PLATE FOR JET IMPINGEMENT IN CROSSFLOW (α=60°)

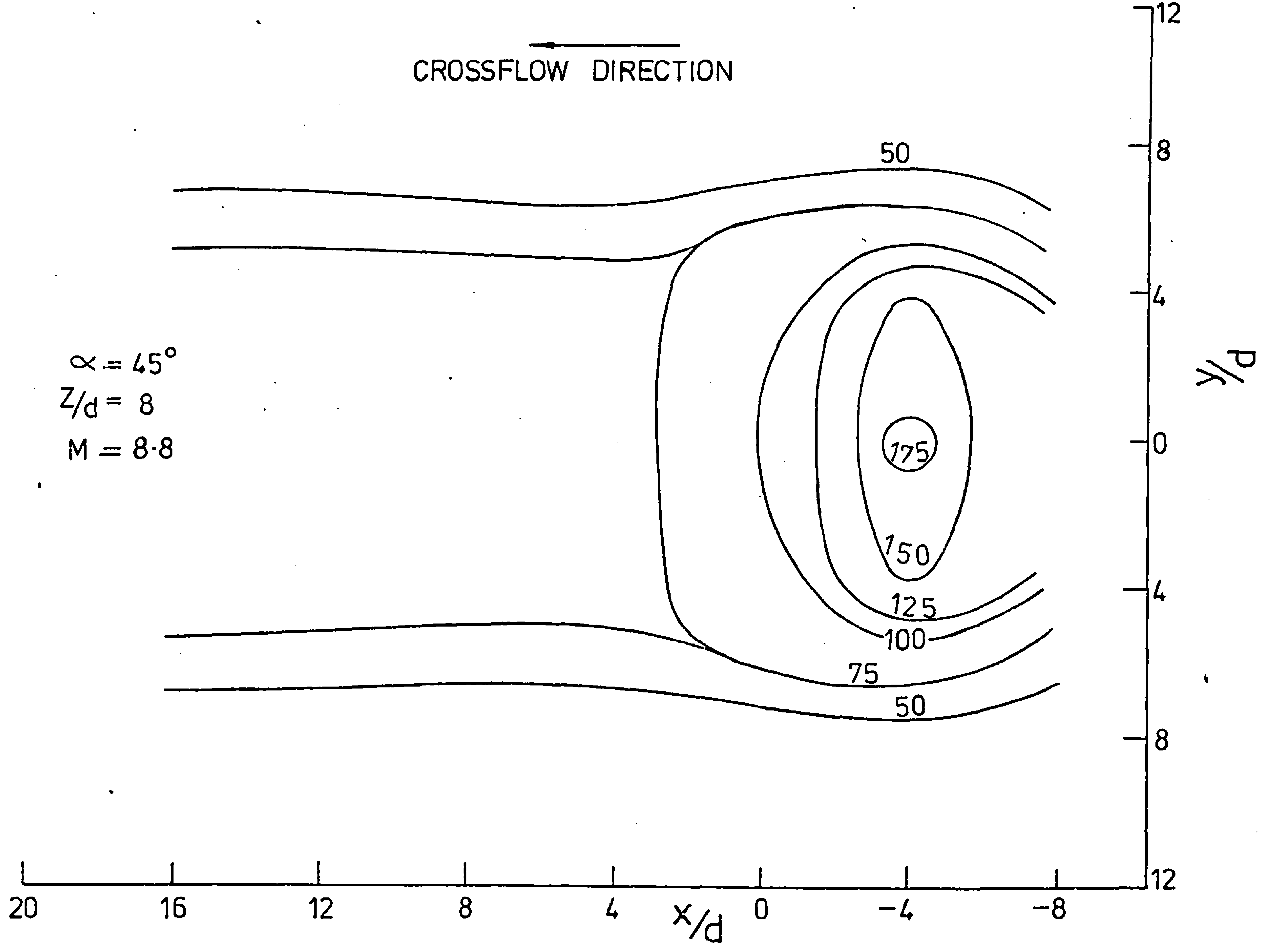

FIG. 7. 74. VARIATION OF LOCAL CONVECTIVE HEAT TRANSFER ON TARGET PLATE FOR JET IMPINGEMENT IN CROSSFLOW (α = 45°)

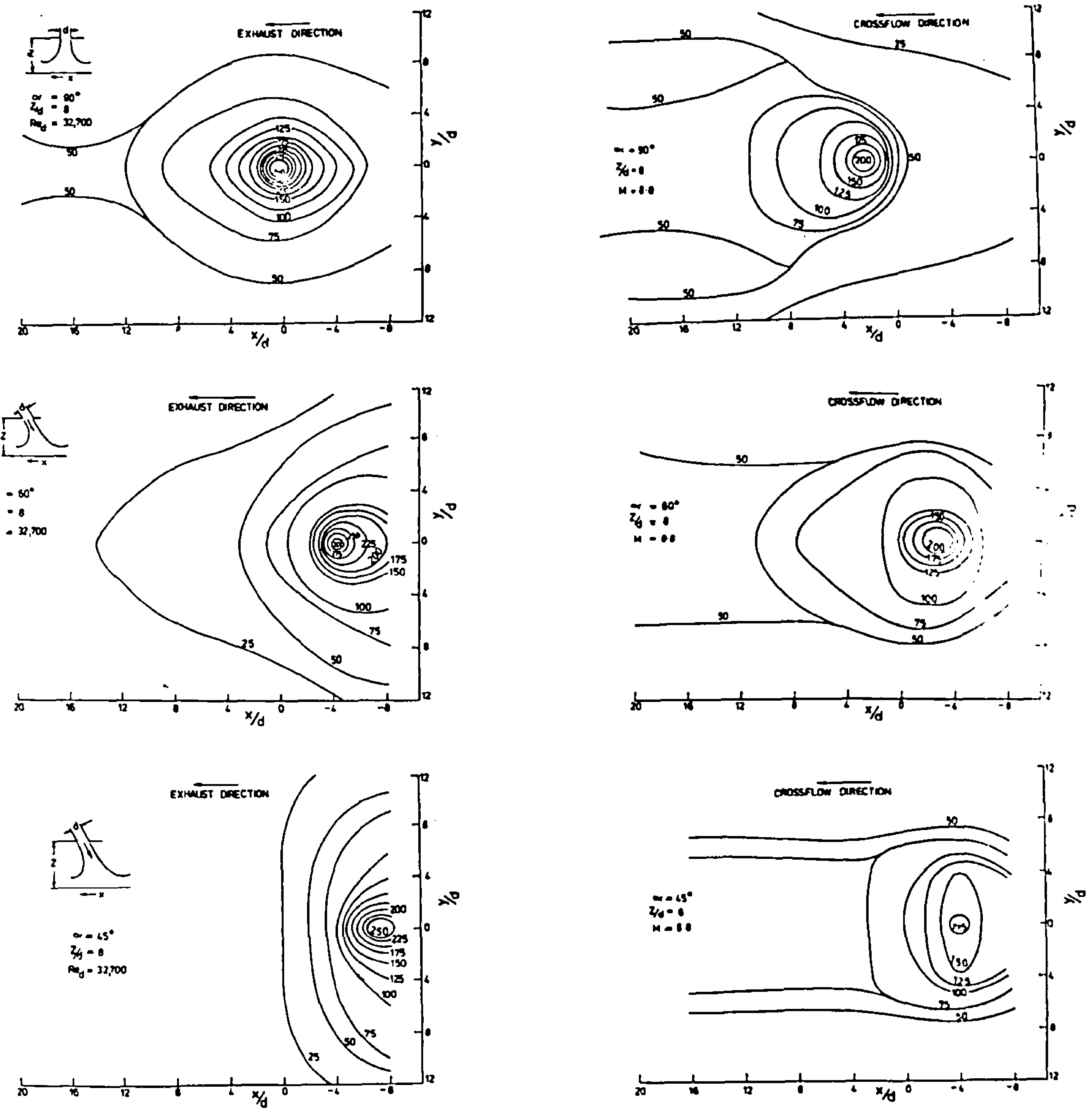

(a) VARIATION OF LOCAL CONVECTIVE HEAT TRANSFER ON TARGET PLATE FOR JET IMPINGEMENT IN STAGNANT SURROUNDINGS

(b) VARIATION OF LOCAL CONVECTIVE HEAT TRANSFER ON TARGET PLATE FOR JET IMPINGEMENT IN CROSSFLOW

FIG. 7. 75. EFFECTS OF CROSSFLOW AND IMPINGEMENT ANGLE ON DISTRIBUTION OF LOCAL CONVECTIVE HEAT TRANSFER COEFFICIENT.

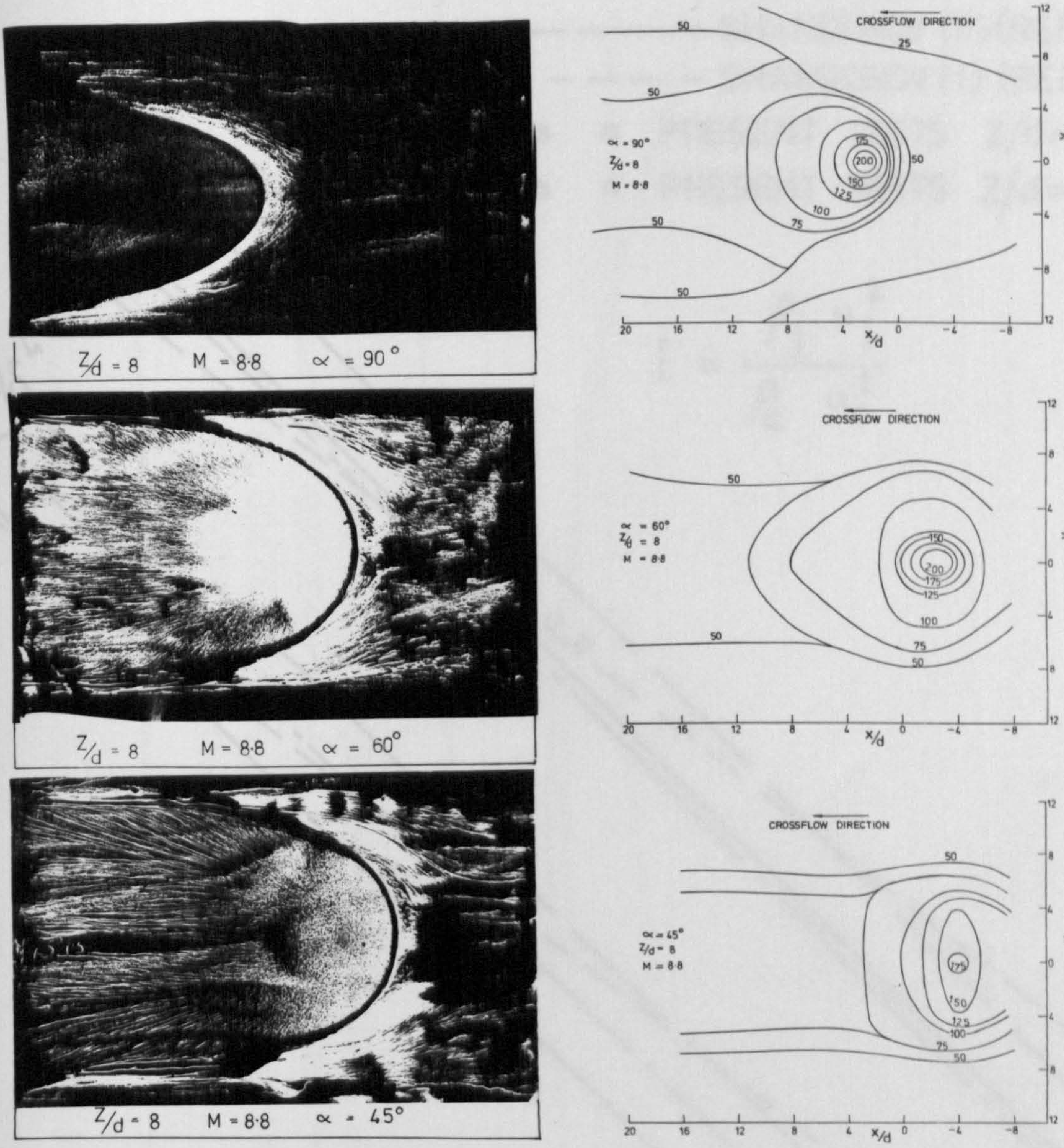

(a) EFFECT OF IMPINGEMENT ANGLE ON SURFACE FLOW PATTERNS ASSOCIATED WITH JET IMPINGEMENT IN CROSSFLOW

(b) VARIATION OF LOCAL CONVECTIVE HEAT TRANSFER ON TARGET PLATE FOR JET IMPINGEMENT IN CROSSFLOW

FIG. 7.76. EFFECT OF IMPINGEMENT ANGLE ON THE DISTRIBUTION OF LOCAL CONVECTIVE HEAT TRANSFER FOR JET IMPINGEMENT IN CROSSFLOW — DIRECT COMPARISON WITH ASSOCIATED SURFACE FLOW PATTERNS

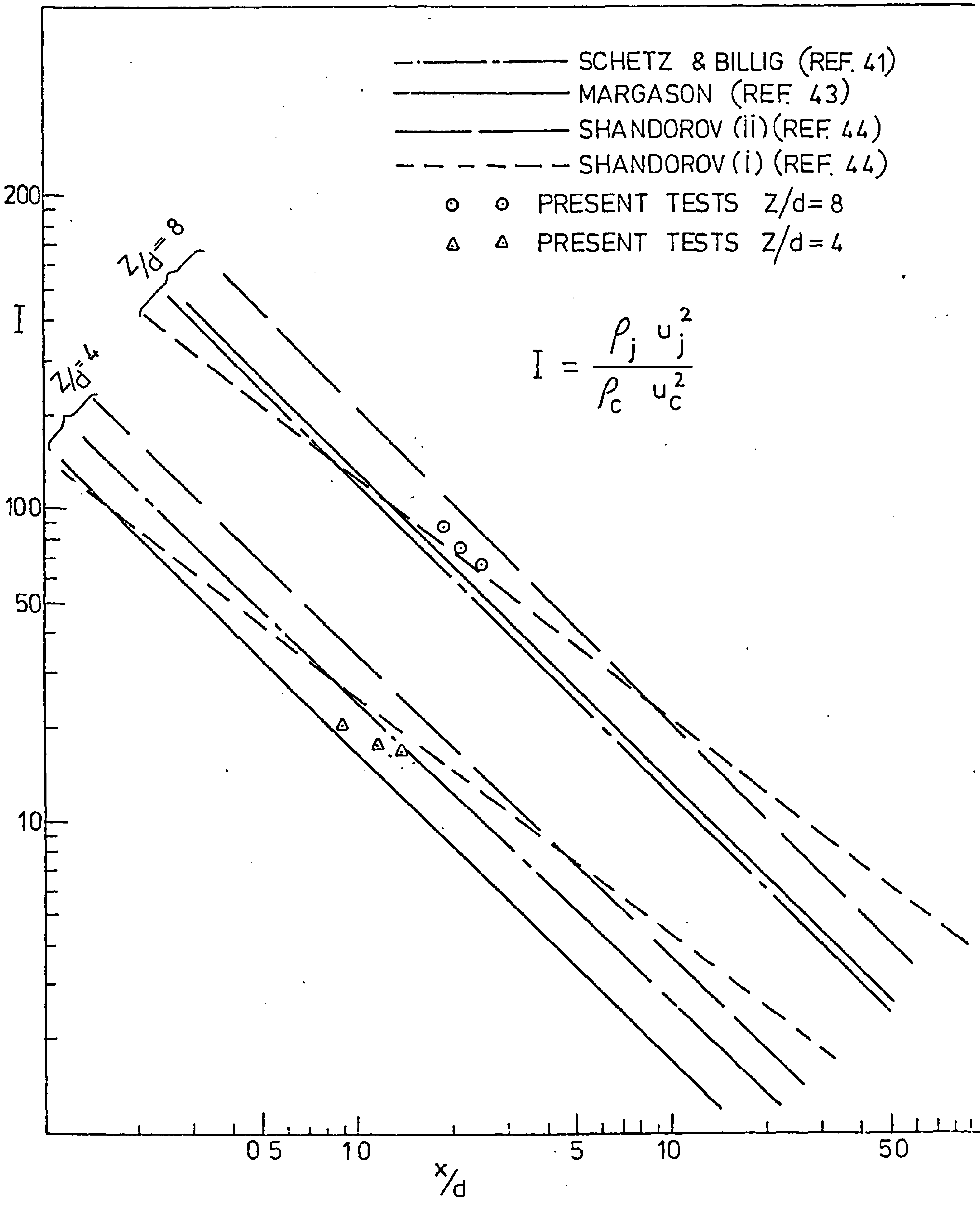

FIG. 7. 77. LOCATION OF JET CENTRE

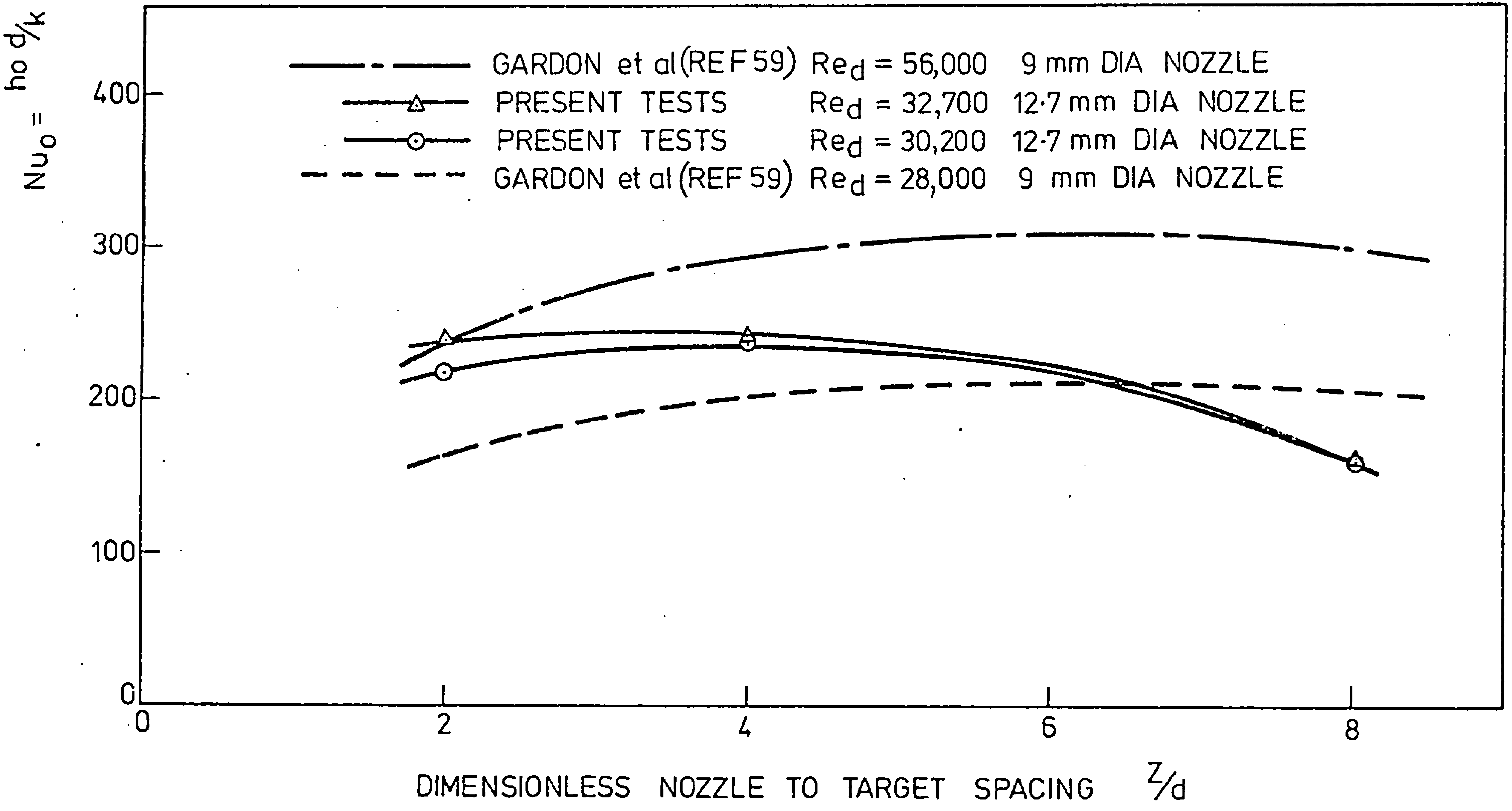

FIG. 7.78. STAGNATION POINT HEAT TRANSFER – COMPARISON WITH PREVIOUS STUDIES

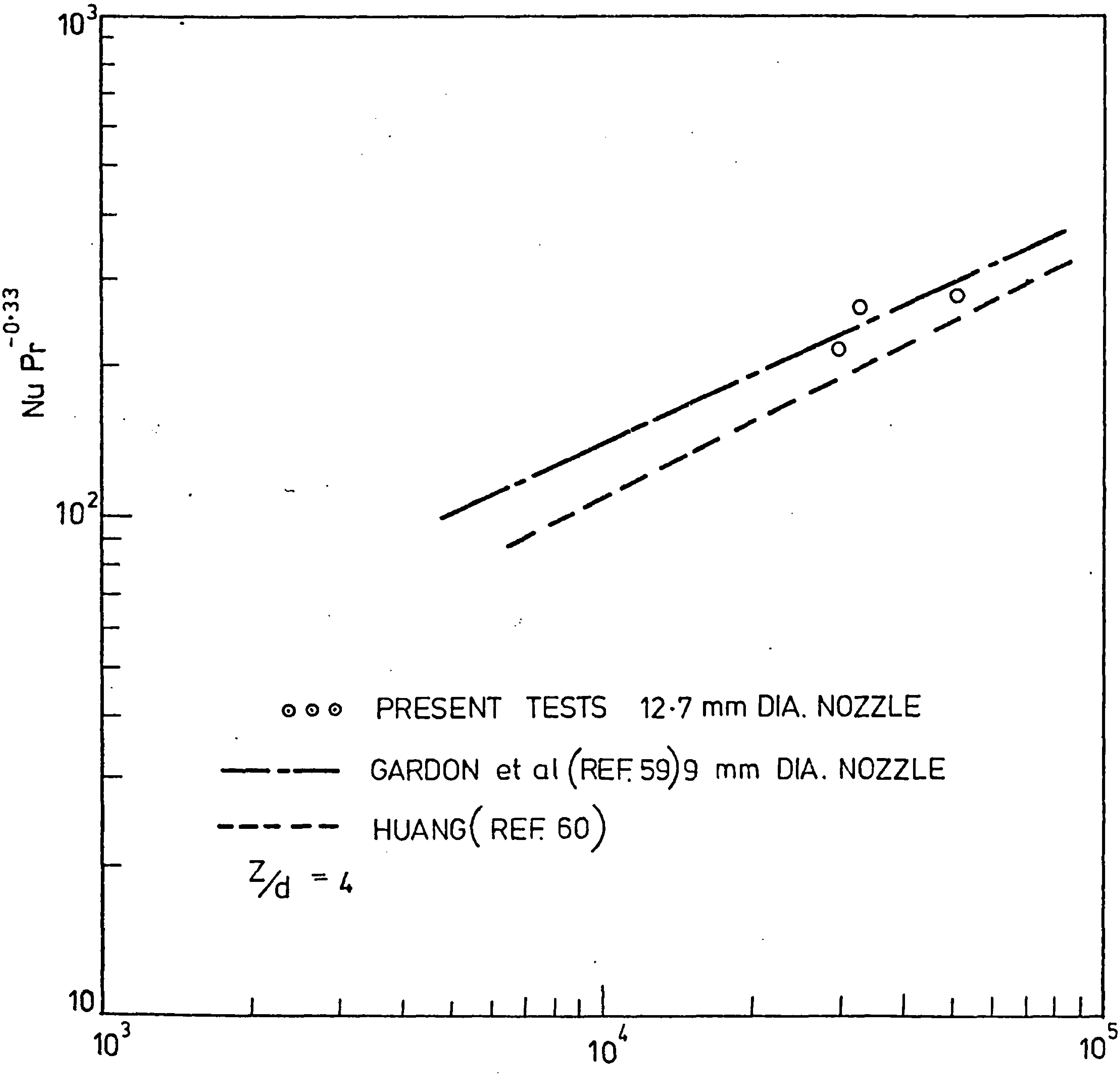

FIG.7.79. EFFECT OF REYNOLDS NUMBER ON STAGNATION POINT HEAT TRANSFER – COMPARISON WITH PREVIOUS STUDIES

CHAPTER 8

CONCLUSIONS AND RECOMMENDATIONS FOR FUTURE WORK

8.1 Conclusions

(a) Flow Visualisation Studies

(i) The oil film and smoke flow visualisation techniques employed in this present study are suitable methods of obtaining information concerning the flow patterns associated with impinging jets in both stagnant and crossflow conditions. The behaviour observed using these techniques was generally in good qualitative agreement with that reported in the published literature.

(ii) For jet impingement in crossflows, these flow visualisation methods have shown that two distinct conditions are possible, depending on the jet to crossflow blowing rate, and the nozzle to target spacing. At high blowing rates the wall jet formed after impingement penetrates upstream before formation of a vortex upon separation from the surface. This vortex is characterised by a horse-shoe shaped separation line. At a low blowing rate, the jet does not have sufficient momentum for impingement to take place, so that the jet flow is simply flushed out by the crossflowing stream. Limiting conditions were defined for these cases.

(iii) Using the oil film technique, the profiles of these separation lines were obtained together with estimates of the location of the stagnation point. As the jet is inclined into the crossflow, the area enclosed by these lines is increased, thus indicating greater wall jet spread. The angled jet also penetrates further upstream than the orthogonal configuration.

(b) Heat Transfer Studies

The following conclusions can be drawn from the present investigation concerned with the impingement of both orthogonal and inclined jets in initially stagnant and crossflowing surroundings:

(i) The use of the Chilton-Colburn heat-mass transfer analogy together with the sublimation of naphthalene appears to be a suitable method of determining local heat transfer coefficients associated with impinging jets. In general when comparisons are possible, the present results are in reasonable agreement with those reported previously.

(ii) For jets exiting into otherwise quiescent surroundings non-orthogonal impingement has the effect of reducing the stagnation heat transfer coefficient. This effect is slight for an impingement angle of 60° to the horizontal but is marked at an angle of 45°. In the present tests, (for all conditions) the mean reductions in stagnation heat transfer (compared with the orthogonal case) were 3% at an angle of 60°, and 18% at 45°. As would be expected, the distribution of local heat transfers is not symmetrical in the inclined cases.

(iii) Crossflows, generally decrease the stagnation point heat transfers and effectively displace the regions of high heat transfer downstream. The local heat transfers upstream of the impingement region are generally decreased under crossflow, whereas heat transfers downstream are generally increased. The 'upstream degradation' and subsequent 'downstream enhancement' of local heat transfers can be explained by consideration of the flow phenomena. The upstream degradation is caused by the deceleration of the crossflowing stream as it approaches the jet (due to the blockage effect). In the downstream zone however, jet flow impingement as well as the flushing influence of the crossflowing stream cause higher heat transfers as the fluid is swept out of the test section (accelerating in the process).

(iv) Inclination of the jet into the crossflow (increases) decreases the reduction of stagnation point heat transfers. In fact in many instances with the inclined jets, the heat transfers at a particular crossflow were virtually independent of the jet inclination.

(v) The usual secondary peaks (associated with the transition from laminar to turbulent flow in the wall jet) were observed for orthogonally impinging jets at low nozzle to target spacings. Under crossflow conditions however, these secondary peaks were not observed. This study thus suggests that crossflows tend to smooth-out the secondary peaks at low nozzle to target spacings.

8.2 Recommendations for Future Work

(i) The heat transfer measurements reported in this thesis are associated with a limited range of conditions. Thus the measurements should be extended to both the higher nozzle to target spacings ($Z/d > 8$) and lower nozzle to target spacings ($Z/d < 2$) which were not covered in this investigation. Further tests should also be conducted for a wider range of jet Reynolds numbers and jet blowing rates. In addition, a wider range of impingement angles should be examined.

(ii) To cover the wide range of conditions of interest in practice may be extremely difficult and time consuming by experimental methods, so that the possibility of employing numerical simulations should be examined.

(iii) The programme of work reported in this thesis is solely for single jets. In many practical applications arrays of these jets are employed. It is therefore desirable to extend the measurements to include arrays of orthogonal and inclined circular jets in crossflows as well as in stagnant surroundings. Local as well as average heat transfers should be studied.

(iv) It is sometimes claimed that a slot jet gives a higher heat transfer performance than a circular jet under otherwise identical operating conditions. To resolve this, it is clearly desirable to extend the experimental techniques adopted in this study to the impingement of orthogonal and inclined slot jets in crossflows as well as in otherwise quiescent surroundings.

REFERENCES

I. LAWRENCE, M.N.
Forced Convection Technique for Gas Fired Rapid Billet Heating.
J. Inst. Gas. Eng. Vol. 63, p. 515, 1965.

2. PERRY, J.
WINTER, E.F.
WILCOCK, R.
Rapid Heating of Steel for Hot Working Steel Times.
Vol. 194, p. 761, 1967.
Vol. 195, p. 111, 1967.
Vol. 195, p. 170, 1967.

3. CHEN, D.C.C.
McGRATH, J.A.
BROWN, R.M.
WINTER, E.F.
Introduction to the Principle and Technique of High-Speed Convective Heating.
Symp. on Controlled Atmospheres and Rapid Heating. Paper 1, MOR 343F, Shell Int. Petroleum Co. Ltd., London. 1968.

4. BOXALL, T.D.
Metallurgical Improvements in the Reheating of Steel by Jet-Impingement.
Symp. on Controlled Atmospheres and Rapid Heating. Paper 2, Shell Int. Petroleum Co. Ltd. London 1968.

5. SOULAGES, J.
Practical Applications of the Jet Impingement Heating Technique in France.
Symp. on Controlled Atmospheres and Rapid Heating., Paper 3, Shell Int. Petroleum Co. Ltd., London. 1968.

6. THOMPSON, D.I.
Developments and Future Possibilities in the use of the Jet Impingement Heating Technique
Symp. on Controlled Atmospheres and Rapid Heating. Paper 4, Shell Int. Petroleum Co. Ltd., London 1968.

7. LUCAS, D.M.
MASTERS, J.
TOTH, H.E.
Prediction of the Performance of Rapid Heating Furnaces.
J. Inst. Gas. Eng. Vol. 67, p. 397, 1969.

8. CHEETHAM, H.A.
LANDRY, R.S.
Rapid Heating of Metals by Jet Impingement.
Hamworthy Eng. Ltd., Poole, 1971.

9. WINTER, E.F.
Jet Impingement. A Versatile Gas-Fired System for Process Heating of Metals.
Shell International Gas Ltd., Report No. SIG 71/7, 1971.

10. DUGGAN, A.P.
ISSAC, J.G.
THOMAS, J.R.
Convective Heating Investigations and Recent Developments.
Iron and Steel Institute, Slab Reheating Conference, Bournemouth.
21/22 June, 1972.

11. BURGESS, B.W.
CHAPMAN, S.M.
SETO, W.
The Papridryer Process.
Parts 1&11
Pulp Paper Mag. Can.,
Vol. 73, No. 11
p. 314, 1972.

12. SCHEUTER, K.R.
DOSDOGRU, G.A.
Investigation of Impinging Air Jet Dryers with Respect to Possible Automation.
Tech. Assoc. of Graphic Arts (Taga) Proc. 224, 1971.

13. HARDISTY, H.
Industrial Drying Using Impinging Air Jets.
Report Nos. 226 & 227.
The University of Bath School of Mechanical Engineering 1973.

14. BLACK, J.
HARDISTY, H.
Heat and Mass Transfer in Ink Drying and Infra-Red Dryness Measurements.
J. of Mech. Eng. Science.
Vol. 18, p. 99, 1976.

15. VAN HEININGEN, A.R.P.
MUJUMDAR, A.S.
DOUGLAS, W.J.M.
Numerical Prediction of the Flow Field and Impingement Heat Transfer caused by a Laminar Slot Jet.
Int. J. of Heat Transfer
Vol. 19, p. 654, 1976.

16. CCLIN, P.E.
OLIVARI, D.
The Impingement of a Circular Jet Normal to a Flat Surface with and without Crossflow.
Von Karman Institute for Fluid Mechanics. 1969.

17. STRAND, T.
Inviscid Incompressible Flow Theory of Normal and Slightly Oblique Impingement of a Static Round Jet on the ground.
J. of Aircraft.
Vol. 4, No. 5, p. 446, 1967.

18. SCHRADER, H.
Drying of Moist Surfaces by means of Hot Air Jets: Flow Characteristics and Mass Transfer.
Forschungsh. Ver. Deutsch.
Ing. 484. 1961.

19. GLAUERT, M.B.
The Wall Jet.
Journal of Fluid Mechanics
Vol. 1, p. 625, 1956.

20. BAKKE, P.
An Experimental Investigation of a Wall Jet
J. of Fluid Mechanics
Vol. 2, p. 467, 1957.

21. BRADSHAW, P.
LOVE, E. M.
The Normal Impingement of a Circular Jet on a Flat Surface
A.R.C. Rand M . 3205. 1959.

22\. POT, P. — The Impingement of a Circular Jet Normal to a Flat Surface with and without Crossflows. VKI Project Report 1968.

23\. SCHACH, W. — The Deflection of a Circular Fluid Jet by a Flat Plate Perpendicular to the Flow Direction Ingenieur Archiv, Vol. 6, p. 51, 1935.

24\. SHEN, Y.C. — Theoretical Analysis of Jet-Ground Plane Interaction. Institute of the Aerospace Sciences. Paper No. 62-144 1962.

25\. LUDWIG, G.R.
BRADY, W.G. — Theoretical and Experimental Studies of Impinging Uniform and Non-Uniform Jets. Cornell Aeronautical. Lab. Buffalo N.Y. CAL Rep TG. 1818-G 1964.

26\. PAI, S-I. — Fluid Dynamics of Jets. D. Van Nostrand Co. Inc. London 1954.

27\. BIRKHOFF — Applied Mathamatics and Mechanics Vol. 2, Academic Press Inc, London 1957.

28\. SCHLICHTING, H. — Boundary Layer Theory, 4th edition McGraw-Hill Book Co., New York, 1962.

29. ABRAMOVICH, G.N. The Theory of Turbulent Jets M.I.T. Press. Cambridge, Mass. 1963.

30. NORSTER, E.R. Second Report on Jet Penetration and Mixing Studies. Dept. of Aircraft Populsion. Report No. PD/JP2. Cranfield Institute of Technology 1964.

31. GAUNTNER, J.W. LIVINGWOOD, P.H. Survey of Literature on Flow Characteristics of a Single Turbulent Jet Impinging on a Flat Plate. NASA. TN. D-5652. 1970.

32. WOLFSHTEIN, M. Some Solutions of the Plane Turbulent Impinging Jet. Trans. ASME, J. Basic Eng, Vol. 92, p. 915, 1970.

33. WOLFSHTEIN, M. STROTTER, A. Heat Transfer between an Impinging Jet and a Flat Surface. Israel Journal of Technology. Vol. 2, p. 131, 1964.

34. CORRSIN, S. Investigation of Flow in an Initially Symmetrical Heated Jet of Air. NACA. Wartime Reports, Series WR-94 1943.

35. SNEL, H. A Model for the calculation of the Properties of a Jet in a Crossflow. National Aerospace Laboratory Report No. NLR. TR. 74080. U. 1974.

36.	KEFFER, J.F. BAINES, W.D.	The Round Turbulent Jet in a Cross-wind. J. Fluid Mech. Vol. 15, p. 481, 1963.
37.	JORDISON, R.	Flow in a Jet Directed Normal to the Wind. Aero. Res. Council. R and M No. 3074, 1958.
38.	TYLER, R.A. WILLIAMSON, R.G.	Observation of Tunnel Flow Separation Induced by an Impinging Jet. National Research Council of Canada. NCR No. 11617, 1970.
39.	TYLER, R.A. WILLIAMSON, R.G.	Tunnel Flow Breakdown from Inclined Jets. National Research Council of Canada. NCR No. 11994, 1971.
40.	CALLAGHAN, E. RUGGERI, R.S.	Investigation of the Penetration of an Air Jet Directed Perpendicularly to an Air Stream. NACA Tech Note 1615, 1948.
41.	SCHETZ, J.A. BILLIG, F.S.	Penetration of Gaseous Jets Injected into a Supersonic Stream. J. of. Spacecraft Vol. 3, No. 11. P. 1658, 1966.
42.	REILLY, R.S.	Investigation of the Deformation and Penetration of a Turbulent Subsonic Jet Issuing Transversely into a Uniform Mainstream. PhD. Thesis., University of Maryland, 1968.

43. MARGASON, R.J.
The Path of a Jet Directed at Large Angles to a Subsonic Free Stream.
NASA. TN. T-4919. 1968.

44. SHANDOROV, G.S.
Flow from a Channel into a Stationary and Moving Media.
Zh. Tekhn. Fiz, 37, 1, 1957.

45. PLATTEN, J.K.
KEFFER, J.F.
Deflected Turbulent Jet Flows
Journal of Appl. Mech. Trans. ASME, Vol. 93. p. 756, 1971.

46. WOOLER, P.T.
BURGHART, G.H.
GALLAGHER, J.T.
Pressure Distribution on a Rectangular Wing with a Jet Exhausting Normally into an Airstream.
J. Aircraft, Vol. 4. p. 537, 1967.

47. RAMSEY, J.W.
GOLDSTEIN, R.J.
Interaction of a Heated Jet with a Deflecting Stream.
ASME Paper No. 71-HT-2. p. 1, 1971.

48. KAMOTANI, Y.
GREBER, I.
Experiments on a Turbulent Jet in a crossflow.
AIAA Journal
Vol. 10, p. 1425, 1972.

49. STOY, R.L.
BEN-HAIM, Y.
Turbulent Jets in Confined Crossflow.
Trans. ASME, J. of Fluids Eng., Vol. 95, p. 551, 1973.

50.	FEARN, L. WESTON, P.	Induced Pressure Distribution of a Jet in Crossflow. NASA TN D-7916, 1975.
51.	TAYLOR, P.	An Investigation of an Inclined Jet in a Crosswind. The Aeronautical Quartarly. Vol. 28, Part 1, p. 51, 1977.
52.	RUDINGER, G. MOON, L.F.	Laser Doppler Measurement in a Subsonic Jet Injected into a Subsonic Crossflow. J. of Fluid. Eng. Vol. 98, p. 516, 1976.
53.	LEE, C.C.	A Review of Research on the Interaction of a Jet with an External Stream. Brown Eng. Co. Inc. Huntsville. Ala. Research Labs. Report No. IN-R-184. Defence Documentation Centre. Acquisition No. AD 630294, 1966.
54.	SKIFSTAD, J.G.	Aerodynamics of Jets Pertinent to VTOL Aircraft. J. Aircraft . Vol. 7, No. 3, p. 193. 1970.
55.	ARGANBRIGHT, D.G. RESCH, H.	A review of Basic Aspects of Heat Transfer Under Impinging Air Jets. Wood Science and Technology. Vol. 5, p. 73, 1971.
56.	PERRY, K.P.	Heat Transfer by Convection from a Hot Gas Jet to a Plane Surface. Proc. I. Mech. E. Vol. 168, p. 775, 1954.

57. THURLOW, G.G. — Communication on Ref. 56. Proc. I. Mech. Eng. Vol. 168, p. 781, 1954.

58. SMIRNOV, V.A.; VEREVOCHKIN, G.E.; BRDLICK, P.M. — Heat Transfer Between a Jet and a Held Plate normal to Flow. J. Heat Mass Transfer. Vol. 2, p. 1, 1961.

59. GARDON, R.; COBONDUE, J. — Heat Transfer Between a Flat Plate and Jets of Air Impinging on it. Int. Develop in Heat Transfer, ASME. New York. p. 454, 1962.

60. HUANG, G.C. — Investigations of Heat Transfer Coeficients for Air Flow through Round Jets Impinging Normal to a Heat Transfer Surface. J. Heat Transfer. Vol. 85, p. 237, 1963.

61. DONALDSON, C. du. P.; SNEDEKER, R.S.; MARGOLIS, D.P. — A study of free jet impingement Part. 1. Mean properties of free and impinging jets. J. of Fluid Mechanics. Vol. 45, p. 281, 1971.

62. DONALDSON, C.du.P.; SNEDEKER, R.S.; MARGOLIS, D.P. — A study of free jet impingement Part. 2. Free Jet Turbulent Structure and Impingement Heat Transfer. J. of Fluid Mechanics. Vol. 45, p. 477, 1971.

63. ROSENBAUM, H.; DONALDSON, C.du.P. — A Theoretical Study of Free Jet Impingement. Aeronautical Reasearch Associates of Princeton Inc. Report No. 101, 1967.

64.	VICKERS, J.M.F.	Heat Transfer Coefficients between Fluid Jets and Normal Surfaces. Ind. Chem. Eng. Vol. 51, No. 8, p. 967, 1959.
65.	WARD, J. IDERIAH, F.J.K. PROBERT, S.D. DUGGAN, A.	Mass Transfer Technique for Investigation of Heat Transfer by Jet Impingement Systems. J. Mech. Eng. Sci. Vol. 14, No. 6, p. 389, 1972.
66.	KOOPMAN, R.N.	Local and Average Transfer Coefficients for Multiple Impinging Jets. Ph. D. Thesis, University of Minnesota. 1975.
67.	DAANE, R.A. HAN, S.T.	An Analysis of Air Impingement Drying. TAPPI, Vol. 44, No. 1, p. 73, 1961.
68.	GARDON, R. AKFIRAT, J.C.	The role of Turbulence in Determining the Heat Transfer Characteristics of Impinging Jets. Int. J. Heat Mass Transfer. Vol. 8, p. 1261, 1965.
69.	OUDEN, C. DEN. HOOGENDOORN, C.J.	Local Convective Heat Transfer Coefficients for Jets Impinging on a Plate-Experiments using a Liquid-crystal Technique. 5th Int. Heat Transfer Conference, Tokyo, Japan, Vol. 5, p. 293, 1974.
70.	KESTIN, J. WOOD, R.T.	The Influence of Turbulence on Mass Transfer from Cylinders. J. of Heat Transfer. Vol. 93, p. 321, 1971.

71. KATAOKA, K. MIZUSHINA, T. Local Enhancement of the Rate of Heat Transfer in an Impinging Round Jet by Free-stream Turbulence. 5th Int. Heat Transfer Conference. Tokyo, Japan, Vol. 2, p. 305, 1974.

72. SCHLUNDER, E.U. GNIELINSKI, V. Heat and Mass Transfer between Material and Impinging Jet. Chem. Ing. Techn. Vol. 39, p. 578, 1967.

73. ECKERT, E. Die Berechnung des Warme ubergangs in der laminaren Grenzschicht Umstromter Korper VDI-forschungsheft. 416, B, Vol. 13, Sell Hoctote. 1942.

74. LEWIS, J. S. A Heat and Mass Transfer Analogy and its Application to Finned Surfaces. Ph. D. Thesis, University of Strathclyde Glasgow. 1969.

75. GARDON, R. AKFIRAT, J.C. Heat Transfer Characteristics of Impinging Two-Dimensional Air Jets. Trans. ASME. Journal of Heat Transfer. Vol. 88, p. 101, 1966.

76. KORGER, M. KRIZEK, F. Mass Transfer Coefficients in Impingement Flow from Slotted Nozzles. Int. J. Heat Mass Transfer. Vol. 9, pp. 337-344, 1966.

77. HILGEROTH, E. Heat Exchange into Jet Streams Perpendicular to the Exchange Surface. Chem. Ing. Tech. Vol. 37, pp. 1264-1272, 1965.

78. METZGER, D.E.
KORSTAD, R.J.
Effects of Crossflow on Impingement Heat Transfer.
Trans. ASME. Journal of Engineering for Power. Vol. 94, p. 35, 1972.

79. KERCHER, D.M.
TABAKOFF, W.
Heat Transfer by a Square Array of Round Air Jets Impinging Perpendicular to a Flat Surface Including the Effect of Spent Air.
Trans. ASME, J. of Engineering for Power, Vol. 92, p. 73, 1970.

80. WALZ, D.R.
Spot Cooling and Heating of Surfaces with High Velocity Impinging Jets.
Water Jets on Plane and Curved Surfaces
Slot Jets on Curved Surfaces.
Tech Report No. 61. Dept. of Mech. Eng. Stanford University, Stanford California. 1964.

81. BOUCHEZ, J.F.A.
Heat Transfer to an Impinging Circular Jet in a Crossflow.
Ph.D Thesis, University of Minnesota 1973.

82. SPARROW, E.M.
GOLDSTEIN, R.J.
ROUF, M.A.
Effect of Nozzle-Surface Seperation Distance on Impingement Heat Transfer for a Jet in a Crossflow.
J. Heat and Mass Transfer.
Vol. 18, p. 528, 1975.

83. REYNOLDS, O.
On the Extent and Action of the Heating Surface of Steam Boilers.
Proc. of Manchester Lit. & Phil. Soc., Vol. 7, p. 14, 1874.

84.	REYNOLDS, O.	Scientific Papers Vol. 1, p. 81, Cambridge University Press, 1901.
85.	PRANDTL, L.	Eine Bezie hung Zwischen Warmeaustausch und Stromung Zwiderstand der Flussigkeiten Phys. Zeitschen, Vol. 11, p. 1072, 1910.
86.	TAYLOR, G.I.	Conditions at the surface of a body exposed to the wind. A.R.C. R & M. 272, 1919.
87.	VON KARMAN, T.	The analogy between fluid fiction and Heat Transfer. Trans. A.S.M.E, J. of Heat Transfer. Vol. 61,.p. 705, 1939.
88.	COLBURN, A.P.	A method of Correlating Forced Convection Heat Transfer Data and a comparison with Fluid Friction. Trans. A.I. Chem. Eng. Vol. 29, p. 14, 1933.
89.	CHILTON, T.H. COLBURN, A.P.	Mass Transfer (Absorption) Coefficients. Ind. Eng. Chem. Vol. 26, p. 1183, 1934.
90.	KLEIN, V.	Dissertation Tech. Hochsch, Hanover, 1933.
91.	WINDING, C.C. CHENEY, A.J.	Mass and Heat Transfer in Tube Banks. Ind. Eng. Chem. Vol. 40, p. 1087, 1948.

92. BEDINGFIELD, C.H.
DREW, T.B.
Analogy between Heat Transfer and Mass Transfer.
A Psychrometric Study.
Ind. Eng. Chem. Vol. 42, p. 1164, 1950.

93. SHERWOOD, T.K.
Heat Transfer, Mass Transfer and Fluid Friction relationships in Turbulent flow.
Ind. Eng. Chem. Vol. 42, p. 10, 1950.
Mass. Heat and Momentum Transfer between phases.
Chem. Eng. Progress, Symposium Series 55(25) 1959.

94. SHERWOOD, T.K.
BRYANT, H.S.
Mass Transfer through Compressible Boundary Layers.
Canadian Journal of Chem. Eng. Vol. 35, p. 51, 1957.

95. CHRISTIAN, W.J.
KEZIOS, S.D.
Experimental Investigations of Mass Transfer by Sublimation from Sharp Edged Cylinders in Axi-symmetric Flow with Laminar Boundary Layer.
Heat Transfer and Fluid Mech. Inst. Pasadena, California. 359. 1957.

96. KREITH, F.
TAYLOR, J.H.
CHONG, J.P.
Heat and Mass Transfer from a rotating disc.
Trans. ASME, J of Heat Transfer. Vol. 82, p. 13, 1960.

97. SHERWOOD, T.K.
TRASS, O.
Sublimation Mass Transfer through Compressible Boundary Layers on a Flat Plate.
Trans. ASME, J of Heat Transfer. Vol. 82, p. 313, 1960.

98. HOUSTON, R.M.
Nozzle Heat Transfer Predictions from Sublimation Measurements on a Model of a Solid Fuel Rocket.
M. Sc. Thesis, Cranfield Inst. of Tech. Cranfield. 1960.

99. MACLEOD, N.
COX, M.D.
TODD, R.S.
A Profilometric Technique for Determining Local Mass Transfer Rates.
Chem. Eng. Sci. Vol. 17, p. 923, 1962.

100. LUIKOV, A.V.
Heat and Mass Transfer with Transpiration Cooling.
Int. J. Heat & Mass Transfer. Vol. 6, p. 559, 1963.

101. WONG, P.W.
Mass and Heat Transfer from Circular Finned Cylinders.
J. I. H. V. E. Vol. 34, p. 1, 1966.

102. SOUTH, V.
Heat and Mass Transfer Rates Associated with the Drying of Plywood Veneer using Superheated Steam at Various Angles of Impingement.
M. Sc. Thesis, Oregon State Univ, 1967.

103. NASH, K.L.
MAXWELL, R.W.
Convective Mass Transfer from Stationary and Moving Surfaces.
Engineering Department, University of Leicester Report 70-13. 1970.

104. FRANCIS, W.E.
Studies of Flow Patterns and Convection in Rapid Heating Furnaces using Model Techniques.
J. Inst. Gas. Eng. Vol. 7, p. 335, 1967.

105. KOOPMAN, R.N.
SPARROW, E.M.
Local and Average Transfer Coefficients due to an Impinging Row of Jets.
Int. J. Heat Mass Transfer.
Vol. 19, p. 673, 1976.

106. MACLEOD, N.
TODD, R.B.
The Experimental Determination of Wall-Fluid Mass Transfer Coefficients Using Plasticized Polymer Surface Coatings.
Int. J. Heat Mass Transfer.
Vol. 16, p. 485, 1973.

107. NEAL, S.B.H.
The Development of The Thin-Film Napthalene Mass-Transfer Anologue Technique for the Direct Measurement of Heat-Transfer Coefficients.
Int. J. Heat Mass Transfer Vol. 18, p.539, 1975.

108. NEAL, S.B.H.C.
NORTHOVER, E.W.
HITCHCOCK, J.A.
The Development of a Technique for Applying Napthalene to surfaces for Mass Transfer Analogue Investigations.
J. Phys. E. Scient. Instrum.
Vol. 3, p. 636, 1970.

109. LEWIS, J.S.
A Heat-Mass Transfer Anology Applied To Fully Developed Turbulent Flow In Annulus.
J. Mech. Eng. Sci. Vol. 13, No 4. p. 286, 1971.

110. WARD, J.
DIXON, M.
PROBERT, S.D.
Jet Impingement Heating of Steel Slabs.
School of Mech. Eng. Cranfield Institute of Technology.
Final Report, S.R.C. Contract No. B/RG/15139. 1974.

111.	DAVIES, R.M. LUCAS, D.M. MOPPETT, B.E. GALSWORTHY, R.A.	Isothermal Model Studies of Rapid Heating Furnaces. Journal of the Institute of Fuel, Vol. 44, p. 453, 1971.
112.	JAYATILLAKA, C.U.L.	The Influence of Prandtl Number and Surface Roughness on the Resistance of the Laminer Sublayer to Momentum and Heat Transfer. Progress in Heat and Mass Transfer, Vol. 1, p. 193, Pergamon Press, Oxford 1969.
113.		International Critical Tables McGraw-Hill Book Co. Inc., New York. Vol. 3, p. 208, 1926.
114.	SOGIN, H.H.	Sublimation from Discs to Air Streams Flowing Normal to their Surfaces. Trans. ASME, J. Heat Transfer. Vol. 80, p. 61, 1958.
115.		Handbook of Chemistry and Physics 46th Edition, Chemical Rubber, Cy. Cleveland, Ohio 1965.
116.	SPARROW, E.M. LEE, L.	Analysis of Flow-field and Impingement Heat/Mass Transfer due to a Non-uniform Slot Jet. Trans. ASME, J. Heat Transfer, Vol. 97, p. 191, 1975.
117.	POPE, A. HARPER, J.J.	Low-speed Wind Tunnel Testing John Wiley and Sons Inc. New York 1966.

118. STERLAND, P.R. HOLLINGSWORTH, M.A. An Experimental Study of Multiple Jets Directed Normally to a Crossflow. J. Mech. Eng. Science Vol. 17, No. 3. p. 117, 1975.

119. PANKHURST, R.C. HOLDER. D.W. Wind Tunnel Technique., an account of Experimental Methods in Low- and High-speed Wind Tunnels. Pitman, London 1952.

120. BRADSHAW, P. Experimental Fluid Mechanics Pergamon Press, New York 1964.

121. STANBROOK, A. The Surface Oil Flow Technique used in High Speed Wind Tunnels in the United Kingdom. RAE. Tech. Note No. Aero 2712, 1960.

122. HILLS, R. Use of Wind Tunnel Model Data in Aerodynamic Design. J. Royal Aeronautical Society, Vol. 55, p. 1, 1951.

123. BLACK, J. A Note on the Vortex Patterns in the Boundary Layer Flow of a Swept-back Wing. J. Royal Aeronautical Society, Vol. 56, p. 279, 1952.

124. STALKER, R.J. A Study of the China-film Technique for Flow Indication. A.R.L. Report A 96, 1955.

125. STANBROOK, A. Experimental Observation of Vortices in Wing-Body Junctions. R.A.E. Report No. AERO 2589, 1957.

126. MALTBY, R.L. KEATING, R.F.A. Flow Visualisation in Low-speed Wind Tunnels, Current British Practice. RAE Tech. Note, No. AERO 2715, 1960.

127. WU, J.C. McMAHON, H.M. MOSHER, D.K. WRIGHT, M.A. Experimental and Analytical Investigations of Jets Exhausting into a Deflecting Stream. J. of Aircraft. Vol. 7, p. 44, 1970.

128. SQUIRE, L.C. The Motion of a Thin Oil Sheet Under the Boundary Layer on a Body. R.A.E. Report No. AERO 2636, 1960.

129. TANNER, L.H. BLOWS, L.G. A Study of the Motion of Oil Films on Surfaces in Air Flow, with Applications to the Measurement of Skin Friction. Journal of Physics E. Scientific Instruments. Vol. 9, p. 194, 1976.

130. POPE, A. GOIN, K.L. High Speed Tunnel Testing John Wiley and Sons, Inc. New York 1965.

131. HOLDER, D.W. NORTH, R.J. Schlieren Methods. National Phys. Lab. Notes on Applied Sc. No. 31, H.M.S.O. London 1963.

132. PATRICK, M.A. Experimental Investigations of Mixing and Flow in a Round Turbulent Jet Injected Perpendicularly into a Main Stream. Journal of the Institute of Fuel. Vol. 39, p. 425, 1967.

133. MOUSLEY, L.J.
BOOTHROYD, D.N.
A Device for Producing Small Bubbles for use in the Visualisation of Air Movement.
J. Agric, Engng. Res., Vol. 16, p. 364, 1971.

134. COLLADAY, R.S.
RUSSELL, L.M.
LANE, J.M.
Streak-line Flow Visualisation of Discrete Hole Film Cooling with Holes Inclined 30° to Surface.
NASA Tech. Note. No. D8175, 1976.

135. ZANDBERGEN, T.
JOOSEN, C.J.J.
Experimental Investigation of Round Turbulent Jets in a Crossflow.
National Aerospace Laboratory.
The Netherlands.
Report No. NLR. TR 74013, 1973.

136. POPIEL, C.O.
TULISZKA, E.
Heat Transfer from a Rotating Disc in an Impinging Round Air Jet.
5th Int. Heat Transfer Conference,
Tokyo Japan. Vol. 3, p. 212, 1974.

137. REMINGTON, J.S.
FRANCIS, W.
Pigments their Manufacture Properties and Use.
Leonard Hill, Ltd. London 1954.

138. WOLFSHTEIN, M.
Empirical Correlations for the Evaluation of Stanton Number in Impinging Jets.
Aeronautical Research Council
Heat and Mass Transfer Sub-Committee.
A.R.C. 27613, 1966.

139. PARADINE, C.G.
RIVETT, B.H.P.
Statistical Methods for Technologists
The English Universities Press Ltd.
London 1960.

140. RAMSEY, J.W.
The Interaction of a Heated Air Jet with a Deflecting Flow.
Ph.D. Thesis, University of Minnesota, 1969.

141. MAYHEW, Y.R.
ROGERS, G.F.C.
Thermodynamic and Transport Properties of Fluids .
Basil Blackwell, Oxford, 1971.

142. GORDIER, R.L.
Studies of Fluid Jets Discharging Normally into Moving Liquid.
St. Anthony Falls Hydraulic Lab. Tech. Paper No. 28, Series B, Minnesota, 1959.

143. REYNOLDS, A.J,
Turbulent Flows in Engineering
John Wiley and Sons Ltd. London 1974.

144. CHIPLUNKER, D.
Heat Transfer in Jet Impingement Furnaces.
M.Sc. Thesis, Cranfield Institute of Technology, 1973.

145. JONES, R.E.
Hot Spot Formation in Rapid Heating Furnace Walls.
M.Sc. Thesis, Cranfield Institute of Technology, 1974.

146. PERRY, C.J.
Heat Transfers from Impinging Swirling Jets.
M.Sc. Thesis, Cranfield Institute of Technology, 1975.

147. HINZE, J.O.
Turbulence
McGraw-Hill Book Co. Ltd.,
New York, 1959.

APPENDICES

APPENDIX A

MOMENTUM, HEAT AND MASS TRANSFER EQUATIONS.

(1) Momentum Transfer

Laminar flow: $\tau_L/\rho = -\frac{\mu}{\rho}\partial U/\partial y = -\nu\frac{\partial U}{\partial y}$

Turbulent flow: $\tau_T/\rho = -\frac{\mu_t}{\rho}\partial U/\partial y = -\epsilon_m\frac{\partial U}{\partial y}$

Complete equation: $\tau/\rho = -(\nu + \epsilon_m)\frac{\partial U}{\partial y}$

where μ = molecular viscosity of momentum transfer

μ_t = eddy viscosity of momentum transfer

ν = kinematic viscosity of molecular diffusivity of momentum

ϵ_m = eddy diffusivity of momentum

(2) Heat Transfer

Laminar flow: $q_L = -k\,\partial T/\partial y$

Turbulent flow: $q_T = -\rho c_p \epsilon_h \partial T/\partial y$

Complete equation: $q/\rho c_p = -(\alpha + \epsilon_h)\partial T/\partial y$

where α = molecular diffusivity of heat $(k/\rho c_p)$

ϵ_h = turbulent eddy diffusivity of heat

(3) Mass Transfer

Laminar flow: $N_L = -D\partial c/\partial y$

Turbulent flow: $N_T = -\epsilon_D \partial c/\partial y$

Complete equation: $N = -(D + \epsilon_D)\partial c/\partial y$

where D = molecular diffusivity of mass
ϵ_D = turbulent eddy diffusivity of mass.

APPENDIX B

ESTABLISHED ANALOGIES FOR HEAT, MASS AND MOMENTUM TRANSFER.

This Appendix examines briefly some analytical models which have so far been used to establish analogies between the transport processes. The original analogies relating Heat, and momentum transfer are first of all presented. This presentation is followed by a discussion of the various heat-mass transfer analogies which have been so far proposed. Dimensionless mass transfer equations are also presented and the analogies (particularly those relevant to this investigation) are critically examined.

B1 The Analogy Between Heat and Momentum Transfer.

Reynolds analogy can only be obeyed exactly in boundary layer flows under certain conditions. However, by making certain assumptions, analogies have been proposed which are obeyed approximately for both pipe and boundary layer flows.

Now
$$\tau/\rho = (\nu + \epsilon_m)dU/dy \qquad (B.1)$$

$$q/\rho c_p = (\alpha + \epsilon_h)dt/dy \qquad (B.2)$$

where ϵ_m, ϵ_h are turbulent eddy diffusivities of momentum and heat.
The equations (B.1) and (B.2) can be made non-dimensional by the following substitution:

$$U^+ = U/\sqrt{\frac{\tau_w}{\rho}} \qquad y^+ = \frac{y\sqrt{\tau_w/\rho}}{\nu}$$

$$t^+ = \frac{t_w - t}{q_w}\rho c_p\sqrt{\tau_w/\rho}, \quad t_w = \text{wall temperature (const.)}$$

Yielding
$$\tau/\tau_w = \left(\frac{\nu + \epsilon_m}{\nu}\right)dU^+/dy^+ \qquad (B.3)$$

$$q/q_w = \left(\frac{\alpha + \epsilon_h}{\nu}\right)dt^+/dy^+ \qquad (B.4)$$

Reynolds analogy assumes:-

(1) that $\tau/\tau_w = q/q_w$ i.e. the same distribution of shear stress and heat flux.

This is strictly true only in certain cases (e.g. heat generating fluid in a constant temperature duct).

(2) that $\epsilon_m = \epsilon_h$

(3) that $\nu = \alpha$ or $Pr = 1$.

Thus we obtain $dt^+ = dU^+$

or $t^+ = U^+$ since $U^+_w = t^+_w = 0$ at the wall.

Now Stanton number $(St) = h/(\rho C_p U_b) = 1/(t^+_b U^+_b)$

where U_b = bulk mean velocity

Also $C_f/2 = 1/U_b^{+2}$

Hence $St = C_f/2$

B1.1 Prandtl-Taylor Analogy

Prandtl and, independently, Taylor improved upon Reynolds analogy by distinquishing a region of molecular diffusion near the wall (of the same thickness for velocity and temperature), and a fully turbulent outer core where, in effect, Reynolds analogy is valid, with $Pr_t = 1$. The Prandtl-Taylor analogy is an extension of Reynolds analogy to Prandtl numbers greater than unity ($Pr > 1$)

The flow is considered to consist of a laminar sublayer and a turbulent core, and certain simplifying assumptions were made about both layers:

(a) The sublayer

In this layer, it was assumed that $\epsilon_m = \epsilon_h = 0$ and that $\tau = \tau_w$ and $q = q_w$.

Referring to the original equations (B.3) and (B.4)

Therefore $dU^+/dy^+ = 1$ and $dt^+/dy^+ = Pr$

Therefore $U^+ = y^+$ and $t^+ = Pr.y^+$

At the edge of the sublayer,

$$t^+_1 = Pr.U^+_1$$

(b) The turbulent core

In this region, it was assumed that:-

$$\epsilon_m = \epsilon_h$$

and $\tau/\tau_w = q/q_w$

$$\alpha = \nu \longrightarrow 0 \qquad \text{(for } Pr \gg 1)$$

$$dU^+ = dt^+$$

Therefore $$\int_{U_1^+}^{U_b^+} dU^+ = \int_{t_1^+}^{t_b^+} dt^+$$

Therefore $$U_b^+ - U_1^+ = t_b^+ - t_1^+$$

$$= t_b^+ - Pr.U_1^+$$

or $$t_b^+ = U_b^+ + U_1^+(Pr - 1)$$

Therefore $$St = 1/(t_b^+ U_b^+)$$

$$t_b^+ U_b^+ = U_b^{+2} + U_1^+ U_b^+(Pr - 1)$$

U_1^+ can be shown to be approx. 12

Thus $$St = \frac{1}{2/C_f + 12\sqrt{2/C_f}(Pr - 1)}$$

Although the assumptions involved are clearly unrealistic, this model illustrates an approach which is capable of considerable development, and provides a framework to which empirical results can be fitted. In actual fact, the expression predicts heat transfer for turbulent flow in tubes and boundary layers quite well, but the value of $U_1^+ = 12$, is somewhat uncertain.

B.1.2 Von Karman Analogy

Von Karman advanced the discussion by distinquishing a buffer layer, in which both molecular and turbulent diffusion are active. He maintained the same boundaries for the several layers of the velocity and temperature variations, and took $Pr_t = 1$ in the turbulent core. As mentioned earlier, the use of $U_1^+ = 12$ in the Prandtl-Taylor analogy is a rough approximation to the sublayer structure. Von Karman used a better fit, so that this is an improvement of the earlier analogies.

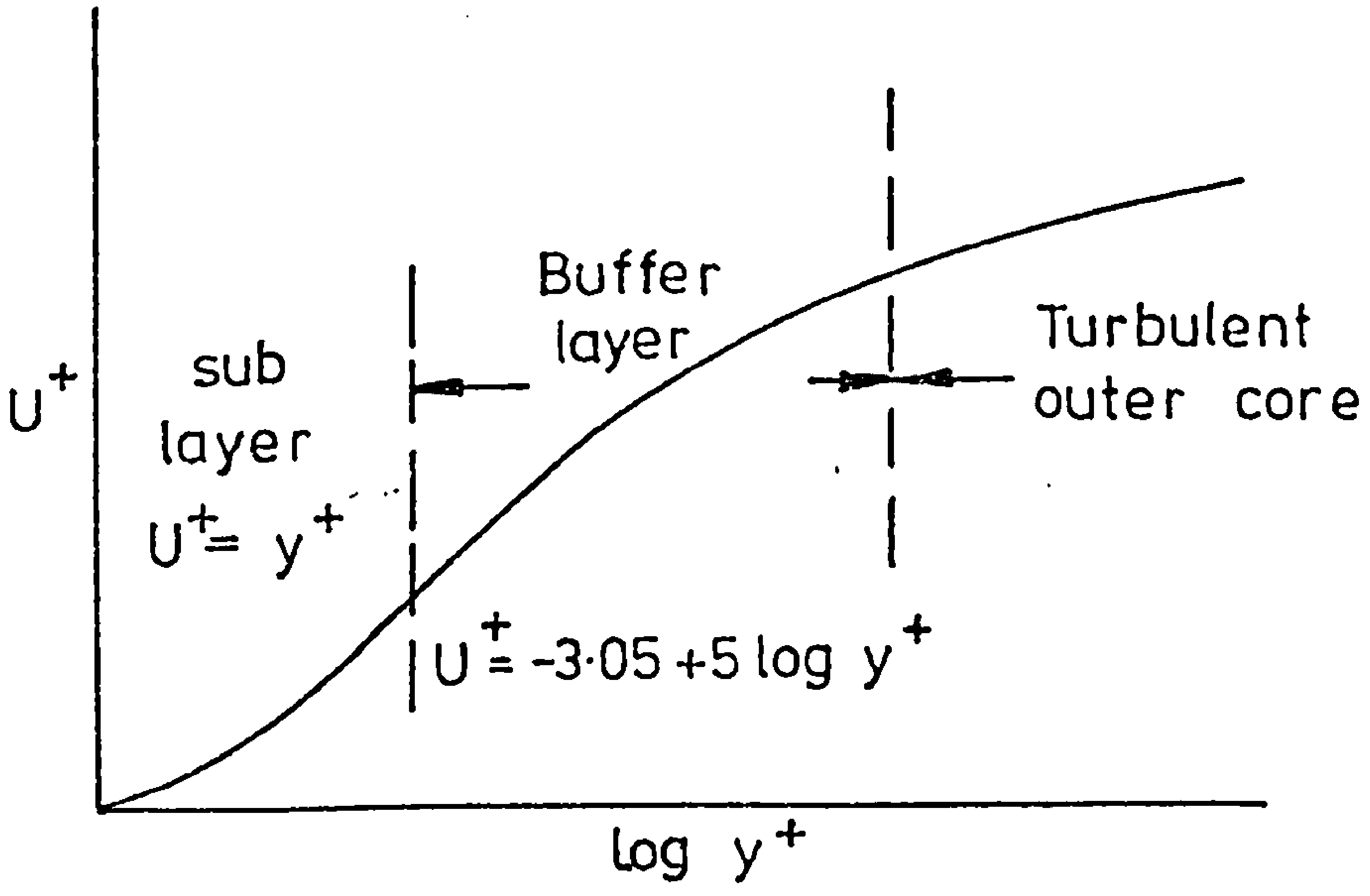

Fig. B.1.

From the original eqns. (B.3) and (B.4)

$$\frac{q/q_w}{dt^+/dy^+} - \frac{\tau/\tau_w}{dU^+/dy^+} = 1/Pr - 1 \qquad (B.1.2)$$

$(q = q_w, \tau = \tau_w, dU^+/dy^+ = 1)$

(a) Laminar sublayer $0 < y^+ < 5$

As before, $t^+ = Pr.y^+$

(b) Buffer Layer $5 < y^+ < 30$

He assumed that $\tau = \tau_w$, and $q = q_w$

$$U^+ = -3.05 + 5\log y^+$$

$$\therefore \frac{dU^+}{dy^+} = 5/y^+$$

Substituting this in equation (B.1.2)

Therefore $1/(dt^+/dy^+) - y^+/5 = 1/Pr - 1$

$$\frac{dt^+}{dy^+} = \frac{1}{y^+/5 + 1/Pr - 1}$$

Integrating,

$$t^+ = 5\log(y^+/5 + 1/Pr - 1) + \text{const.}$$

But $t^+ = 5Pr$ at $y^+ = 5$

Therefore constant $= 5Pr - 5\log(1/Pr)$

Thus in the buffer layer:

$$t^+ = 5\log(Pr.y^+/5 + 1 - Pr) + 5Pr$$

(c) Turbulent core $y^+ > 30$

He assumed $q/q_w = \tau/\tau_w$

Therefore $dU^+/dy^+ = dt^+/dy^+$ $(Pr > 1)$

i.e. $t^+ = U^+ + \text{constant}$

At $y^+ = 30$ $t^+ = 5\log(5Pr + 1) + 5Pr$

$$U^+ = -3.05 + 5\log 30$$

$$= 5 + 5\log 6$$

$$\therefore \text{const.} = t^+ - U^+$$

$$= 5\log(5Pr + 1) + 5Pr - 5 - 5\log 6$$

$$= 5(Pr - 1 + \log((5Pr + 1)/6))$$

Hence in the turbulent core:

$$t^+ = U^+ + 5(Pr-1 + \log_e((5Pr + 1)/6))$$

Thus:-

$$t_b^+U_b^+ = U_b^+ + 5U_b^+(Pr - 1 + \log_e((5Pr + 1)/6))$$

$$1/St = 2/C_f + 5\sqrt{2/C_f}\,(Pr-1 + \log_e((5Pr + 1)/6))$$

$$St = \frac{C_f/2}{1 + 5\sqrt{(C_f/2)}\left[(Pr-1) + \log_e((5Pr + 1)/6)\right]}$$

This extends the Prandtl number range, giving better predictions at higher Prandtl numbers than the Prandtl-Taylor analogy.

Later models include those due to:-

(i) Martinelli who retained Von Karman's distribution of eddy viscosity in the viscous layer, but took a more realistic account of the turbulent region, allowing $Pr_t \neq 1$, and taking the heat flux $\dot{q}$ to vary linearly, i.e. in the same way as the shear stress.

(ii) Lyon who improved upon Martinelli's model by taking account of non-linearity of $\dot{q}$ distribution but still retained Von Karman's eddy diffusivities.

(iii) Rannie, Diessler, and Rohsenow and Cohen who made improvements of the earlier analogies using their own assumptions.

B.2 Heat-Mass Transfer Analogy

Heat, mass and momentum transfers are related for a fluid flowing over the laminar sublayer of a surface in terms of a hypothetical velocity characterising turbulent mixing. The analogy states that the transfer phenomena for heat and mass are physically similar. In order to employ a heat-mass transfer analogy, it is necessary to consider the heat transfer process as the diffusion of hot molecules in one direction, and the diffusion of cold molecules through the hot molecules in the opposite direction.

The similarity between the mechanics of heat transfer and mass transfer by diffusion was used by Chilton and Colburn (Ref. 89) to establish a correlation between the rate of mass transfer and friction factor for a limited number of geometrical shapes. A theoretical relationship between heat transfer and skin friction had already been established by Colburn (Ref. 88), so it was then possible to obtain heat transfer data using mass transfer techniques.

The well established analogy between heat and mass transfer due to Chilton and Colburn (Ref. 89) states that under conditions of geometric, dynamic, and kinematic similarity, the dimensionless heat and mass transfer coefficients are equal. For heat transfer, the dimensionless coefficient is:-

$$j_H = (h/(\rho U C_p))Pr^{\frac{2}{3}} \qquad (1)$$

and for mass transfer,

$$j_M = (b/U).Sc^{\frac{2}{3}} \qquad (2)$$

Equating (1) and (2),

$$h = b.\rho.C_p\ (Sc/Pr)^{\frac{2}{3}} \qquad (3)$$

A more rigorous heat-mass transfer analogy has been produced by Neal (Ref. 107), and the thin-film technique also reported in Neal's paper is currently being developed for swirling jet studies here at Cranfield. Recent work by Lewis (Refs. 74 & 109) has shown that the Chilton-Colburn analogy has limitations due to its use of a constant empirical factor $(Sc/Pr)^{\frac{2}{3}}$ which does not allow for changes in heat and mass diffusivities which occur due to changes of flow rates etc.

An accurate form of heat-mass transfer analogy must take into account the varying contributions of molecular and turbulent diffusivity across a boundary layer. Although values of molecular diffusivities are accurately known, turbulent diffusivities are difficult to measure. The modified Von Karman's universal velocity profile concept may be employed to derive an expression for the temperature difference across a turbulent boundary layer in terms of friction factor and Prandtl number. The analogy factor then becomes St/St_M, where:-

$$St = \frac{C_f/2}{1 + 5(C_f/2)^{\frac{1}{2}}\left[Pr - 1 + \log((5Pr+1)/6)\right]}$$

And

$$St_M = \frac{c_f/2}{1 + 5(c_f/2)^{\frac{1}{2}}\left[Sc - 1 + \log((5Sc+1)/6)\right]}$$

Another recent study of a heat-mass transfer analogy was conducted by Jayatillaka (Ref. 112) who also proposed an analogy factor St/St_M where:-

$$St = \frac{(c_f/2)^{\frac{1}{2}}}{Pr_t(2/c_f)^{\frac{1}{2}} + A\left[(Pr/Pr_t)^{\frac{3}{4}} - 1\right]\left[1 + 0.28\exp(-0.007\frac{Pr}{Pr_t})\right]}$$

where $A = 8.32$ for $Pr_t = 0.9$

and $A = 9$ for $Pr_t = 1$

The corresponding mass-Stanton number is calculated by substituting Sc for Pr in the above expression.

Owing to difficulties in predicting analogy factor, the Chilton-Colburn analogy which has been used successfully in the past was used in this investigation. Except for the limitations indicated by Lewis' work (Ref. 109), the good correlations obtained between actual heat transfers, and those obtained from mass transfer models, have shown that this is a relatively simple technique which can be applied successfully. Previous users in a variety of important problems (see for example Ward et al (Ref. 65) Davies et al (Ref. 111)), have obtained results well within the accuracy to be expected when estimating heat transfer coefficients (considering that it is very difficult to predict or measure heat transfer coefficients to within an accuracy of 10%). Wolfshtein (Ref. 138), has in fact, shown in his empirical correlations for the evaluation of heat and mass transfer between isothermal surfaces and impinging jets that an estimate can only be obtained to an accuracy of ±30%.

B.3 Dimensionless Heat-Mass Transfer Relationships and their Significance

(a) Schmidt Number, $Sc = \frac{\nu}{D}$

$$= \frac{\text{Molecular diffusivity}}{\text{Mass diffusivity}} = \frac{\mu}{\rho D}$$

The Schmidt number, therefore relates concentration profiles to velocity profiles; and for situations of unity Schmidt number, the dimensionless velocity and concentration profiles will be identical.

(b) Prandtl Number Pr $= \frac{\nu}{\alpha}$

$= \frac{\text{momentum diffusivity}}{\text{thermal diffusivity}}$

$= \frac{\mu C_p}{k}$

The Prandtl number relates the temperature and velocity profiles. For situations of unity Prandtl number, the dimensionless velocity and temperature profiles will be identical.

(c) Lewis Number Le $= \frac{\alpha}{D}$

$= \frac{\text{thermal diffusivity}}{\text{mass diffusivity}}$

$= \frac{k}{\rho C_p D}$

The Lewis number thus relates the dimensionless temperature profile to the concentration profile; and situations where the Lewis number is unity will have identical temperature and concentration profiles.

(d) Reynolds Number, Re_d $= \frac{Ud}{\nu}$

$= \frac{\rho Ud}{\mu}$

$= \frac{\rho U^2}{\mu U/d}$

$= \frac{\text{Inertia force}}{\text{Viscous force}}$

The Reynolds number is therefore a measure of the relative magnitude of the inertial to the viscous forces occurring in the flow. In other words, it relates the inertia to the viscous forces. The higher the Reynolds number, the greater is the relative contribution of inertia effects. The smaller the Reynolds number, the greater the relative magnitude of the viscous effects and vice versa.

Other relevant dimensionless heat-mass entities are Nusselt number (hd/k), Sherwood number (bd/D) and Stanton number $(h/(\rho C_p U))$, and are all defined in the Nomenclature. It is important to note that the Prandtl (Pr) and Schmidt numbers (Sc) as defined above relate the molecular diffusivities of the fluid, and that those are properties of the fluid and the diffusing substance. In turbulent cases however, the story is different. In this case, turbulent Prandtl and Schmidt numbers are related as follows:-

$$Pr_t = \epsilon m / \epsilon h$$

And $$Sc_t = \epsilon m / \epsilon D$$

These are properties of the flow and of the position in it, as well as of the fluid and diffusing substance.

APPENDIX C

PROPERTIES OF NAPHTHALENE AND DETAILS OF THE CASTING TECHNIQUE.

(a) General Information

Physical Description : Naphthalene is a white crystalline solid, and has a characteristic Aromatic odour. It produces volatile flakes.

Chemical Formula : $C_{10}H_8$

Physical Properties :

Molecular weight : 128.16
Melting point : 80.1°C
Boiling point : 217.9°C
Flash point 86.0°C
Density : 1145 kg/m^3 at 20°C
Lower explosive limit in air : 0.9% by volume
Upper explosive limit in air : 5.9% by volume
Auto-ignition temperature : 526°C
Vapour pressure : 1 mm mercury at 52.6°C
Vapour density : 4.42
Gas constant R_v : 64.7 J/kg°K
Latent heat of sublimation : 559.0 kJ/kg
Coefficient of volumetric expansion : 0.00028 /deg. C

(b) Uses of Naphthalene

It is mainly used in the production of Phthalic anhydride. It is also used domestically as 'moth balls'. In heat transfer studies, it is used as a cold isothermal mass transfer substance.

(c) Hazard Analysis.

In industrial use : Virtually nil

Toxic Hazard rating :

Acute Local : Irritant, Ingestion - May involve both reversible and irreversible changes not severe enough to cause permanent injury (moderate)

Inhalation - Causes readily reversible changes which disappear after exposure (slight)

Acute Systematic :

Ingestion - as above

Inhalation - as above

Chronic Local :

Irritant - Causes readily reversible changes which disappear after exposure

Chronic Systematic :

Ingestion - as above

Inhalation - as above

Toxicity : - May be used as an insecticide

Threshhold Limit values - American Conference of Government and Industrial Hygienists (recommended) 10 parts per million of air, i.e. 50 milligrams per cubic meter of air

Fire Hazard - Moderate when exposed to heat or flame; reacts with oxidising materials.

Spontaneous Heating - No

Explosion Hazard - Moderate, in the form of dust, when exposed to heat or flame.

Countermeasures:

Fire extinction : Water, carbon dioxide, dry chemical or carbon tetrachloride.

Personal protection :
Respirator not usually needed.

Acute poisoning : This is unknown in industrial circles

Chronic poisoning :
Symptoms of nausea, vomiting, headache, and damage to the eye have been described rarely, and are in any case, mild and transitory. Mild skin irritation is also possible.

(d) Saturation Vapour pressure of Naphthalene.

The following formula by Sherwood and Bryant (Ref. 94) was used for the calculation of the saturation vapour pressure of naphthalene:

$$\log_{10}P_N = 11.55 - 3765/T_o \quad \text{for } 0<T_o<303^\circ K$$

where P_N is in torr. and T_o is in $^\circ K$
This variation is displaced in Fig. 3.2

(e) The Schmidt Number for Naphthalene in Air.

This has been estimated by Sherwood and Trass (Ref. 97) to be:

$$Sc = 7.00T_o^{-0.185}$$

for T_o in the range 100 $^\circ K$ to $500^\circ K$

(f) Naphthalene Casting Procedure.

Since the flash point is $86^\circ C$, and the melting point is $80^\circ C$, the best method of casting the material was to use a hot domestic Iron with a flat base. Crystalline naphthalene was poured into the target tray, and the hot Iron applied until the naphthalene was molten. More naphthalene was added, and the 'Ironing' procedure repeated until the molten mass of naphthalene reached the brim of the target tray. Finally, to get a smooth, flat solid surface, the Iron was traversed flush with the edge of the target plate. The process was repeated until a generally flat and smooth surface could be observed. The naphthalene was then left to cool overnight. This method resulted in a fairly smooth, flat solid surface with very few air bubbles. As a result, there was little or no flaking of the naphthalene after casting.

After cooling, the naphthalene surface was subsequently smoothed by successive use of a bench file, and fine emery paper. The flatness was subsequently checked by traversing the surface profile transducer over the surface. This procedure was repeated until a reasonably flat and smooth working surface was obtained.

The local change in profile of the naphthalene surface during a test was of the order of 0.025 mm to 1.0 mm, so that a surface flatness of at least ± 0.013 mm was required prior to the test. Hence it was essential to check the surface flatness and the alignment of the lathe before actually conducting each test.

Difficulties experienced during casting.

(a) Casting temperature.

The use of a hot Iron (of temperature well above 80°C) allowed the naphthalene to melt and flow easily into the casting mould. However, 'over-ironing' resulted in the naphthalene becoming less viscous and more free-flowing. In this state, the formation of air pockets was unavoidable. In order to avoid any air pockets and prevent flaking, it is important not to leave the Iron switched on for too long during casting.

(b) Naphthalene Shrinkage.

On solidification, naphthalene undergoes a volume shrinkage of approximately 17% at about 20°C. If header space is not provided, it is necessary to add more molten naphthalene as the mould solidifies.

(c) Surface Finish.

To avoid the formation of air pockets within the cast naphthalene, it is also necessary to cool slowly. This was effected by leaving the casting covered overnight, avoiding premature solidification at the exposed surface. Large air pockets were removed by melting the surface with the hot Iron. The casting procedure also resulted in the formation of large crystals. These large grain sizes were found to resist flaking off during impingement of the test air on the surface.

APPENDIX D

THE HOT WIRE ANEMOMETER

D.1 General Information

The hot wire anemometer has been developed over several decades, and is now extensively employed in the measurement of turbulence characteristics. It has the required features of rapid response, and fine resolution. Although a standard instrument, it has inherent limitations:

(a) The probe is easily damaged.

(b) The probe can be contaminated by oil and dust so that the calibration changes.

(c) The anemometer makes use of the dependence of wire temperature and hence electrical resistance on the velocity of the fluid passing the probe. It is thus also sensitive to fluctuations in the mainstream fluid temperature.

D.2 Hot Wire Anemometry Heat Transfer Relationship

The rate of heat transfer per unit length ($\dot{Q}/L$) from a long, fine wire positioned normal to a uniform gas stream of velocity U depends on:-

d	the wire diameter
λ	the mean free-path of the gas molecules
T_w, T_f	absolute temperatures of wire and free stream fluid
k,	the fluid thermal conductivity, and diffusivities of momentum at the free-stream temperature.

The heat transfer relationship may be expressed in dimensionless form, in terms of the Nusselt number as:-

$$Nu = f(Re, Pr, \frac{T_w}{T_f}, Kn) \qquad (D.1)$$

where $Nu = \dot{Q}d/(k(\pi dL)(T_w - T_f))$ i.e. the Nusselt number based on wire diameter and surface area.

$$= \frac{\dot{Q}/L}{\pi k(T_w - T_f)}$$

Re = Ud/ν Reynolds number based on wire diameter

Pr = ν/k Prandtl number of fluid

$\frac{T_w}{T_f}$ = the temperature ratio which may be used to take account of variations in fluid properies around the wire.

Kn = λ/d Knudsen number indicating whether continuum flow is established around the wire

Although all the parameters on the right hand side of equation (D.1) can be combined into a few basic groups, the mechanism of heat transfer depends on the special effect of each parameter. It is therefore best to examine the effect of individual parameters on heat transfer, although it may not be necessary to include all of them in the heat transfer relationship. The Prandtl number is nearly constant for all gases over normal operating temperatures. It is taken into account by calibrating in the fluid in which measurements are made.

For gases, continuum flow is established for $Kn < 0.015$; once establishment occurs, the role of Knudsen number is negligible. Normal operating conditions lie near this limit, but so long as the gas density does not change much between the calibration and the measurement conditions, calibration will absorb non-continuum effects.

Eqn. (D.1) neglects the effects of density changes associated with supersonic flows, or otherwise the Mach number would have been included. It also neglects the effects of fluid buoyancy, and therefore free convection effects are not taken into account. The heat transfer relationship can thus be expressed by the basic and simple equation widely known as King's law, and this was used in this investigation. King's law expresses heat transfer from the wire as

$$Nu = A + BU^{\frac{1}{2}} \tag{D.2}$$

Since hot-wire readings are read in terms of voltages eqn. (D.2) is normally written in general terms as

$$E^2 = E_o^2 + BU^n \tag{D.3}$$

and this is valid for $0.45 \leqslant n \leqslant 0.5$

where E_o is the D.V.M. reading for the probe in still air, U is the gas velocity, n and B are constants which can be determined from calibration.

In this investigation, calibration was accomplished by measuring the mean voltage across the wire at a number of mean velocities in the range in which the probe was to be used. From the readings, a graph of $\log(E^2-E_o^2)$ against logU was plotted, from which n was obtained as the gradient and B the intercept on the $\log(E^2-E_o^2)$ axis.

For a more reliable calibration, the data analysis program discussed later was used to find the constants n and B. This program had as input U and E_o in the range 2.5 to 3 in steps of 0.01, and by curve-fitting gave an output for B, n and a correlation coefficient for the range of E_o given as input. The best estimates of E_o, B, and n were obtained from the values corresponding to the value of correlation coefficient nearest unity.

Collis and Williams also obtained a correlation for the heat transfer from the hot-wire which can be used in hot-wire anemometry investigations. They showed that for air, the heat transfer relationship could be expressed as

$$Nu = \left(\frac{T_m}{T_f}\right)^{0.17}(0.24 + 0.56Re^{0.45}) \quad \text{for } 0.02 \; Re \; 44 \qquad (D.4)$$

where the temperature $Tm = \dfrac{T_w + T_f}{2}$ is the mean film temperature.
If the free stream temperature and temperature dependent properties remain constant, and if in addition, the pressure is uniform and the temperature loading factor T_f/T_m does not vary significantly, the relationship suggested between heat transfer and velocity is

$$\dot{Q}/(T_w-T_f) = A + BU^{0.45} \qquad (D.5)$$

where A and B are constants.

The heat transfer from the sensor of a hot-wire anemometer is influenced by several factors not considered by King's law or Collis and Williamson's expressions. These include:-

(1) non-uniformities in temperature and flow pattern near the ends of the sensor

(2) the accretion of 'dirt' during operation. These include dust, lint and oil in the gases.

(3) 'ageing', i.e. the physical and geometric changes which occur during prolonged use at high temperatures and velocities.

(4) rapid variations in the direction and intensity of the turbulence and velocity around the wire, and

(5) variations in the temperature and other properties of the ambient fluid.

However, the general nature of the heat transfer characteristics of a hot-wire probe is indicated by eqns. (D.3) and (D.5), and many aspects of some of these complications are accommodated by calibration.

D.3 Probe Calibration and Data Analysis Programs

D.3.1 Probe Calibration Program

Theory

In hot-wire anemometry, King's law is expressed as:-

$$E^2 = E_o^2 + BU^n \qquad \text{(eqn. D.3)}$$

where E, E_o, B, U, and n are as defined in the Nomenclature.

$$\text{Therefore } \log(E^2 - E_o^2) = \log B + n\log U \qquad (D.6)$$

In order to get the constants E_o^2 and B and the index n in equation (D.6), this program finds the best fit to the plot of $\log(E^2 - E_o^2)$ against log U.

D.3.2 Data Analysis Programs

The following programs were used to calculate velocity and turbulence intensity distributions.

Theory

From the hot-wire relationship

$$E^2 = E_o^2 + BU^n \qquad \text{(eqn. D.3)}$$

The velocity U may be expressed as

$$U = ((E^2 - E_o^2)/B)^{1/n} \qquad (D.7)$$

where E_o^2, B, and n are known from the previous program.

The turbulence intensity is:-

$$\frac{dU}{U} = \frac{2E.dE}{n(E^2 - E_o^2)} \qquad (D.8)$$

where dE is the r.m.s. meter reading of the DISA Unit and dU/U is the turbulence intensity based on the local velocity.

$$\frac{dU}{U_{max}} = U/U_{max}\left[\frac{2E.dE}{n(E^2 - E_o^2)}\right] \qquad (D.9)$$

This expression gives the radial turbulence intensity based on the centre-line velocity at any section along the jet's axis. The Wang 600 Series calculator was used in the calculation.

APPENDIX E

FLOW VISUALISATION

E1. Characteristics of Oils Commonly used in Surface Flow Visualisation

The following is a brief description of some oils which can be used in oil film flow visualisation. SAE motor oil classifications are also shown in Fig. 6.2.

(a) Service Oils.

OM-13 : A light mineral oil of low pour point (-46°C) containing 0.05 to 0.1% of Stearic acid.

OM-15 : Aviation hydraulic fluid. This has a petroleum base together with an oxidation inhibitor, a viscosity index improver, and an anti-wear agent (pour point is -59°C)

OM-108 : A refined filtered mineral oil of SAE 30 grade (pour point is -18°C).

OM-160 : A refined mineral oil (pour point is -12°C).

OM-270 : A plain mineral oil (pour point is -12°C).

(b) Proprietary Oils.

Shell Group Oils

Carnea 35 : A plain mineral oil (pour point is -12°C). Specific gravity at 15.6°C is 0.933

Limea 931 : A plain mineral oil (pour point is -12°C). Specific gravity at 15.6°C is 0.935

Macoma 76 : A mineral oil with mild E.P. additive in the form of soap (pour point is -7°C). Specific gravity at 15.6°C = 0.936

Nassa 79 : A plain mineral oil (pour point is 10°C). Specific gravity at 15.6°C is 0.905.

Nassa 87 : A plain mineral oil (pour point is 7°C). Specific gravity at 15.6°C = 0.908

Rimula 30 : A mineral oil of SAE 30 grade with polar detergent additive (pour point is -18°C). Specific gravity at 15.6°C is 0.912

Vtrea 72 : A plain mineral oil (pour point is -7°C) Specific gravity at 15.6°C = 0.880

Edgar Vaughan & Co. Ltd. Oils.

EVCO Medium Turbine Oil : Specific gravity at 15.6°C = 0.880

(c) Other Oils.

Various vegetable oils such as castor oil and linseed oil, all of which contain fatty acids are also used together with various paraffins (as in the present investigation).

(d) Silicone Fluids.

Midland Silicone MS 200/500 cs
MS 200/1000 cs
MS 200/12,500 cs

These are dimethyl Silicone fluids with characteristically high viscosity index.

E2 Oil-Film Mixture Development and Application for Surface Flow Visualisation

E2.1 General

The oil mixture should be of such a consistency that under the test conditions, it can run and flow under the action of the fluid surface flow, and leave behind clearly defined streaks of pigment to mark the local flow directions. These patterns should also be bold enough for examination and photography, and yet fine enough to portray all the significant details of the surface flow. Ideally, the oil should only start to run under the influence of the surface fluid flow, and moreover, the pattern should be sufficiently dry for examination within a fairly short time. In order to meet the above conditions, and produce patterns of consistently good photographic quality, considerable care is needed in preparing the oil mixture. This involved an appropriate choice of oil, pigment and additives. It was also important for them to be mixed in suitable proportions.

E2.1.1 Choice of a Suitable Oil.

The choice of a suitable oil is largely determined by the time necessary for a clearly defined pattern to develop. This of course, depends on the wind-tunnel operating conditions. A light oil (of low viscosity) such as kerosene is suitable for low wind-tunnel speeds while heavy oils (e.g. diesel oil) are suitable for high speed flows. The major factors affecting the rate of flow are the oil viscosity and the skin friction (Ref. 126), provided the film is sufficiently thin (Ref. 129). Stanbrook (Ref. 121), established a theoretical relationship for the approximate running time for a pattern to develop. His relationship is given by:-

$$t = \text{Constant} \times \frac{\mu_{oil}}{q \times C_f}$$

where C_f = local skin friction coefficient

μ = dynamic viscosity $(\rho\nu)$

q = dynamic pressure, and

the constant = 36,00 ±12,000

In this investigation, paraffin was used, and after 15 minutes test time the clearly defined patterns were sufficiently dry for examination.

E2.1.2 Choice of Pigment.

The pigments act as the tracer particles. The stiffness of the oil mixture and the formation of streaks depend on the size of the pigment particles and the forces of attraction between them (Refs. 121, 126 & 137) as well as the oil viscosity. It is therefore necessary for the chosen pigment to have the correct flow characteristics and to produce a clear pattern against the background surface.

Titanium dioxide, an opaque non-toxic pigment is often used for making high contrast patterns on a dark background. In this investigation however, lampblack was used and it gave good contrast against the background provided by white photographic paper. Lampblack is a greyish carbon pigment with a basic particle diameter of the order of 0.1 µm. It is marketed by:-

Fisons Scientific Apparatus Ltd.
Loughborough, Leics.

Other substances used in oil film compositions have included China Clay (Kaolin), Anthracene $C_{14}H_{10}$, Chrysene $C_{18}H_{12}$ and 'Dayglo' pigments.

E2.1.3 Function and Choice of Additives.

Additives can be used as anti-coagulants or dispersing agents. They control the size of the conglomerations (flocs) formed by the pigments in an oil suspension. They join individual pigment particles to individual fluid molecules, the additive forming the link. Without the additive, the finely divided solid pigment particles tend to link together in a net-work on the test surface and resist the skin friction effect. With excess additives, the pigments get fully dispersed, and move individually. In either of these extremes, no streaks can be formed. So it is important to use the correct quantities of pigment and an appropriate additive.

A large variety of additives are known, of which Oleic acid and linseed oil are commonly available examples. However, oleic acid, in common with most of the fatty acid dispersing agents, tends to lose its effectiveness gradually through oxidation and polymerisation. Trial and error methods are inevitable to determine suitable quantities when additives are used in oil mixture compositions. In this investigation, oleic acid was employed.

E2.2 Procedure for Preparation of an Oil Film Mixture.

30 gm. of lampblack and approximately 30 ml of oleic acid were added to 250 ml of paraffin oil contained in a beaker. The mixture was stirred thoroughly using a brush, and the contrast with the photographic paper checked. The sharpness of the contrast depends a good deal on the background so that trial and error methods are inevitable in mixing these constituents in appropriate proportions to obtain the required contrast. The above composition was used in the present study, and may be regarded as a rough guide for the composition of an oil mixture. Slight variations may be necessary, depending on the quality of the contrast required.

It was noticed that if the mixture was stored for a few days, the composition and therefore the quality of contrast changed. This was due to the fact that the paraffin volatilised and decreased in concentration, and the oleic acid changed its effectiveness through oxidation. Consequently, the concentration of lampblack was increasing, resulting in the contrast changes. Mixtures stored for a few days therefore required the addition of further oleic acid and paraffin in appropriate proportions.

E3 Application of the Oil Film Mixture.

This is a simple operation but great care is needed to obtain good results. The oil film was painted on to the photographic paper. This film was applied in single strokes, with the axis of the brush slewed to the direction of motion. This resulted in an even film. Some trials were, however, required to determine the correct thickness of the film coating. When the film was too thin, the mixture dried up before a well-defined pattern could be obtained. When the film was too thick, it took too long to dry, and there was the added risk of oil seeping through to the underside of the photographic paper (this side is not resistant to oil). The paper was then soaked

TABLE E.1

OIL FILM FLOW VISUALISATION MIXTURES

QUANTITY	CONSTITUENT
(a) High Speed Flow	
10 ml	Titanium Dioxide
20 ml	Silicon Oil (500 centistokes)
2 ml	Oleic Acid
(b) Low Speed Flow	
50 gms	Titanium Dioxide
150 ml	Paraffin
12-15 ml	Oleic Acid

N.B. Less Oleic Acid is required if the mixture is prepared well in advance of the test.

Suppliers

Titanium Dioxide TiO_2
May and Baker

Silicon Oil
Midland Silicones (MS.200)

Oleic Acid - Pictograph

and the contrast destroyed. Therefore, in all tests, considerable care was taken to ensure that a moderate oil-film thickness was obtained to avoid either of the above extreme situations.

E4 Additional Information on Surface Flow Visualisation.

As previously mentioned, Titanium dioxide is another tracer particle commonly used in oil film mixtures. Silicon oil has been used in the past in oil flow investigations, and the appropriate compositions of Silicon-oleic acid-Silicon oil film mixtures for low and high speed flow investigations are given in Table E.1.

E5 Smoke Flow Structure Visualisation

The smoke pellets used in the present investigation can also be used to generate smoke for a variety of engineering purposes. These include:-

(1) Tracing faults in chimneys
(2) Testing Extractor fans
(3) Adjusting the throw of fans and unit heaters
(4) Testing drains, soils, pipes and old heating systems for leaks.
(5) Testing newly erected boilers for air in-leaks
(6) Testing plenum, ducted ventilation and air-conditioning plants.

In all these applications, including the present investigation, the smoke, according to the manufacturers is harmless, but should not be inhaled unnecessarily. If the smoke is generated inside rooms, all bright metallic objects should be covered or removed as there is a danger of tarnishing. The smoke pellets used in this investigation are marketed by:-

P.H. Smoke Products Ltd.
Fairfield Works,
Eldwick, Yorkshire.

APPENDIX F

ERROR ESTIMATION AND PRECAUTIONS FOR ACCURACY IN THE EXPERIMENTAL WORK

For any input quantity E_i producing an output quantity E_o, their relationship can be expressed mathematically as:-

$$E_o = f(E_i) \qquad (F.1)$$

Generally, no instrument will obey this exact relationship but the output can be expressed as:-

$$E'_o = f(E_i) + R \qquad (F.2)$$

where R is an absolute error, i.e. the difference between the observed output and what it should be. The fractional error is:-

$$\frac{R}{E_o} = \frac{R}{E'_o} \qquad (F.3)$$

This is composed of several components:-

(a) Human error which is an error due to the observer e.g. a scale error which can be due to parallax in a scale reading or a dynamic error which can be caused by an observer's finite reaction time or an over-optimistic anticipation of the expected results.

(b) Random error which includes frictional effects, sufface tension effects, noise and drift in the electrical equipment.

(c) Systematic error which is solely due to the measuring system. This can be subdivided into:-

(i) a response to the conditions of the environment e.g. changes in temperature, humidity, pressure, and electric fields.

(ii) a dynamic error in which the output does not faithfully follow changes with time of the input quantity, and
(iii) a scale error in which the output deviates from the correct output by an amount which is a constant additive factor for the range of the instrument. The observed output for instance, can deviate from the correct output value by a constant multiplying factor.

A statistical analysis and other related information for the theory of errors are given in Paradine and Rivett (Ref. 139). In this investigation, instrument errors, or errors associated with quantities calculated from other measurements which were liable to error were estimated statistically as follows:-

(i) Fractional Errors Associated with Instrument Readings, $\frac{R}{E'_o}$

Let $y = f(E'_o, e'_o)$ (F.4)

Then $\delta y = \frac{\partial f}{\partial E'_o}\delta E'_o + \frac{\partial f}{\partial e'_o}\delta e'_o$ (F.5)

where y is a function of the two readings E'_o, and e'_o.

δy is the absolute error in $\delta E'_o = R$

A knowledge of the instrument error therefore makes it possible for their effects on values derived from the readings to be ascertained.

(ii) Uncertainty Associated with Combined Errors

The uncertainty (σ) in y (eqn. F.4) is given by:-

$$\sigma_y^2 = \left(\frac{\partial f}{\partial E'_o}\right)^2 \sigma^2_{E'_o} + \left(\frac{\partial f}{\partial e'_o}\right)^2 \sigma^2_{e'_o} \qquad \text{(F.6)}$$

where σ_y^2, $\sigma^2_{E'_o}$, and $\sigma^2_{e'_o}$ are the variances of y, E'_o, and e'_o respectively.

Equations (F.5), and (F.6) were the relevant statistical relationships used to introduce corrections on the measured or estimated quantities in this investigation.

Typical results of statistically determined or estimated errors for some of the important parameters are:-

(a) Hot Wire Calibration Errors

The calibration program incorporated statistical estimates of calibration errors, and from the output:

The standard error in the index n = 0.6%

Standard error in the constant B = 1%

Sources and magnitude of other errors are tabulated below.

(b) Measurements of local variations of naphthalene loss.	This was measured with the linear transducer calibrated to ±0.3%. The readings were clearly influenced by reading errors (approx. estimated at ±1% on individual readings) and random errors discussed earlier in this Appendix.
(c) Assumption that naphthalene surface and ambient temperatures were equal.	Small differences existed between the ambient air temperature, and naphthalene surface, but the use of coolers minimised this to approximately 2 degrees C generally (and no more than 2°C). Thus expansion errors will be small.
(d) Temperature measurements	Reading ranges and accuracies were given in chapter 4. For the mercury-in-glass thermometers, the error is approximately ±0.6% on individual readings.
(e) Measurement of air flow and delivery pressure.	The tolerance on the calibration of the orifice plates was 1.5%. The error in the pressure readings was ±0.05-in water gauge.

Precautions for Accuracy in the Experimental Work

Although some of the following may appear obvious or trivial, they are included to assist researchers engaged in this field and employing similar techniques and procedures. A brief summary of some of the important precautions mentioned earlier is also included, and it is hoped this will assist in avoiding similar errors in future investigations. They are also intended to assist in minimising Human, Random, and Systematic errors described in the opening paragraphs of this Appendix.

(1) The position of the test rig is of major importance. This should be in a draught-free position, but set well clear of other objects. The proximity of walls, etc. was found to have an adverse effect on the air flow over the naphthalene surface. At least 0.7 m should separate the test rig from other surfaces.

(2) The naphthalene surface in the target tray was very prone to damage. It was noted that if a rough surace existed at the start of a test, the roughness tended to increase during the test, making the profile readings difficult.

(3) The source of greatest possible error, is the drift in the air temperature, and hence the naphthalene surface temperature, particularly during along test. To overcome this problem, temperature readings were taken at regular intervals of 30 minutes, and an average used. Also, over tests of long duration, the barometric pressure can alter considerably. Again, an average of several readings was used.

(4) In the course of a test, it is important to ensure that air cannot escape through the joints, particularly after orifice-metering. Joints should be masked with plasticine. Also, flexible piping is prone to damage and this can be difficult to detect. Therefore, considerable care is needed in handling the flexible piping and other connections downstream of the orifice-metering station. Regular checks are needed.

(5) The instrumentation requires care to ensure accuracy in the measurements. Errors associated with instrumentation readings and their analysis was discussed earlier in this Appendix. It was found that the manometers needed to be perfectly clean to read correctly, since foreign bodies in the tubes can greatly affect the accuracy. Imperfect joints and leakages made manometer readings unreliable. The joints therefore needed considerable care and attention.

(6) Thermometers should be examined carefully before use so that breaks in the mercury thread can be detected.

(7) In a laboratory used by many people, damage to, or adjustment of equipment during absences cannot be ignored. It was found that the X-Y recorder with transducer connections, once set up needed care as the slightest adjustment, inadvertent vibrations, or knocks necessitated recalibration. It was therefore necessary to check the calibration of both short and long stroke transducers before and after each test run.

(8) Electric and electronic instrumentation requires a considerable period of time to 'warm up'. The X-Y recorder in particular, tended to move erratically for the first 30 minutes after switching on. For this reason, all electrically powered instruments were allowed at least half an hour to settle before readings were taken. For tests of short duration, the instruments were left switched on.

(9) In the flow visualisation tests, the pipes leading into and out of the smoke drum tended to be clogged with thick greasy wastes; after carrying out smoke tests for a considerable length of time. This impairs the quality of smoke marking the path of the jet, and is undesirable. To obtain dense white smoke, it was essential to clean these pipes fairly often, preferably after each test.

APPENDIX G

SAMPLE CALCULATIONS

(a) Volume Flow Calculations.

All volume flow calculations were carried out in accordance with BS1042 Part 1, 1964.

Barometric Pressure (P_a) = 29.9" Hg
= 14.68 lbf/in^2

Inlet Pressure to Orifice (P_L) = 8.04" H_2O
= 0.2905lbf/in^2

Total Pressure at Orifice Inlet (P_T) = 14.97 lbf/in^2

Line Temperature (T_L) = 14°C
= 287°K

Average Temperature at Naphthalene Surface (T_N) = 16.7°C
= 289.7°K

$$\frac{\text{Orifice diameter, } d}{\text{Pipe diameter } D} = \frac{1.5}{3.25} = 0.462$$

From P. 208 (BS1042) $mE = 0.2180$
$E = 1.0234$
Therefore $m = 0.213$

From P. 120 (BS1042) $C = 0.6045$

From P. 41 (BS1042) $\delta = 1$

From P. 50 (BS1042) $K = 1$

Assuming dry air (Clause 26 BS1042)

$$\rho_L = \frac{2.7 \times \delta \times P_T}{K.T_L} = \frac{2.7 \times 1 \times 14.97}{1 \times 517.2} = 0.0782\ \mathrm{lb/ft^3}$$

From P. 61 (BS1042) $\mu = 1.75\times10^{-4}$ poise

From P. 120 (BS1042) $Z\epsilon = 1$

Approximate Volume Flow $Q_A = 359.2.C.Z\epsilon.E.d^2\sqrt{(h/\rho_L)}$

where h = Pressure difference across orifice in "H_2O
and d = Orifice diameter.

Reynolds number based on Orifice diameter Re_d

$$= \frac{Q_A \cdot \rho_L}{15.8 x \mu x d}$$

$$= 11,177$$

From PP. 120-121 (BS1042) $Z = Z_R.Z_D$

$$= 1.017$$

$$\gamma = 1.4$$

$$h/P_T = 0.007$$

From P. 122 (BS1042) $\epsilon = 1$

Corrected Volume Flow Rate $Q_c = Q_A.Z.\epsilon$

$$= 603.29 \text{ ft}^3/\text{hr.}$$

Volume Flow at Naphthalene Surface, Q_N

$$= Q_c(P_T.T_N)/(P_a.T_L)$$

$$= 621 \text{ ft}^3/\text{hr.}$$

$$= 0.0049 \text{ m}^3\text{s}^{-1}$$

(b) Calculation of Jet Velocity and Reynolds Number Based on Nozzle Diameter and Arrival Velocity of Jets.

ρ air at T_N (from Ref. 141) $= 1.2198 \text{ kg/m}^3$

Area of Nozzle A

$$= \frac{\pi x d^2}{4}$$

$$= \frac{\pi x 12.7^2 x 10^{-6}}{4} \text{ m}^2$$

$$= 1.267\times10^{-4} \text{ m}^2$$

Jet Velocity $U_j = Q_N/A$

$$= 38.6 \text{ ms}^{-1}$$

Reynolds Number (Re_d) $= \frac{\rho . U . d}{\mu}$

$= \frac{1.2198 \times 38.6 \times 0.5 \times 0.3048}{1.8276 \times 10^{-5} \times 12}$

$= 32,719$

$= 32,700$ (approx.)

(c) Calculation of Local Heat Transfer Coefficients For the Target Plate.

The Saturation Vapour Pressure of Naphthalene is given by:-

$\log_{10} P_N = 11.55 - 3765/T_N$

$= 11.55 - 3765/287$

This gives $P_N = 0.0358$ mm Hg

$= 4.771$ N/m^2

Schmidt Number (Sc) $= 7.0 \times T_N^{-0.185}$

$= 2.45216$

$(Sc)^{\frac{2}{3}} = 1.8187$

Density of Naphthalene ρ_N at T_N = 1145 kg/m^3

Gas Constant for Naphthalene Vapour R_v = 64.7 J/kgK

Duration of test (t) = 11160 s

At T_N $C_{p_{air}}$ = 1.00446 kJ/kgK

= 1004.46 J/kgK

$$Pr = 0.7094$$

$$Pr^{\frac{2}{3}} = 0.7954$$

$$(Sc/Pr)^{\frac{2}{3}} = 2.287$$

$$h = \frac{\rho_N \cdot R_v \cdot T_N \cdot \rho_{air} \cdot C_{p_{air}} \cdot (Sc/Pr)^{\frac{2}{3}} \cdot \Delta x 10^{-3}}{t x P_N} \quad W/m^2K$$

where Δ is the naphthalene loss in mm and
C_p is expressed in J/kgK

$$h = 1129.2\Delta \quad W/m^2K$$

(d) Calculation of Stagnation Point Nusselt Number Nu_o

$$Nu_o = h_o d/K$$

$$= \frac{320 x 12.7 x 10^{-3}}{0.025456}$$

$$= 160$$

Predicted Stagnation Point Nusselt Number:

$$Nu_O = 0.0233 Re^{0.87} Pr^{0.33} \qquad \text{(Huang Ref. 60).}$$

$$= 0.0233(32,700)^{0.87}(0.7094)^{0.33}$$

$$= 176$$

APPENDIX H

ADDITIONAL WORK

Fig. H.1 shows the effect of crossflows on stagnation point heat transfers. It presents the ratio of the heat transfer in crossflow to the no crossflow case as a function of jet blowing rate, for orthogonally impinging jets. It may be noticed that at a fixed nozzle to target spacing (e,g. Z/d = 8), dimensionless stagnation point heat transfers generally decrease as the blowing rate decreases, i,e. stagnation heat transfers generally decrease as crossflow is applied. A similar effect was observed by Sparrow et al (Ref. 82), and the approximate reductions observed by these investigators at Z/d = 8 and Z/d = 4 are also included. It should be emphasised that Sparrow did not conduct tests in the absence of crossflow. Thus the stagnation heat transfers at a high blowing rate of 12 has been used as the datum. The stagnation heat transfer 'degradation' curves are generally S-shaped.

At the nozzle to target spacing of 2 jet diameters, the decrease in stagnation point heat transfers is much less pronounced over a considerable range of blowing rates. It is thus interesting to note that Bouchez (Ref. 81) recorded slightly higher stagnation point heat transfers at low nozzle to target spacings under crossflows. At the lowest nozzle to target spacing, this investigation further suggests that the stagnation heat transfers in crossflows are generally of about the same order as those obtained in the absence of crossflows, over a wider range of blowing rates than those at higher nozzle to target spacings. This present investigation also suggests that for all nozzle to target spacings, the 'degradation' curves for stagnation heat transfers decrease asymptotically towards the values due to crossflow alone. Apart from these, the local heat transfer variations show similar trends to those observed by Sparrow et al (Ref. 82).

Fig. H.2 shows the repeatability of the measurements. The results of 3 tests are presented as the axial heat transfer variations. The conditions were maintained constant during these tests, and refer to an impinging orthogonal jet at a nozzle to target spacing of 8 jet diameters. It is interesting to note that in all three rums, the distribution curves are 'bell-shaped' as described previously. It is also worthy of notice that, in agreement with previously reported results, obtained using the naphthalene sublimation technique, the present result exhibits good repeatability, since it is very difficult to predict or measure heat transfers to an accuracy of ±10% (Ref. 146).

FIG. H.4. EFFECT OF CROSSFLOWS ON DIMENSIONLESS STAGNATION POINT HEAT TRANSFERS FOR IMPINGING ORTHOGONAL JETS

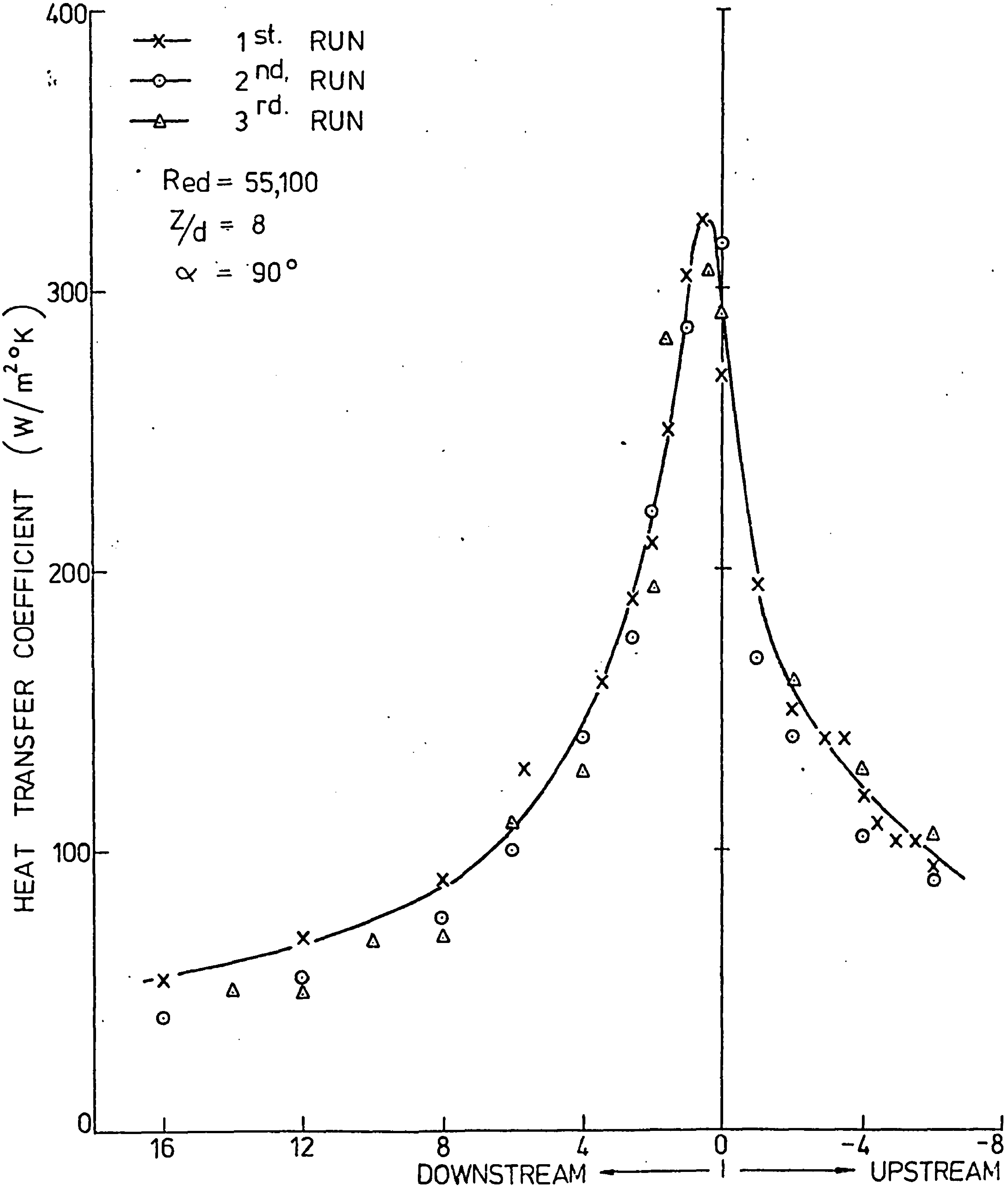

DIMENSIONLESS DISTANCE(X/d) MEASURED FROM CENTRE-LINE OF INITIALLY ORTHOGONAL JET.

FIG. H.2. REPEATABILITY CURVES FOR AXIAL VARIATION OF LOCAL HEAT TRANSFER COEFFICIENTS